Universidad de Valladolid

Escuela de Doctorado Universidad de Valladolid

PROGRAMA DE DOCTORADO EN INGENIERÍA INDUSTRIAL

TESIS DOCTORAL:

Study of Premixed Combustion Induced by Controlled Hot Surface Ignition in Stationary Gas Engines

Presentada por Fino Scholl para optar al grado de Doctor/a por la Universidad de Valladolid

Dirigida por:
Dr. Blanca Giménez Olavarría
&
Dr.-Ing. Maurice Kettner

Universidad de Valladolid

Doctoral Thesis

Study of Premixed Combustion Induced by Controlled Hot Surface Ignition in Stationary Gas Engines

Presented by:

Fino Scholl, M.Sc.

Directed by:

Dr. Blanca Giménez Olavarría

&

Dr.-Ing. Maurice Kettner

Valladolid/Karlsruhe, 2017

Examining board

President: Dr. Francisco Tinaut Fluixá

Secretary: Dr. Magín Lapuerta Amigo

Speaker: Dr.-Ing. Ulrich Spicher

Acknowledgements

The present thesis was written during my time working as a research fellow at the Institute of Refrigeration, Air Conditioning and Environmental Engineering (IKKU), Hochschule Karlsruhe - Technik und Wirtschaft, Germany. It is the result of an intensive and highly fruitful, binational cooperation with the Department of Energy and Fluid Mechanics Engineering at University of Valladolid, Spain.

First and foremost I would like to express my deepest gratitute to the directors of my thesis, Dr. Blanca Giménez Olavarría from Valladolid and Prof. Dr.-Ing. Maurice Kettner from Karlsruhe, for the continuous support and guidance, the uncountable technical discussions, and for giving me the opportunity of pursuing a Ph.D. in the first place. I am certain that the trust they put in me combined with the liberties I was given during project management, especially from my direct superior Prof. Kettner, were decisive factors that motivated me to go on and never lose the passion for research. Furthermore I want to thank my tutor Dr. Andrés Melgar Bachiller who encouraged me to develop the 0D model, allowed me to conduct large sets of experiments using the installations in Valladolid and opened my „engineer“ mind to a more „scientific“ way of thinking.

For their time, interest in my work and helpful comments I would like to thank the members of the examining board, Dr. Francisco Tinaut Fluixá, Dr. Magín Lapuerta Amigo and Prof. Dr.-Ing. Ulrich Spicher as well as the external reviewers Dr. Rizalman Mamat and Dr. Luigi Sequino.

Special thanks go to the former dean of the Faculty of Mechanical Engineering and Mechatronics and now rector of Hochschule Karlsruhe, Prof. Dr.-Ing. Frank Artinger, for his backing and financial support, and to the faculty workshop for machining several components for the test bed and manufacturing countless prototypes. Over the past years, many students were involved in this project in one way or the other. For their contribution and assistance, which were essential, I am also very grateful.

I very much appreciate the support given by SenerTec Kraft-Wärme-Energiesysteme GmbH by prodiving the test bed engine, consumables and the assistance during engine

setup and trouble-shooting. Without the numerous discussions and helpful input from Dr.-Ing. Markus Klaissle und Danny Schwarz, this work would not have been possible. Furthermore, I would like to thank Dr.-Ing. Jochen Hammer and Ulrich Stephan from BorgWarner BERU Systems for providing all glow plugs used in engine testing, Dr.-Ing. Kai Beck from MOT GmbH for his support during the design and manufacturing phase of the optical adapters and AVL List GmbH for granting licenses for running 1D/3D CFD simulations.

Over the past years, the work atmosphere and team spirit in the growing IKKU Engine Research team have been exceptional and incomparable. I want to thank my current and former colleagues for the unforgettable time and hope that our paths will cross again. While Jürgen Bauer and Waldemar Rieb have been missed for quite some time now, Artur Martel and Jörn Judith will certainly keep the *engine running*. I would never say this to his face but sharing the past twelve years with my colleague Denis Neher, starting with the first semester in university, has been rather *pleasant*. I cherish the numerous memories, spanning from fancy dress parties in Cardiff, extensive study sessions with *Maultaschen* and coffee, late-night paper corrections, nerve-wrecking test-bed reparations to "*would you rather…?*" Q&A sessions to stay awake while driving back from Valladolid to Karlsruhe. As president of the FIOFA[1], it further is my duty, yet also my pleasure, to thank the members of the association, Ephraim Gukelberger, Jörn Judith and Denis Neher for the spectacular, not seldom controversial, matches. Keep the tradition alive!

Last but not least, I would like to thank my family: my mother Gabriela and both my fathers, Jürgen and Rolf, without whose support none of this would have been possible. They gave me the freedom to decide and enabled me to follow this path. For that I am forever grateful; my brother Andro and his own little family for always being there; and Aline for her continuous encouragement, her unlimited patience and her ability to fully take my mind off work and focus on other things in life.

Karlsruhe, September 2017 Fino Scholl

[1] FIOFA: Fédération Internationale de Office Football Association

Abstract

Lean-burn combustion of premixed air-natural-gas mixtures enables small-scale stationary gas engines to operate at high engine efficiency while emitting low levels of CO_2 and pollutants. Increasingly stringent limits for nitrogen oxides, however, pose a major challenge to lean-burn operation if the aim is to meet the new limits through combustion-related measures without losses in engine efficiency. As alternative to spark ignition, a new Hot Surface Ignition (HSI) system was developed that facilitates a rapid and safe ignition of more diluted mixtures. The system essentially consists of a shielded ceramic glow plug, whose temperature can be controlled in a highly dynamic manner by adjusting the voltage applied, thereby allowing for the phasing of combustion to be adjusted during engine operation.

The present work describes the systematic methodology adopted to study the process of HSI induced combustion. For an in-depth analysis of the ignition process and the subsequent flame propagation, a combined approach of 3D fluid dynamics and combustion simulation and engine experiments with multiple single-fibre optical accesses to the combustion chamber is pursued. Design of Experiments (DoE) methods are used to determine the ignition system's operation limits and to study the effect of several operating parameters, like intake manifold pressure and relative air-fuel ratio, on the combustion process and the thermo-electric properties of the glow plug. The direct comparison to state-of-the-art prechamber spark ignition unfolds the positive and negative aspects of the current HSI design and allows for future steps in system development and optimisation to be derived.

Keywords: Gas Engine – Hot Surface Ignition – Lean-burn Combustion – Natural Gas

Resumen

La combustión de mezclas pobres de aire y gas natural premezcladas permite que motores a gas usados en unidades de micro-cogeneración funcionen con alto rendimiento, produciendo, al mismo tiempo, bajos niveles de CO_2 y emisiones contaminantes. Sin embargo, normativas medioambientales cada vez más restrictivas, sobretodo con respecto a los óxidos de nitrógeno (NO_x), suponen un reto para la combustión de mezclas probres si se trata de cumplir las normativas sólo a través de medidas relacionadas con la combustión, sin pérdidas en el rendimiento del motor.

Como alternativa al encendido por chispa, se ha desarrollado un nuevo sistema de encendido por superficies calientes controladas (Hot Surface Ignition - HSI) que facilita una ignición rápida y segura de mezclas muy diluidas. El sistema consiste de una bujía incandescente cerámica "apantallada", cuya temperatura puede ser controlada de forma altamente dinámica mediante el ajuste de la tensión aplicada. Eso permite ajustar el comienzo del proceso de combustión durante el funcionamiento del motor.

La presente tesis doctoral describe la metodología sistemática adoptada para estudiar el proceso de combustión inducida por HSI. Para un análisis profundo del proceso de ignición y de la propagación de la llama, se combinan simulaciones de dinámica de fluidos en 3D y combustión con experimentos usando múltiples accesos ópticos a la cámara de combustión del motor. Métodos de diseño de experimentos (DoE) se utilizan para determinar los límites de funcionamiento del sistema de encendido y para estudiar el efecto de varios parámetros de operación, como la presión del colector de admisión y el dosado relativo de la mezcla, sobre el proceso de combustión y las propiedades termoeléctricas de la bujía incandescente. La comparación directa con el encendido por chispa en precámara, la tecnología del estado del arte, despliega los aspectos positivos y negativos del diseño actual de HSI y permite derivar pasos futuros en el desarrollo y la optimización del sistema.

Palabras clave: Motor a gas – Encendido por superficies calientes – Combustión pobre – Gas natural

Kurzfassung

In stationären erdgasbetriebenen Gasmotoren kleinerer Leistungsklassen ermöglicht die Verbrennung homogener magerer Gemische hohe mechanische Wirkungsgrade bei gleichzeitig geringem CO_2- und Schadstoffausstoß. Insbesondere verschärfte Stickoxidgrenzwerte stellen den Magerbetrieb vor die Herausforderung, diese innermotorisch ohne Wirkungsgradeinbußen einhalten zu können. Um als Alternative zur Funkenzündung, stärker verdünnte Gemische schnell und sicher entflammen zu können, wurde ein auf der Zündung an heißen Oberflächen basierendes Zündsystem entwickelt (HSI – Hot Surface Ignition). Es besteht im Wesentlichen aus einer abgeschirmten keramischen Glühkerze, deren Temperatur durch Variation der Bestromung hochdynamisch geregelt werden kann und dadurch das Anpassen der Verbrennungsschwerpunktlage im Motorbetrieb ermöglicht.

Die vorliegende Arbeit beschreibt die systematische Vorgehensweise zur Untersuchung der durch HSI eingeleiteten Verbrennung. Die Analyse des Entflammungsvorgangs und der anschließenden Flammenausbreitung erfolgt mittels Kombination aus dreidimensionaler Strömungs- und Verbrennungssimulation und Mehrlichtwellenleitertechnik zur Aufzeichnung von Verbrennungsstrahlung im motorischen Betrieb. Unter Verwendung von Methoden der statistischen Versuchsplanung (DoE - Design of Experiments) erfolgt die Bestimmung der Betriebsgrenzen des Zündsystems sowie die Untersuchung des Einflusses verschiedener Betriebsparameter, wie Saugrohrdruck und Verbrennungsluftverhältnis, auf den Verbrennungsprozess und das thermoelektrische Verhalten des Glühstifts. Durch den direkten Vergleich zum Referenz-Zündsystem, der Vorkammerfunkenzündung, können die Vor- und Nachteile des aktuellen Konstruktionsstands bestimmt und künftige Entwicklungs- und Optimierungsschritte abgeleitet werden.

Schlagworte: Gasmotor – Oberflächenzündung – Magerverbrennung – Erdgas

Contents

Abbreviations and Symbols

Abbreviations

	Description
0/1/3D	0/1/3 Dimensional
A/B/C/D/E	DoE Factors
ADC	Analogue-Digital Converter
AFR	Air-fuel Ratio
AI	Analogue In
AIT	Autoignition Temperature
ANOVA	Analysis of Variance
AO	Analogue Out
ASTM	American Society for Testing and Materials
ATDC	After Top Dead Centre
BImSchG	Bundes-Immissionsschutzgesetz
BMEP	Brake Mean Effective Pressure
BPI	Bowl Prechamber Ignition
BSFC	Brake Specific Fuel Consumption
BTDC	Before Top Dead Centre
CCV	Cycle-by-cycle Variations
CD	Combustion Duration
CFD	Computational Fluid Dynamics
CFM	Coherent Flame Model
CGP	Ceramic Glow Plug
CHP	Combined Heat and Power
CHSI	Catalytic Hot Surface Ignition
CPT	Catalytic Plasma Torch
CVCC	Constant Volume Combustion Chamber
DAC	Digital-Analogue Converter
DC	Direct Current
df	Degrees of Freedom
DI	Direct Injection
DIG	Direct-injected Gas

DIN	Deutsche Industrienorm
DING	Direct-injected/Direct Induction Natural Gas
DoE	Design of Experiments
ECFM-3z	Extended Coherent Flame Model – 3 Zones
ECU	Electronic Control Unit
EGA	Exhaust Gas Analysis
EGR	Exhaust Gas Recirculation
EN	European Norm
EOC	End of Combustion
EU	European Union
FDS	Fraction of Design Space (DoE)
FMEP	Friction Mean Effective Pressure
F-value	Ratio of Variances (ANOVA)
HC	Unburnt Hydrocarbons
HCCI	Homogeneous Charge Compression Ignition
HFM	Heißfilm-Luftmassenmesser
HS	Hot Surface
HSI	Hot Surface Ignition
HsKA	Hochschule Karlsruhe - Karlsruhe University of Applied Sciences
ICE	Internal Combustion Engine
IEC	International Electrotechnical Commission
IFKM	Institut für Kolbenmaschinen
IKKU	Institut für Kälte-, Klima- und Umwelttechnik
IMEP	Indicated Mean Effective Pressure
IR	Infrared
ISFC	Indicated Specific Fuel Consumption
IVC	Inlet Valve Closing
IVO	Inlet Valve Opening
KIT	Karlsruhe Institute of Technology
LBL	Lean-burn Limit
LFL	Lower Flammability Limit
MAF	Mass Air Flow Sensor
MBT	Maximum Brake Torque
MFB	Mass Fraction Burnt
MLC	Multilinear Constraints (DoE)
NG	Natural Gas
NO_x	Nitrogen Oxides
NROHR	Net Rate of Heat Release
NSC	NO_x Storage Catalyst
NTC	Negative Temperature Coefficient
OFAT	One-factor-at-a-time
OP	Operating Point
PA	Polyamide
PAH	Polycyclic Aromatic Hydrocarbons
PCSI	Prechamber Spark Ignition

PFI	Port Fuel Injection
PGI	Performance Gas Injection
PI	Proportional-integral
PM	Photomultiplier
PTC	Positive Temperature Coefficient
PtG	Power to Gas
p-Value	Probability Value (ANOVA)
RCM	Rapid Compression Machine
RG	Residual Gas
RMS	Root Mean Square
ROHR	Rate of Heat Release
RP	Replicate Point
RSM	Response Surface Methodology
RT	Resistance-temperature
SCR	Selective Catalytic Reduction
SEM	Standard Error of Mean (DoE)
SDEV	Standard Deviation
SI	Spark Ignition
SMPS	Switched-mode Power Supply
SOC	Start of Combustion (Inflammation Timing)
SPV	Scaled Prediction Variance (DoE)
STP	Standard Temperature and Pressure
TDC	Top Dead Centre
THC	See HC
UFL	Upper Flammability Limit
UHC	See HC
UV	Ultraviolet
UVa	Universidad de Valladolid
VIS	Visible
WOT	Wide Open Throttle
WRAF	Wide Range Air-fuel Ratio

Latin Symbols

	Unit	Description
A	m^2	Surface Area
A_{pre}		Pre-exponential Factor
B		Fitted Ignition Delay Parameter
CA(x)	°CA ATDC	Crank Angle of x % Mass Fraction Burnt
CA5	°CA ATDC	Start of Main Combustion/5 % Mass Fraction Burnt
CA50	°CA ATDC	Combustion Phasing/50 % Mass Fraction Burnt (DoE Factor)
CA90	°CA ATDC	End of Main Combustion/90 % Mass Fraction Burnt
COV_x		Coefficient of Variance of Variable x
C_0		Constant for Determining Nu

ED	mm	Electrode Distance
E_a	kcal/mol	Activation Energy
E_{min}	mJ	Minimum Ignition Energy
$F_{1\rightarrow2}$		View Factor
H_i	kcal/mol	Lower Heating Value
I	A	Electric Current
I_{HSI}	A	Electric Current of HSI System
I_{pr}		Pre-reaction State
K_i		Integral Gain of PI Controller
K_p		Proportional Gain of PI Controller
Nu		Nusselt Number
P	W	Power
Pr		Prandtl Number
P_{HC}	W	Electric Power Dissipated in Heating Cap of Glow Plug
P_{HSI}	W	Electric Power of HSI System
P_{leads}	W	Electric Power Dissipated in Electrical Leads of Glow Plug
Q_H	J	Heat from Combustion
$\dot{Q}_{cond}$	W	Conductive Heat Transfer
$\dot{Q}_{conv}$	W	Convective Heat Transfer
$\dot{Q}_{rad}$	W	Heat Transfer through Radiation
	Ω, mΩ	Electrical Resistance
R		Correlation Coefficient
	kcal/molK	Universal Gas Constant
Re		Reynolds Number
R_0	mΩ	Glow Plug Cold Resistance
R_{ageing}	mΩ	Increase of R_{HSI} Caused by Glow Plug Ageing
$R_{HSI,trans}$	mΩ	HSI Resistance at Transition from Section 1 to Section 2
R_{HSI}	mΩ	Electrical Resistance of HSI System
ST	°CA ATDC	Spark Timing
T	K, °C	Temperature
T_0	°C	Glow Plug Temperature at R_0
T_{ad}	K	Adiabatic flame temperature
$T_{adapter}$	°C	HSI Adapter Temperature
$T_{coolant}$	°C	Coolant Inlet Temperature of CHP Unit (DoE Factor)
T_{crit}	K	Critical Ignition Temperature
T_{HS}	K, °C	Hot Surface Temperature
T_{intake}	°C	Intake Temperature of CHP Unit (DoE Factor)
U	V	Voltage
U_{HSI}	V	DC Voltage of HSI System
V	m^3	Volume
X		Information Matrix (DoE)
Y_{FM}		Mixture Fraction (AVL Fire)
Y_P		Tracking Species for Autoignition (AVL Fire)
a		Integration Constant
	K/mΩ	Gradient of RT correlation

		Response Surface Coefficient
		Vibe Parameter
a_{HC}	K/mΩ	RT Gradient of Glow Plug Heating Cap
a_{leads}	K/mΩ	RT Gradient of Glow Plug Electric Leads
b		Integration Constant
c		Reaction Progress Variable (AVL Fire)
c_m		Mass Flow Correction Factor
c_p	J/kgK	Specific Heat Capacity (constant pressure)
c_v	J/kgK	Specific Heat Capacity (constant volume)
c_x		Concentration of species x
d	m	Characteristic length
	m	Diameter
e		Controller Error or Deviation
		Error (DoE)
f	Hz	Frequency
h	W/m²K	Heat transfer coefficient
k	W/mK	Thermal Conductivity
k_0	cm³/mol·s	Reaction Rate Constant (2. Order)
m	kg	Mass
		Vibe Form Parameter
$\dot{m}$	kg/h, g/s	Massflow
	1/min	Engine Speed
n		Fitted Ignition Delay Parameter
		Parameter for Problem Type
p	Pa, bar, mbar	Pressure
p_{man}		Intake Mainfold Pressure (DoE Factor)
p_{max}	bar	Maximum In-cylinder Pressure
$\dot{q}_{loss}$	W/m³	Heat Liberated by Chemical Reaction
$\dot{q}_{prod}$	W/m³	Heat Liberated by Chemical Reaction
r		Compression Ratio
	mol/cm³s	Reaction Rate (2. Order)
r_0		Constant for Determining Nu
s	m	Wall Thickness for Conductive Heat Transfer
s_F	m/s	Transport Velocity
s_{FF}	m/s	Flame Front Propagation Velocity
s_L	m/s	Laminar Burning Velocity
s_T	m/s	Turbulent Burning velocity
t	s	Time
u'	m/s	Turbulence intensity
v	m/s	Flow velocity
x		Factor, Input, Variable (DoE)
(x)		Concentration of chain carriers
$(x)_c$		Critical concentration of chain carriers
x_{RG}		Residual Gas Fraction

y	Response, Output (DoE)

Greek Symbols

	Unit	Description
α	°CA	Crank angle
α_K	1/K	Characteristic Glow Plug Constant
γ		Ratio of Specific Heat Capacities
δ_{crit}		Critical Parameter for Mixture Ignition
ε		Emissivity
η		Efficiency
η_h		Glow Plug Heating Efficiency
Θ		Dimensionless Temperature
λ		Relative Air-fuel Ratio (DoE Factor)
ξ		Dimensionless Distance
ρ	kg/m^3	Density
σ_x		Standard Deviation of Variable x
τ	ms	Ignition Delay
ϕ		Equivalence Ratio

1 Introduction

1.1 Background and Motivation

With the Paris Agreement [141], the world's first comprehensive climate agreement entered into force on 4th of November 2016. As of September 2017, 164 of 197 parties have ratified the agreement, with the aim of lowering greenhouse gas emissions, in particular by fossil fuel divestment, in order to keep the increase in the global average temperature to well below 2 °C above pre-industrial levels, recognising that this would significantly reduce the risks and impacts of climate change. The contribution that each individual country should make in order to achieve the worldwide goal are determined on a national level. The German government, for example, set the ambiguous target of reducing the emission of greenhouse gases by 80 to 95 % respective to 1990 by year 2050 [27]. This is to be achieved through a consequent transition toward sustainable energy (ger: "Energiewende"), with decentralised renewable energy and energy efficiency being the main pillars of this process. As of 2016, however, only a reduction of 27,6 % had been achieved [138], which made clear that large efforts still need to be made to reach the intermediate target of a 40 % reduction in 2020. The declared long-term goal is the creation of an energy system based on 60 % renewable energy by 2050, with at least 80 % of electric power stemming from renewable sources [27]. As part of this turnaround in climate policy, cogeneration gas engines (combined heat and power - CHP), play an important role in the decentralised energy supply of the future. The simultaneous production of heat and electricity from natural gas allows for a significant reduction of CO_2 emissions compared with onsite heating and conventional power plants, particularly to those burning coal or fuel oil. Natural gas (NG) is characterised by its low specific CO_2 emissions, clean burning nature in terms of particulate matter, its good transportability and the larger reserves compared to oil. Stationary gas engines are more than just a bridge technology, since

they do not solely rely on natural gas but can be partially or even fully operated with fuels produced from renewable sources, like biogas or synthetic natural gas or hydrogen. A very promising approach are Power-to-Gas (PtG) production schemes, where the excess power from wind generators or solar arrays is used to produce methane or hydrogen. The gases are then stored in the natural gas network and available for generating heat and electric power when intermittent and hardly predictable renewable energy sources are not generating.

Many countries worldwide have taken measures to encourage CHP growth by financial incentives, grant support and increased feed-in remuneration. An important part of the emerging CHP market are so called "micro-CHP" and "mini-CHP", installations with a rated electric power ranging from 2 to 10 kW_{el} and 10 to 50 kW_{el}, respectively. Large number of these units are driven by naturally aspirated lean-burn (overstoichiometric, relative air-fuel ratio $\lambda > 1$) internal combustion engines to achieve high engine efficiencies at relatively low emissions, heat losses, knock tendency, peak combustion pressures as well as combustion and exhaust gas temperatures. To this day, their output of pollutants is not subject to any regulations in Germany, but it is common practice to meet the emission limits defined by TA Luft [28] that apply to larger gas engines, as most subsidies are linked to this requirement. In response to the increasing amount of installed units, however, a new European commission regulation (No. 813/2013) [47] will enter into force in 2018 and subject small CHP units up to 50 kW_{el} to a more stringent NO_x emission limit.

For existing naturally aspirated production gas engines operating with lean air-fuel mixtures, there are two possible ways of meeting the new limit: The first is a transition to stoichiometric combustion ($\lambda = 1$) in combination with aftertreatment through 3-way catalysts, as already practiced by some CHP manufacturers. The second is to maintain lean-burn operation and attempt to reduce emissions either through adjusted combustion parameters or aftertreatment, e.g. NSC (NO_x storage catalysts) or SCR systems (selective catalytic reaction). Stoichiometric operation can be easily achieved by increasing the mass flow of fuel supplied. This, however, results in an increase of engine power if engine speed remains constant, thus requiring an electric generator with higher nominal power, a decrease in thermal engine efficiency and a higher thermal load on engine components. Further leaning of the mixture to reduce combustion temperature, and therefore NO_x, on the other hand, does not require changes in engine periphery but reduces engine power as a result of the lesser energy input. Furthermore, leaning increases combustion duration, thus reducing the efficiency of the combustion process, and is limited by increasing combustion instability. Aftertreatment systems are an alternative solution but are complex, may require additional consumables and are currently not suitable for economical use in small cogeneration units.

Another major challenge of small CHP units are the higher specific maintenance costs

compared to the high-power range. Depending on the manufacturer, the specific maintenance costs lie in the range 2.5 – 8 ct/kWh$_{el}$ (in €) for units up to 50 kW$_{el,}$ thus being much higher than the values for large units above 1 MW$_{el}$ (0.4 – 0.9 ct/kWh$_{el}$) [8].

1.2 Scope and Organisation of Thesis

Motivated by the need of future reduction of NO_x emissions and the high specific maintenance costs of small cogeneration engines, among others caused by frequent spark plug replacement, an alternative ignition system based on controlled hot surface ignition (HSI) was developed. Unlike conventional spark plugs, a heated rod, e.g. in the form of a glow plug, is not subject to the electrode wear caused by spark erosion. Production ceramic glow plugs (CGP) are known to exhibit long life-times in Diesel operation and are inexpensive compared to prechamber spark plugs commonly used to ignite the air-fuel mixture in lean-burn applications. Combustion related advantages expected of HSI arise from the size of the hot surface compared to that of the spark. The inflamed mixture volume that forms the initial flame kernel and induces a propagating flame is increased significantly. This is expected to accelerate the combustion process, increase the probability of mixture ignition and allow for an enhancement of the lean-burn limit. The ability to ignite leaner mixtures reliably, yet with shorter combustion duration, yields the potential of reducing the NO_x output and meet future emission limits, without experiencing significant losses in engine efficiency.

Over the past decades, several interesting approaches to ignite air-fuel mixtures by means of hot surfaces in internal combustion engines have been presented and can be loosely divided into homogeneous (premixed) and stratified (direct injection) combustion processes. Most work on premixed air-fuel mixtures deals with fairly reactive liquid fuels (e.g. petrol) and/or catalytic materials to decrease the activation energy of ignition while operating the engine at rather low speeds. For this setting, ignition delay is primarily governed by hot surface temperature and the residence time of reactive air-fuel mixture in its vicinity. To the author's knowledge, natural gas (NG) has only been investigated in combination with high pressure direct injection where the purpose of the hot surface is to induce a Diesel-like diffusion combustion. Here, start of combustion is mainly determined by the instant when the fuel jet impinges on the hot surface. In the present work, on the other hand, a systematic study of HSI for premixed air-NG mixtures in naturally aspirated engines is conducted for the first time. This task is highly challenging for three main reasons: First, the timing of mixture inflammation needs to be controlled solely by adjusting hot surface temperature; Second, methane, the main NG constituent, is very stable and exhibits the highest ignition temperature of all hydrocarbons; Third, the ignition system is to be employed at relatively high engine speeds of around 2450 1/min. The last two factors are in requirement of high surface temperatures, making high demands on the thermal ignition system itself. At the same time, mixture ignition needs to be timed such that combustion phasing can be set appropriately and in a reproducible manner. There-

fore, the objective of this thesis is to address the following key questions:

1. How stable is the ignition process, what parameters determine engine stability in terms of cycle-by-cycle variations (CCV)?
2. What is the operating range of HSI and which factors are responsible for its limitation?
3. In what way do controllable engine parameters, like intake manifold pressure or relative air-fuel ratio, exert influence on the ignition process and the parameters of HSI?
4. Is HSI a viable alternative to prechamber spark ignition (PCSI) in terms of improving the fuel consumption-NO_x trade-off and meet future emission limits?
5. Does the hot surface (glow plug) show signs of degradation that indicate reduced durability?
6. What measures can be taken to improve the ignition system?

The methodology used to study the process of HSI induced combustion and meet the objectives relies on an extensive review of the state-of-the-art and theoretical fundamentals and a combination of both numerical and experimental investigations. The approach chosen is reflected in the organisation of the thesis, divided into eight chapters. After the introduction, Chapter 2 emphasises on fundamental concepts of ignition and combustion of air-fuel mixtures and presents the challenges, particularly in terms of lean-burn combustion, that engine development is currently facing. Furthermore, it expands on the state-of-the-art technology for igniting lean mixtures and introduces alternative approaches. Chapter 3 deals with the theoretical fundamentals of the ignition on hot surfaces and reviews the most relevant publications on surface ignition in internal combustion engines. Chapter 4 describes the developed HSI system for a single-cylinder cogeneration gas engine, with a focus on its design, its components and the controller employed to time mixture ignition in engine operation. Chapter 5 outlines the experimental setup and the statistical tools employed to design and evaluate the experiments. Design of Experiments (DoE) methods are used to determine the ignition system's operation limits as well as the engine operation parameters that are most significant to HSI operation and to derive empirical correlations. In addition, the chapter presents the numerical tools employed and developed to simulate the interaction between the hot surface and the mixture. This includes a commercial 3D CFD (Computational Fluid Dynamics) code with simple reaction kinetics, used to analyse the process of mixture formation and ignition, and a proprietary 0D HSI engine process simulation model, developed in Matlab/Simulink to broaden the understanding of the thermo-electric and control behaviour of the glow plug. The preliminary investigations in Chapter 6 give a foundation for the experimental core of the present work (Chapter 7). First, the ignition process is analysed through a combined approach of CFD simulations and engine experiments using multiple optical accesses to the combustion chamber, used to detect combustion radiation. Second, the influence of glow plug manufacturing tolerances on HSI operation is

assessed using several glow plug specimens. Third, an empirical correlation to determine hot surface temperature during engine operation is presented. The aim of Chapter 7 is to determine the limits of HSI operation, evaluate the effect of individually adjustable engine parameters, like intake manifold pressure and relative air-fuel ratio and draw a direct comparison to prechamber spark ignition. Moreover, glow plug ageing along the experiments is discussed and possible system improvements are presented. Finally, a summary of the findings and an outlook to suggested future research topics are given in Chapter 8.

2 Fundamentals

2.1 Ignition of Air-Fuel Mixtures

The process of combustion in internal combustion engines (ICE) allows the chemical energy stored in the fuel to be converted into thermal and, subsequently, into mechanical energy. The characteristics of this chemical reaction, such as its timing and duration, are of fundamental importance to engine efficiency and engine-out emissions. When mixed with an oxidiser (commonly air), conventional fuels for ICE like hydrocarbons do not combust abruptly. Instead, the mixture needs to be activated either by an external energy source (e.g. the spark in conventional SI engines) or through autoignition, induced by pressure and temperature rise from compressing the mixture in the cylinder (e.g. conventional Diesel combustion). This time-dependent process is termed ignition and describes all reactions taking place during the transition from a non-reactive air-fuel mixture towards a steadily burning flame [90, 145]. Nevertheless, a flame is only able to propagate freely when fuel concentration lies between the upper (rich) and lower (lean) flammability limit (LFL and UFL). While strongly depending on the type of fuel, these limits are usually given at ambient conditions and vary with temperature, pressure, humidity and even with way ignition is induced [73] and how much energy is provided [17, 93]. Experimental data found in literature suggests that both the lean and the rich limits for a particular fuel correspond to a common minimum flame temperature. For pure methane, for instance, this is about 1400 K, as compared to a stoichiometric flame temperature of about 2200 K [83]. Figure 2.1 (left) shows a typical ignition diagram of the CH_4-O_2-N_2 system, where the intersection between the line *Air* and the range of ignitable mixtures yields both LFL and UFL. The adjacent table gives an overview of the flammability limits in air of selected fuels at ambient conditions, which may differ slightly depending on the source due to not standardised test apparatus and conditions. It can be seen that for

alkanes both LFL and UFL decrease with the number of C-atoms.

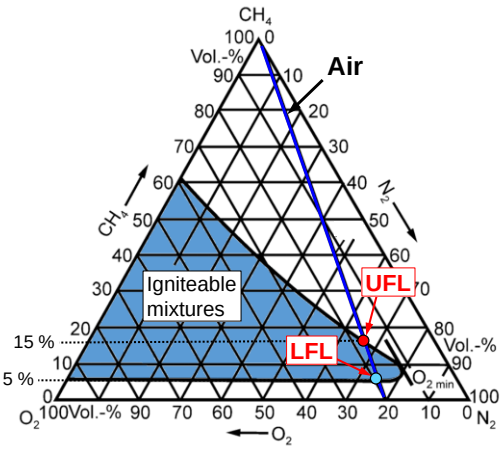

Fuel	LFL [Vol.-%]	UFL [Vol.-%]
CH4	4.8 - 5.0	15.0 – 16.0
C2H6	2.2 - 3.0	11.2 - 12.5
C3H8	2.1	9.5 – 10.0
n-C4H10	1.5	8.5
n-C5H12	1.4	7.8
n-C6H14	1.25	7.0
n-C7H16	1.0	6.0
n-C8H18	0.95	3.2
CO	12.5 - 15.0	70.0 – 75.0
H2	4.0 - 6.5	74.5 - 76.0
Natural Gas	≈ 4.8	≈ 13.5
Petrol	1.4	7.6

Figure 2.1: Ignition diagram of the CH_4-O_2-N_2 system, derived from [73] (left), and lower (LFL) and upper (UFL) flammability limits of selected fuels at 20 °C and ambient pressure in air [17, 73, 83] (right).

2.1.1 Minimum Ignition Energy and Autoignition Temperature

The ignitability of air-fuel mixture is mainly characterised by its minimum ignition energy and its autoignition temperature.

Minimum Ignition Energy:

The minimum ignition energy E_{min} is the lowest energy required to heat up a small mixture volume to its adiabatic flame temperature and cause the system to ignite [84, 145]. According to the theory of Ballal and Lefebvre [14], this volume is equal to the quenching distance of the given mixture, i.e. the critical size that the inflamed volume must attain in a short time to allow a stable self-sustained flame propagation and not be quenched. Conventional spark ignition systems deliver much higher spark energies than those required for igniting the mixture [69], with typical values of around 60 mJ [88]. However, due to heat losses caused by the proximity of the electrodes to the created plasma, only a fraction of that energy (between $20-40$ % [93]) is employed to raise mixture temperature in the spark gap and to generate active radicals required for inducing the combustion. Lefebvre and Ballal [84] propose Eq. (2-1) to calculate the minimum ignition energy for turbulent flows, where ΔT_{ad} is the temperature difference to the adiabatic flame temperature, k the thermal conductivity, s_T and u' the turbulent burning velocity and the turbulence intensity, respectively (see Section 2.2.1), c_p is the specific heat capacity at constant pressure and ρ_0 the density of the mixture:

$$E_{min} = 5.24 \cdot \Delta T_{ad} \frac{[k(s_T - 0.63u')^{-1}]^3}{(c_p \rho_0)^2} \tag{2-1}$$

From the above equation it can be derived directly that mixture temperature has a reducing effect on the minimum ignition energy as less energy is required to raise it to the

adiabatic flame temperature. Rising levels of turbulence, on the other hand, require an increase of E_{min}, caused by the increased quenching distance [84]. From $p = \rho_0 RT$ it follows that the pressure dependence of E_{min} can be expressed as $E_{min} \sim p^{-2}$, as illustrated exemplarily in Figure 2.2 (right) for spark-ignited air-propane mixtures. While this is not obvious from Eq. (2-1), the effects of equivalence ratio ϕ (inverse of the relative air-fuel ratio λ) and flow velocity are also highly significant to E_{min}: Figure 2.2 (left) shows the measured minimum ignition energy of air-propane mixtures exemplarily as a function of ϕ and flow speed. The curves exhibit a minimum for stoichiometric to slightly rich mixtures, with a large slope to either side, especially for non-stagnant mixtures. As a result, E_{min} increases rapidly as the mixture is leaned out. From the foregoing it follows that the most challenging conditions for mixture ignition in ICE are very lean air-fuel mixtures at low in-cylinder pressures, pronounced charge motion and high levels of turbulence.

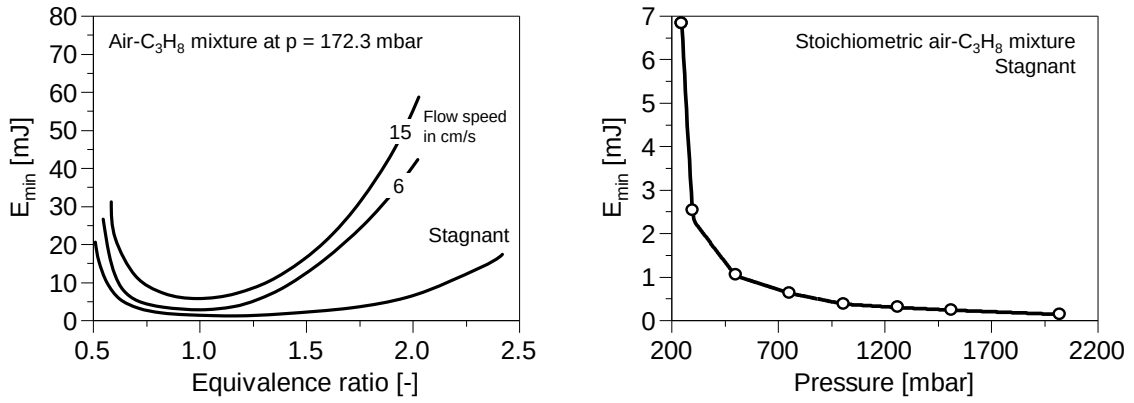

Figure 2.2: Minimum ignition energy E_{min} as a function of equivalence ratio and flow speed in the spark gap (left, [13]) and as a function of pressure (right, [50]) for air-propane (C_3H_8) mixtures.

Autoignition temperature:

The autoignition temperature (AIT) is usually defined as the lowest temperature to which a given mixture must be heated to combust spontaneously in the absence of an ignition source [30], yet there are other definitions that also include the time span until autoignition occurs as a factor [2]. The temperature range of the air-fuel mixture in which ignition and a stable self-sustaining combustion can take place is subject to limitations. The flash point shown in Figure 2.3 (left) as a function of relative fuel density (1 = water) describes the minimum temperature at which a liquid fuel gives off sufficient vapour to form a flammable mixture with air and allow for a flame to propagate when ignited locally by an external source. As this temperature is directly related to the its density, short-chained hydrocarbons like methane or propane have a flash point way below ambient temperature as a result of their gaseous state, allowing them to be burnt in a very wide temperature range. Heavy long chain hydrocarbons that appear in liquid form under atmospheric conditions like Diesel, fuel oils or vegetable oils, on the other hand, require a certain mixture temperature to sustain a propagating flame. For temperatures above the depicted autoignition limit in Figure 2.3 (left), no external energy source is required for inducing combustion and a spontaneous self-inflammation of the

mixtures ensues. In the same manner, Figure 2.3 (right) depicts the autoignition limit for selected gaseous fuels, namely alkanes/paraffins from C1 (methane) to C8 (n-octane) as a function of relative density (1 = air) exemplarily. It should be noted, however, that the boiling point of the substance rises with its number of carbon atoms. As a result, the standard state of higher alkanes greater than C4 is liquid at ambient pressure and temperature. It can be seen that the AIT decreases sharply with increasing rel. density and number of C atoms, though it remains almost constant from C7 to C16 [5]. In other words, heavier hydrocarbons tend to autoignite before lighter hydrocarbons, with the simplest hydrocarbon CH_4 showing the highest autoignition temperature (around 600 °C). The main difference between methane and other alkanes is found in their molecular structure: While methane only has strong C-H bonds, higher alkanes have at least one C-C weaker bond. Since those bonds need to be broken in order to initiate the ignition process, methane will require a higher energy to break up.

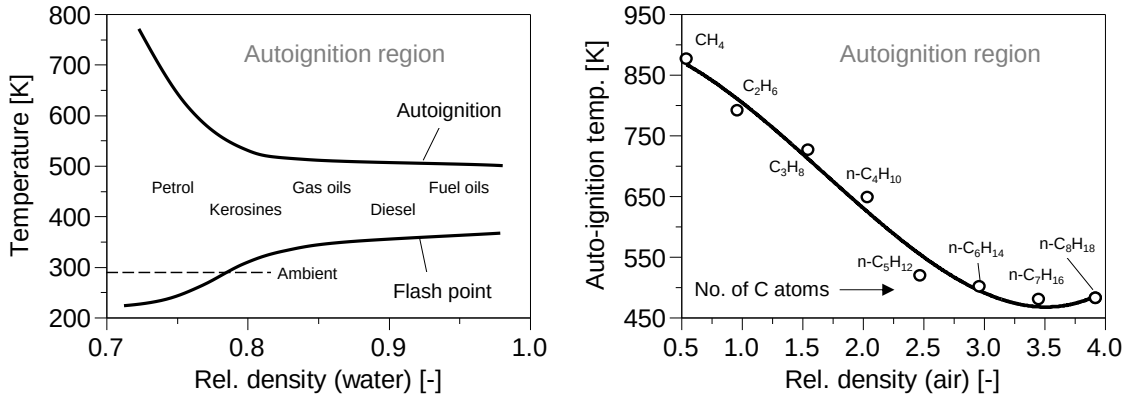

Figure 2.3: Flash point and autoignition temperatures for liquid petroleum fuels (left, acc. to [83]) and autoignition temperatures of C1-C8 alkanes (paraffins) at ambient pressure (right, experimental data extracted from IEC 60079-20-1).

The AIT of liquid and gaseous fuels is of major concern in technical installations, where the risk of fuel coming into direct contact with hot surfaces in the case of a system failure or leakage is given. This is the reason why most experiments on autoignition temperatures found in literature are conducted under ambient pressure in open vessels (isobaric). Over the years, a variety of methods have been used to determine autoignition temperatures of pure hydrocarbons, yielding a considerable spread in the absolute values published. It is a well-known fact that the minimum autoignition temperature given by a specific method does not necessarily represent the minimum temperature at which a fuel will self-ignite in air. In fact, it is not an intrinsic property of a given gas mixture, but highly dependent on the dynamic state of the gas (flow and turbulence), the shape, size and material of the test vessel, and the mode of heat supply [7, 46, 78, 94]. To this end, several standard tests to determine a reproducible autoignition temperature of liquids and gases up to 650 °C have been developed and perpetually updated, namely DIN 51794, DIN EN 14522, IEC 60079-20-1 and ASTM E659. These standardised methods use flasks open to the atmosphere, either in form of a 200 ml Erlenmeyer flask (EN 14522,

DIN 51794 and IEC 60079-20-1) or a 500 ml round bottom flask (ASTM E659). The flasks are positioned inside a hot air oven that ensures a uniform temperature inside the test vessel. An example of a test apparatus according to EN 14522 is shown in Figure 2.4. For a test, the experimenter introduces the substance from the flask opening, waits and observes through a mirror whether ignition ocurrs. The amount of substance and the temperature of the test vessel are then varied to find the lowest temperature that causes an ignition, which is usually for slightly rich mixtures [73].

Figure 2.4: Simplified schematic diagram (left) [17] and actual test apparatus (right, Source: Anko) for determining the autoignition temperature after DIN 51794, DIN EN 14522 and IEC 60079-20-1.

Due to the complex nature and the numerous factors influencing the autoignition phenomenon, the results obtained through the mentioned standardised methods only have a limited range of applicability. Nevertheless, they give important insights into the combustion characteristics of fuels and allow comparisons among them. Figure 2.5 depicts the influence of pressure on the autoignition limits of a typical hydrocarbon, discussed in detail by e.g. Warnatz et al. [145]. Due to the high pressures and temperatures during the compression stroke of internal combustion engines, the third explosion limit, or thermal explosion limit, shown is most relevant to engine operation. The phenomena cool flames and two-stage ignition that are typical for most hydrocarbons, alcohols, aldehydes, ketones, oils and ethers take place at high pressures and comparatively low temperatures, also called NTC regime (negative temperature coefficient), and are of considerable practical relevance to the processes of engine knocking or low-temperature compression ignition (e.g. HCCI). Cool flames only consume a small fraction of the fuel, followed by a minimal temperature increase of the mixture. They produce intermediate products by degenerate-branching mechanisms, which may, after a certain induction time, form enough active radicals to initiate a hot flame [69] – hence the term “two-stage ignition”. For many years methane was believed not to give rise to the phenomenon of cool flames but the experiments for fuel-rich mixtures conducted by Vanpee [144] and Caron et al. [30] showed that cool flames regions are found at higher temperatures, for very rich mixtures and are much narrower than for higher hydrocarbons.

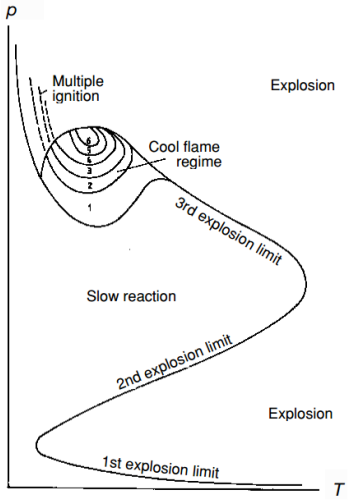

Figure 2.5: $p - T$ explosion diagram showing the ignition limits for hydrocarbons schematically [145].

2.1.2 Ignition Delay

In the theories of thermal explosion of Semenov [124] (1935) and Frank-Kamenetskii [51] (1955) (see detailed explanation in Section 3.1), system temperature increases promptly after heat production from chemical reactions in the system outweigh the heat losses to the surrounding, thus leading to an instant thermal explosion of the air-fuel mixture (see Figure 2.6, left). In the case of hydrogen- and hydrocarbon-air mixtures, however, this temperature increase and the ensuing explosion only take place after a certain induction time referred to as ignition delay time, or simply ignition delay τ (see Figure 2.6, right). This phenomenon is characteristic of radical-chain explosions where reactive radicals are formed by chain-branching mechanisms. During the induction time, radical concentration increases at an exponential rate, yet the amount of fuel consumed, and hence the amount of heat released, are too small to increase system temperature noticeably. Finally, once the fraction of radicals becomes large enough to consume significant amounts of fuel, temperature increases and the chemical explosion is initiated.

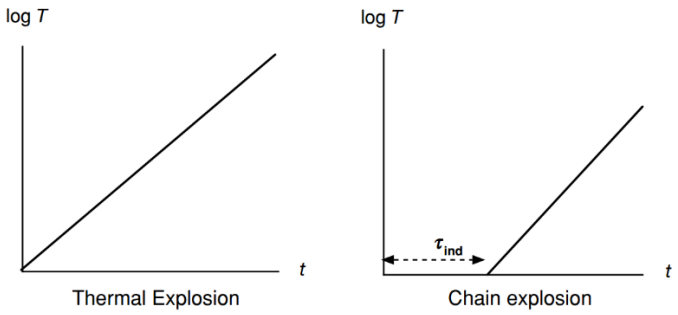

Figure 2.6: Simplified time-dependent behaviour of a thermal (left) and a chain-branching (right) explosion in an adiabatic system [145].

Due to the temperature dependence of the involved elementary reactions, particularly of

their reaction rate constant k, ignition delay time strongly depends on temperature. Figure 2.7 shows ignition delay times (logarithmic ordinate axis) for several air-hydrocarbon mixtures as a function of inverse temperature in a typical Arrhenius plot. It can be seen that it is possible to approximate the ignition delay with an exponential regression dependent on the reciprocal temperature. These relations can be expressed in the form

$$\tau = A_{pre} \cdot p^{-n} \cdot e^{B/T} \tag{2-2}$$

where T is the temperature, p the pressure and A_{pre}, n and B fitted parameters that depend on the fuel. As can be seen from Eq. (2-2), ignition delay is also inversely correlated with pressure, yet to a minor extent. The term B describes the pendent of the linear regressions shown in Figure 2.7.

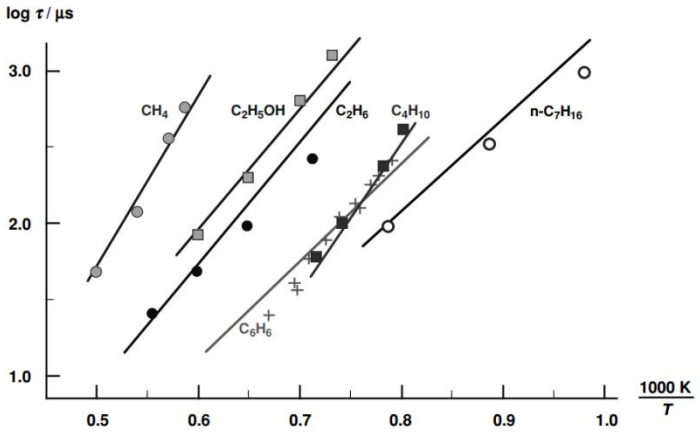

Figure 2.7: Calculated and measured ignition delay times for different air-hydrocarbon mixtures [145].

Since the ignition system presented in this work was primarily developed for igniting air-NG mixtures, the following sections will focus on the main constituents of natural gas, like methane, ethane and propane. Most experimental ignition delay for pure fuels or fuel mixtures found in literature were obtained either by the use of rapid compression machines (RCM) or through shock tube experiments. Spadaccini and Colket [129] conducted a comprehensive literature review, complemented by own shock tube experiments, on the ignition delay of pure methane, methane with small fractions of either ethane, propane or butane and typical multi-component NG mixtures at high temperatures (1300 – 2000 K), moderate pressures (3 – 15 atm) and equivalence ratios between 0.45 and 1.25. They proved that small concentrations of higher hydrocarbons shorten ignition delay times compared with those of pure methane due to an earlier formation of radicals. All tested alkanes had a similar effect on the ignition delay, sharply reducing the induction time of the mixture. Based on their own work and a large data pool from literature they derived a generalised empirical correlation for the ignition delay valid for typical NG mixtures (formula modified according to [106]):

$$\tau = 1.77 \cdot 10^{-14} \cdot [CH_4]^{0.66} \cdot [O_2]^{-1.05} \cdot [HC]^{-0.39} \cdot \exp\left(\frac{37.1}{RT}\right) \tag{2-3}$$

where the ignition delay is in seconds; R is the universal gas constant in kcal/molK; T is the temperature in K; the activation energy (E_a), i.e. the energy that needs to be overcome during the reaction, is 37.1 kcal/mol; the concentrations of CH_4 and O_2 are expressed in mol/cm^3 ($[x] = p_x/RT$), with p_x being the partial pressure of the component; and the HC factor represents the total molar concentration of all non-methane hydrocarbons. The overall pressure dependence is $p^{-0.78}$. It is common in literature to not include the pressure dependency in the formula but to scale ignition delay times using the correction factor. Petersen et al. [107] investigated higher pressures and presented a correlation for methane-oxygen-dilute mixtures valid for a wider pressure range spanning 3 - 300 atm, with a pressure dependence of $p^{-0.72}$, and a temperature range of 1400 - 2050 K:

$$\tau = 4.05 \cdot 10^{-15} \cdot [CH_4]^{0.33} \cdot [O_2]^{-1.05} \cdot \exp\left(\frac{51.8}{RT}\right) \tag{2-4}$$

In later shock tube experiments, Petersen et al. [106] also investigated blends containing CH_4, C_2H_6, C_3H_8 and H_2 in air, yet at higher non-methane fuel concentrations and for pressures between 0.54 and 30 atm, temperatures from 1090 to 2001 K and a constant equivalence ratio of 0.5. Analogous to the findings in [129], they concluded that ignition delay decreases with increasing volumetric fraction of larger alkanes, and also of hydrogen. At the same time, no significant changes in activation energies when compared to methane-only results were observed.

Healy et al. [64, 65] published the perhaps largest and most extensive data set for ignition delay times of methane/ethane/propane mixtures up to date. They analysed the effects of fuel composition, pressure and equivalence ratio at low, intermediate and high temperatures in both shock tube and RCM experiments. The plots in Figure 2.8, showing the ignition delay times for a blend of 90% CH_4/6.6% C_2H_6/3.3% C_3H_8, allow illustrating several important dependencies exemplarily: evidently, ignition delay decreases with temperature; increasing pressures do, in fact, accelerate the ignition process, however, the effect is most pronounced at low pressures; leaning the mixture only has a minor effect on ignition delay. The change in slope for ignition delay at lower temperatures (reversed s-shape) is caused by the characteristic low-temperature chemistry of propane, leading to a marked change in activation energy at around 1000 K. As a side note, the authors were able to achieve a significant overlap in the experimental range of shock tube and rapid compression machine experiments and proved a good agreement among the data.

A vast amount of reaction mechanisms have been developed over the years and validated with experimental data over wide ranges of temperature and pressure in order to understand the process of ignition and predict ignition delay times, e.g. for the use in CFD codes. One of the more complex, openly accessible and widely used mechanisms, particularly developed for methane and natural gas combustion, is GRI-Mech 3.0 [128]. It contains 53 species and 325 elementary reactions and is optimised for a temperature range

between 1000 and 2500 K, a pressure range of 0.13 to 10 bar and equivalence ratios between 0.1 and 5 ($\lambda = 0.2 - 10$). Figure 2.9 (left) shows the effect of pressure and temperature on the computed ignition delay for pure lean air-methane mixtures at $\lambda = 1.5$. The results were obtained using the open-source chemical kinetics solver Cantera Version 2.2.1 through a Matlab interface [58].

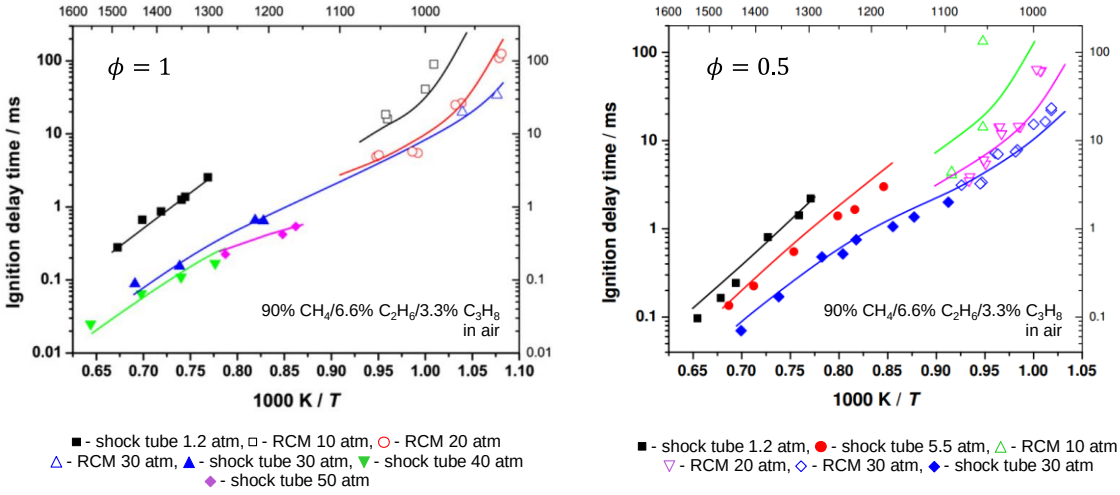

Figure 2.8: Ignition delay time against inverse temperature for 90% CH_4/6.6% C_2H_6/3.3% C_3H_8 blends in "air" at $\phi = 1$ (left) and $\phi = 0.5$ (right) for different pressures [64, 65].

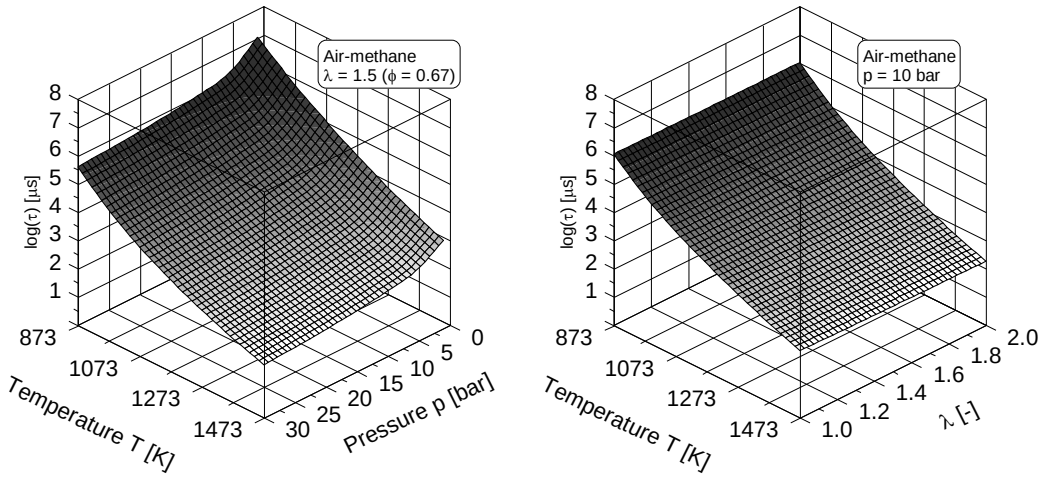

Figure 2.9: Calculated ignition delay times (as log(τ)) for air-methane mixtures as a function of temperature T and pressure p (left) and temperature T and relative air-fuel ratio λ (right), Gri-Mech 3.0/Cantera 2.2.1.

It is easy to deduct that temperature exerts the highest influence on ignition delay, causing an exponential decay in τ as the temperature is increased. The effect of pressure is highest in the region 1-5 bar. For higher pressures, ignition delay still decreases gradually, albeit with a reduced gradient, thus agreeing qualitatively with the experimental results from Healy et al. [64]. The right plot in Figure 2.9 illustrates the dependency of ignition delay on both temperature and relative air-fuel ratio at constant pressure. As compared to temperature, mixture dilution appears to only have a minor effect. In fact, τ decreases slightly as the mixture is leaned, a contrasting finding compared to other hy-

drocarbons. However, this causal relationship has also been observed by Spadaccini and Colket [129] and Hu et al. [71] for pure methane. The rather unique inhibiting effect of methane on ignition delay, as indicated by the negative reaction order in equations (2-3) and (2-4), is closely related to the formation of the methyl radical CH_3, which competes with a chain-branching step for H, converting active H atoms to less active CH_3 radicals [81]. With the aim of employing the reaction mechanism in ICE and gas turbine simulations, Hu et al. evaluated the performance of several methane reaction mechanisms including GRI-Mech 3.0 at pressures from 1 to 10 atm. They found that ignition delay is well predicted for stoichiometric to lean mixtures ($\phi = 0.5$) in the pressure range 1 - 5 atm, while being underpredicted for 10 atm. This needs to be accounted for, especially when leaving the validated pressure range of the mechanism.

In summary, ignition delay is generally a function of mixture temperature and pressure, relative air-fuel ratio, and fuel composition. However, the experimental and numerical correlations presented only represent a special case where the physical state of the mixture in terms of pressure, temperature and chemical composition can be regarded as constant. In an ICE, however, the physical state is time-dependent as a result of piston motion. A more simple, empirical approach to determine the timing of autoignition that accounts for the changing environment to which the air-fuel mixture is subjected is the widely used Livengood and Wu correlation [86]. It assumes that autoignition is triggered once the concentration of chain carriers (x) from a hypothetical gross pre-reaction reaches a critical value $(x)_c$. The time-dependent evolution of the concentration of these reactive species is given by:

$$\frac{d}{dt}\left[\frac{(x)}{(x)_c}\right] = \phi\left(\frac{t}{\tau}\right) \tag{2-5}$$

From Eq. (2-5) it follows that:

$$\frac{(x)}{(x)_c} = \int_{t=0}^{t=t_c} \phi\left(\frac{t}{\tau}\right) dt = 1 \tag{2-6}$$

where t_c is the overall reaction time. Since the physical state of the mixture (or end gas if the aim is to predict knocking combustion) is not constant, leading to changing reaction rates over time, function ϕ cannot be obtained directly from experimental data. However, if it is assumed that the reaction rate does not change for a fixed time step (zero order reaction), $\phi(t/\tau) = 1/\tau$, Eq. (2-6) can be written as:

$$I_{pr} = \int_{t=0}^{t=t_c} \frac{1}{\tau} dt = 1 \tag{2-7}$$

where $(x)/(x)_c$ is replaced by variable I_{pr}, henceforth referred to as “pre-reaction state”. Using the general definition of ignition delay τ from Eq. (2-2) with parameters A, n and B fitted to experimental data for which autoignition occurs, the timing of the autoigni-

tion event can be calculated by integration, based on the recorded or simulated pressure and temperature histories as a function of crank angle:

$$I_{pr} = \frac{1}{6n} \cdot \frac{1}{A} \int_{\alpha=\alpha_{IVC}}^{\alpha=\alpha_c} \left(p(\alpha)^n \cdot e^{-B/T(\alpha)} \right) d\alpha = 1 \tag{2-8}$$

where $dt = (1/6n)d\alpha$ and n is the engine speed. Due to its simplicity and low computational cost, the integral method is particularly suitable for CFD applications or online knock control, with fixed state ignition delay data in the relevant range of pressure and temperature, provided either by experiments or detailed reaction mechanisms.

2.2 Combustion

For premixed air-fuel mixtures, the formation of the flame kernel through induced ignition is followed by spatial flame propagation towards the end of the compression stroke, termed deflagration. The requirement for this to occur is that the number of chain-branching reactions outweighs those of chain-termination, i.e. the energy release from the chemical reaction in the plasma front exceeds the losses due to conduction and diffusion to the unburned gas ahead of the front [69]. In an ideal combustion process, fuel molecules react with oxygen to produce carbon dioxide and water. When ambient air provides the oxidiser and air humidity and fractions of residual gas are neglected, the complete combustion of hydrocarbons can be described by the following general chemical equation as a function of the relative air-fuel ratio λ:

$$\mathrm{C_xH_y} + \lambda\left(x + \frac{y}{4}\right)\left(\mathrm{O_2} + \frac{c_{N_2}}{c_{O_2}}\mathrm{N_2}\right) = x\mathrm{CO_2} + \frac{y}{2}\mathrm{H_2O} + \left(x + \frac{y}{4}\right)\left((\lambda - 1)\mathrm{O_2} + \lambda\frac{c_{N_2}}{c_{O_2}}\mathrm{N_2}\right) \tag{2-9}$$

where x and y are the number of carbon and hydrogen atoms of the hydrocarbon or hydrocarbon mixture, and c_{N_2} and c_{O_2} are the concentrations of N_2 and O_2 in air (other inerts like CO_2 and Ar are neglected). The stoichiometry of combustion is used to describe the combustion macroscopically; it does not describe the actual chemical reactions taking place in the flame front. Instead, the combustion process follows highly complex reaction schemes that mainly depend on the type of hydrocarbon, the amount of oxidiser and diluents as well as on pressure and temperature.

2.2.1 Flame speed

The rate of heat release or mass-burning of the combustion process of premixed mixtures is directly correlated to the speed at which the flame front propagates through the combustion chamber. In turn, flame front propagation velocity s_{FF} is a function of the turbulent burning velocity s_T (velocity relative to the unburnt gas) and the transport or flow velocity s_F caused by the gas exchange process and piston motion (unburnt gas velocity). It calculates as:

$$\vec{s}_{FF} = \vec{s}_T + \vec{s}_F \tag{2-10}$$

After mixture ignition, flame kernel growth is initially governed by the laminar burning velocity s_L, as the kernel is small compared to the eddies of the flow field. Shortly after, the flame undergoes a transition to a fully turbulent flow [48]. With the introduction of turbulence, the flame begins to wrinkle and corrugate, eventually leading to enhanced transport properties caused by turbulent eddies in the flame zone. As a result, the flame front propagates at a speed that is not only a function of the mixture's chemical and transport properties but also by those of turbulence, reaching values several factors higher than the laminar burning velocity [69]. Using the laminar flamelet model, turbulent flame propagation can be described by the following geometrical argument:

$$\dot{m} = \rho_u A_T s_T = \rho_u A_L s_L \tag{2-11}$$

Put in words, Eq. (2-11) describes that the mass flow entering the reaction zone of the flame front can be calculated either from the macroscopic speed of the turbulent flame s_T and its mean flame front surface area A_T, or from the local laminar burning velocity normal to the wrinkled flame and its much larger surface area A_L. As a result, turbulent flame speed becomes a function of the ratio between both surface areas and the laminar flame speed, as illustrated in Figure 2.10:

$$s_T = \frac{A_L}{A_T} s_L \tag{2-12}$$

where A_L/A_T can be determined by the following approach after Damköhler [45], introducing the turbulence intensity or fluctuating speed component u', calculated from the root mean square (RMS) of the velocity fluctuation:

$$\frac{A_L}{A_T} = 1 + \frac{u'}{s_L} \tag{2-13}$$

Finally, one obtains a simple equation for the turbulent flame speed, only dependent on the laminar burning velocity and the turbulence intensity:

$$s_T = s_L + u' \tag{2-14}$$

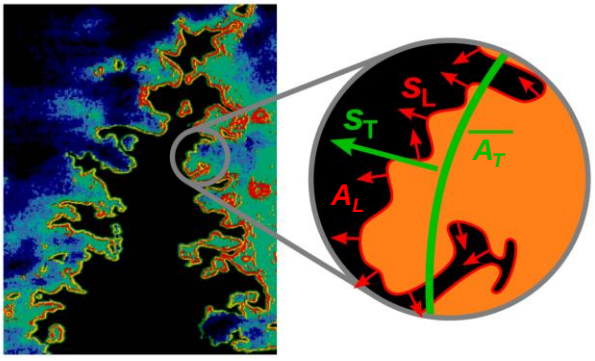

Figure 2.10: Abstraction of a real turbulent flame (laser induced fluorescence of a methane burner flame) through the flamelet approach [116].

Eq. (2-14) represents the simplest approach to compute the turbulent flame speed, sufficient to illustrate the two main influencing factors, but its agreement with experimental data can be improved if it is enhanced by additional terms, see e.g. [10, 76, 77, 90]. Turbulence intensity u' is proportional to engine speed [90] and primarily governed by the flow field inside the cylinder, shaped by intake port and piston geometry (swirl, tumble and squish). Laminar burning velocity s_L is determined by reaction kinetics and heat transfer and diffusion processes in the flame front and is an intrinsic property of a fuel at specific air-fuel ratio, diluent composition, pressure and temperature [38]. s_L can be determined experimentally or using detailed reaction mechanisms (e.g. in Chemkin or Cantera). An overview of experimental methods, such as burner, constant volume combustion chamber (CVCC) or soap bubble methods, can be found in [29, 114].

Figure 2.11 plots laminar burning velocities measured in a CVCC as a function of equivalence ratio for alkanes C1-C8 at constant temperature and pressure. It can be seen that methane (CH_4) has the lowest and ethane (C_2H_6) the highest burning velocity. Those of C3 and larger linear alkanes are nearly equivalent, intermediate between methane and ethane. All traces show a maximum for slightly rich-of-stoichiometric mixtures, decreasing rapidly to either side as a function of equivalence ratio.

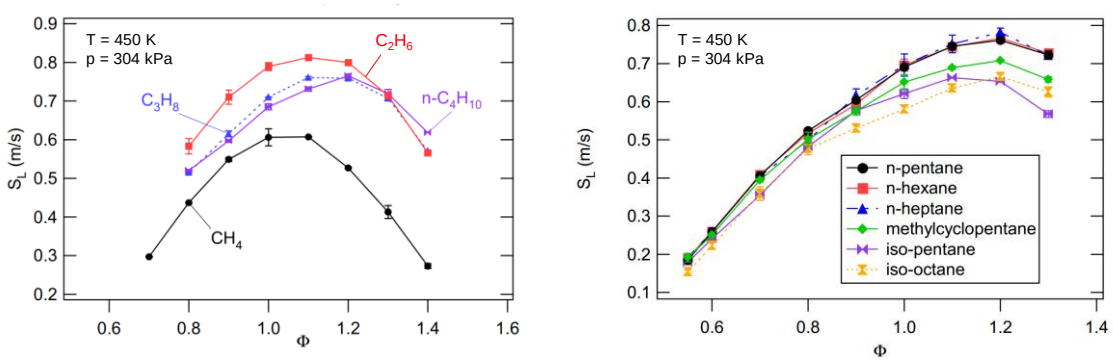

Figure 2.11: Laminar burning velocity measurements as a function of the equivalence ratio ϕ for C1-C4 alkanes (left) and for C5-C8 alkanes (right) at $T = 450$ K and $p = 304$ kPa [49].

For stoichiometric to increasingly lean air-methane mixtures, Figure 2.12 shows GRI-Mech 3.0 results on the effect of pressure on the laminar burning velocity at two different temperatures of $T = 300/1100$ K. With increasing mixture pressure, the importance of the recombination reaction $H + O_2 + M \rightarrow HO_2 + M$ increases, leading to a slowed heat release and a decreased laminar burning velocity [150]. An increasing mixture temperature, on the other hand, leads to a significant increase in s_L, caused by the increased adiabatic flame temperature that promotes the reaction rate in the flame front. As mentioned before, leaning decreases the laminar burning velocity, though the effect becomes more significant with pressure and less significant with temperature [150]. This is of particular interest for low-temperature lean-burn operation in ICE, as combustion duration is directly linked to the speed of flame propagation, with a slowing combustion typically being adverse to engine efficiency.

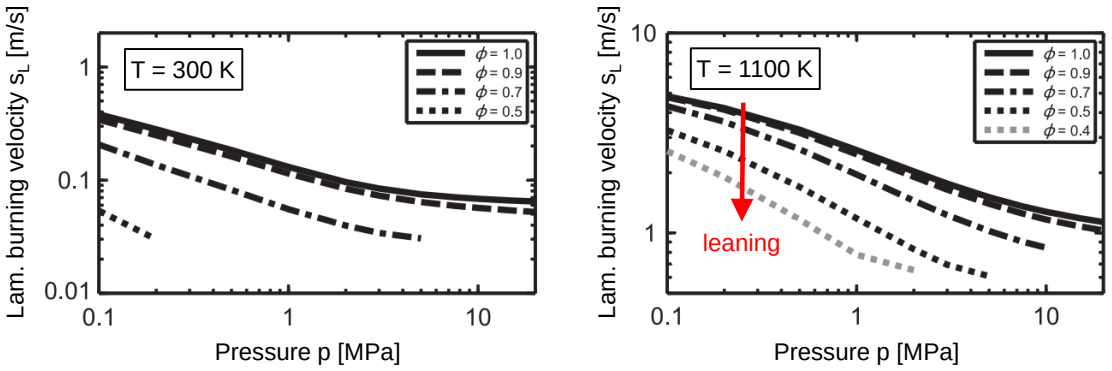

Figure 2.12: Effect of pressure p and equivalence ratio ϕ on the laminar burning velocity s_L of air-methane mixture at T = 300/1100 K (GRI-Mech 3.0) [117].

2.2.2 Lean-Burn Operation

Operating an engine with more oxygen than that required for complete combustion is and has been applied in a variety of different applications and for different reasons. It is a common practice in four-stroke stationary gas engines for cogeneration, with natural gas and biogas being the most common sources of fuel. At the bottom end of the power range, lean-burn engines are usually naturally aspirated (e.g. SenerTec Dachs G5.5 with P_{el} = 5.5 kW), while being turbocharged (up to two stages) in the upper power range (e.g. MAN 51/60G TS with P_{el} = 20.4 MW). Other fields of application are large-bore marine engines (SI or Diesel pilot injection), heavy-duty on-road engines (e.g. CNG busses up to EURO V) or as a part-load concept to reduce pumping losses in automotive spark ignited DI engines.

The most evident advantage of lean-burn operation is the increased thermal efficiency of the high pressure phase. Thermal efficiency of an ideal SI engine, represented by the thermodynamic Otto cycle, can be described by Eq. (2-15), where r is the engine's compression ratio and γ the ratio of specific heat capacities of the mixture:

$$\eta = 1 - \frac{1}{r^{(\gamma-1)}} \tag{2-15}$$

At ambient conditions, air has a γ of about 1.4 while that of hydrocarbons usually lies in the range of 1 - 1.3. Evidently, increasing the fraction of air (leaning), increases γ, but this alone does not explain any significant improvement in thermal efficiency. Since $\gamma = c_p/c_v$ and both c_p and c_v increase with temperature, but differ from each other by a fixed constant, it applies that γ decreases with temperature. Due to the direct correlation between relative air-fuel ratio and the amount of heat released, combustion temperatures are highest for near-stoichiometric mixtures, leading to the most significant drop of γ over the cycle. For the ideal engine, with isochoric heat release at TDC, real gas properties (e.g. using JANAF tables) and no wall heat losses, one obtains the arbitrarily selected traces of thermal efficiency versus compression ratio for stoichiometric ($\lambda = 1$) and

lean ($\lambda = 1.6$) combustion shown in Figure 2.13. Exemplarily, for a compression ratio of 9, leaning the mixture would result in an increase of thermal efficiency of 4 %-points.

A secondary but vital benefit of leaning out the mixture is the lowered tendency to engine knocking [152]. Depending on whether the engine is naturally aspirated or turbocharged, this can be taken advantage of in two ways:

- *Naturally aspirated engines*: Increase of the compression ratio to obtain further gains in thermal efficiency, as indicated in Figure 2.13. Increasing r from 9 to 13.2 allows for an additional gain in thermal efficiency of 6 %-points.
- *Turbocharged engines*: Increase of compression ratio and boost pressure to enable higher engine power for same engine displacement, leading to improved engine efficiencies, comparable to Diesel engines, due to the increased IMEP/FMEP ratio.

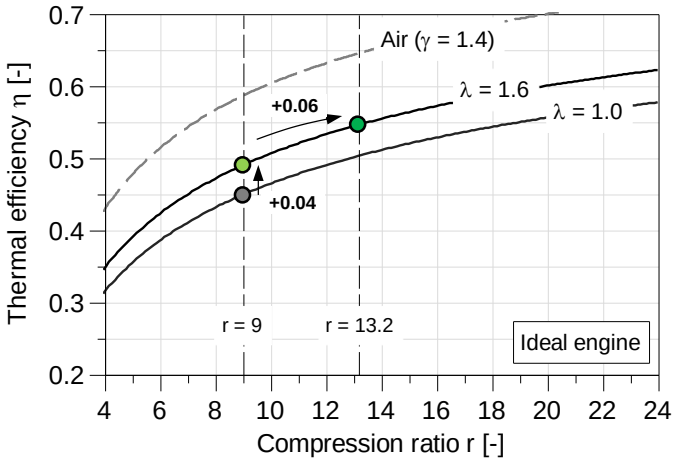

Figure 2.13: Ideal engine, isochoric combustion at TDC, no wall heat losses (after [85]).

The lower combustion temperatures in lean-burn operation are also responsible for reduced heat losses to the cylinder walls, allowing for more fuel energy to be transformed into engine work [10]. In addition, the overall thermal stress on critical components, such as exhaust valves and valve seats, is reduced, being particularly important for engine durability in stationary applications. Nonetheless, several disadvantages pose eminent challenges in the development of lean-burn combustion processes:

- Increased overall combustion duration as a result of reduced laminar flame speed (see Section 2.2.1): As combustion diverges further from the optimal constant volume combustion at TDC, thermal efficiency decreases and the heat transfer losses to the cylinder walls increase [35].
- Higher demand of ignition energy owing to the necessity of advancing spark timing and the reduced ignition quality caused by both mixture dilution and the less favourable thermodynamic conditions at spark timing (lower temperature and pressure) [75].
- Lower combustion temperatures that increase emissions of HC and enhance the risk

of partial burns.
- Increased delay in the time of flame kernel formation, causing higher cycle-by-cycle variations (see Section 2.2.3).
- Three-way catalysts do not function to reduce NO_x under excess of oxygen and it needs to be reduced either by lowering combustion temperatures or by costly after-treatment systems (see Section 2.2.2). From this it follows that the best way to operate a lean-burn engine is often a trade-off between engine efficiency and low emissions.
- *For naturally aspirated engines*: Leaning is achieved by providing less fuel to the combustion chamber. This leads to a drop in IMEP and engine power. As absolute friction losses remain practically constant, this will result in a worsened IMEP/FMEP ratio and may cause fuel penalty (increased BSFC) if thermal efficiency of the combustion process is not improved significantly (reduced ISFC).

It becomes evident that both the engine and its ignition system need to be designed for lean-burn operation in order to make use of the thermodynamic advantages. When the aim is to mitigate the NO_x output by further leaning of the mixture, particular attention needs to be paid to the process of flame kernel development and the flow conditions during flame propagation.

2.2.3 Cycle-by-Cycle Variations

Cycle-by-cycle variations (CCV) in internal combustion engines are defined as any observable differences in the in-cylinder pressure trace on a cycle-by-cycle basis. This cyclic variability is usually attributed to unavoidable stochastic fluctuations in mixture composition, temperature and flow field due to the turbulent nature of the in-cylinder flow, but can, under certain circumstances, be further influenced by deterministic effects. Spatial and time-dependent inhomogeneities in the proximity of the ignition source (e.g. in the spark gap) affect rate and location of flame kernel development, leading to both varying timings of the start of combustion and variable shapes of the early flame front. As a result of the turbulent flow field of the bulk gas in the combustion chamber, the subsequent flame propagation is also subject to CCV, leading to cyclic variations in combustion duration. The degree of cyclic variations is known to increase with mixture dilution as a result of the slowing flame development rate and reduced laminar flame speed [103]. CCV are undesirable as they cause losses in power and efficiency and increase the risk of engine knocking in cycles with overadvanced combustion phasing and that of partial burns and misfires in cycles with very long flame initiation periods. As shown later in this work, CCV can also be detrimental to the amount of emitted pollutants.

Increasing cycle-by-cycle variations is what defines the lean-burn limit (LBL) of an engine, i.e. the maximum excess air the engine can be operated with under acceptable combustion instability. Reducing CCV in order to increase engine stability and enhance the

lean-burn limit is therefore an important target of today's lean-burn engine development. Several statistical parameters, mostly derived from the in-cylinder pressure signal, have been commonly used to quantify CCV. These include the standard deviation and the coefficient of variance of IMEP, σ_{IMEP} and COV_{IMEP}, and the standard deviation of the angular position of p_{max}. In this work, the lean-burn limit is arbitrarily defined as $COV_{IMEP} = 10$ %. Cyclic variations in the heat release profile are expressed as $\sigma_{\mathrm{CA}x}$ and σ_{CD}, where CAx is the position of x % mass fraction burnt (MBF) in degrees crank angle (°CA) and CD the combustion duration.

2.2.4 Emissions

Combustion does not follow the one-step reaction from Eq. (2-9). Instead, the complex nature of chemical reactions inside the propagating flame front leads to an incomplete combustion and thus to additional combustion products in the exhaust gas. For gaseous fuels, the most relevant pollutants are carbon monoxide (CO), unburnt hydrocarbons (HC) and nitrogen oxides (NO_x), while for solid and liquid fuels, particularly for diffusive combustion in directly injected Diesel and SI engines, soot and particles may also be formed. Typical dependencies for a gas engine for CO, HC and NO_x as a function of the relative air-fuel ratio λ are shown in Figure 2.14.

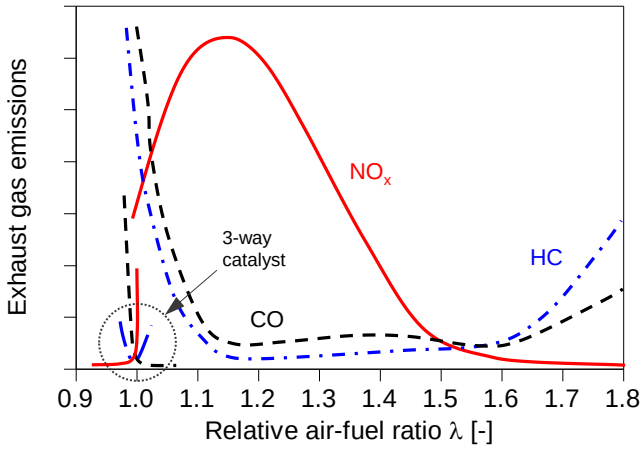

Figure 2.14: Typical qualitative pollutant concentration in the exhaust gas of a gas engine as a function of relative air-fuel ratio λ (based on [154]).

To understand what causes the formation of CO, HC and NO_x during the combustion process of premixed air-fuel mixtures in ICE and how they can be limited, the following subsections give a brief overview of the most relevant emission formation mechanisms.

2.2.4.1 Carbon Monoxide (CO)

Carbon monoxide (CO) is an intermediate product of the oxidation of hydrocarbons and highly dependent on air-fuel ratio and temperature. It is toxic to humans and can result in fatality when exposed to levels of 1000 ppm after one hour of exposure [102]. For rich combustion at $\lambda < 1$, large amounts of CO will remain in the exhaust gas owing to the

lack of enough oxygen to complete the reaction to CO_2. For stoichiometric ($\lambda = 1$) and moderately lean ($\lambda > 1$) conditions, CO levels remain low as combustion temperatures are sufficiently high for the principal CO oxidation reaction

$$CO + OH \leftrightarrow CO_2 + H \tag{2-16}$$

to take place. For very lean mixtures, low combustion temperatures cause incomplete combustion in the cold cylinder wall areas, inhibiting the kinetically controlled reaction (2-16) and leading to slight but gradual increase of emitted CO.

2.2.4.2 Unburnt Hydrocarbons (HC)

The impact of emitted unburned hydrocarbons (HC, UHC or THC – total hydrocarbons) on the environment depends strongly on their composition. While some hydrocarbons like polycyclic aromatic hydrocarbons (PAH) are carcinogenic and pose an immediate threat to human health, lighter volatile hydrocarbons, primarily methane, are harmful on a macroscopic scale due to their high global warming potential in the atmosphere [140]. Furthermore, emitted hydrocarbons can react with NO_x in the presence of sunlight to form photochemical smog [84].

Just like CO, HC are the result of an incomplete combustion of the hydrocarbon fuel and follow a similar trend over the relative air-fuel ratio. Nevertheless, the formation of CO is predominant for fuel-rich mixtures, leading to an increasingly smaller HC/CO ratio as the mixture is enriched further [120]. For mixtures at $\lambda > 1$, there is no significant HC concentration behind the flame front [89], but HC is rather formed in areas that cannot be reached by the flame. These processes are highly complex, depending on numerous factors such as the combustion process (e.g. SI, Diesel, HCCI), the state of the fuel (gaseous or liquid), the type of mixture preparation (premixed or stratified), combustion phasing and the shape of the combustion chamber. The most commonly cited origins of unburnt hydrocarbons in premixed homogenous combustion can be summarised as follows [69, 73, 89, 143, 145]:

- Flame extinction in small crevice volumes due to excessive cooling of the flame front's reaction zone
- Flame quenching at cold combustion chamber walls
- Absorption and desorption of fuel vapour in oil layers and deposits on the cylinder liner and walls
- Hydrocarbons from lubricants
- Misfires of partial burns when combustion quality is low (e.g. at high λ or EGR rates or poor combustion phasing)
- Flame extinction due to flame strain, particularly relevant for rich and lean mixtures, caused either by highly turbulent flows or too low flame speeds during the expansion stroke

– Scavenging of unburnt mixture into the exhaust path during the valve overlap

From this it follows that unburnt hydrocarbons that escape the combustion chamber are mainly formed at lower temperatures. As they mix with the significantly hotter exhaust gas in the exhaust gas manifold, substantial post-oxidation may occur, thus leading to lower HC emissions at the tail-pipe than those present in immediate vicinity to the exhaust valve [69].

2.2.4.3 Nitrogen Oxides (NO_x)

Nitrogen oxides (NO_x), mostly comprised by nitric oxide (NO) and nitrogen dioxide (NO_2), are a major contributor of photochemical smog and ozone in urban air and participates in the chain reaction removing ozone from the stratosphere [145] and are in part responsible for acid rain. Furthermore, direct exposure to NO_2 may harm the respiratory ways of humans [151]. For stoichiometric and moderately lean combustion, most NO_x is emitted as NO, but will eventually oxidise to NO_2 in the atmosphere, given a sufficiently long time [83, 90]. The generally accepted routes of NO_x formation are thermal NO and NO_2, prompt NO, NO via the N_2O mechanisms and fuel NO. However, the contribution of the three latter, for lean-burn operation in particular, is usually of reduced significance.

Thermal NO:

The most significant and arguably best-understood NO formation mechanisms is that of thermal NO, first suggested by Zeldovich (1946) and then extended by Lavoie et al. [80]. In conventional internal combustion processes, thermal NO is formed at high temperatures and pressures in both the flame front and the burnt post-flame gases [69] and is the main contributor to total engine-out NO. While the maximum value of the adiabatic flame temperature occurs for slightly rich air-fuel mixtures as a result of dissociation processes [82], the NO peak is shifted to slightly lean mixtures. This can be explained by the increasing fraction of O_2 when leaning out the mixture that initially offsets the falling gas temperatures [69]. The NO formation mechanism consists of the three elementary reactions (1-3):

$$O + N_2 \overset{k_1}{\leftrightarrow} NO + N \tag{2-17}$$

$$N + O_2 \overset{k_2}{\leftrightarrow} NO + O \tag{2-18}$$

$$N + OH \overset{k_3}{\leftrightarrow} NO + H \tag{2-19}$$

where the forward (f) and reverse (r) reaction rate constants k are determined experimentally (see examples in [69, 90, 145]). According to steps 1-3, the rate of NO formation/consumption can be expressed as:

$$\frac{d[NO]}{dt} = k_{1,f}[O][N_2] + k_{2,f}[N][O_2] + k_{3,f}[N][OH] - k_{1,r}[NO][N] - k_{2,r}[NO][O] - k_{3,r}[NO][H] \quad (2\text{-}20)$$

where [ ] denotes species concentrations in mol/cm³ when k is expressed in cm³/mol·s. In the same manner, the rate of N formation/consumption can be written as

$$\frac{d[N]}{dt} = k_{1,f}[O][N_2] - k_{2,f}[N][O_2] - k_{3,f}[N][OH] - k_{1,r}[NO][N] + k_{2,r}[NO][O] + k_{3,r}[NO][H] \quad (2\text{-}21)$$

Due to the high reaction rates in steps 2 and 3, the atomic nitrogen formed in step 1 reacts immediately and its concentration can be assumed to be in steady-state, thus yielding $d[N]/dt = 0$ [69, 89, 145]. With this assumption, the unknown concentration $[N]$ can be isolated in Eq. (2-21) and used to eliminate it from the first elementary reaction in Eq. (2-20).

Step 1 has a very high activation energy and is the rate limiting step of thermal NO formation due to its much smaller reaction rate compared with steps 2 and 3, by several orders of magnitude [145]. From this, it can be easily deduced that NO formation is primarily a function of the temperature dependent $k_{1,f}$ and the concentrations of both O and N_2. As a result of this strong exponential temperature dependence, NO formation is described to be kinetically controlled [90]. The combination of a slow controlling reaction rate and the short residence times at high temperatures in the combustion chamber, hinder reactions 1-3 from reaching chemical equilibrium, leading to "frozen" NO concentrations in the exhaust. This mechanism is illustrated in Figure 2.15.

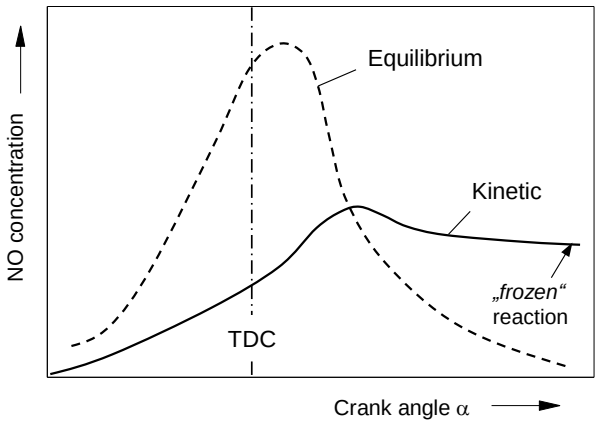

Figure 2.15: Qualitative NO concentration over crank angle for chemical equilibrium and kinetically controlled NO formation [90].

Thermal NO_2:

The primary reaction for NO_2 formation is given by Eq. (2-22) [85]:

$$NO + HO_2 \rightarrow NO_2 + OH \quad (2\text{-}22)$$

Since the formation of HO_2 is retarded by the presence of NO, NO is the principal constituent when NO_x levels are high [101]. In contrast, when maximum combustion temperatures and NO_x levels are low, e.g. for high mixture dilution or late combustion phasings, more HO_2 is available and the NO/NO_2 equilibrium may shift to the NO_2 side, leading to a predominant formation of NO_2 [70, 101, 120].

2.2.4.4 Emission Limits for Stationary Gas Engines

The amount of pollutants that the engine is allowed to emit to the atmosphere is usually subject to European, national, state or even local regulation, though the type of regulated pollutants and their limit vary depending on several factors such as the type of application, the engine's power output, the type of fuel employed or the type of combustion process. In Germany, for example, the pollutant emission of large-bore stationary gas engines used in combined heat and power installations with a fuel input power above a rated thermal input of 1 MW are limited by TA Luft 2002 (Technical Instruction on Air Quality Control) [28], though a more stringent amendment is expected towards the end of 2017 [26]. The emissions of smaller gas engines, typical for micro- and mini-CHP units, however, are currently not subject to specific emission requirements. §22 of the BImSchG (Federal Immission Control Act) merely states the requirement to "take all measures feasible according to the state of the art in order to avoid air contamination by pollutant emission". Most subsidy programmes initiated to promote the expansion of small CHP systems have set meeting the TA Luft limits as one or their fundamental requirements. In practice, this has led to most producers of CHP units below 1 MW meeting TA Luft. In 2018, however, the more stringent EU Commission Regulation No. 813/2013 [47] will enter into force across the whole European Union and be applicable to all CHP units with a rated electric power below 50 kW_{el}. Table 2.1 gives a comparison of the limits of TA Luft and CR EU No. 813/2013:

Table 2.1. Emission limits for TA Luft [28] (for lean-burn NG engines, ≥ 1 MW of fuel input, dry NO_x at 5 % O_2) and CR EU No. 813/2013 [47] (below 50 kW of generated electric power).

	TA-Luft 2002	CR EU No. 813/2013
CO	300 mg/m_N^3	-
THC	-	-
NO_x	500 mg/m_N^3 *(equivalent to ≈ 200 ppm at λ = 1.6)*	240 mg/kWh in terms of higher heating value of total fuel input (HHV) *(equivalent to slightly below ½ TA Luft)*
Formaldehyde	60 mg/m_N^3	-

Where combustion related measures do not suffice, the conventional approach to mitigate CO in the exhaust of natural gas driven cogeneration engines is by aftertreatment using oxidation catalysts (OC). Given a good condition of the catalyst (no thermal ageing or sulphur poisoning) and a sufficiently high catalyst temperature above the CO light-off temperature, they operate very effectively for slightly rich, stoichiometric and lean ex-

haust gas. OC are also used to reduce unburnt hydrocarbons, though aftertreating methane-HC is much more challenging due to its unwillingness to react at low exhaust gas temperatures. As exhaust gas temperature is a function of λ, HC can be oxidised fairly well for combustion close to stoichiometric. As the mixture is leaned, however, exhaust gas temperatures drop, leading to poor HC conversion rates inside the catalyst. For this reason, methane-OC for lean-burn operation need to be allocated close to engine outlet and usually contain large fractions of palladium to reduce the catalyst's light-off temperature and increase conversion efficiency at low temperatures. While the aforementioned emission limits do not relate to THC, the focus on methane, having a much larger global warming potential than CO_2, may intensify in the future. Engine-out NO_x emissions can be reduced fairly easy in oxidation catalysts when the engine is operated at stoichiometric conditions, but the excess of oxygen during lean-burn operation inhibits the three-way reaction. As a result, alternative approaches, either combustion-related by reducing combustion temperature (e.g. EGR, water injection, further leaning or retarded combustion phasing), or in the form of lean-burn aftertreatment systems like SCR (Selective Catalytic Reduction) or NSC (NO_x Storage and Reduction Catalyst) systems need to be pursued, without significant drawbacks in engine efficiency. On one level with engine and component durability, this constitutes one of the biggest challenges in today's lean-burn engine development and will be addressed in the present work.

2.3 Ignition Systems for Lean-Burn Operation

The reduced ignitability of lean mixtures and the need to minimise cycle-by-cycle variations in the flame development phase make high demands on the ignition system. In particular for stationary applications, where high operating hours require the engine components need to be robust and durable, the limits of conventional spark ignition are reached. This chapter gives a brief overview of established lean-burn spark ignition systems and their limitations and presents alternative approaches that are currently subject to research.

2.3.1 Spark Ignition and Prechamber Spark Ignition

Spark ignition (SI) represents the state-of-the-art technology for initiating the combustion process in lean-burn gas engines. It relies on an electric discharge between two electrodes towards the end of the compression stroke that produces a high-temperature plasma, capable of forming enough radicals in the spark gap to induce a self-sustained, propagating flame front. According to the Paschen's Law (1889), breakdown voltage is a direct function of pressure p and electrode distance ED if temperature is regarded as constant (see Figure 2.16, left). As a result, all measures that increase in-cylinder pressure at spark timing, i.e. higher compression ratios and mean effective pressures, cause an increase in ignition voltage. According to Rager [112], the arc discharge phase after the

breakdown is responsible for most spark erosion. For platinum electrodes, he found that spark erosion, expressed as the volume of removed electrode material per spark, is a linear function of ignition voltage (see Figure 2.16, right). The erosion process, in turn, increases the spark gap and therefore the ignition voltage until the ignition system can no longer sustain the secondary voltage and misfire results, thus being the main factor limiting spark plug durability [88].

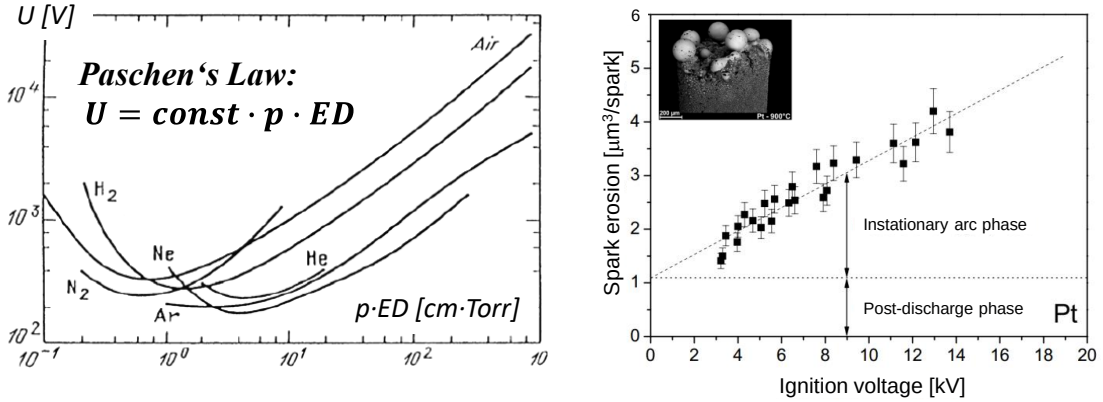

Figure 2.16: Breakdown voltage for several gasses at constant temperature (left) and spark erosion of platinum (Pt) electrodes as a function of ignition voltage (right) [112].

In terms of durability, the development of spark plugs for stationary lean-burn operation is more challenging compared to conventional spark plugs for mobile applications with stoichiometric mixtures for several reasons:

- Longer operating hours (replacing intervals of 4000 h and above as opposed to roughly 600 – 1200 h for conventional automotive spark plugs)
- Increased ignition energy and spark gap to safely ignite the mixture and reduce CCV
- Higher compression ratios and increased mean effective pressures, leading to higher pressures at spark timing

Figure 2.17 shows examples of spark plugs and spark ignition concepts for lean-burn operation for increasingly lean main mixtures. The range spans from standard J-gap spark plugs with platinum and/or iridium alloy reinforced electrodes for increased life-time, over spark plugs with multiple ground electrodes to distribute the wear, to passive and scavenged prechambers.

Passive prechambers are designed to enhance the lean-burn limit by reducing the time of flame development and the variability in the flame development angle (duration between spark timing and the formation of a stable flame kernel), and to accelerate the combustion process. Systems found in series operation, usually in the form of a prechamber spark plugs, show one major difference to conventional spark plugs: The electrode is positioned inside a small prechamber, usually about 1-3 % of the compression volume [76, 109], connected to the main combustion chamber via a determined amount of orifices or channels. By doing so, the flow conditions inside the prechamber and, in particular, in

the spark gap, can be partly decoupled from the main in-cylinder flow and its cyclic variability. Instead, the flow conditions become a function of the pressure difference between the main combustion chamber and the prechamber and the amount, size and orientation of the prechamber bores, often distributed such that moderate swirl is created inside the prechamber. When the mixture is ignited, a flame develops, thereby increasing the pressure difference to the main chamber. As a result, turbulent flame jets or torches of burning and partly burnt mixture penetrate into the main chamber, thereby initiating the combustion process widely and rapidly due to the increased surface area of the numerous inflammation sites.

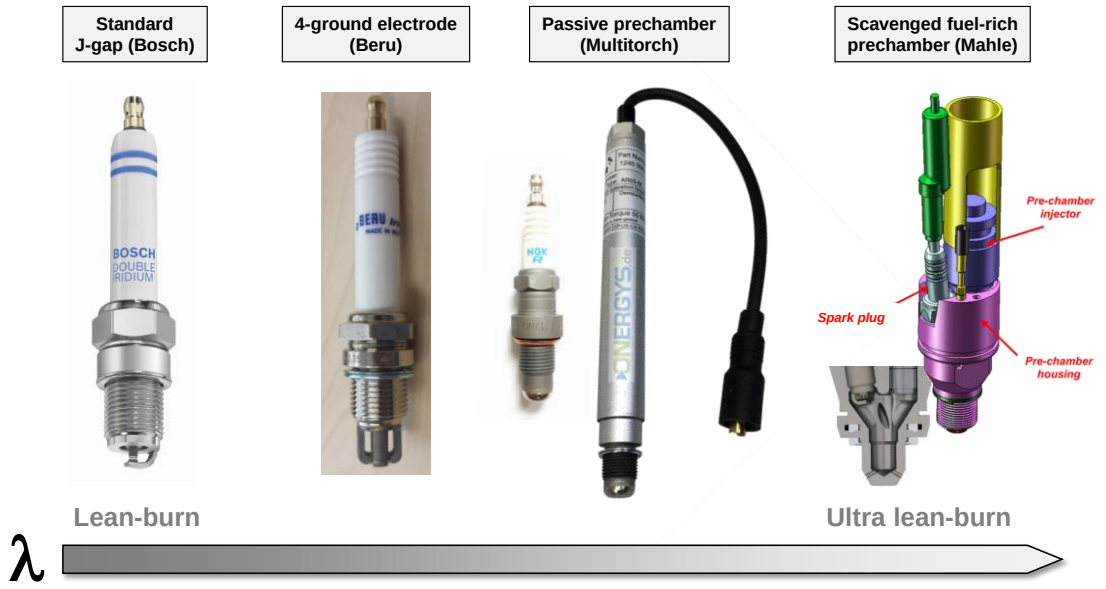

Figure 2.17: Examples of spark plugs and spark ignition concepts for lean-burn engines.

Figure 2.18 depicts examples of optical images of the propagating flame front, recorded for conventional spark ignition and prechamber spark ignition (PCSI) on transparent engines. While a fairly spherical flame front develops from a single flame kernel in the spark gap for conventional spark ignition, multiple, distributed and lengthened ignition sites are formed by the jets for PCSI. The large penetration depth, which is primarily a function of the rate of heat release inside the prechamber and the number and diameter of orifices, enables a rapid combustion of the main charge.

Large-bore turbo-charged gas engines also make use of the advantages of the prechamber concept. Passive prechamber spark plugs do, however, not suffice to ignite the very lean mixtures ($\lambda \geq 2.0$) at high mean effective pressures (BMEP > 22 bar) at which the engines need to be operated in order to attain highest engine efficiency ($\eta_e > 50\,\%$) and meet stringent emission limits. The most common approach is to improve ignition quality by injecting additional fuel or mixture directly into the prechamber to minimise the residual gas fraction and create a highly reactive stoichiometric mixture (scavenged prechamber). Examples are the currently most powerful SI gas engine MAN 51/60G [21] with $P_{el} = 20.7$ MW or the GE Jenbacher J920 with $P_{el} = 10.3$ MW [137]. The fast-

burning high-energy jets penetrate the main combustion chamber, increase the level of turbulence, thus allowing for a fast and efficient fuel depletion, even of highly diluted or low-grade mixtures, such as biogas and landfill gas. Scavenged prechambers have also been studied for mobile light-duty applications (e.g. [9, 25, 57]) and heavy-duty commercial applications [125]. According to [61], the concept has alledgedly been introduced by Ferrari and Mahle in Formula One.

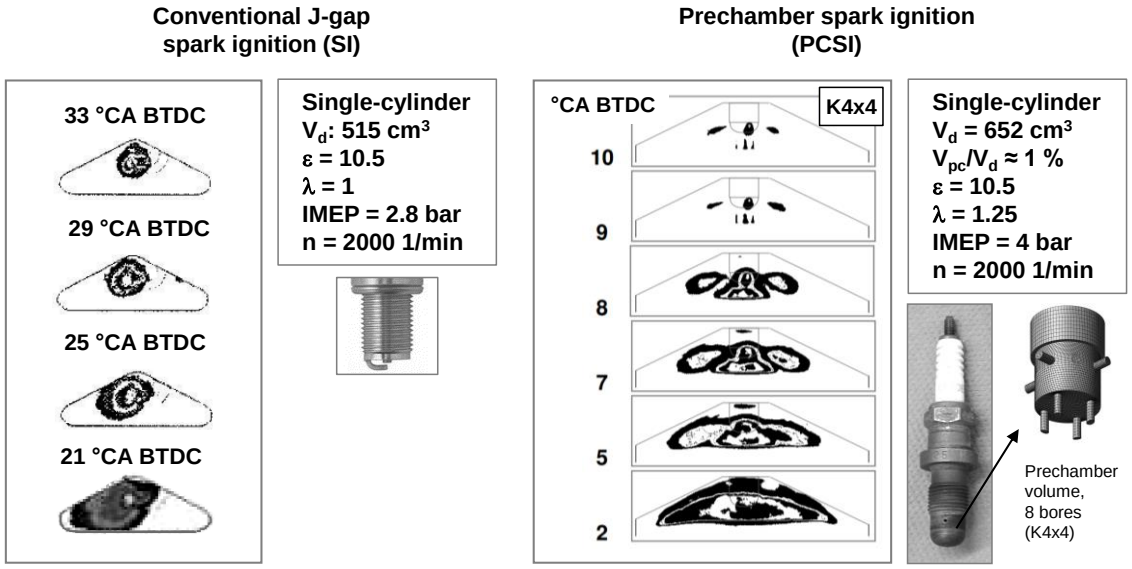

Figure 2.18: Exemplary visualisation of flame propagation in transparent engines for conventional spark ignition (SI) [109] and prechamber spark ignition (PCSI) [76] recorded with an ICCD camera to detect flame OH radiation.

BPI (Bowl Prechamber Ignition) is another approach to enrich the mixture inside the prechamber and enhance the lean-burn limit. After creating a fairly homogeneous main mixture by a first injection of about 98 % of fuel during the intake stroke, the remaining 2 % is injected into a small centrally arranged piston bowl during the compression stroke. As the piston moves upwards, a specially designed prechamber dips into the bowl and the locally enriched mixture is transported into the prechamber, thereby creating near-stoichiometric conditions in the spark gap at spark timing. Detailed information can be found in [76, 147].

2.3.2 Alternative Ignition Systems

In recent years, large number of alternative ignition systems have been developed and investigated, all aiming to improve combustion stability and efficiency in highly diluted (lean-burn and EGR) operation while avoiding the inherent problem of spark ignition: electrode wear. Concepts that have received most attention but are still in the research or development phase, namely corona and laser ignition, shall be reviewed briefly here.

Recently, Corona or high-frequency ignition has been in the focus of many research papers, e.g. [20, 22, 36, 60, 62, 108, 136]. Its principle is based on electric discharges, gener-

ated by a strong inhomogeneous electric field at sharp or spiked electrodes. The discharges produce a large chemically activated, non-thermal plasma (see Figure 2.19, left), with a reactive mixture volume that is up to three orders of magnitude larger than that of conventional spark ignition [62]. This has several advantages: First, the burning delay, defined as the delay between ignition timing and 5 % mass fraction burnt (CA5), is reduced, allowing for a reduction in cyclic combustion variability [36, 60, 62, 136]. Second, the volume ignition causes a faster heat release that allows for ignition timing to be retarded for same combustion phasing or combustion phasing to be advanced due to the reduced knocking tendency [20, 22, 108]. Since the size of the Corona discharge is inversely dependent on pressure [20], Corona ignition seems most promising for igniting highly diluted mixtures at lower engine load [60]. As of 2017, however, corona ignition systems have not yet been introduced in series applications and it is not clear how they would perform in terms of durability and cost efficiency in stationary gas engines.

Laser ignition is based on short intensive laser pulse that is introduced into the combustion chamber through an optical access. The pulse is focused by a convex lens (see Figure 2.19, right), thereby providing sufficient energy to form at hot plasma at the ignition site at the focal point of the lens. The main advantage of this system, making it particularly interesting for premixed high-load lean-burn operation, are the decrease of required ignition energy as in-cylinder pressure rises [142], and the high flexibility in focal point location [56]. The latter enables short flame distances, retarded pulse timings and reduces the risk of knocking. Current disadvantages that hinder its market introduction are high system complexity and costs, and an insufficient durability of the optical components [142].

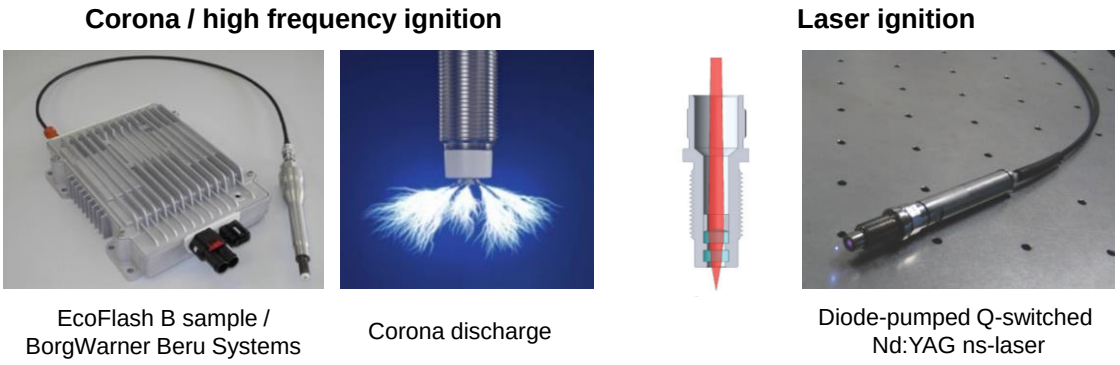

Figure 2.19: Examples of a high frequency Corona ignition system from BorgWarner Beru Systems [22, 142] and a Nd:YAG ns-laser ignition system [135].

Currently, neither of the ignition systems presented above appears to be a viable replacement for prechamber spark ignition in small cogeneration engines, mostly due to the unproportionally high system cost. The hot surface ignition (HSI) system developed and presented herein offers a more simplified and inexpensive solution, as it relies on production components and can be retrofitted in any engine without design modifications. The same main benefits are expected in terms of mixture ignition: increased combustion stability through an increased reactive volume, thus allowing for an extension of the lean-

burn limit and a reduction of NO_x. At the same time, electrode wear is avoided, which holds out the prospect of longer ignition system life time and reduced maintenance costs.

3 Hot Surface Ignition

Most work published in literature addresses the topic of hot surface ignition (HSI) from the point of view of explosion prevention when liquid, gaseous or solid fuels interact with hot components under ambient conditions, or as an undesired pre-ignition phenomenon in internal combustion engines. In other cases, the interaction with a glowing surface is intentional, e.g. in the case of hot surface igniters in gas furnaces, or glow plugs in Diesel engines, used to promote ignition quality of the mixture during cold start. In this work, however, HSI is not seen as a hazard or enabler, but as an alternative to spark ignition in Otto engines running on natural gas. Therefore, after introducing the fundamental aspects of ignition on hot surfaces, this chapter will focus on reviewing the state-of-the-art on deliberate surface ignition in ICE.

3.1 Fundamentals of Hot Surface Ignition

Describing the chemical reactions taking place in a boundary layer that is exposed to some sort of flow is a highly complex task, even more so if the flow field is turbulent and subject to temporal change. Most technically relevant problem formulations, hot surface ignition being one of them, require assumptions and simplifications to be solvable by analytical methods.

3.1.1 Thermal Explosion Theory

The majority of simplified analytical approaches that describe the ignition process and the critical conditions for ignition on hot surfaces are based on the thermal ignition and explosion theories of Semenov [124] (1935) and Frank-Kamenetskii [51] (1955). Their core element is the equilibrium or non-equilibrium between heat production by chemical reac-

tions and heat losses to the surrounding. Therefore, hot surface ignition is dominantly influenced by reaction kinetics and heat dissipation and it is assumed that there is no induction time nor reactant consumption prior to ignition and molecular diffusion is neglected. The main difference between both approaches is that Semenov assumes homogeneous temperature in the entire control volume with heat losses being calculated through Newton's law of cooling, while Frank-Kamenetskii considers a temperature profile of the mixture, determined by Fourier's law of heat conduction. The heat liberated by the chemical reaction is given by:

$$\dot{q}_{prod} = H_i \cdot r \tag{3-1}$$

where H_i is the lower heating value of the fuel in kcal/mol and r the reaction rate describing the amount of heat release by time and volume unit. Assuming a chemical reaction of second order, r adopts the unit mol/cm^{3}s and can be calculated through Eq. (3-2):

$$r = k_0 \cdot c_1 \cdot c_2 \tag{3-2}$$

where k_0 denotes the temperature-dependent reaction rate constant, and c_1 and c_2 the concentration of fuel and oxidiser in mol/cm^3, respectively. k_0 depends on chemical kinetics and needs to be determined either experimentally or numerically through reaction mechanisms. Conventionally, it is expressed in the following Arrhenius form:

$$k_0 = A_{pre} \cdot T^n \cdot e^{\frac{-E_a}{RT}} \tag{3-3}$$

with the apparent activation energy E_a in kcal/mol, the universal gas constant R in kcal/molK and the mixture temperature T in K. According to the theory of Semenov, heat losses can be calculated based on the convective heat transfer coefficient h, the control volume V and its surface area A and the cold wall temperature T_0:

$$\dot{q}_{loss} = h \cdot \frac{A}{V} \cdot (T - T_0) \tag{3-4}$$

Figure 3.1 shows the dependency of heat production and losses qualitatively as a function of mean gas temperature for different cold wall of the control volume. Four different cases can be distinguished:

1. **Case A:** A is a stable point since every small disturbance will bring the system back to point A.
2. **Case B:** If the cold wall temperature is increased to $T_{0,2}$ and the traces of chemical heat production and heat loss intersect at point B, the partial equilibrium gives the critical conditions for mixture ignition. Disturbances regarding a decreased temperature will bring back the system to point B, while increasing temperatures will cause an exponential increase of $\dot{q}_{prod}$ and lead to thermal explosion.

3. **Case C:** Point C is unstable as disturbances will either cause the system to fall back to point A or to point D.
4. **Case D:** If a heterogeneous reaction, where diffusion processes are not sufficient to feed enough unburnt mixture into the reaction zone at the same rate as the reactants are consumed by $\dot{q}_{prod}$, is considered instead of a homogeneous reaction with practically unlimited reaction rate as a function of temperature, another stable case, point D, may exist. Transport processes limit the heat production rate, as indicated by the dashed curve.

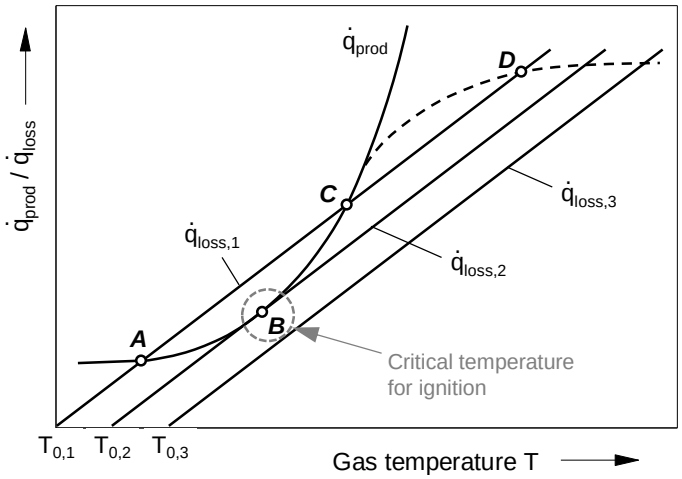

Figure 3.1: Schematic representation of heat production and heat losses in the control volume for different cold wall temperatures T_0 (acc.to [105]).

Several researchers [1, 2, 23, 79, 105] provide more or less detailed examples of how to calculate the critical ignition temperature from Case B through the thermal approach of Frank-Kamenetskii for a steady-state one-dimensional problem without reactant consumption prior to ignition. The temperature field in the vicinity of the hot surface, illustrated qualitatively in Figure 3.2, can be determined by the following energy conservation equation:

$$\rho \cdot c_p \cdot \frac{dT}{dt} = k\left(\frac{\partial^2 T}{\partial x^2} + \frac{n}{x} \cdot \frac{\partial T}{\partial x}\right) + \dot{q}_{prod} \tag{3-5}$$

where k is the thermal conductivity of the gas and n a parameter for the type of problem (infinite slab: $n = 0$; rotationally symmetric/cylinder: $n = 1$ and spherically symmetric/sphere: $n = 2$), though the equation cannot be solved analytically for cylinder and sphere problems [23, 105]. As the case considered is that of a flat surface in steady state, it applies that $n = 0$ and $dT/dt = 0$. When inserting the definition $\dot{q}_{prod}$, Eq. (3-5) simplifies to:

$$\frac{d^2 T}{dx^2} = -\frac{H_i}{k} \cdot r \tag{3-6}$$

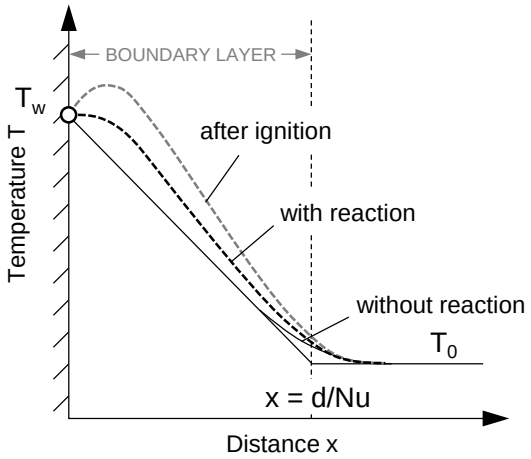

Figure 3.2: Gas temperature in the boundary layer with thickness d/Nu in the vicinity of the hot surface with and without exothermal chemical reaction.

The thickness of boundary layer is defined by d/Nu, where d is the characteristic length of the body (here the diameter of the glow plug pin). d/Nu describes the thickness of the zone in which temperature would decrease from hot wall temperature T_w, e.g. hot surface temperature, to cold wall temperature T_0 solely due to heat conduction (see Figure 3.2, "without reaction"). Being a function of the Nusselt number, it is affected by the flow field and the size of the hot surface.

For the ignition on hot surfaces, following boundary conditions are formulated:

$x = 0: \quad T = T_w$

$x = d/Nu: \quad T = T_0$

The exponent of the e function E_a/RT can be written as:

$$\frac{E_a}{RT} = \frac{E_a}{RT_w} \cdot \frac{1}{1 + \frac{T - T_w}{T_w}} = \frac{E_a}{RT_w} \cdot \left[1 - \frac{T - T_w}{T_w} + \left(\frac{T - T_w}{T_w}\right)^2 - \cdots\right] \tag{3-7}$$

For temperatures in the vicinity of the hot surface, stopping after the second term of the Taylor series yields satisfactory results [105]. In a next step, the dimensionless temperature

$$\Theta = \frac{E_a}{RT_w{}^2}(T - T_w) \tag{3-8}$$

and the dimensionless distance

$$\xi = \frac{x}{d/Nu} \tag{3-9}$$

are introduced. Together with Eq. (3-7), this allows expressing Eq. (3-6) as:

$$\frac{d^2\Theta}{d\xi^2} = -\frac{H_i}{k} \cdot \frac{E_a}{RT_w{}^2} \cdot \left(\frac{d}{Nu}\right)^2 \cdot k_0 \cdot c_1 \cdot c_2 \cdot e^{\Theta} \tag{3-10}$$

or simply:

$$\frac{d^2\Theta}{d\xi^2} = -\delta \cdot e^{\Theta} \tag{3-11}$$

with

$$\delta = \frac{H_i}{k} \cdot \frac{E_a}{RT_w{}^2} \cdot \left(\frac{d}{Nu}\right)^2 \cdot k_0 \cdot c_1 \cdot c_2 \tag{3-12}$$

Frank-Kamenetzki [52] gives following solution to Eq. (3-10), describing the temperature distribution in the computational field in question:

$$e^{\Theta} = \frac{a}{\cosh^2\left(b + \sqrt{\frac{a\delta}{2}}\,\xi\right)} \tag{3-13}$$

where the integration constants a and b can be determined by means of the two dimensionless boundary conditions:

$$\xi = 0: \quad \Theta = 0$$

$$\xi = 1: \quad \Theta = \Theta_0 = \frac{E_a}{RT_w{}^2}(T_0 - T_w)$$

Inserting the boundary conditions yields:

$$b = \pm arcosh\sqrt{a} \tag{3-14}$$

and

$$e^{\Theta_0} = \frac{a}{\cosh^2\left(b + \sqrt{\frac{a\delta}{2}}\right)} \tag{3-15}$$

Equations (3-14) and (3-15) combined give parameter δ after eliminating b:

$$\delta = \frac{2}{a} \cdot \left[arcosh\sqrt{\frac{a}{e^{\Theta_0}}} \pm arcosh\sqrt{a}\right]^2 \tag{3-16}$$

When plotting δ for constant Θ_0 as a function of a (see e.g. [105]), it can be seen that there exists a $\delta_{max} = \delta_{crit}$ above which no value for a gives a solution to Eq.(3-11), and the equilibrium between heat production and losses cannot be sustained (Case B in Figure 3.1). Below this maximum, two solutions for each δ exist (Cases A and C). $d\delta/da = 0$ gives the required value for a which can be inserted in Eq. (3-16) to deter-

mine δ_{crit} only as a function of Θ_0, as shown in Figure 3.3 (left). Through linear regression, Boulouchos [23] derived the following simple equation, particularly valid for larger values of $-\Theta_0$:

$$\delta_{crit} = (-0.667 \cdot \Theta_0 + 1.5)^2 \tag{3-17}$$

Combining equations (3-12) and (3-17) yields the following expression, illustrated qualitatively in Figure 3.3, right:

$$\frac{H_i}{k} \cdot \frac{E_a}{RT_w{}^2} \cdot \left(\frac{d}{Nu}\right)^2 \cdot k_0 \cdot c_1 \cdot c_2 = \left(-0.667 \cdot \frac{E_a}{RT_w{}^2}(T_0 - T_w) + 1.5\right)^2 \tag{3-18}$$

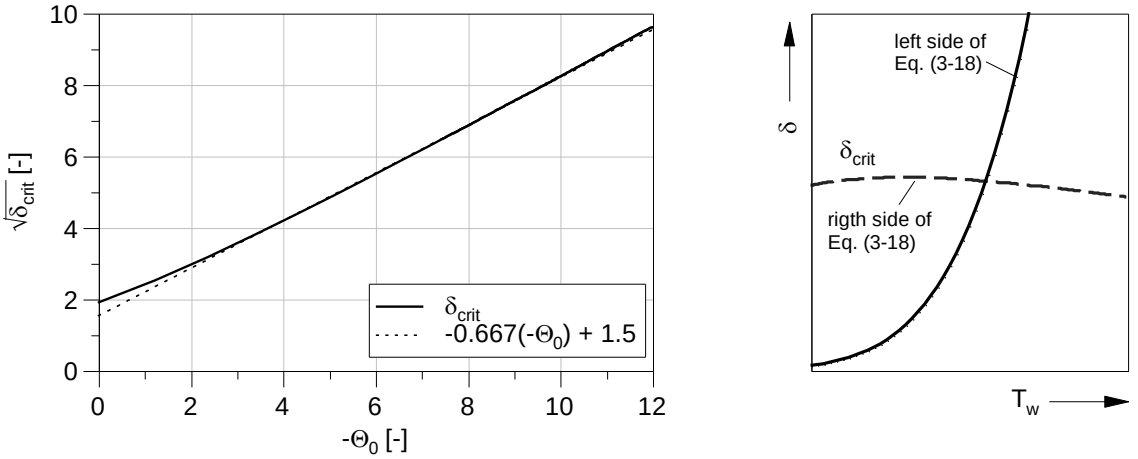

Figure 3.3: Parameter δ_{crit} as a function of dimensionless temperature Θ_0 (left) and graphical representation of the critical conditions that yield the critical ignition temperature T_{crit} (right). δ_{crit} (left) was calculated numerically by forming the derivative $d\delta/da = 0$ of Eq. (3-16) and solving for a.

By setting $\delta = \delta_{crit}$, i.e. the intersection of both curves, combinations of parameters that lead to thermal explosion can be found. The approach accounts for the following factors [105]:

- The type of mixture (heating value H_i, reaction rate r, activation energy E_a and heat conductivity k).
- Mixture pressure (pressure dependent concentration parameters c_1 and c_2).
- The influence of the flow field and hot surface geometry (Nusselt number Nu and characteristic length d that determine the boundary layer thickness d/Nu and the convective heat transfer coefficient h).
- The influence of mixture temperature T_0, predominantly through factor δ_{crit} itself.

Neglecting reactant consumption and mass diffusion processes in the reaction zone as well as the assumption of steady-state conditions are arguably the largest simplifications of the thermal explosion theory. However, its relative simplicity allows deriving useful dependencies based on only few input parameters, even when system knowledge is limited.

For this reason, the δ_{crit} method will be used in the following subsection to determine basic correlations relevant to hot surface ignition in internal combustion engines.

3.1.2 Theoretical Dependencies of Critical Ignition Temperature

The main challenge in determining the critical ignition temperature through Eq. (3-18) is knowing the reaction rate constant k_0 and the exact activation energy E_a. For air-isooctane mixtures, Peters [105] resorted to literature values for E_a and calculated k_0 from experiments in a heated, optically accessible CCVC at $p = 1$ ata/$\lambda = 1/T_0 = 523$ K under stagnant conditions ($Nu \approx 2$) and a measured ignition temperature of $T_w = 1225$ K. Knowing all other parameters, it was possible to calculate constant k_0, which was subsequently used for calculating the reaction rate for other configurations. In the present work, such experimental data was not available. For this reason, reaction rate was calculated by assuming an overall one-step reaction with data taken from [148] for methane:

$$r = \frac{d[CH4]}{dt} = 1.3 \cdot 10^9 \cdot [CH_4]^{-0.3} \cdot [O_2]^{1.3} \cdot e^{\frac{-E_a}{RT}} \tag{3-19}$$

with $E_a = 48.4$ kcal/mol. In due consideration of the low fractions of fuel in the air-fuel mixture, physical properties of the mixture, like kinematic viscosity, density and thermal conductivity, were calculated assuming pure air, at the geometric mean reference temperature $T_{ref} = (T_w + T_0)/2$.

The convective heat transport in forced convection is governed by the Nusselt number, which describes the ratio of convective to conductive heat transfer normal to the boundary layer:

$$Nu = \frac{h \cdot d}{k} \tag{3-20}$$

Generally, Nu is a function of the Reynolds (Re) and Prandtl (Pr) numbers. With the air-fuel mixture being in gaseous state, Pr is fairly constant over a wide range of pressures and temperatures ($Pr \approx 0.7$) [90]. Hence, with the simplification of constant Pr, Nu becomes a sole function of Re. However, in technical systems where a surface is exposed to particular flow conditions, Nu is not constant for the entire surface. For a heated cylinder positioned in a turbulent cross flow, for example, Schmidt and Wenner [119] determined that local Nu shows a minimum at around $\varphi = +/- 90$ °, i.e. on either sides of the hot surface, regardless of the Reynolds number (see Figure 3.4). When applied to hot surface ignition, these points provide the most beneficial conditions for mixture ignition as heat losses of the reaction zone are minimised [23].
Because determining the local Nusselt number is impractical and the actual flow inside the cylinder is neither unidirectional not steady, a simplified correlation after Kreith and Black (as cited in [2]) giving a mean value for Nu for a cylinder in a cross-flow is used,

where constants C_0 and r_0 are calculated according to Table 3.1.

$$:Nu = C_0 \cdot Re^{r_0} \cdot Pr^{1/3} \tag{3-21}$$

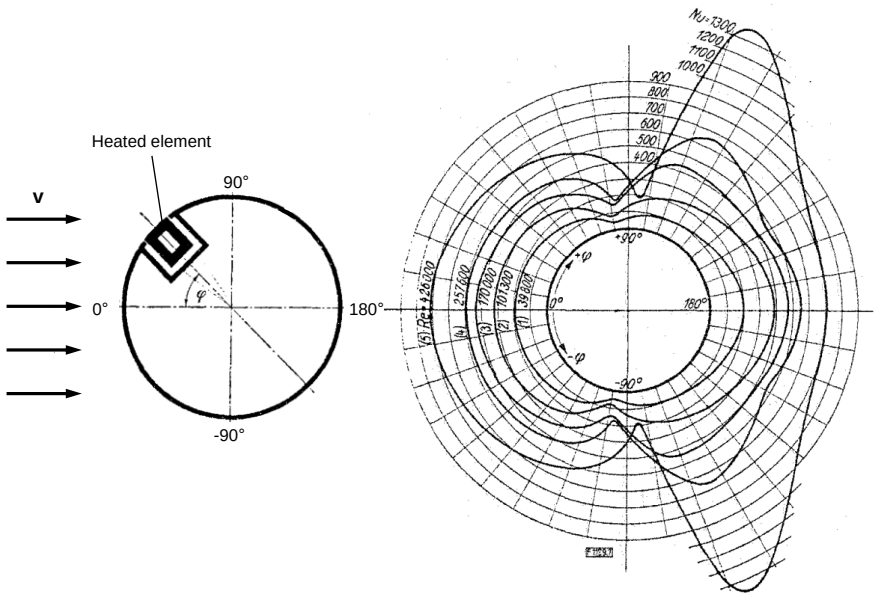

Figure 3.4: Local Nusselt number Nu in a turbulent flow as a function of cylinder angle φ [119].

Table 3.1: Constants for determining the Nusselt number for a cylinder in a cross-flow after Kreith and Black (data taken from [2])

Re	C_0	r_0
0.4 – 4	0.989	0.330
4 – 40	0.911	0.385
40 – 4000	0.683	0.618
4000 – 40000	0.193	0.618
40000 – 400000	0.0266	0.805

In general, thermal conductivity of gases increases significantly with temperature. This was accounted for by a correlation for air proposed by Stephan and Laesecke [133].

Figure 3.5, left, shows how the critical ignition temperature for varying mixture temperature and pressure configurations is determined graphically under quiescent conditions. It can be seen that the increase of both parameters lowers the HS temperature (here: T_w) required for ignition, a finding supported by experimental data from Peters [105] for iso-octane- and benzol-air mixtures. While the effect of mixture temperature is fairly constant over the entire pressure range, the reduction in T_{crit} is substantial when increasing pressure in the lower range, but reaches saturation in the high-pressure range, most relevant for engine operation. The effect of relative air-fuel ratio is presented in Figure 3.5, right. When leaning out the mixture, the concentration of fuel is reduced while that of oxidiser is increased and Eq. (3-19) gives a higher reaction rate. Since the heat losses in the boundary layer remain constant, T_{crit} is reduced moderately, albeit the reduction

becomes even less significant as system pressure is increased. The results agree with published experimental data [78, 139] that observed how the critical surface temperatures that cause ignition increase with increasing equivalence ratio for methane- and hydrogen-air mixtures, while the reverse is true for higher alkanes or methane with fractions of higher alkanes. This suggests that the trend observed for methane may reverse for natural gas, mostly depending on the fractions of ethane and propane.

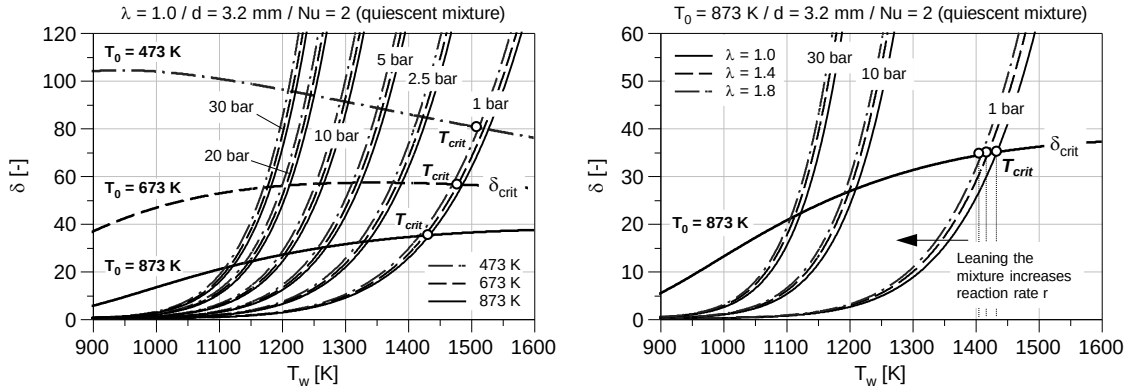

Figure 3.5: Parameters δ (left side of Eq. (3-18)) and δ_{crit} (right side of Eq. (3-18)) as a function of wall temperature T_w, pressure p and mixture temperature T_0 (left) and relative air-fuel ratio λ (right) for quiescent air-methane mixtures. The intersection of both curves yields the critical ignition temperature T_{crit}.

The effects of hot surface diameter d and flow velocity v on the critical temperature, also determined from Eq. (3-18), are shown in Figure 3.6. T_{crit} is highest for small diameters but decreases sharply with increasing diameter. With the size of the hot surface, the thickness of the boundary layer increases (d/Nu), leading to reduced heat losses to the mixture, more favourable to mixture ignition. Due to the simultaneous increase of turbulence, and thus the Nusselt number Nu, T_{crit} converges for larger diameters. The same qualitative relationship has been reported from experiments with methane by Laurendeau [79] and isooctane by Peters [105]. For quiescent mixtures, Nu is small, thereby forming a thick boundary layer with a distinct low-gradient temperature profile. This limits the heat losses by thermal diffusion, and the critical temperature for which heat losses and heat production equal can be reduced. In contrast, when the hot surface is exposed to a flow, Nu increases as a function of flow velocity and thins the boundary layer. To facilitate mixture ignition, the rising heat losses need to be counteracted by an increase of HS temperature. Very similar experimental trends are shown by Adomeit [1] for town-gas mixtures (main constituents: CH_4, H_2 and CO). It can be seen that even at high pressure and mixture temperature, both of which have a promoting effect on ignition, increasing flow velocities require excessively high temperatures to induce combustion, as a result of the low computed reaction rates for methane. It can therefore be assumed that measures to reduce the much larger flow velocities that arise inside an engine combustion chamber, e.g. by shielding the hot surface, are required to facilitate mixture ignition at viable temperatures.

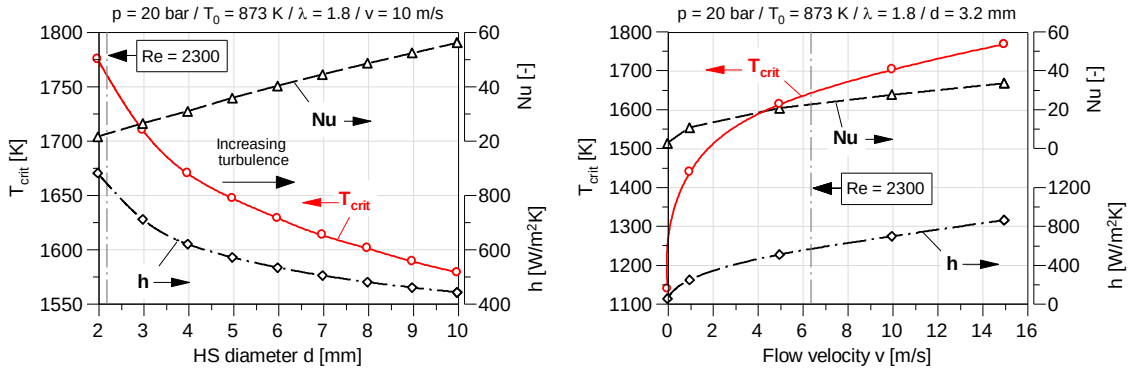

Figure 3.6: Critical ignition temperature for air/methane as a function of hot surface diameter d and flow velocity v.

3.1.3 Theoretical Considerations on Ignition Delay and Combustion Phasing

All considerations presented thus far assume a steady physical state of the mixture, as defined by temperature and pressure and its chemical constitution and neglect the factor time. In an ICE, however, piston motion leads to changing conditions that not only affect pressure and temperature but also the spatial species concentration and the flow field in the vicinity of the hot surface. Furthermore, not only the critical temperature at which an air-fuel mixture will ignite when subjected to a particular thermodynamic state is crucial but also the induction time, i.e. the time that elapses from the first contact between the mixture and the hot surface and the start of the combustion process (mixture inflammation). A properly timed start of combustion is a basic requirement for setting the phasing of heat release such that most heat is released and converted to engine work close to TDC. For premixed air-fuel mixtures, as stated towards the end of Section 2.1.2, the integrated autoignition delay at constant relative air-fuel ratio is a function of the time histories of mixture pressure and temperature. Prior to the onset of combustion, these traces are chiefly predetermined by mixture mass and density at inlet valve closing (IVC), instantaneous cylinder volume (compression ratio and crank drive geometry), heat losses to the cylinder walls and blow-by losses. During the gas exchange until IVC, the formation rate of chain carriers is negligible due to low pressures and temperatures. During the compression stroke, however, the concentration of reactive species increases rapidly, mostly due to the inverse and exponential dependency of the reaction rate on temperature. When the integral method is applied to hot surface ignition, the mixture that is located in the vicinity of the hot surface is permanently exposed to significantly higher temperatures than the remaining bulk. Evidently, this will lead to increased reaction rates in the boundary layer and facilitate the ignition of mixtures that would not autoignite by compression alone. From this reasoning it follows that ignition delay in HSI engine operation is primarily governed by the physical state of the bulk mixture and, additionally, by hot surface temperature. Therefore, just like spark timing in SI engines, HS temperature represents the control variable that enables shifting the start of combustion and, in turn, combustion phasing at otherwise constant operating conditions. By

raising or lowering HS temperature combustion phasing can be advanced or retarded, respectively, as illustrated qualitatively using the integral method in Figure 3.7 (left).

As shown previously, the effect of relative air-fuel ratio on the absolute ignition delay and the critical ignition temperature of air-methane mixtures is only of minor importance. Nonetheless, λ has a strong bearing on the laminar burning velocity, causing a slower heat release and longer combustion durations as the mixture is leaned. Assuming a constant ignition delay, Figure 3.7 (right) visualises the effect of leaning out the mixture on heat release and in-cylinder pressure when the slower combustion process is not accounted for by increasing HS temperature in order to advance combustion phasing.

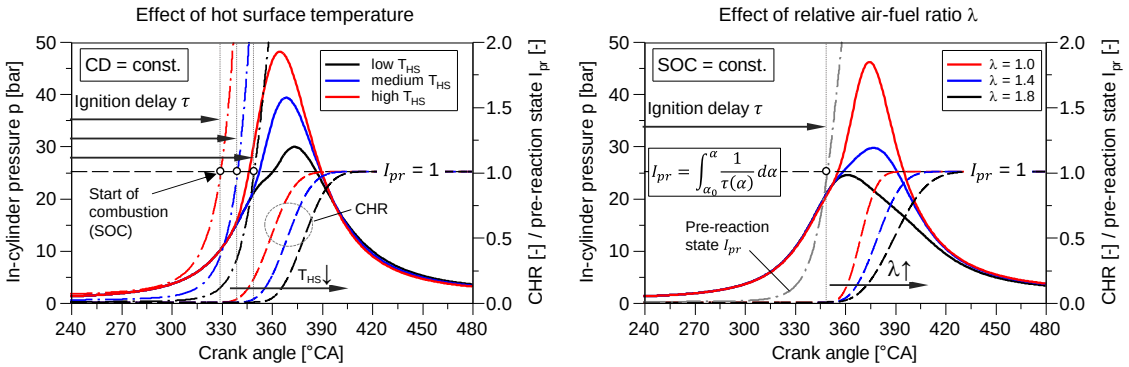

Figure 3.7: Qualitative effects of hot surface temperature (lfet) and relative air-fuel ratio λ (right) on the start of combustion, the cumulative heat release (CHR) and the pressure history against crank angle.

3.2 Hot Surface Ignition in Internal Combustion Engines

Intentional or deliberate surface ignition in internal combustion engines has been investigated with different objectives for numerous different applications and a multitude of different parameters. Table 3.2 attempts to classify the works reviewed in this section, based on specific properties of engine operation and the surface ignition system itself:

Table 3.2: Classification of reviewed research work on deliberate surface ignition

Property	Characteristic		
Fuel state	*gaseous*	*liquid*	
Mixture preparation	*premixed/homogeneous*	*homogeneous with enrichment*	*stratified/DI*
Compression ratio	*low (Otto type)*	*high (Diesel type)*	
Surface type	*reactive (catalytic)*	*inert (purely thermal)*	
Flow conditions	*unshielded*	*shielded*	*inside prechamber*
Control	*no control (self-sustained)*	*voltage/current control*	*temperature control*
Engine size	*small-bore*	*medium-bore*	*large-bore*

The history of deliberate surface ignition in internal combustion engines goes back until the end of the 19th century, when Herbert-Akroyd Stuart filed a patent for the first commercially successful “hot-bulb” engine for heavy-oils, entitled “Improvements in Engines Operated by the Explosion of Mixtures of Combustible Vapour or Gas and Air” [134]. Combustion was initiated by autoignition on the hot surface of a smaller separated combustion chamber, the “vapouriser” or “hot bulb”, mounted on the cylinder head, into

which liquid fuel was injected. It was connected to the main combustion chamber by a narrow passage and was heated either by the cylinder's coolant or self-sustained by the hot exhaust gases during operation. An external flame such as a blowtorch was used for cold-start. Shortly after, Gottlieb Daimler patented a so-called „glow tube ignition“ to ignite gaseous air-fuel mixtures in 4-stroke gas engines [44]. A continuously burning flame was used to heat the tube (see *f* in Figure 3.8) externally. During the compression stroke, mixture would be pressed into the glowing tube, ignite and initiate combustion in the main combustion chamber. The development of spark ignition (SI) several years later, however, made this type of surface ignition become redundant, especially due to the advantages of SI in transient and mobile operation, the higher degree of freedom regarding the timing of mixture inflammation and the reduced system complexity.

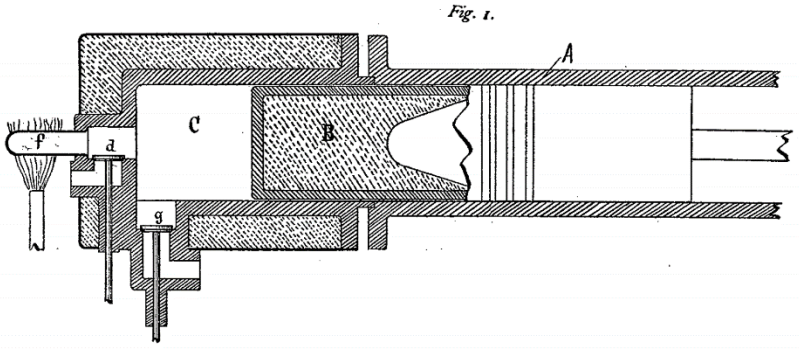

Figure 3.8: Gas engine with “glow tube ignition” patented by Daimler in 1893 [44].

More recently, in 1976, Rohde [118] conducted experiments on HSI induced combustion in a 4-cylinder 1.6 l SI engine, primarily on air-petrol mixtures. In preliminary test, he evaluated the functionality of the design variants shown in Figure 3.9 (left), finding that many were not suitable for stable engine operation, either due to uncontrollable starts of combustion, or their inability to ignite the mixture safely. The most promising concept stood out to be configuration 1, a single glow plug that protrudes directly into the combustion chamber, called *unshielded* HSI herein, for reasons of consistency. With unshielded HSI, he determined basic dependencies between both hot surface temperature and electric heating power and relative air-fuel ratio, volumetric efficiency (i.e. intake manifold pressure) and engine speed at MBT (Maximum Brake Torque) combustion phasing. HS temperature was measured with a thermocouple welded onto the glow plug tip. To avoid damaging the igniter by excessive currents and temperatures at cold start, HSI required SI assistance during the engine start procedure. In the upper plot in Figure 3.9 (right) it can be seen that HS temperature only needed to be adjusted when varying engine speed, while being rather independent of λ and the volumetric efficiency. While the actual duration of combustion in seconds may even fall due to an increased turbulence level in the combustion chamber when increasing engine speed, combustion duration, expressed in °CA, is increased. Therefore, in order to retain optimal combustion phasing, start of combustion needs to be advanced by raising HS temperature. As for the electric heating power, it showed a minimum for stoichiometric mixtures due to the maximum

heat released from combustion. The increase of heating power with volumetric efficiency is attributed to the higher energy content of the mixture and the higher combustion temperature, also enhancing the heat flux from hot combustion gases to the glow plug.

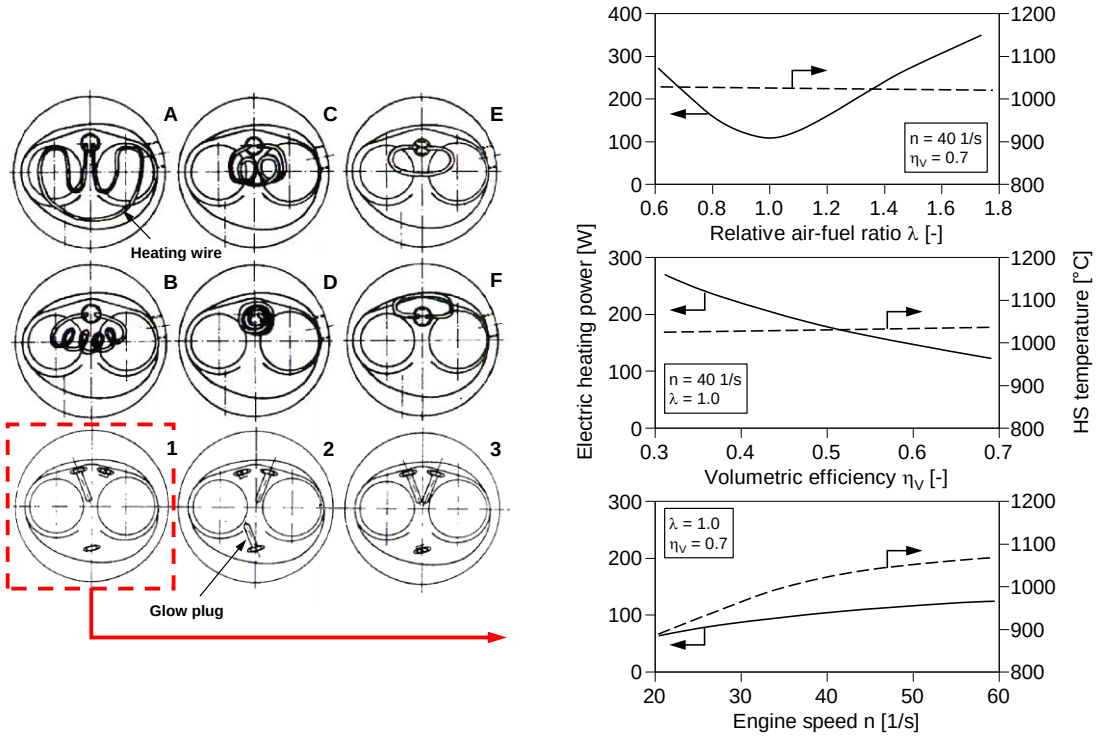

Figure 3.9: Left: Several types of hot surface igniters tested in [118]. A-F: Heating wires with varying volume of mixture activation; 1-3: Varying number and position of glow plugs. Right: Effect of relative-air fuel ratio λ, volumetric efficiency η_V and engine speed n on required HS temperature and electic heating power using variant 1 [118].

The impractical necessity of an additional thermocouple to control HS temperature as well as the low durability of the tested concept triggered the development of several active and passive hot surface igniters allocated inside unscavenged prechambers (*prechamber* HSI) with varying volume and diameter of the single connecting channel (see Figure 3.10). In this context, *active* HSI is one that allows electric heating of the hot surface while for *passive* HSI hot surface temperature is a dependent parameter. The aim of the prechamber was to avoid interaction between fresh mixture and HS before the compression stroke, which was believed to require higher HS temperatures for ignition but allow for improved combustion stability. The sub-prechamber's function was to hinder fresh mixture from impinging directly upon the glow plug. The lack of a closed-loop HS temperature control required manual adjustment of the electric heating power. Is it expected that it was therefore not possible to set comparable and reproducible combustion phasings, which makes data interpretation among all tested variants difficult. While several crucial parameters influencing HSI operation were not addressed, most likely due to limitations of the experimental installation, the author's general observations on both unshielded (Figure 3.9, variant 1) and prechamber HSI (Figure 3.10) can be summarised as follows:

- Unshielded HSI allows for a significant enhancement of the lean-burn limit compared to SI by increasing the reactive mixture volume and the amount of energy provided for mixture inflammation. The induced combustion is characterised by higher burn rates and shorter combustion duration, resulting in higher maximum pressures, combustion temperatures and NO_x emissions. Simultaneously, CO and HC emissions are reduced.
- Prechamber HSI has a similar operating range to SI but produces less NO_x and HC at similar levels of CO. However, both engine work and efficiency are reduced.

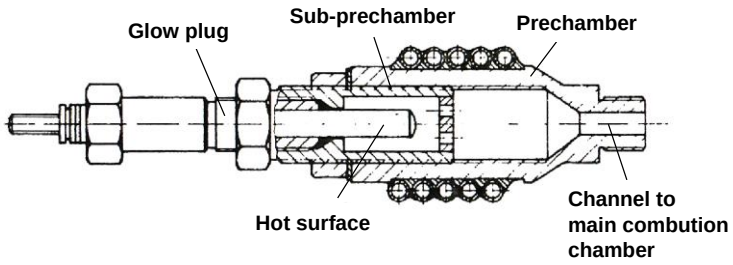

Figure 3.10: Prechamber HSI employed by Rohde for most experiments [118].

In 1980, Nagalingam et al. [96] presented an approach to ignite air-alcohol mixtures (namely ethanol and methanol) in conventional Diesel engines. They developed a hot surface igniter made of a slab of insulator material wound with a few strands of heating wire (Kanthal), positioned inside a prechamber that was mounted on top of the cylinder head of a 553 cc single-cylinder Diesel engine (see Figure 3.11, *a.*). The fuel injector was oriented such that a part of the spray would impinge on the heated surface and initiate combustion. Due to the low thermal conductivity of the asbestos slab, it would reach temperatures sufficient to initiate ignition without the aid of resistance heating from the wires, thus enabling self-sustained HSI (*passive* HSI) after only a few minutes.

The authors conducted engine trials for compression ratios of 8.84 and 14.65 at engine speeds of 1000, 1500 and 2000 1/min to determine brake thermal efficiency as a function of engine power. Injection timing was constant at 31 °CA BTDC and in most tests the engine was run on methanol, though it was also able to operate with ethanol and petrol satisfactorily. The experiments revealed longer delay periods, lower peak pressures and rates of pressure rise with increasing engine speed, leading to partially worsened engine efficiency and higher CCV. The assumption was that this may be caused by the specific shape of the combustion chamber and throttling effects from the connecting passage between prechamber and the cylinder. While those may be additional influencing factors, it is more likely that the shorter cycle time in seconds, or put differently, the higher °CA/s rate at higher engine speeds, leads to apparently longer ignition delays in °CA, reduced rates of heat realease (in J/°CA) and retarded combustion phasing if HS temperature is not increased accordingly. Despite the limited life-time of about 6-10 h of the employed asbestos sheets, the authors were able to prove the basic functionality of a self-sustaining HSI system for alcohol-fuelled Diesel engines.

In 1992, Ramesh et al. [115], from the same institute, readdressed the topic and developed two types of surface igniters: a similar concept to the one in [96] but accommodated on the cylinder head (see ***b.*** in Figure 3.11), and a glow plug (***c.*** in Figure 3.11). Instead of asbestos, the 4 mm thick hot surface plate was made of partially stabilised zirconia, a tougher and more shock resistant material, thus increasing life-time of the igniter. Again, Kanthal wires were used for resistance heating and fixed onto the surface. Tests were conducted on a 904 cc air-cooled Diesel single-cylinder engine with a compression ratio of 16.9, mostly running on methanol at 1800 1/min. After several design changes, a hot surface design variant having a shield with an opening at the periphery only stood out to be suitable for operating the engine at high speeds (*shielded* HSI). Ignition delay responded well to heater input, enabling the adjustment of combustion phasing to MBT. Part load required electric heating power of about 120 W and performance proved to be unsatisfactory due to poor ignition and combustion at low mixture temperatures. At higher loads, however, brake thermal efficiency was higher compared to Diesel operation and resistance heating could be switched off (*passive* HSI). The effect on NO_x emissions and cycle-by-cycle variations was not investigated. In comparison, the glow plug concept allowed for a slight increase in thermal efficiency at high loads, but also showed poor low-load combustion stability due to excessive cooling of the hot surface. While the power input required at low loads was about 180 W, it could be reduced with increasing engine load, yet not brought to zero as in the case of the ceramic plate HSI. Combustion induced by the ceramic plate was characterised by higher rates of heat release and shorter combustion durations, while the beginning of the main combustion was more sluggish when using the glow plug, reportedly caused by its smaller surface. The authors concluded that controlling the electric input and optimising injection timing are key factors for good engine performance.

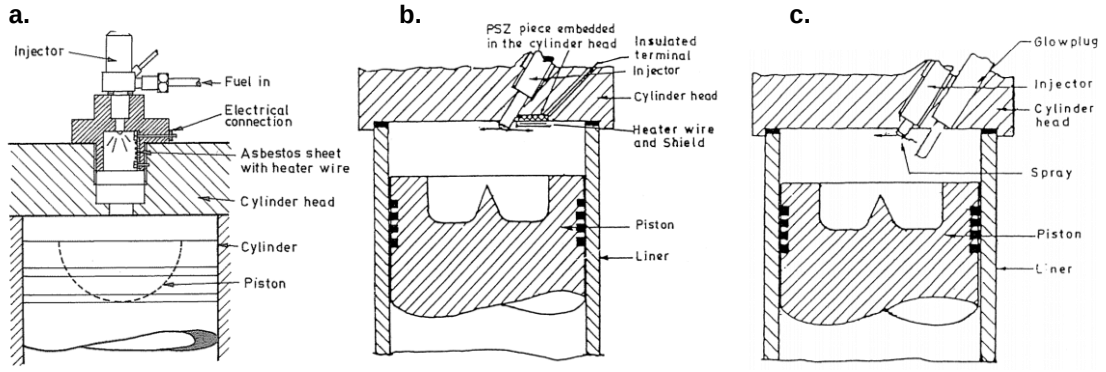

Figure 3.11: Prechamber hot surface igniter developed and tested by Nagalingam et al. (a.) [96] and unshielded/shielded hot surface igniters by Ramesh et al. (b. and c.) [115].

In attempt to minimise heating power at lower loads, the Kanthal wire was subsequently replaced by one made of platinum of same dimensions. The catalytic properties of the material lower the activation energy of the air-fuel mixture, leading to enhanced reaction rates, i.e. reduced ignition delay times under the assumption that hot surface temperature remains constant. Alternatively, ignition delay can be kept constant despite reducing

the temperature, which corresponds to the approach taken by the authors. Nevertheless, in spite of enabling very low electric inputs for ignition, stable operation over a wider range was not possible using the catalytic igniter. It is not clear, however, if the sensing capabilities of the platinum wire were used to determine HS temperature.

Following the same rationale, Boulouchos [23] developed a catalytic hot surface igniter (CHSI) using a platinum-wire coil as both heating element and temperature sensor a few years before, in 1984 (see Figure 3.12). The practically linear specific resistance-temperature dependence of platinum enabled him to implement a constant temperature controller. He investigated unshielded CHSI with premixed lean air-petrol mixtures and, like Rohde [118], showed that the lean-burn limit could be enhanced significantly compared with spark ignition, due to an accelerated main combustion.

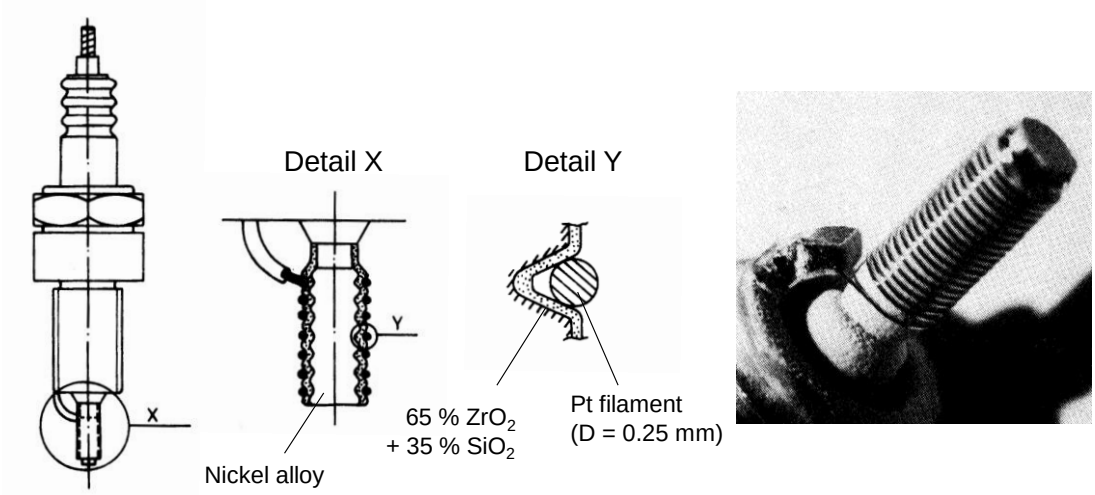

Figure 3.12: Catalytic hot surface igniter (CHSI) developed and employed by Boulouchos [23].

He was aware of the influence of cyclic dispersions in flow field, mixture and temperature in the combustion chamber on the critical ignition temperature and visualised the qualitative dependencies, see Figure 3.13:

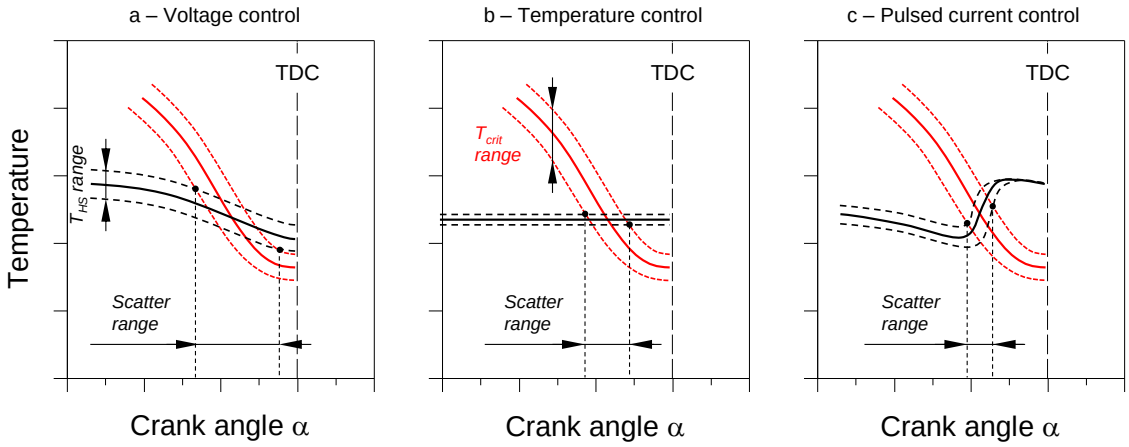

Figure 3.13: Trace of hot surface temperature (T_{HS}) and critical ignition temperature (T_{crit}) against crank angle during the compression stroke for a: voltage control, b: hot surface temperature control, c: pulsed current control (acc. to [23]).

The three plots depict HS temperature and critical ignition temperature as a function of crank angle during the compression stroke for uncontrolled temperature, i.e. voltage control, (*a*), constant temperature control (*b*) and pulsed current control (*c*). The upper and lower bounds of the critical ignition temperature trace (T_{crit} range) represent the effect of the aforementioned CCV. Since HS temperature is also subject to more or less pronounced cyclic variations, it also shows an upper and lower bound (T_{HS} range). Evidently, mixture inflammation ensues once the actual temperature traces intersect. In case *a*, the increasing charge motion during the compression stroke enhances the convective heat flux from hot surface to mixture by an increased heat transfer coefficient, thereby leading to gradual decrease in HS temperature as TDC is approached. Assuming that HS temperature is still sufficiently high for mixture inflammation close to TDC, the characteristics of the subsequent combustion (i.e. phasing and duration) determine HS temperature in the next engine cycle. As a result, the temperature spread between the T_{HS} bounds becomes significant, leading to a large scatter range of ignition timing/start of combustion from cycle to cycle. In theory, the scatter range can be constrained considerably by controlling HS temperature (*b*), and even further when applying a timed current pulse (*c*). For minimising the scatter range in approach *c*, the induced temperature increase of the hot surface needs to be as steep as possible. This makes high demands on the power source as a high electric currents and powers need to be provided, though for a very short time.

The author conducted experiments on two different 2-valve engines with port fuel injection (PFI), a 1.6 l 4-cylinder and 1.8 l 4-cylinder engine, both with heron-shaped combustion chambers, and compression ratios of 7.2/8.2 and 10.0, respectively. In both cases, conventional SI was replaced by the surface igniter in only one cylinder, in an angle to the cylinder axis of 29° and 33°, respectively. Preliminary experiments with current pulse control revealed that currents of 70-100 A at electric powers of 10-20 kW were required to increase HS temperature by about 100 K for a triggered pulse of 100 µs during the compression stroke. While it enabled stable engine operation, pulsed current control was then discarded and all experiments conducted employing HS temperature control (*b*) due to the short durability of the heating wire and high system complexity. The total resistance of the heating coil, being directly correlated to its temperature, is measured and compared to a set value given by a potentiometer. In function of the error, an analogous controller adjusts the voltage applied to the heating coil, with a response time that is limited by its inductance. This setting allowed keeping HS temperature constant in a range of +/- 5 K. The findings of his experiments can be summarised as follows:

- Resistance of the heating coil is the equivalent to spark timing in SI operation and represents the means to adjust combustion phasing. The higher the resistance, i.e. hot surface temperature, the earlier the mixture will ignite in the cycle. The usual resistance range spanned from 1.0 to 1.4 Ω.
- The required HS temperature for MBT combustion phasing increases with engine

speed and air-fuel ratio and decreases with volumetric efficiency, i.e. intake manifold pressure.

- In an engine unfavourable to lean-burn operation, CHSI allows for the lean-burn limit to be shifted by about $\Delta\lambda = 0.15\text{-}0.2$ over the whole investigated range from low part-load to wide-open throttle (see Figure 3.14).
- Based on the statistical analysis of 60 consecutive cycles, CHSI always showed higher maximum in-cylinder pressure p_{max} and generally higher standard deviations σp_{max} and $\sigma pos_{p_{max}}$.
- At constant air-fuel ratio, surface ignition produces higher NO_x emissions, which is solely ascribed to the faster combustion in the experimental discussion chapter. Nevertheless, the trade-off between brake specific fuel consumption (BSFC) and NO_x was generally improved at part-load (BMEP < 6 bar) and for lean combustion at full-load ($\lambda \geq 1.2$) due to the accelerated heat release. However, the results of fuel consumption and emission output should be treated with caution due to the integral measurement method for all 4 cylinders. That is to say, that the effects caused by the one cylinder running on CHSI can be attenuated or even go unnoticed due to those caused by the remaining spark ignited cylinders, that may run at more or less favourable conditions.

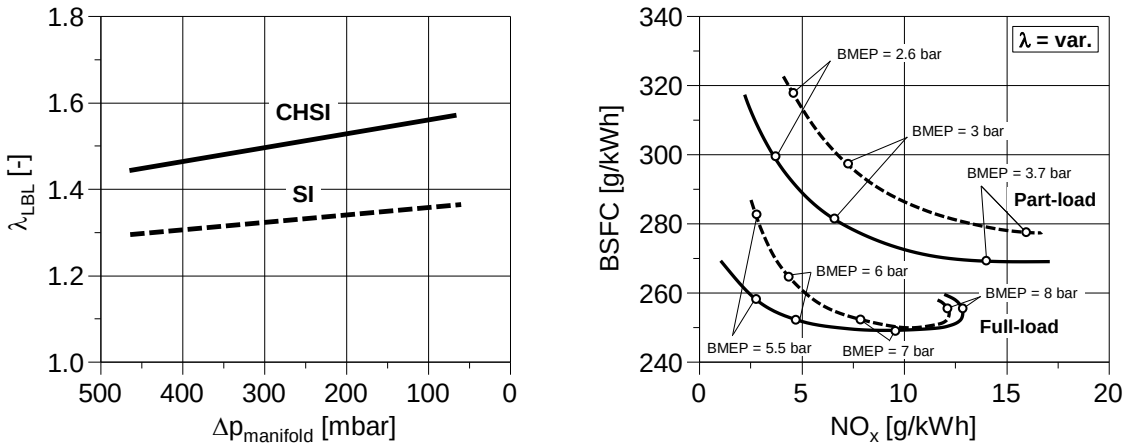

Figure 3.14: Lean-burn limit (LBL) for catalytic hot surface ignition (CHSI) and spark ignition (SI) over intake manifold pressure difference $\Delta p_{manifold}$ (left) and comparison of BSFC-NO_x trade-off between CHSI and SI operation at full and part-load (right) [23].

One of the author's most remarkable conclusions is that the timing of mixture inflammation would even then be subject to a certain degree of cycle-by-cycle variations, if hot surface temperature were to be perfectly constant, and he suggests to attenuate the stochastic effect of the flow field by conditioning the flow conditions in the vicinity of the hot surface.

Also in 1984, Furuhama and Kobayashi [53] presented a 1.1 l 3-cylinder two-stroke catalytic surface ignition hydrogen DI engine with a 0.5 mm platinum wire wound around a porcelain bar as ignition device. The compression ratio was 12:1 and hydrogen was in-

jected at up to 80 bar using a specially developed pump/injector design. They proposed that at least one fuel jet should be oriented towards the hot surface (see Figure 3.15). Varying the distance l between the jet and the hot surface proved to be most significant to ignition delay. Increasing hot surface temperature also allowed accelerating mixture inflammation, while simultaneously reducing CCV in combustion phasing. However, the improvement was only significant until about 1000 °C, for what reason most experiments were conducted at this temperature. The authors do not mention whether the igniter was temperature or voltage controlled and neither air-fuel ratio nor combustion phasing were adjusted systematically. Nevertheless, they achieved a power increase of 25 % in reference to the SI counterpart in petrol operation, while substantially reducing NO_x. In a test using a conventional Diesel glow plug without catalytic properties, they found that smooth operation was not possible due to increased ignition delays, causing large fluctuations from cycle to cycle.

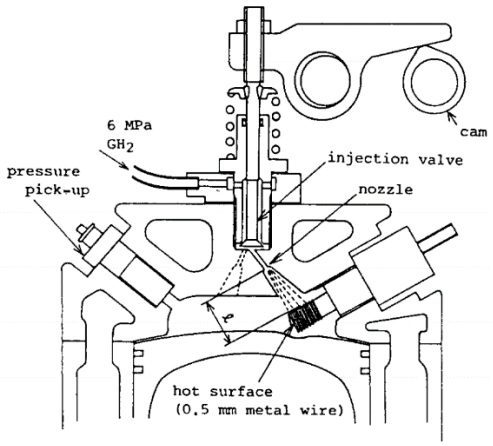

Figure 3.15: Cross-section of the two-stroke engine showing the catalytic surface igniter employed by [53].

To the author's knowledge, Cherry et al. [32–34] were the first to apply the torch-jet prechamber principle known from spark ignition to surface ignition in the early 1990s. With the aim of designing a simple ignition system with no moving parts or sophisticated electronic controls and no need of auxiliary energy, they developed a "catalytic plasma torch" (CPT) ignition system for homogenous charge operation (commercial name: *SmartPlugs*). The CPT is a self-contained ignition system that may be retrofitted to existing spark-ignition and compression ignition engines. It is made of a brass prechamber ($V_{pc}/V_c \approx 10$ %) adjacent to the main combustion chamber that contains a ceramic rod with a catalytic platinum heating element at the tip (see Figure 3.16). Cold starting and part-load operation require a small amount of electrical heating, while the system is self-sustaining at full-load allowing the auxiliary power to be switched off. The functioning principle that defines ignition timing is based on the gas-spring effect inside the prechamber: The prechamber, which at the beginning of the compression stroke is filled with residual gas from the previous cycle, admits fresh mixture from the main combustion chamber through its connecting channels as in-cylinder pressure increases due to piston motion. Under the assumption that there is no mixing between residual gas and fresh mixture in the process, the position of the interface between both gas phases is a direct

function of in-cylinder pressure, i.e. piston position. Once the interface, i.e. fresh mixture, contacts with the hot surface, after a very short ignition delay due to promoted reaction rates by the catalyst, mixture inflammation ensues. Interface response remains constant, regardless of engine load or speed. As a result, the contact angle of the fresh charge with the catalyst is only dependent on prechamber length, the hot surface' relative position therein and the compression ratio of the engine. Nevertheless, the contact angle is not the sole parameter determining ignition timing: With increasing mixture density, being directly linked to engine load, the mass of activated mixture increases. The larger number of radicals formed enhances the probability of inducing chain-branching reactions, thereby accelerating the ignition delay. Furthermore, all other parameters affecting ignition delay discussed in Section 2.1.2, like air-fuel ratio, EGR and temperature, also apply, yet to a lesser extent due to catalytic surface reactions.

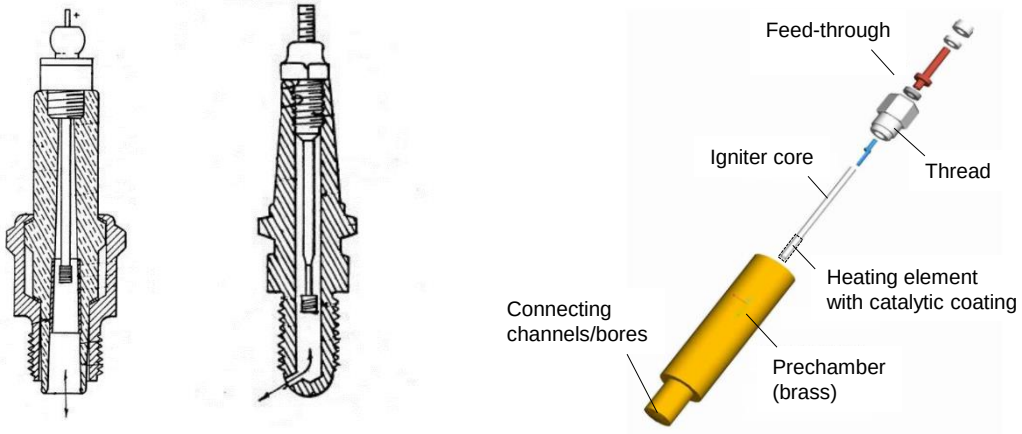

Figure 3.16: Cut view of early designs of the CPT igniter as shielded and prechamber version (left) [132] and explosion view of the improved prechamber design (right) [40].

The first study on CPT engine operation was presented in [34]. While it is not mentioned unambiguously, all experiments appear to have been conducted with stoichiometric air-NG mixtures, at engine speeds from 1300-2800 1/min and 30, 60 and 100 % engine load. Compression ratio of the 4-cylinder 2.3 l natural gas engine was 10:1, albeit prechamber volume was apparently not considered in its calculation. Heating power for the platinum coil was provided by a constant current power source. In first preliminary tests, the use of a shielded design gave proof of the theoretical consideration, that ignition timing can be adjusted by varying prechamber length and the hot surface's location. Since the combustion phasing attained was considerably too advanced, several design parameters were changed, yielding a prechamber version with 8 tangential bores at an angle of 120 ° that showed best combustion characteristics compared to SI. Mass burn rates nearly doubled, leading to a reduction in combustion duration from about 36 to 15 °CA. By monitoring platinum wire resistance, it was possible to determine the contact angle between interface and heating element, which turned out to be highly reproducible and, as expected, independent of engine load and speed. All early CPT designs had the common feature of combustion phasing advancing with load. Therefore, in order to keep full-load operation

at MBT, part-load timing had to be sacrificed and the position of peak in-cylinder pressure would vary as much as 60 °CA between full- and part-load. On these grounds, they proposed the concept of a "mass controlled timing" that would allow for retarding combustion automatically with load, but were not yet able to present any results.

Cherry's invention was the starting point of numerous research projects and publications from a team of researchers at University of Idaho in the following years, dealing with the analysis and further improvement of the CPT system [39–42, 91, 100]. CPT igniters proved to be particularly suitable for fuels or mixtures that cannot be easily ignited by conventional ignition sources, such as alcohols and alcohol-water mixtures, but durability and the fabrication process seem to be an issue and are still subject of current research and development [131, 132].

In an attempt to increase engine power without the risk of engine knocking, several researchers applied the direct injection concept from Diesel to medium to large natural gas engines, using high pressure gas injectors to provide the fuel for a controlled diffusive main combustion [2, 149]. This approach is often named DIG (*direct-injected gas*) or DING (*direct-injected/direct induction natural gas*). In 1996, Æsøy [2] used hot surfaces in the form of glow plugs to assist compression ignition of natural gas in large-bore DI Diesel engines for marine applications. HSI was chosen over SI as the conditions at high engine loads are detrimental to spark plug durability (see Section 2.3.1). The test engine was a 4-cylinder four-stroke low-speed turbocharged Diesel engine with a compression ratio of 12.1:1 and a displacement volume of approximately 28 l/cylinder. Only one cylinder was modified for gas operation, where an electronic injector would inject the gaseous fuel directly into the cylinder at 200 – 300 bar at the end of the compression stroke. A standard 6 mm Bosch pin-shaped DC glow plug with an internal thermocouple, oriented such that the fuel jet would impinge thereon, was used as a hot surface (see Figure 3.17).

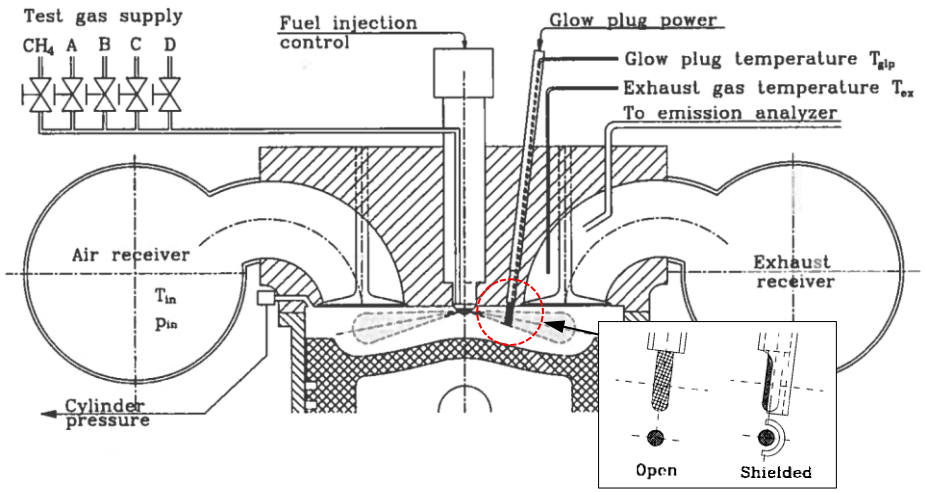

Figure 3.17: Test cylinder arrangement of the hot surface ignition assisted compression ignition DI natural gas engine tested in [2–4].

As the temperature measurement was found to not represent HS temperature confidently, the electric power of the glow plug was used to characterise its thermal state instead. High laboratory expenses and limited experimental time restricted the author to conduct only few engine trials. The focus of the experiments was to analyse the ignition characteristics when varying glow plug electric power, engine load, gas injection pressure and fuel composition. The electric power required by the glow plug was found to be a function of heat exchange in the combustion engine environment. Under atmospheric conditions, the glow plug needed to be powered with around 125 W to raise and maintain its temperature at 1200 K. With running engine (750 1/min) and forced convection under Diesel combustion, the required power increased to about 260 W using the "open" glow plug arrangement (*unshielded* HSI), see Figure 3.17. Evidently, charge motion, caused by gas exchange, piston motion and fuel injection, increases the Nu number, reduces the size of the boundary layer and enhances, therefore, the heat losses during the cycle. In fact, the losses were so high, that initiating combustion was not possible without damaging the glow plug by overload. As a countermeasure, a partly shielded design was developed (see Figure 3.17), which allowed reducing electric power to still substantial 200 W for the same conditions. By conditioning the jet flow produced by the fuel injector, the shield proved to enable secure ignition, even at lowered temperatures, and was therefore used for all subsequent experiments. Figure 3.18 (left) shows different pressure traces under varying electric power for otherwise constant operating conditions. Increasing the supplied power decidedly reduces ignition delay and advances combustion phasing, as can be seen from the earlier rise in the rate of heat release (ROHR) or the position of p_{max}. Such direct correlation between electric power, HS temperature and combustion phasing is inherent to the type of mixture preparation and the thermal behaviour of the glow plug used in this work. Section 7.3.1 will show that these dependencies do not always apply.

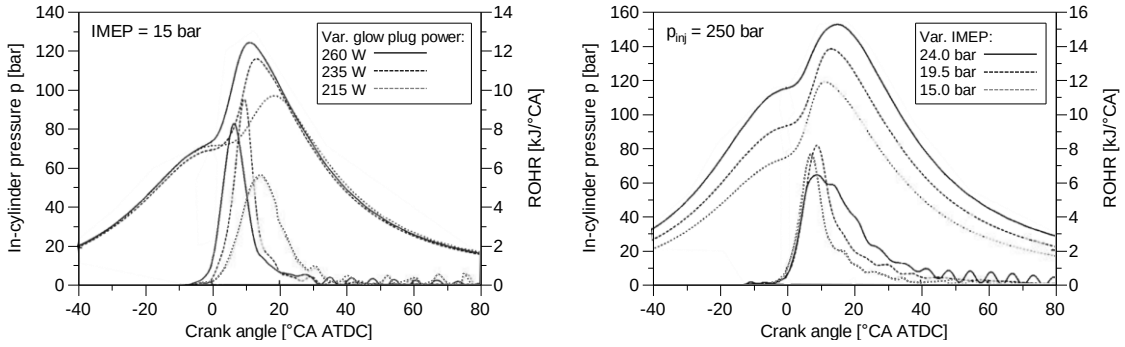

Figure 3.18: In-cylinder pressure and rate of heat release (ROHR) traces for variable electric glow plug power (left) and variable engine load p_{mi}/IMEP (right) in hot surface assisted compression ignition [2].

In Figure 3.18 (right), the same traces are plotted for varying engine load, showing that the influence of load on the start of combustion is not significant. The author attributed this effect to both the altered jet flow and the altered HS temperature when mixture density inside the cylinder is increased while keeping injection pressure, glow plug power and

intake air temperature constant. Combustion phasing, on the other hand, is retarded with increasing load as a result of the reduced flame speed, which can be addressed by increasing the electric power, i.e. HS temperature. Gas injection pressure not only determines the physical delay time that the fuel needs for its trajectory from the injector nozzle to the hot surface, but also the flow conditions in the hot surface's proximity. It was found, that ignition delay followed a concave upward dependency on injection pressure, with shortest induction times and lowest CCV at 215 bar for IMEP = 15 bar. When increasing engine load, the curve would shift towards higher injection pressures, due to the hindered jet flow when cylinder charge increases. Ignition delays exceeding 3 ms led to a dramatic increase in CCV and losses in engine efficiency.

The direct comparison between engine operation with pure methane and natural gas with common composition ($CH_4 = 92$ %, higher alkanes mostly C_2H_6) showed the ability of higher alkanes to improve ignition quality. It was possible to preserve the critical ignition delay, despite reducing the electric power of the glow plug. Alternatively, glow plug power can be kept constant, thus reducing ignition delay and CCV in heat release. In his conclusion, the author highlights the problem of hot surface durability that should be addressed in future work.

In 2000, Bartunek and Hilger [19] presented a HSI assisted direct injection natural gas system similar to [2], but for heavy-duty commercial vehicles, which allowed for dethrottled operation at high compression ratios of 16 – 18. The developed system, depicted in Figure 3.19, is also comprised by a high pressure injector (up to 300 bar) and a conventional Diesel glow plug as a hot surface. The glow plug was shielded by a cover to reduce thermal losses to the in-cylinder charge, as tests showed this reduced its electric power requirement and, therefore, the thermal stress on the glow plug. Perforating the shield proved necessary to ensure contact between the air/fuel mixture and the glow plug over a wide range of operation, as well as to promote combustion by increasing the initial reactive volume. In [18], Bartunek et al. published the results of a comprehensive development process, where the effects of shield geometry (number and diameter of bores), auxiliary glow plug power, injection parameters (nozzle number, injection pressure and injection timing), compression ratio and EGR rate were investigated on a 12 l turbocharged 6-cylinder Diesel engine (OM447 hLA). The chief observations during their experiments were the following:

- The required glow plug electric power for stable engine operation decreases with load. For n = 1200 1/min it was about 70 W at IMEP = 3 bar and could be brought down to zero at IMEP = 9 bar.
- Ignition delay is affected by the number of injector nozzles and their orientation respective to the glow plug, but proved to be most sensitive to injection timing and pressure.
- Injection timing needs to be advanced with engine speed in order to operate the en-

gine at maximum fuel economy.
- Increasing compression ratio reduces ignition delay, which results in advanced combustion phasing.
- Adding EGR to combustion increases ignition delay and promotes CCV, leading to a physical EGR rate limit above which stable engine operation is not possible.

While reaching comparable efficiencies to the baseline Diesel engines, the system showed some limitations at high engine loads and speeds as the amount of gaseous fuel required could not be provided in the given time. According to the authors, future development steps should focus on injector optimisation and, subsequently, on engine mapping.

Hanenkamp et al. [63] presented a turbocharged large-bore stationary gas engine (MAN 32/40, 12-cylinder, 32 l/cylinder) operating with a newly developed *Performance Gas Injection* (PGI) system in 2006. While the key components, high pressure fuel injector and glow plug, remain the same, the PGI system shows two substantial differences to the direct injection concept from [2]:

1. The main in-cylinder charge is not stratified but homogeneous. The main combustion chamber is filled with highly diluted air-fuel mixture ($\lambda > 2$).
2. Both injector and glow plug are positioned inside a prechamber (see Figure 3.19, right) in order to combine the advantages of scavenged prechambers with those of HSI at high mean effective pressures. The timed pilot injection (about 1 % of total fuel energy [110], 230 bar) creates stoichiometric conditions inside the prechamber. Due to the high ignition quality and energy content of the mixture, inflammation ensues rapidly once the mixture impinges on the ceramic glow plug. Eventually, torch jets exit the prechamber, leading to a wide and dispersed ignition of the poorly reactive lean bulk mixture in the main combustion chamber.

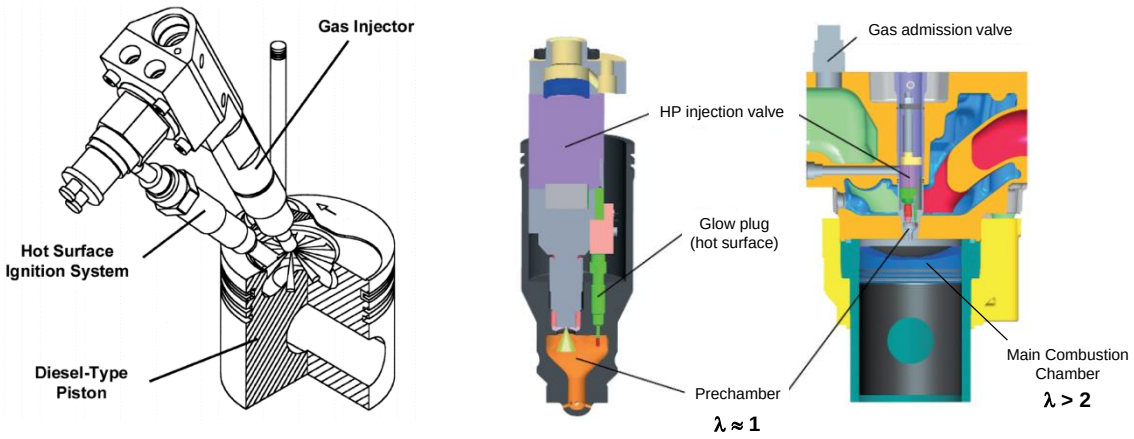

Figure 3.19: Hot surface assisted Direct Induction Natural Gas system for heavy-duty transient operation [19] (left), Perfomance Gas Injection (PGI) system for large-bore stationary gas engines [63].

The higher ignition energy provided by the prechamber enhances the lean-burn limit compared to conventional SI lean-burn gas engines, thus allowing the reduction of en-

gine-out NO_x emissions. Unlike for spark ignition, increasing pressures in the reaction zone are not detrimental to surface ignition. Therefore, the level of intake pressure provided by the turbocharger can be increased, enabling brake mean effective pressures above 22 bar.

In 2010, Prager [110] conducted experimental trials on a PGI engine and evaluated, among others, the effect of injection timing, load and relative air-fuel ratio on combustion and emission characteristics of the engine. Injection timing, the crucial parameter that determines combustion phasing, could only be adjusted in a very narrow range of max. 6 °CA, being limited by knocking to one side, and by misfires to the other. At medium load of 11 bar, this enabled the engine to operate in a combustion phasing range of approximately 15 °CA, though combustion duration was gradually increased with retarded CA50 due to falling levels of turbulence in the combustion chamber. CCV proved to be directly correlated to combustion phasing, with highest combustion stability at the knock limit. At high engine load, the injection timing range was retarded and constrained further to about 2 °CA, making it essential to control injection timing accurately. Despite the still remarkable rate of heat release, increasing the relative air-fuel ratio in the main combustion chamber had a detrimental effect on engine efficiency, while the lowered combustion temperatures were beneficial for engine-out NO_x. As of 2009, PGI engines had successfully accumulated more than 10,000 operating hours in the field and until recently, the PGI system has still been subject to research activities [67, 74].

Wunsch et al. [153] (2007) and Heyne et al. [68] (2009) presented numerical and experimental results on a novel ignition concept based on autoignition of air-fuel mixtures in a heated unscavenged prechamber for medium-sized natural gas cogeneration applications of around 150 kW. In contrast to all other publications reviewed, the hot surface is not used to ignite the mixture directly but to reduce the heat losses inside the prechamber, allowing for sufficiently high temperatures for autoignition during mixture compression. Prechamber temperature was controlled by resistive heating and allowed adjusting the timing of the autoignition event within a certain range. Nevertheless, the system's operating range proved to be vary narrow, only allowing for stable engine operation at over-advanced combustion phasings (before TDC), adverse to engine efficiency and NO_x. Moreover, the lean-burn quality of the engine was reduced due to high cyclic variations in the start of combustion. The authors claim that means to minimise CCV need to be developed to unfold the full potential of the autoignition prechamber concept.

3.3 Conclusion

The theoretical analysis performed using the thermal explosion approach under steady-state conditions without reactant consumption allows assessing the qualitative effect of the primary factors mixture pressure and temperature, air-fuel ratio, flow velocity and hot surface diameter on the critical ignition temperature of air-CH_4 mixtures. The com-

puted critical ignition temperature was found to decrease significantly with pressure, temperature and diameter and increase with flow velocity. The effect of the air-fuel ratio, on the other hand, proved to be minimal. When hot surface ignition is applied to ICE with premixed air-fuel mixtures, a steady physical state in terms of pressure and temperature can no longer be assumed but becomes a function of piston motion. As the timing of mixture inflammation is what defines engine performance and emission output, it is not only important at what temperature the mixture will ignite but also if the ignition delay is short enough to facilitate a well-timed heat release close to TDC. General considerations based on the integral ignition delay method allow the conclusion that ignition delay is strongly dependent on hot surface temperature. This holds out the prospect of using it as a control variable to adjust combustion phasing in engine operation, similar to spark timing in conventional SI engines.

On account of the analytical approaches presented, useful dependencies can be derived that help to better understand the entire process of mixture inflammation on hot surfaces. Nevertheless, when the system is highly complex, subject to time-changing arbitrary geometric constraints, flow fields and temperatures, it becomes difficult, if not impossible, to reproduce its behaviour in simple numerical models. In the case of the present work, a priori knowledge on the vital importance of the transient flow field in proximity of the hot surface was available. Prior experiments revealed that changing minor geometric parameters (e.g. position of the hot surface) and boundary conditions (e.g. hot surface temperature, air-fuel ratio) would greatly affect the reaction kinetics in the process of mixture ignition and alter combustion phasing without exhibiting evident trends. With the primary objective of understanding how the interaction between hot surface and mixture functions and how the combustion process is initiated, it was decided to follow a detailed 3D CFD approach, presented in detail in Section 5.3.

The literature review on hot surface ignition presented revealed not only the large range of different applications for which hot surfaces have been used in ICE but also confirm the complexity of the interactions governing mixture ignition. This leads to most findings reported not being universally applicable but depending on the particular tested configuration. Nevertheless, one common ground can be established for those cases where the hot surface is used to ignite the mixture directly: HSI operation is sensitive to all factors that exert an influence either on the ignitability of the mixture and on the energy balance in the boundary layer of the hot surface, or a combination of both. Examples of parameters that affect ignitability are the air-fuel ratio and intake manifold pressure, while factors affecting the energy balance are e.g. HS temperature and the flow field in the surface's proximity. To the author's knowledge, no work on controlled hot surface ignition in premixed natural gas operation has been published before. The technical progress in recent years has spawned innovations in the field of hot surfaces (e.g. ceramic glow plugs with long life-time), given raise to the development powerful numerical tools, such as CFD solvers and multidomain dynamic system modellers, and promoted the de-

velopment of comprehensive tools for real-time combustion analysis (e.g. pressure indication systems and optical metrology). The new techniques available combined with the higher experimental flexibility (e.g. by freely programmable real-time ECU) yield more degrees of freedom in research that may, in turn, provide a deeper understanding of the process of HSI induced combustion and allow for its optimisation. Advanced methods of experimental planning (DoE - *Design of Experiments*) further allow a more systematic approach, in particular when several quantitative factors determine system response or interactions among them is expected. Using the aforementioned tools, the present work aims at studying the characteristics of HSI induced combustion in a naturally aspirated gas engine, determine the limits of HSI operation and analyse its potential with respect to spark ignition. To this end, the ignition system presented in the next chapter was developed.

4 Ignition System Development

Research activities on Hot Surface Ignition began at Hochschule Karlsruhe (HsKA) in 2010. The initial goal was to design a working prototype based on an inexpensive, robust production glow plug that allows autonomous engine start and stable engine operation in a small stationary single-cylinder production CHP gas engine running on natural gas. Ever since this target was met, large effort has been put into understanding what factors and phenomena set limits to HSI operation and how the ignition system can be further optimised. Along the early development stages, several authored and co-authored papers have been published [98, 99, 121–123]. The entire development process up to date is represented in the flow chart in Figure 4.1. With exception of the optical engine trials in Chapter 6, all experiments presented in this work were conducted after the controller design freeze with a high frequency resistance controller at the latest optimisation stage.

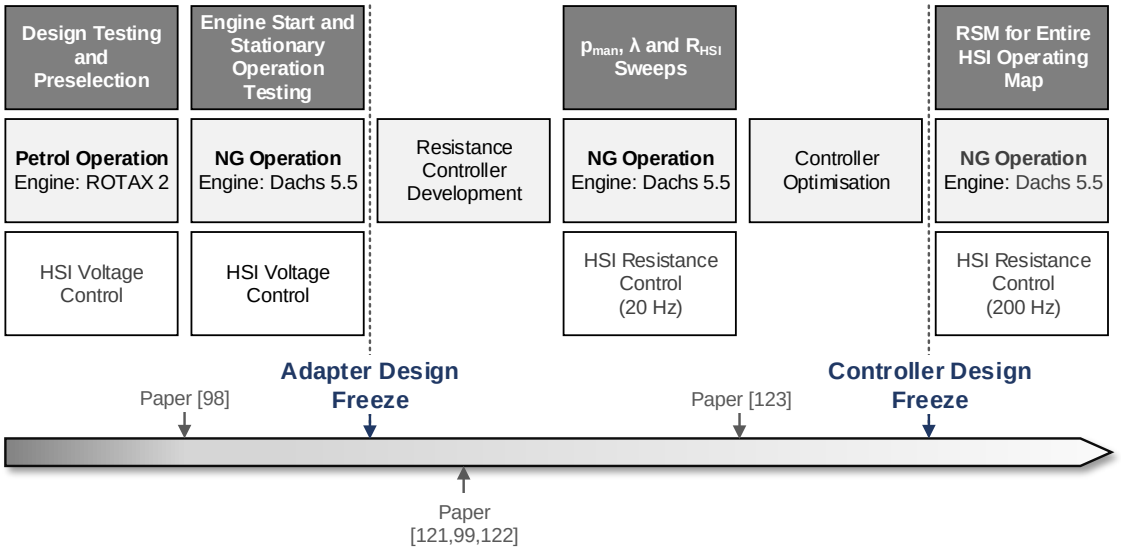

Figure 4.1: Timeline of HSI development and testing.

4.1 HSI Adapter design

Thermal ignition of an air-fuel mixture strongly depends on the temporal and spatial distribution of species and their thermodynamic properties. Many factors, either influenced by the engine operating point (e.g. engine speed, throttle position…) or the specific engine design (swirl or tumble ports, squish area, stroke/bore ratio…), have a significant effect on the flow conditions inside the cylinder. With the aim of investigating an increasing degree of decoupling from the main in-cylinder flow, three basically different HSI adapters were initially designed and manufactured. The variants unshielded, shielded and prechamber HSI (see Figure 4.2) were tested at the Institute of Reciprocating Engines (IFKM) at Karlsruhe Institute of Technology (KIT) in a 652 cm^3 ROTAX 2 single-cylinder research engine running on premixed lean petrol-air mixtures, with a compression ratio of 9.7:1. These first generation prototypes comprising a production steel glow plug were to prove the HSI system's basic functionality and allow a preselection of designs to be further tested in NG operation once the test bed at Hochschule Karlsruhe had been put into operation.

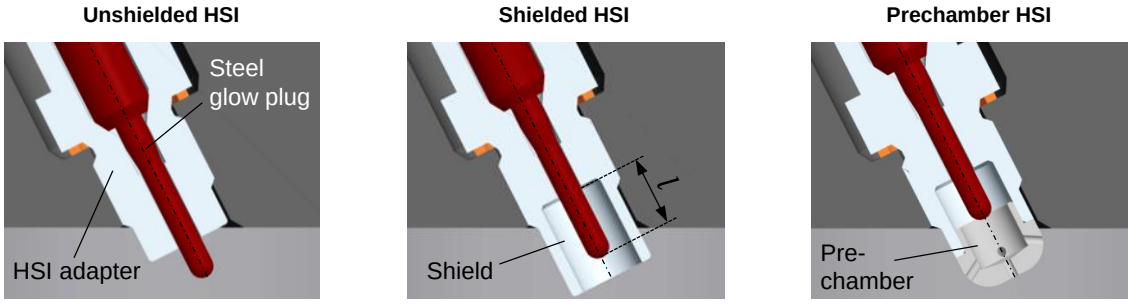

Figure 4.2: HSI designs of first generation for preliminary trials in petrol operation: unshielded, shielded and prechamber HSI (FLTR).

The protruding length (see l in Figure 4.2) of the glow plug into the combustion chamber is a design constraint that affects the area of the hot surface that is in direct contact with the mixture and induces its ignition. The heated length of the initially employed steel glow plug was about 10 mm, for what reason this was set as the maximum protruding length. Values below lead to a decrease of the reactive mixture volume and were therefore expected to reduce reaction rate, particularly during flame kernel formation.

For *unshielded* HSI, the heated glow plug pin is directly exposed to the turbulent in-cylinder flow. Engine trials at constant glow plug voltage revealed that the direct exposure to fresh mixture during the intake stroke leads to premature mixture ignition and combustion phasings before TDC. Furthermore, cycle-by-cycle variations (CCV) in the flow field, mixture composition and temperature prevented setting stable operating points due to irregular start of combustion (SOC) timings. With the aim of attenuating the effect of gas dynamics and avoid premature ignition, a *shielded* variant was designed. The glow plug tip is surrounded by a cylinder-shaped casing, with a one-sided opening to the

combustion chamber to facilitate the gas exchange. In order to intensify the ignition process, several designs with radial bores in the shield were tested. The bores were expected to increase microturbulence in the glow plug vicinity, thus accelerating the phase of early flame development. Also, an influence on the gas exchange was expected, as the shielding effect is reduced. The experiments proved that stable engine operation was possible for all shielded designs S10-Rx with x = 0, 4, 8 and 16 radial bores. However, only variants S10 and S10-R4 allowed for an improvement of the ISFC-NO_x trade-off in the low-NO_x regime compared with prechamber spark ignition (see Figure 4.3) and were therefore selected for subsequent NG trials.

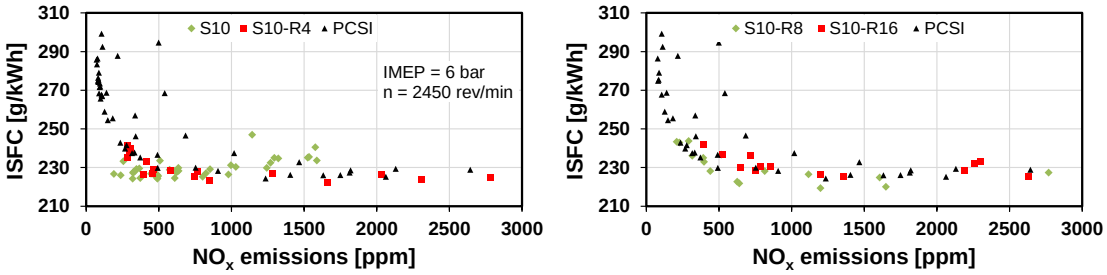

Figure 4.3: ISFC-NO_x trade-off for shielded HSI designs (S10 and S10-Rx) and prechamber spark ignition (PCSI) at constant engine speed and IMEP and variable λ in petrol operation (ROTAX 2) [99].

Following the principle of prechamber spark plugs and the concluding remarks from [23], several *prechamber* designs were developed, where the glow plug tip protrudes into a small rotationally symmetric volume that is connected to the main combustion via 4 or 5 orifices with radial or tangential orientation. This approach was expected to reduce CCV in the start of combustion by virtue of more reproducible flow conditions in the vicinity of the hot surface. The design of the prechamber was derived from the baseline prechamber spark plug being used in the cogeneration unit, using the same prechamber/compression volume ratio (≈ 1.4 %) and bore diameter (1.2 mm). As the prechamber is practically not involved in the gas exchange, it is filled with exhaust gas of the prior cycle until gas exchange BDC, leading to reduced convective heat losses from the glow plug to the mixture. When the compression stroke begins, air-fuel mixture flows through the orifices and mixes with the inner residual gas. In the case of tangentially positioned bores, they cause a vortex flow inside the prechamber with high velocities and small-scale turbulence surrounding the glow plug pin [122]. After the mixture is inflamed, flame jets were expected to penetrate the main combustion chamber as a result of the pressure rise inside the prechamber, leading to a wide and intensive inflammation of the bulk mixture. As a consequence of the great heat input into the small prechamber volume, the maximum protruding length had to be reduced to avoid premature mixture inflammation and facilitate stable engine operation. Designs with lengths of 5, 7 and 9 mm were tested in voltage sweeps. Nonetheless, due to highly irregular combustion phasings, none of the prechamber HSI designs enabled the engine to operate at relative air-fuel ratios above λ = 1.3, showing high NO_x emissions and poor fuel economy overall. Combustion proved to be slower than for PCSI, thus indicating a slower heat release inside the pre-

chamber that only produces weak flame jets, unable to initiate a rapid main combustion.

After putting into function the single-cylinder gas engine test bed, a production CHP unit with several modifications (see Section 5.1), designs that allowed for stable engine operation with air-petrol mixtures – shielded and prechamber HSI – were to be tested in NG operation. Enabling autonomous engine start was a crucial requirement for ignition system development. An automated start procedure, controlled by the CHP unit's own controller, actuates a starter motor that brings the engine to a speed of about 280 1/min and opens a start gas valve to create a relatively rich mixture ($\lambda \approx 1.2$). With combustion in idle and no load other than the engine's own inertia and friction, engine speed increases until reaching 2300 1/min, when the asynchronous generator is coupled with the three-phased electric grid. As a result of the grid frequency of 50 Hz and the gear ratio between crank shaft and generator, engine speed stabilises at about 2450 1/min. In the process, the main gas valve is opened and the start gas valve is closed, thereby leaning the mixture to about $\lambda \approx 1.6$. This starting process is particularly challenging for HSI for two reasons:

- Timing of mixture ignition needs to be advanced with increasing engine speed. Consequently, hot surface temperature needs to be increased selectively for each cycle in order to attain adequately timed combustion phasing. An improperly set rate of temperature increase will either result in overadvanced heat release before TDC or in misfires. Both conditions prevent the engine from increasing its speed.
- Transient flow and temperature conditions during engine start imply rapidly changing boundary conditions for the glow plug. As engine speed increases, the convective heat transfer between hot surface and mixture is enhanced. At the same time, the rate of heat release from combustion increases and all components exposed to the hot combustion products heat up. The supply power of the hot surface needs to be adjusted sufficiently fast to avoid unwanted heating-up or cooling-down.

Tests with the steel glow plug showed that its thermal inertia was too high for a sufficiently fast adjustment of the glow plug's temperature. As a consequence, engine speed would not increase and enable coupling the engine to the grid. Based on these findings, it was replaced by a ceramic glow plug with significantly lower thermal inertia and an improved max. heating rate, with the additional benefit of improved durability (see details in the following section). To accommodate the new glow plug, adapter dimensions needed to be adjusted. When finally put to the test, the faster thermal response of the ceramic glow plug enabled starting the engine using the shielded S10 design, while the S10-Rx and prechamber designs were still unable to time combustion correctly, presumably as a result of premature mixture inflammation. The S10 adapter design, depicted in Figure 4.4 with the mounted glow plug, was therefore chosen to be analysed in depth in the frame of this work.

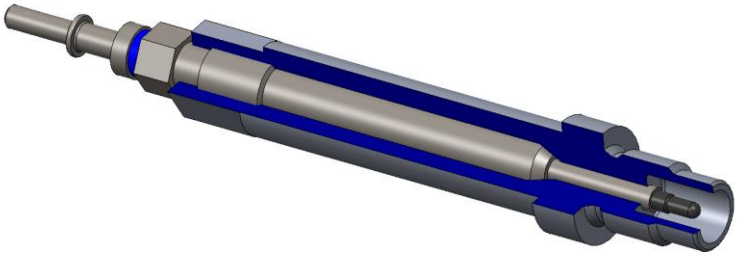

Figure 4.4: S10 HSI adapter design with mounted ceramic glow plug (CGP) used in this work.

4.2 Glow plug

Core element of the latest HSI system design is a ceramic glow plug type CGP 5.4 V from BorgWarner BERU Systems, depicted in Figure 4.5. The glow plug pin, conventionally used to assist during the cold start of Diesel engines in automotive applications, is employed as the hot surface to ignite the air-fuel mixture in replacement for spark ignition. Its use seems particularly promising due to its high rated heating rate of 550 K/s during cold start, a permitted continuous operating temperature of 1200 °C and its long-term durability. Unlike steel glow plugs, it lacks of a resistance coil and has therefore no inductance, leading to an immediate response to changes in applied voltage.

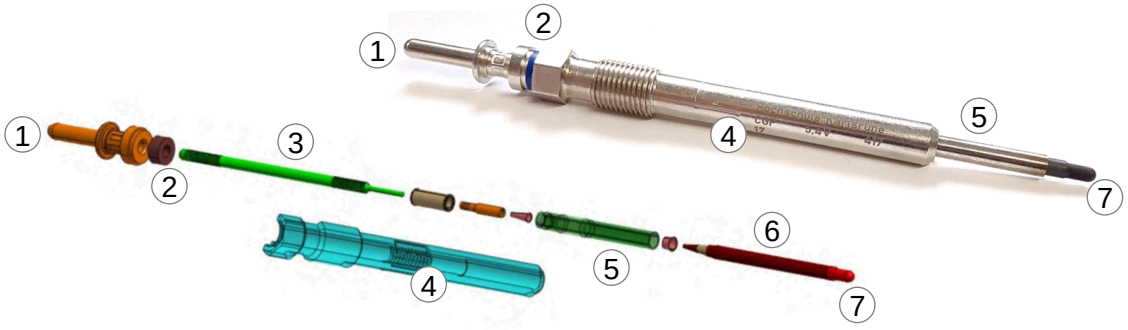

Type	Beru CGP 5.4 V
Max. continuous temperature	1200 °C
Max. peak temperature	1250 °C
Max. current at cold start	≤ 60 A
Heating rate	550 K/s
Cold resistance at room temperature	ca. 210 mΩ
Life time	engine life

Description	Material
1: Push on connector (+)	11SMnPb30+C
2: Insulating bush	PA6.6
3: Metallic lead	unknown
4: Glow plug body (-)	11SMnPb30+C
5: Protective sleeve	Inconel 601 (NiCr23Fe)
6: Ceramic leads	Mostly Si_3N_4 + $MoSi_2$
7: Glow plug pin (hot surface)	Mostly Si_3N_4 + $MoSi_2$

Figure 4.5: Technical specifications and explosion model of ceramic glow plug BERU CGP 5.4 V (Source: BorgWarner BERU Systems).

The left schematic in Figure 4.6 shows a cross section of the glow plug tip, with the inner and outer electric leads, an insulating layer and the heating cap, responsible for generating most heat. The insulating layer is formed by a non-oxide composite, primarily made of silicon nitride with smaller amounts of yttria and alumina. The electrical leads and the heating cap are made from the same ceramic material, but with fractions of molybdenum disilicide to make it electrically conductive. The electrically conductive segments, the heating cap in particular, show a positive temperature coefficient (PTC), meaning that

their resistivity increases when temperature is raised. Accordingly, glow plug resistance can in principle be used as a feedback for its own temperature, as explained later on in this section.

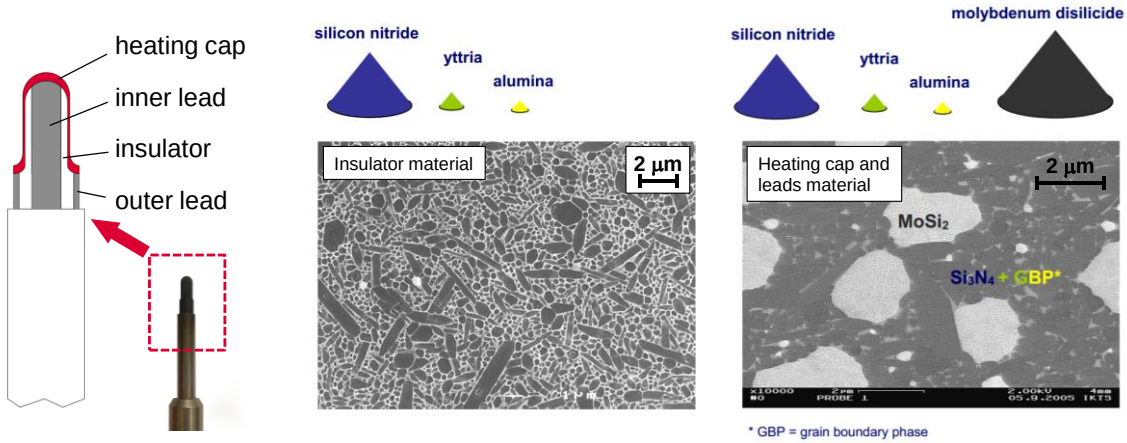

Figure 4.6: Schematic cross-section of the glow plug tip (left) and material composition of insulator and heating cap and electrical leads (right, source: BorgWarner BERU Systems). Heating cap contains smaller amounts of molybdenum disilicide ($MoSi_2$).

Figure 4.7 shows the equivalent circuit of the HSI system that serves as a definition for recurring variables. Because all resistances are connected in series, the electric current is constant over the entire circuit. The monitor outputs for voltage and current of the high-speed programming DC power source were used to determine U_{HSI} (via sensing terminals) and I_{HSI}. Since the glow plug has no inductance, its total resistance can be calculated according to Ohm's law:

$$R_{HSI} = \frac{U_{HSI}}{I_{HSI}} \tag{4-1}$$

Equation (4-2) gives the total electric glow plug power:

$$P_{HSI} = U_{HSI} \cdot I_{HSI} = {I_{HSI}}^2 \cdot R_{HSI} \tag{4-2}$$

P_{HSI} is comprised by the heat generated by the Joule effect in the heating cap layer P_{HC}, i.e. the usable part of the energy provided, and the losses over the electric leads and connectors of the glow plug, P_{loss}. Therefore, it applies that:

$$P_{HSI} = P_{HC} + P_{loss} \tag{4-3}$$

In order to asses how efficient the provided energy is used to raise the temperature of the heating cap, the dimensionless variable η_h, henceforth referred to as "heating efficiency", is introduced. It describes the ratio of electric power consumed by the heating cap to the total power of the HSI system. Equation (4-4) gives its definition:

$$\eta_h = \frac{P_{HC}}{P_{HSI}} = \frac{R_{HC} \cdot {I_{HSI}}^2}{R_{HSI} \cdot {I_{HSI}}^2} = \frac{R_{HC}}{R_{HSI}} \tag{4-4}$$

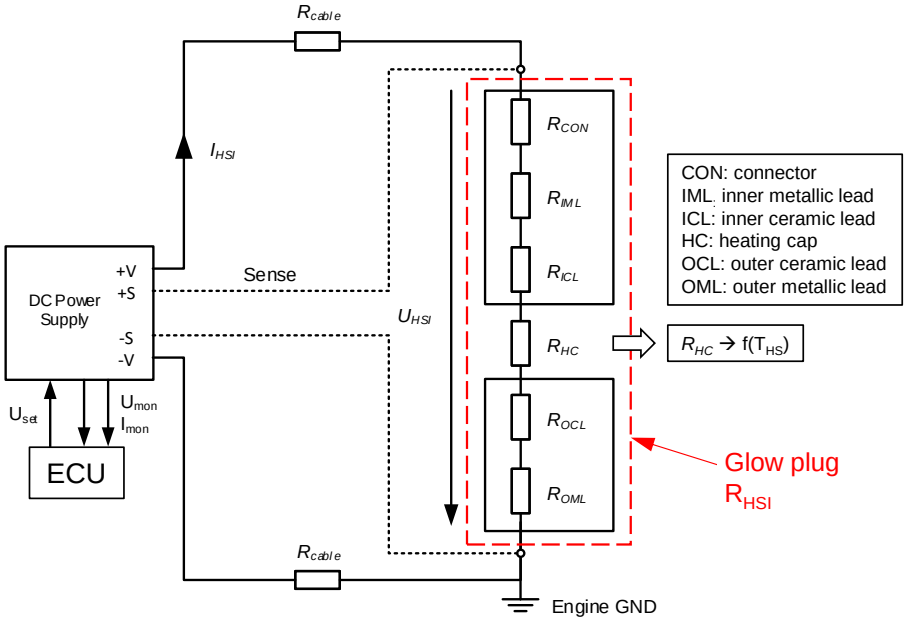

Figure 4.7: Equivalent electric cirquit of the HSI system.

Hot surface temperature, or more specifically the glow plug tip's internal energy, depends on the heat being transferred across the HS system boundary, as illustrated in Figure 4.8. The electric current passing through the heating cap (resistor) converts electric energy into heat, thus increasing both internal energy and HS temperature. Nonetheless, since the system is not adiabatic, it exchanges heat with its surroundings through heat conduction, convection and thermal radiation. The change in internal energy dU/dt can be calculated through the First Law of Thermodynamics according to Eq. (4-5):

$$\frac{dU}{dt} = P_{HC} + \dot{Q}_{conv} + \dot{Q}_{cond} + \dot{Q}_{rad} \tag{4-5}$$

assuming that P_{HC} is distributed evenly across the entire control volume. For HSI, most heat losses are caused by the interaction with the in-cylinder flow as well as the heat transfer through the HSI adapter towards the colder cylinder head. Convective heat transfer $\dot{Q}_{conv}$ is negative during most of the cycle, especially during gas exchange and the compression stroke until the combustion is induced. Once the mixture is ignited and fuel energy is released, gas temperatures exceed that of the hot surface, enabling a positive heat flux from gas to the glow plug. Conductive heat transfer $\dot{Q}_{cond}$, on the other hand, is negative throughout the cycle. While losses through thermal radiation $\dot{Q}_{rad}$ can be neglected for low temperatures, they increase with temperature to the power of 4, almost doubling from 1000 to 1200 °C. For steady-state conditions, i.e. constant HS temperature T_{HS}, it applies that $dU/dt = 0$ and the electric power fed to the heating cap (which is not the same as the total power demand of the HSI system P_{HSI}) needs to compensate for all thermal losses:

$$P_{HC} = -\left(\dot{Q}_{cond} + \dot{Q}_{conv} + \dot{Q}_{rad}\right) \tag{4-6}$$

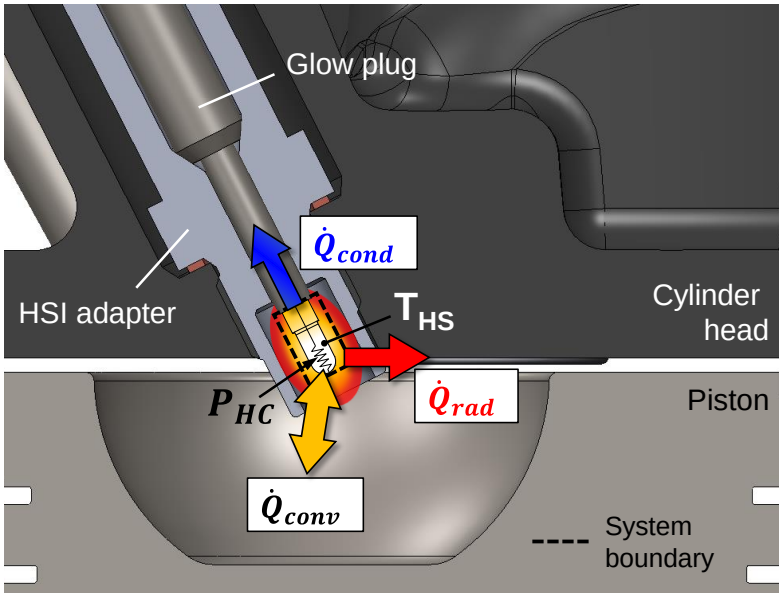

Figure 4.8: Cross section of the Hot Surface Ignition (HSI) system showing the energy balance of the glow plug tip.

Resistance-Temperature Correlation

Due to the dependence of ignition delay on temperature, the ignition process on hot surfaces is kinetically controlled. For this reason, it is important to determine and control the temperature of the glow plug tip during engine operation. Using the glow plug's temperature-sensing capabilities, Rainer [113] describes a method to calculate glow plug temperature based on its actual operating resistance, its cold resistance R_0 (without being powered, at a specific temperature T_0) and a glow plug characteristic constant α_K:

$$T = T_0 + \frac{\left(\frac{R}{R_0} - 1\right)}{\alpha_K} \tag{4-7}$$

Since the handling of Eq. (4-7) is quite impractical, the linear function can also be expressed as:

$$T = (R - R_0) \cdot a + T_0 \tag{4-8}$$

with gradient $a = 1/(R_0 \cdot \alpha_K)$, describing the sensitivity of glow plug temperature to adjustments in glow plug resistance. The glow plug manufacturer provided a total of 33 glow plugs to conduct the experiments. For the ten first specimens of the batch (No. 1 – 10) individual two-point reference measurements were available (T_0, R_0, $T_{1250°C}$ and $R_{1250°C}$), which allowed calculating values for α_K and a and plotting the individual RT correlations shown in Figure 4.9 using Eq. (4-8). Cold resistance R_0 varies significantly among the tested specimens, spanning from 191 to 226 mΩ. The same applies to the values obtained for gradient a, ranging between 1.93 and 2.16 K/mΩ. Since both parameters

are subject to variability and did not show to be correlated, it follows that each glow plug has a distinct thermo-electric behaviour and will reach a different glow plug temperature when a specific resistance is set. This is illustrated in Figure 4.9 using the example of $R = 750$ mΩ, giving a maximum difference in temperature of nearly 140 °C.

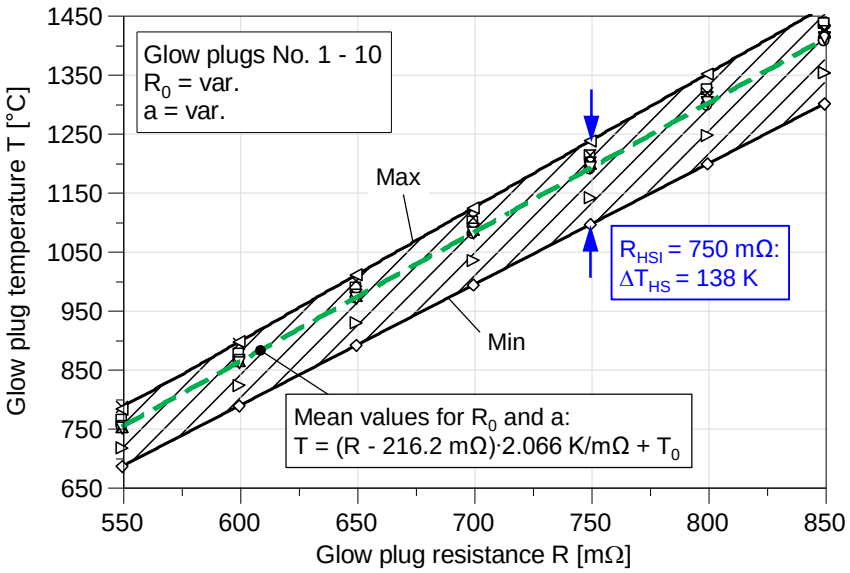

Figure 4.9: Glow plug temperature T as a function of glow plug resistance R for glow plugs No. 1-10, calculated using Eq. (4-8).

The importance of using individual glow plug parameters for accurate temperature sensing can be deduced fairly easily from the foregoing results. Nonetheless, reliable data for the remaining glow plugs from the batch was not available and in-house testing was not possible due to the lack of appropriate equipment. To minimise the error when calculating glow plug temperature, the mean gradient $a_{mean} = 2.07$ K/mΩ of No. 1 - 10 was used, while cold resistance R_0 was determined for each glow plug individually. Due to the very low resistance, setup and method for determining R_0 represents a considerable source of error. Regarding the setup, a bad condition of the push-on connector (e.g. widened or corroded) can reduce the contact area between the connector and the positive terminal of the glow plug, thus increasing the total resistance and giving erroneous readings of R_0. Furthermore, the position where U, i.e. the voltage drop across the glow plug, is measured plays an important role and should be as close as possible to the glow plug terminals. Two methods for determining R_0 were considered: For method A, a low voltage of 0.5 V is applied to the glow plug, and R_0 calculated from voltage and current under steady-state conditions. For method B, a 5 V pulse is applied over 5 ms, and R_0 calculated from the recorded voltage and current traces (using a high speed data acquisition system, e.g. oscilloscope or combustion analyser) right before the 5 ms elapse. Both methods gave reproducible results, although method B proved to be faster and more accurate. Since the short current pulse does not supply enough energy to increase glow plug temperature significantly (≈ 0.5 J), it gives generally lower readings than method A and was therefore chosen to determine the cold resistance of the remaining glow plugs.

4.3 HSI Controller Development

Controller development was a continuous process, constantly driven by new findings and improvements in controller hardware. Figure 4.10 gives a brief development timeline, showing each major development stage. Initially, all engine tests in both petrol and NG operation were conducted controlling glow plug voltage through a simple manual potentiometer, employing a conventional high DC current power source. As this approach did not allow for a satisfactory adjustment of combustion phasing in NG operation, current, resistance and power control were tested. For this purpose, the analogue power source was replaced by one with a digital interface to facilitate a two-way communication between the parametric controller algorithm in LabVIEW and the power source (monitoring and programming of glow plug voltage and current). Following the rationale of a direct RT correlation and the dependency of ignition delay on temperature, implementing a closed-loop resistance controller seems the most viable and obvious approach to adjust combustion phasing (see considerations in Section 3.1.3). In fact, the experiments revealed that all types of control enable stable engine operation under very lean conditions but only the adjustment of HSI resistance has a clear and reproducible effect on combustion phasing.

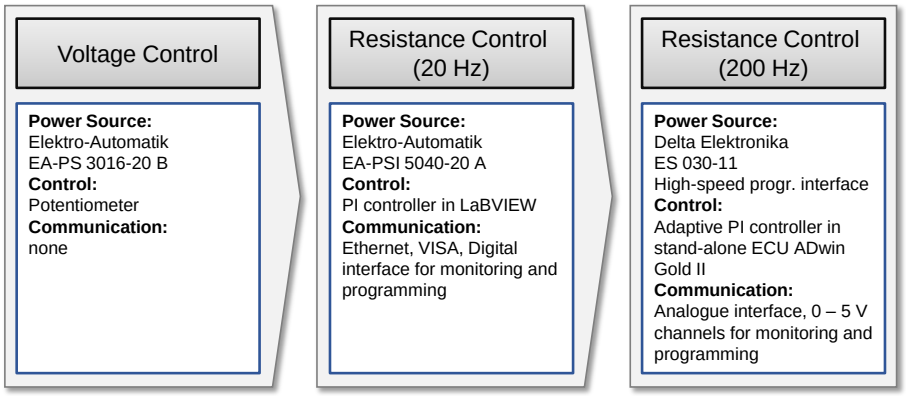

Figure 4.10: Timeline of HSI controller development.

After appropriate tuning of the PI resistance controller parameters, it was possible to enhance the operating range of HSI significantly and conduct a large set of experiments where the influence of intake manifold pressure (800 mbar – 1200 mbar) and relative air-fuel ratio ($\lambda > 1.5$) was examined (see [123]). The finding most relevant to controller development was that fluctuations in heat release when the total net heat release and combustion temperatures are high are detrimental to controller stability. This applies for high engine load, at high intake manifold pressures and mixture strength. The controller is unable to counteract the cyclic changes in convective heat transfer between the mixture and the hot surface sufficiently fast. As a result, HS temperature begins to oscillate, causing high cycle-by-cycle variations in the timing of mixture inflammation. In an attempt to further improve controller stability and expand the limit of HSI operation to lower relative air-fuel ratios, the low resolution in the digitalised signals of HSI voltage

and current (2 digits, approx. resistance resolution: 3 mΩ), and jitter in the execution of the controller loop in LabVIEW were identified as additional sources of instability. As will be shown later in the experimental chapter, a 5 mΩ offset in R_{HSI} can be sufficient to shift combustion phasing by about 1 °CA. Computationally intensive loops of the LabVIEW code, running in parallel to the controller algorithm, proved to prevent precise timings of data acquisition and set value update (real-time module was not employed). This manifested in an intermittent and non-reproducible "freezing" of the set value for up to 0.5 s (≈ 10 engine cycles). On account of the aforementioned limitations, the controller concept was subsequently redefined to accommodate the following requirements:

- Maximum possible controller frequency
- Precise, predictable and reproducible timing of the controller event
- Real time data acquisition and processing
- High resolution in AD/DA conversion
- High monitoring and programming accuracy
- Minimum data noise

The controller hardware derived from these requirements consists of a real-time Electronic Control Unit (ECU) and a DC power supply with an analogue high-speed programming and monitoring interface. This configuration makes it possible to decouple the time-critical processes of data acquisition and control from the remaining test bed automation, yielding a robust, configurable stand-alone HSI controller that does not rely on cyclic inputs from the user interface. Only for set value update and slow data recording, an EtherCAT-based communication link between the ECU and LabVIEW is used. Figure 4.11 shows the control loop of the final HSI resistance controller. The monitor signals of HSI voltage and current are digitalised by an 18 bit ADC to calculate the actual resistance value R_{HSI}, which is then compared to the set value given by the LabVIEW GUI to compute the error e. In function of the error, controller output is updated, converted to the voltage signal U_{prog} by a 16 bit DAC and sent to the programming input of the power supply, which adjusts the voltage applied to the glow plug U_{set}. Special care was taken to ensure that the remote sense wires did not pick up any exterior noise by using shielded twisted-pair wires. This proved very effective in stabilising the readings of U_{HSI} and I_{HSI} and, in turn, minimising the ripple in calculated R_{HSI}. Voltage was chosen over current as a set parameter owing to the self-regulating capability of the PTC surface heater. In normal engine operation, cyclic variations in heat release lead to more or less pronounced fluctuations in combustion phasing. When combustion phasing is either advanced or retarded respective to the mean cycle, the heat input from combustion to the hot surface, and as a direct consequence, hot surface temperature, will increase or fall, respectively. If the temperature is decreased, R_{HSI} will decrease as well, allowing more current to flow through the heating cap, thus heating the tip. Similarly, if the temperature is increased, R_{HSI} is also increased, limiting the current, thus cooling the tip down. If, on the contrary, current were to be set constant, the tip would be heated even more

for increased HS temperatures, and be cooled for decreased temperatures, which would require a larger set value adjustment between controller events.

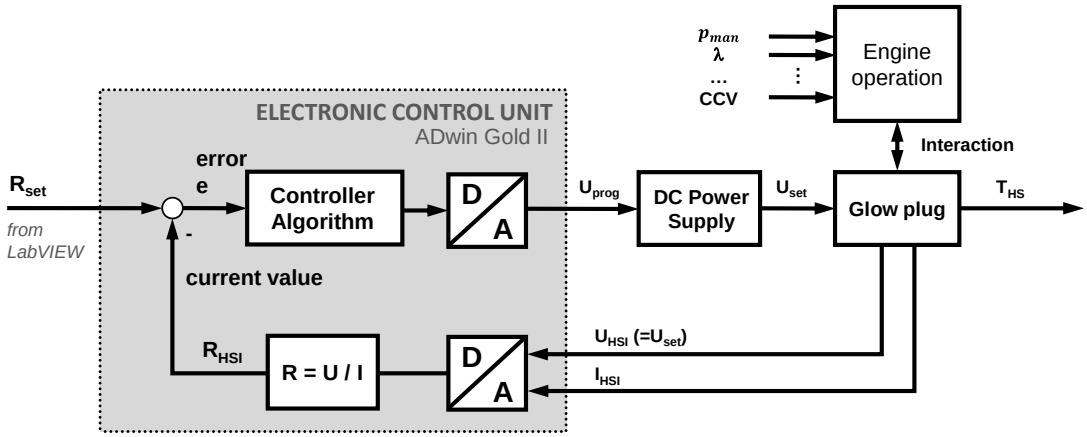

Figure 4.11: Control loop of the current development stage of the HSI resistance controller

4.3.1 Controller Algorithm

Noise is detrimental to controller stability since it makes the process variable appear to deviate from the setpoint without being subject to any real disturbance. If the PI tuning parameters are too aggressive (high proportional gain K_p and integral gain K_i), high noise will cause unwanted unstable steady-state behaviour. This can be improved by reducing the gains, which may, however, lead to a too small control action when responding to system disturbances. The changes in controller hardware did not only allow for an increase in controller frequency to 200 Hz (about 10 events per cycle), but also for higher resolution and reduced noise in the R_{HSI} signal. This made it possible to increase K_p and K_i significantly, leading to a vast improvement of controller speed and robustness to cycle-by-cycle disturbances. The PI controller was implemented in velocity algorithm form with a particular steady-state functionality to further improve controller response to disturbances. For $|e| > 0.5$ mΩ the controller shows normal antiwindup PI behaviour, for $|e| < 0.5$ mΩ (steady-state) the output is adjusted stepwise +/-0.1 V. Because the glow plug is a nonlinear system and R_{HSI} is calculated from measured current and voltage, the voltage set value should never be zero, as this would cause controller instabilities. To avoid this, minimum voltage was limited to 1 V. At the CHP engine's rated speed of 2450 1/min, a controller frequency of $f = 200$ Hz is equivalent to one control event every 73.5 °CA. As the controller is not synchronised with crank angle, the controller events shifts by about 30.6 °CA/s. Synchronised timing (10 events/cycle, $f \approx 204.2$ Hz) with variable phasing respective to TDC (0 – 72 °CA) was tested but did not yield any improvements in controller or engine stability. To illustrate how the controller operates in engine operation, Figure 4.12 shows the traces of all electric variables over one engine cycle using the unsynchronised controller, recorded over crank angle using a high-frequency data logger/combustion analyser (see Section 5.1.1). Peaks in calculated resistance arise from the inductance of the twisted electric wiring that limits the initial current when applying a voltage step and causes a slight phase shift of current respective

to voltage. This leads to marginal but rather reproducible errors in calculated mean R_{HSI}. When applying a manual filter it can bee seen that R_{HSI} decreases gradually during the intake and compression strokes as a result of the convective heat losses that cool down the glow plug tip. In response to that drop in resistance, U_{set} (i.e. U_{HSI}) is increased with every controller event until mixture ignition ensues. The sudden exposure to hot combustion gases produces a steep rise of temperature and heating cap resistance, causing a direct controller response that limits the current flowing through the heating cap and the heat generated therein. Despite it being a very lean operating point with low combustion temperatures, U_{HSI} (i.e. U_{set}) needs to adjusted by more than 0.4 V to counteract the disturbances in R_{HSI}. The approximate increase of R_{HSI} is 5 mΩ, equivalent to about 2 K according to Eq. (4-8).

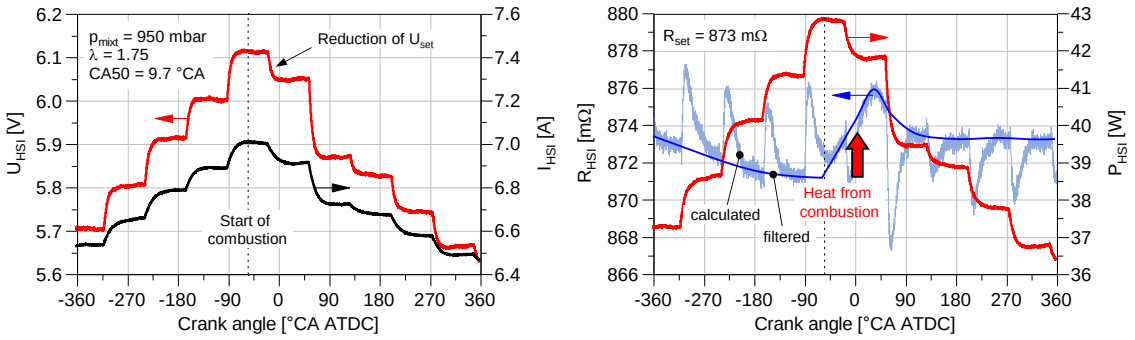

Figure 4.12: Electrical HSI parameters against crank angle for unsynchronised 200 Hz resistance control.

Cyclic variations in heat release lead to fluctuations in absolute convective heat transfer from the mixture to the glow plug tip $\dot{Q}_{conv}$. The impact of these fluctuations on controller stability depends on engine load [121]. Low load in demand of high HS temperatures (e.g. low intake manifold pressure or high λ) leads to high $P_{HC}/\dot{Q}_{conv}$ ratios, making the controller less susceptible to CCV. With increasing $\dot{Q}_{conv}$, however, the $P_{HC}/\dot{Q}_{conv}$ ratio is reduced, requiring larger adjustments of P_{HC} in response to the cyclic disturbances.

Figure 4.13 shows the importance of the implemented high-speed resistance control for an operating point with significant variability in combustion phasing, considering the example of a transition from resistance to voltage control ($U_{HSI,mean}$ = const.). Prior to the switch to voltage control, P_{HSI} varies in a range of about 15 W in order to keep R_{HSI} constant. Once U_{HSI} is held constant, the temperature variation over one engine cycle increases significantly and the self-regulating capability of the glow plug is insufficient to give the same HS temperature at the beginning and the end of each cycle. Since the heat generated in the heating cap is not sufficient, the glow plug cools down and R_{HSI} falls gradually by 20 mΩ ($\Delta T_{HS} \approx 9$ K) in a time span of only 8 s. The falling temperatures translate into reduced reaction rates during mixture ignition, both the start of combustion and combustion phasing are retarded, as can be seen from the lower peak pressures. As a direct result of the falling resistance, the current flowing through the glow plug increases, leading to a slight increase of P_{HSI} of nearly 2 W.

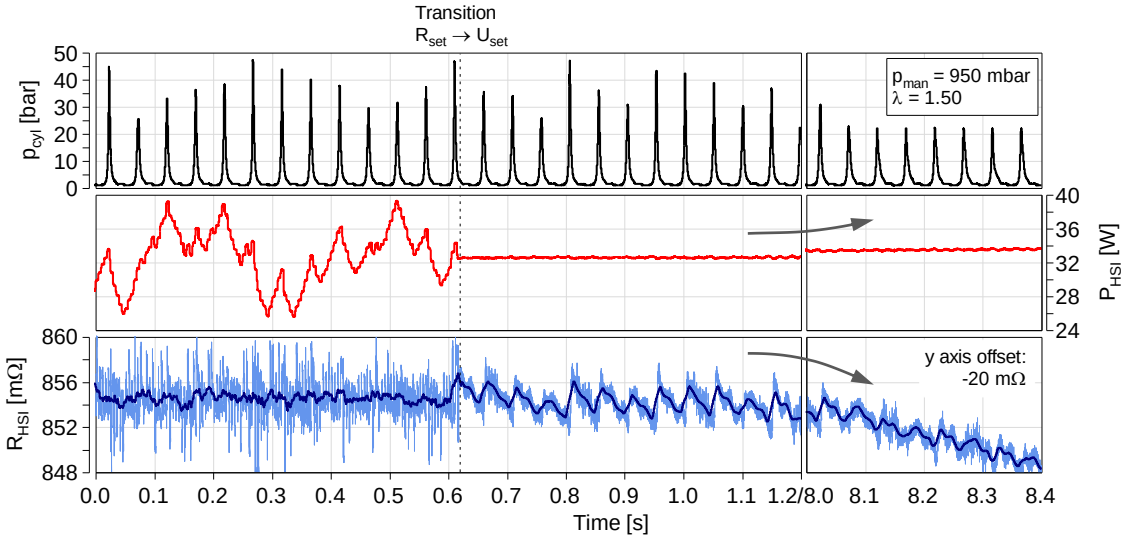

Figure 4.13: Traces of in-cylinder pressure p_{cyl}, HSI power P_{HSI} and resistance R_{HSI} over time for a transition event from resistance to voltage control.

For 1000 cycles (≈ 49 s), Figure 4.14 shows cycle-average HSI and combustion data for four controller transition events, from resistance to voltage control and vice versa:

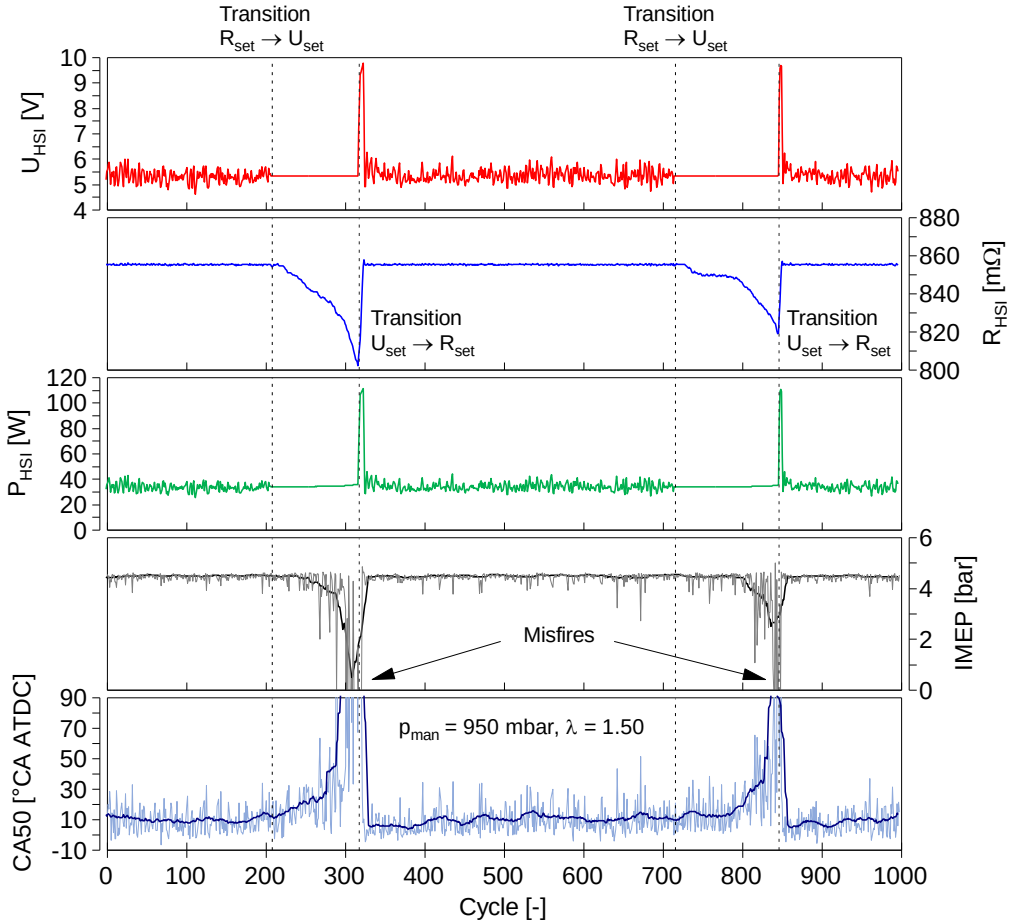

Figure 4.14: Cycle-average data for controller transition events.

Clearly, voltage control is unable to sustain a stable operating point. The falling HS temperature leads to constant retarding of CA50 which eventually causes partial burns and

misfires that further accelerate the cooling rate of the glow plug. The good performance of the resistance controller can be appreciated when switching back to resistance control. A maximum power of about 110 W (limited by the maximum current of the power source) is applied briefly, which leads to well timed combustion after only 3 cycles (≈ 150 ms) and a compensation of the error in R_{HSI} and combustion phasing after 8 cycles (≈ 400 ms).

4.3.2 Engine Start

As mentioned at the beginning of the chapter, engine start proves to be highly challenging owing to the need of HS temperature adjustment as a function of engine speed. Figure 4.15 shows a typical engine start using the S10 adapter. HSI resistance, e.g. hot surface temperature, was increased manually in order to time the heat release such that enough engine work is produced to bring the engine to its nominal speed and couple the generator to the power grid.

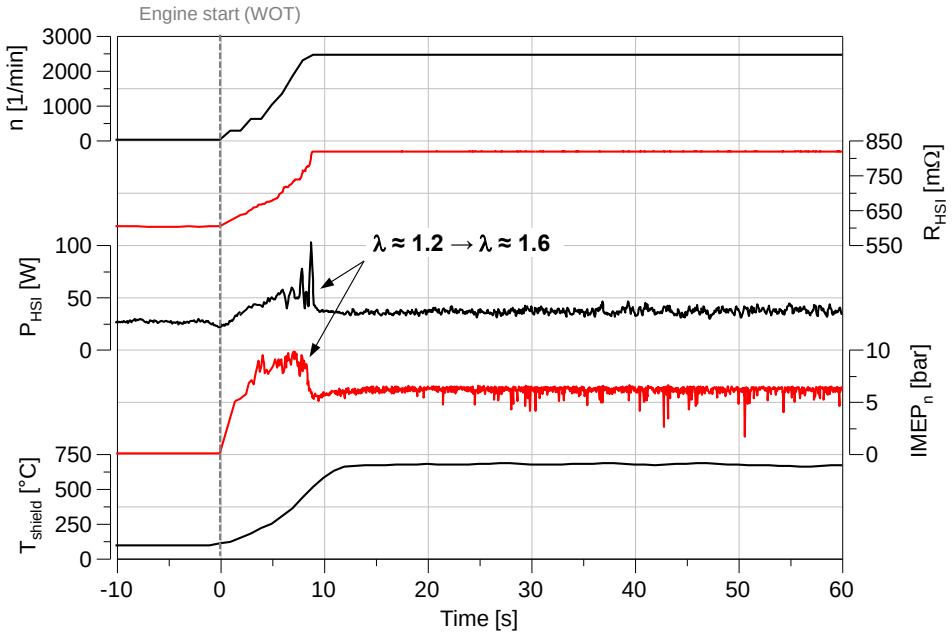

Figure 4.15: Engine start with HSI at wide open throttle (WOT) and manual adjustment of R_{HSI}.

5 Experimental Setup and Employed Tools

The objective of this chapter is to present setup and tools employed to study Hot Surface Ignition of premixed air-NG mixtures. Section 5.1 describes the experimental apparatus and instrumentation used for studying the effect of numerous controllable factors on hot surface ignition operation. Subsequently, Section 5.2 gives an insight into the statistical tools employed to design and evaluate the experiments (Design of Experiments – DoE). Finally, Sections 5.3 and 5.4 present the numerical tools employed and developed to simulate the interaction between the hot surface and the mixture and gain a deeper understanding of the complex underlying thermal, electric, kinetic and flow dynamic processes involved in the ignition process.

5.1 Experimental Setup

In parallel to the preliminary petrol experiments, a 5.5 kW production micro-CHP unit, type *SenerTec Dachs G5.5,* for natural gas operation was installed at the IKKU (Institut für Kälte-, Klima- und Umwelttechnik) facilities (see technical specifications in Figure 5.1). The unit is driven by a water-cooled horizontal four-stroke single-cylinder, whose crank shaft is connected to a three-phase asynchronous generator by a single gear step. The generator is coupled to the 50 Hz power grid leading to a fairly constant engine speed of about 2450 1/min. A very lean air-fuel mixture ($\lambda \approx 2.0$) is created by a fixed Venturi-based gas-air mixer positioned after the air filter of the unit. An additional electronically controlled gas valve is allocated about 1500 mm downstream and 500 mm before the intake port for closed-loop control of engine power depending on actual ambient conditions and the fuel's heating value. A centrally positioned prechamber spark plug with constant spark timing is used to induce combustion of the enriched but still lean mixture ($\lambda = 1.5 - 1.6$) inside a heron shape combustion chamber with flat cylinder head

and piston bowl. Series combustion phasing is set to be retarded respective to MBT in order to meet the TA Luft NO_x limit. The hot exhaust gas is fed to an oxidation catalyst (OC) for reducing both HC and CO emissions and then led through a water-cooled exhaust gas heat exchanger in order to recover waste heat energy for heating or process heat purposes. To this end, a 1000 l stratified heat storage tank is positioned in the CHP coolant circuit. Finally, the gas stream is routed through a muffler to damp the pressure waves and reduce the emitted noise before exiting the unit. In order to limit noise and reduce thermal losses to the ambient and increase the overall efficiency of the installation, the whole unit is surrounded by an insulated casing, leading to an evenly distributed inner air temperature of about 80 – 95 °C, depending on the operating conditions.

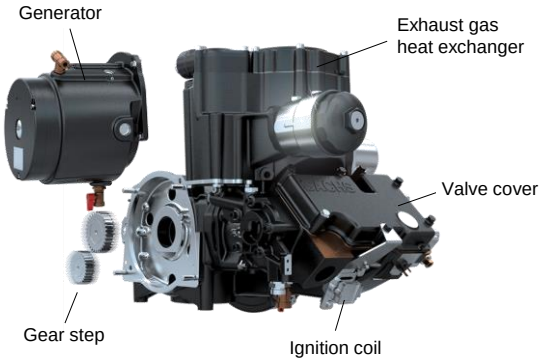

Engine type:	SenerTec Dachs G5.5
Nominal speed:	2450 1/min
Rated electric power:	5.5 kW
Nominal IMEP:	ca. 6.3 bar
Compression ratio (geom.)	13.2:1
Stroke/Bore	91 mm / 90 mm
Displacement volume	578 cm³
Number of valves	2
Series ignition system	prechamber spark plug
NG gas pressure	22 mbar rel. to amb. pressure

Figure 5.1: Single-cylinder cogeneration engine used in test bed (Source: SenerTec Kraft-Wärme-Energiesysteme GmbH).

The CHP unit was converted into a fully instrumented and flexible test bed, making the following modifications to the engine and its periphery:

- Machining of the engine block for cylinder pressure indication.
- Installation of an optical encoder at the flywheel.
- Development of an electronic spark timing adjustment (0.1 °CA resolution).
- Alternative intake piping before the gas mixer, including a larger air-filter, a calming section and an air mass flow meter.
- Installation of a custom-made throttle valve, controlled by a high-resolution stepper motor, to adjust intake manifold pressure.
- Installation of a thermal mass flow meter for natural gas and a modulating control valve before the gas mixer to enable precise fuel mass flow adjustment and closed-loop λ control.
- Installation of an external valve-controlled EGR line.
- Installation of a wideband λ sensor and pressure and temperature sensors
- Use of an uncoated, non-reactive catalyst for measuring engine-out emissions.
- Installation of a PI controlled three-way mixing valve for closed-loop control of CHP coolant inlet temperature (return temperature of the heating system).

A freely programmable electronic control unit (ECU) ADwin-Pro II, was used for engine

control and slow data acquisition. A schematic representation of the test bed, including all measuring positions is given in the Appendix, Section A.1.

5.1.1 Standard Measurement Systems

All fast, crank-angle based data were recorded using an 8-channel DEWE-800-CA combustion analyser. In-cylinder pressure was measured using a Kistler 6125C11 pressure transducer and a 5018A charge amplifier. The resolution was 0.1 °CA (3600 pulses/rev), given by a Heidenhain ROD 426 encoder coupled to the flywheel of the engine. Combustion attributes such as the mass fraction burnt profile, including start and end of combustion (here: 5 % and 90 % mass fraction burnt – CA5 and CA90) and combustion phasing (50 % mass fraction burnt – CA50), were calculated using the fast net heat-release method with a constant ratio of specific heats $\gamma = 1.33$. This simplified approach was chosen as CA50 was one of the control variables to be adjusted real-time during engine operation. Accordingly, the net rate of heat release is approximated by the relation [69]:

$$\frac{dQ_H}{d\alpha} = \frac{\gamma}{\gamma - 1} \cdot p \frac{dV}{d\alpha} + \frac{1}{\gamma - 1} \cdot V \frac{dp}{d\alpha} \tag{5-1}$$

Fuel consumption was monitored using a Bronkhorst F-103-lowΔp thermal mass flow meter for natural gas. Air mass flow was measured using a calibrated hot wire mass airflow sensor (MAF) from Bosch (HFM 5/4.7). A Bosch LSU4.9 wideband λ sensor coupled to an ETAS ES635 lambda meter was employed to monitor relative air-fuel ratio λ after the muffler. Due to the fast sensor response time and overall robustness, the signal was used for closed-loop λ control. Considerations on the accuracy of the λ signal, particularly for varying intake manifold pressures, can be extracted from the Appendix, Section A.2. An ABB AO2020 6-component exhaust gas analyser with heated sample lines was used as standard equipment for measuring exhaust gas emissions. Wet hydrocarbons are measured as C_3H_8 equivalent with a flame ionisation detector (Multi FID 14) and converted to THC (ppmC). Wet NO and NO_2 (NO_x) are measured using a photometer after the DUV-RAS/NDUV (Differential Ultra Violet Resonance Absorption Spectroscopy / Non Dispersive Ultra Violet) principle (Limas 11 HW). Dry CO and CO_2 are measured with an IR photometer (Uras14). Dry O_2 concentration is measured using a Magnos 206, based on the paramagnetic properties of O_2. All fluid temperatures were measured using 1.5 mm K-type thermocouples, positioned in the centre of the stream. Mean gas pressures were recorded using absolute pressure sensors Siemens P200.

Natural gas is a naturally occurring hydrocarbon gas mixture, consisting primarily of methane, but commonly including variable amounts of other higher alkanes (mostly ethane and propane), and often a small percentage of inert components like carbon dioxide CO_2 and molecular nitrogen N_2. Changes in fuel composition affect the heating value of the mixture as well as combustion characteristics like ignition delay, flame tempera-

ture and heat release rate. For this reason, fuel composition (up to C6+) was constantly monitored using an Inficon Micro GC Fusion gas chromatograph. Table 5.1 shows the mean composition of "H gas" available in Karlsruhe during the experimental series from Chapter 7:

Table 5.1: Mean natural gas composition, lower heating value and density (STP) over a period of 3 months (Karlsruhe, Oct-Dec 2016).

		MEAN	MIN	MAX
Methane	Vol.-%	**92.14**	90.72	94.27
Ethane	Vol.-%	**4.972**	3.640	5.907
Propane	Vol.-%	**0.408**	0.015	0.605
i-Butane	Vol.-%	**0.058**	0.034	0.083
n-Butane	Vol.-%	**0.051**	0.034	0.083
n-Pentane	Vol.-%	**0.000**	0.000	0.000
iso-Pentane	Vol.-%	**0.007**	0.000	0.019
n-Hexane	Vol.-%	**0.001**	0.000	0.007
CO_2	Vol.-%	**1.503**	0.962	1.917
N_2	Vol.-%	**0.853**	0.658	1.336
H_i	MJ/kg	**47.17**	46.62	47.96
ρ_N	kg/m_N^3	**0.780**	0.762	0.792

5.1.2 Engine Conditioning

Just like for conventional spark ignition, HSI operation is subject to a large number of controllable and non-controllable factors that affect mixture ignitability and the subsequent combustion, but also the thermo-electric properties of the glow plug. While some factors are independent and can be adjusted at will within specific limits (e.g. intake manifold pressure or air-fuel ratio), others vary in function of independent variables and the characteristics of combustion (e.g. hot surface temperature), or are independent and non-controllable at the same time (e.g. natural gas composition). Table 5.2 gives an overview of the most influential factors for the tested configuration:

Table 5.2: Controllable and non-controllable factors affecting HSI operation for tested configuration.

Indep. control. factors	Dep. non-control. factors	Indep. non-control. factors
Intake manifold pressure Air-fuel ratio HSI resistance (→CA50) Coolant temperature Intake temperature (External EGR rate)	Hot surface temperature HSI adapter temperature Intake manifold temperature Oil temperature Casing temperature Residual gas fraction Engine speed Exhaust backpressure (partly)	Fuel composition Humidity Glow plug ageing (see 7.2) Exhaust backpressure (partly)

During the development process of HSI it became clear that conditioning the intake air, especially intake pressure, and coolant temperature, and waiting for steady-state condi-

tions prior to recording an operating point was crucial for obtaining useful and reproducible data. To this end, the conditioning unit shown in Figure 5.2 was developed. It comprises a motor-driven supercharger in series with a heat exchanger on the discharge side that enable closed-loop control of both pressure and temperature at the inlet of the CHP unit (p_{intake} and T_{intake}). To reduce the pressure at the intake manifold (p_{man}), a stepper motor-controlled throttle valve was installed at about 400 mm upstream of the intake valve. For controlling CHP coolant inlet temperature (henceforth referred to as $T_{coolant}$), an electromagnetic three-way valve mixing cold water from the lowest level of the heat storage tank ($\approx$ 25 °C) with hot CHP coolant outlet temperature ($T_{coolant,out}$ = 78 – 88 °C) was installed.

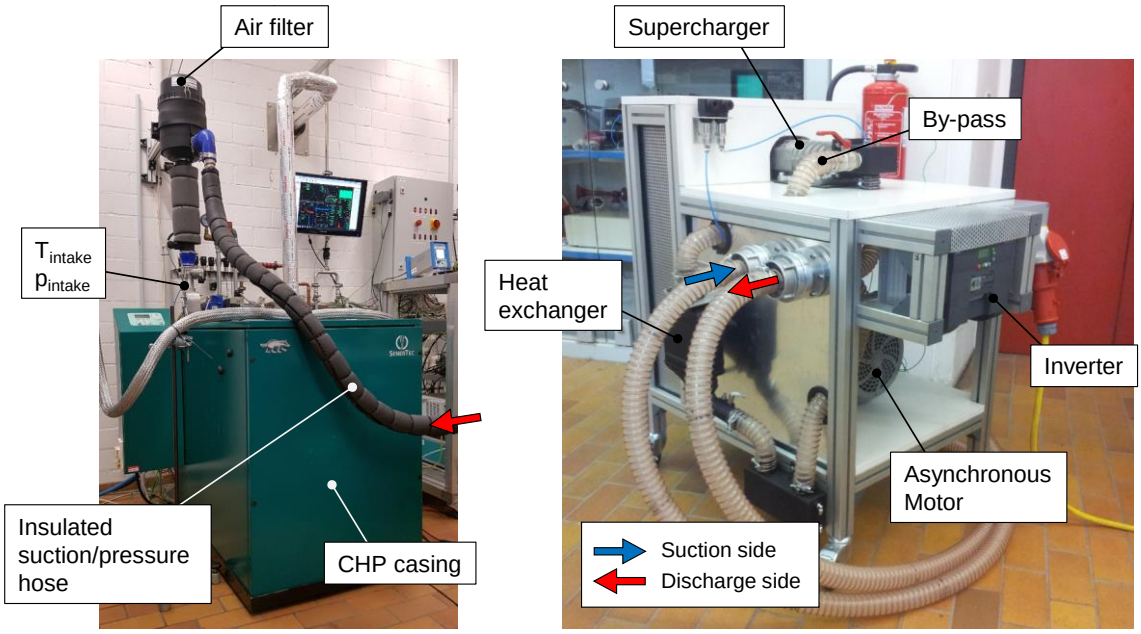

Figure 5.2: Test bed CHP unit with coupled conditioning unit (left), conditioning unit with non-insulated hoses (right). In normal engine operation, hose on suction side is replaced by an air-filter.

5.1.3 Optical Metrology

Over the past years, the analysis of chemiluminescence emitted by chemical reactions in the combustion chamber has become an important auxiliary tool for combustion diagnosis. It helps to gather additional information about the combustion process such as the start of combustion, the instant of maximum heat release or the spatial flame propagation. In this work, several single optical fibres are used to study the early stages of flame development and determine the ignition site.

After exceeding the activation energy required for igniting an air-hydrocarbon, fuel species react and dissociate, enabling the start of chain branching and chain propagation reactions. In the process, radicals form and decompose, emitting radiation as they pass from their excited to their fundamental state. This chemiluminescence can be detected as visible and ultraviolet (UV) light, whereas the appearance of distinct radicals as well as the intensity of their bands strongly depends on the type of fuel and mixture composition

in the flame front. For premixed hydrocarbon flames, most combustion light stems from OH*, CH* and C_2* radicals [55], all of which have their specific emission bands. For lean methane flames, however, the probability of following the reaction mechanism to form C_2 species (C_2H_6) is reduced [66], which results in lower emission in the C_2 band.

To study the process of HSI induced combustion, and, in particular the effect of HSI resistance, i.e. HS temperature, on the start of combustion and combustion phasing, an optical adapter with a total of 8 individual optical accesses to the cylinder was developed (see Figure 5.3, left). Two are positioned in the shield volume and 6 in an outer adapter, distributed equidistantly around the shield. The transmission of radiation is facilitated by monocrystalline sapphires and optical fibres. Radiation is then converted to a voltage signal by a photomultiplier and recorded by the combustion analyser as a function of crank angle. Sapphires are used due to their suitability to be exposed to high temperatures, while conventional silica fibres would decompose in the hot and oxidising environment of the combustion chamber. The sapphires were glued into the optical adapter using high-temperature two-component ceramic adhesive.

Table 5.3 shows technical specifications of the optical measurement chain. All constituent parts are characterised by a good transmission/detection of radiation at wavelengths between 300 nm (ultraviolet) and 600 nm (visible light, orange). Maximum sensitivity is given between 300 and 500 nm (visible light, green), enabling the detection of the most important radical emission bands of natural gas combustion.

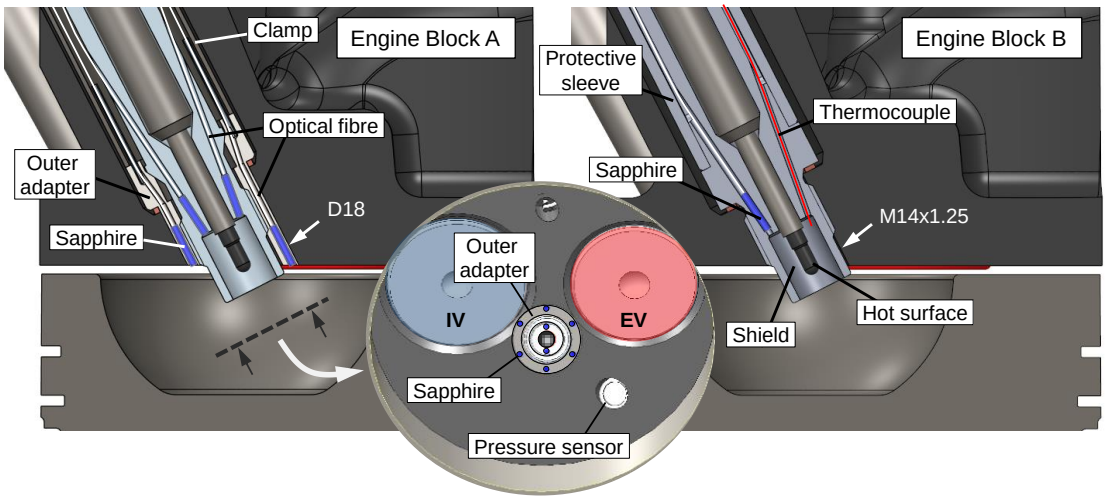

Figure 5.3: Adapter with optical probes (left), mounted adapter in the test bed engine (right).

All engine experiments prior to those discussed in this work, were run on the series engine block. To accommodate the optical adapter, the standard spark plug M14-thread had to be widened into a through-bore of D = 18 mm (see *Engine Block A* in Figure 5.3). The conventional copper gasket was replaced by a tapered sealing for the HSI adapter. With this setup, the preliminary experiments presented in Section 6.1.2 were conducted but owing to problems with adapter durability and leakproofness, the engine block was replaced and a more robust optical adapter that does not require any engine block modi-

fications was developed (see *Engine Block B* in Figure 5.3).

Table 5.3: Technical specification for optical metrology (Sources: Schott AG, LEONI Fiber Optics GmbH, HAMAMATSU Photonics).

	Type/Dimensions	Optimal spectral range	Transmission/ Sensitivity	Admission angle
Sapphire	8 mm x Ø 1 mm (L x D)	300 nm – 4000 nm	> 85 %	12.5 °
Silica fibre (UV/VIS)	2 m x Ø 0.4 mm (L x D)	300 nm – 900 nm	> 90 %	25.4 °
Photomultiplier	Hamamatsu R7400U	200 nm – 600 nm	10 mA/W (200 nm) 66 mA/W (430 nm) 5 mA/W (600 nm)	-

As shown in Figure 5.4, the new adapter contains only one optical access to the shield volume and three 0.5 mm thermocouples to measure body temperature along the adapter, $T_{adapter,front}$ and $T_{adapter,back}$, and gas temperature of the shield mixture (T_{shield}).

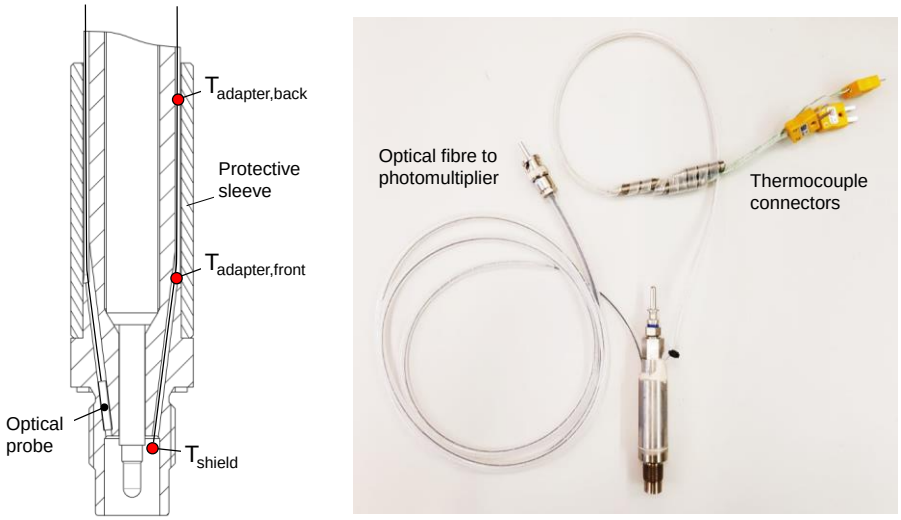

Figure 5.4: Section view of the single-fibre optical HSI adapter (left) and actual assembly used in engine experiments.

5.2 Design of Experiments

When the number of influencing factors is large, traditional one-factor-at-a-time (OFAT) experiments cover only small fractions of the experimental space. They pose the risk of dependencies or interactions between the several parameters varied to go unnoticed and may require numerous runs to derive useful data. For the experimental core of this thesis, a systematic *Design of Experiments* (DoE) approach was taken, for the purpose of deriving most information about the system while maximising experimental time efficiency. *Design Expert 10* from *Stat-Ease Inc* was used for planning the engine trials from Sections 7.1 and 7.4 and for the subsequent statistical analysis. The intention of this section is to give brief introduction to factorial designs and *Response Surface Methodology* (RSM), while detailed derivations and terminology can be found in pertinent literature, e.g. [6, 43, 95, 146].

The aim of RSM is to set up empirical models that describe the relationship between one or several input factors x_i, and a response y. As illustrated in Figure 5.5, this correlation may be superposed by measurement errors as well as known and unknown forms of noise that distort the observed response values, summarised as variable e.

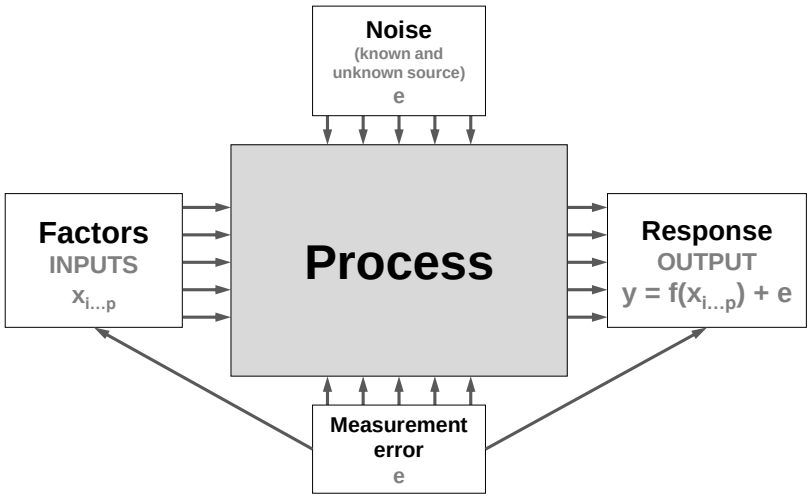

Figure 5.5: Generic model representing the core elements of statistical design of experiments (after [146]).

The surface response equation for calculating y, being of first or second order in most cases, can be expressed according to Table 5.4:

Table 5.4: General form of the response surface equation.

$y = a_0 + \cdots$	Intercept	1
$a_1 \cdot x_1 + a_2 \cdot x_2 + \cdots \ a_p \cdot x_p + \cdots$	Main effects	p
$a_{12} \cdot x_1 \cdot x_2 + a_{13} \cdot x_1 \cdot x_3 + \cdots$ $a_{23} \cdot x_2 \cdot x_3 + a_{24} \cdot x_2 \cdot x_4 + \cdots a_{(p-1)p} \cdot x_{p-1} \cdot x_p + \cdots$	Double interactions	p*(p-1)/2
$a_{11} \cdot {x_1}^2 + a_{22} \cdot {x_2}^2 + a_{pp} \cdot {x_p}^2 + \cdots$	Quadratic effects	p
$a_{111} \cdot {x_1}^3 + \cdots a_{123} \cdot x_1 \cdot x_2 \cdot x_3 + \cdots$	Effects of higher order	depending on order
$+e$	Error	

Or written in matrix notation:

$$\boldsymbol{y = Xa + e} \tag{5-2}$$

where the unknown coefficients a are estimated from experimental data on the process following the method of least squares of the errors e. For processes with large number of factors, it is common to set each factor at just two levels (low and high or -1 and 1 in coded notation) to quickly asses which factors and interactions are significant (trivial and vital factors). These two-level factorial designs, usually called 2^k designs, where k refers to the number of factors, are often used in *screening* experiments to reduce the list of potential factors to only the significant few so that subsequent RSM experiments will require fewer runs and be more efficient. Furthermore, they are particularly suitable to determine operation limits that constrain the region of experimentation. If the design

space is irregular because some parameter combinations cannot be set or higher order effects, e.g. cubic, are expected, it is common practice to resort to flexible computer generated optimal designs to select the factor configurations (model points) to be tested. First, based on the number of factors and responses, constraints and model order (e.g. cubic) a set of candidate points is created using a full-factorial design. Depending on the permissible number of RSM runs defined by the experimenter (much lower number than the candidate points), an initial, randomly selected set of points is set. Subsequently, the set is optimised iteratively according to a chosen optimality criteria, D- and I-optimality being the most commonly applied. A D-optimal algorithm chooses runs that maximise the determinant of the information matrix $\boldsymbol{X'X}$ and is recommended when the goal is to find factors important to the process [130]. I-optimal designs, on the other hand, seek to minimise the integral of the prediction variance across the design space. Therefore, I-optimal designs are to be chosen over D-optimal design if the aim is to attain most accurate model predictions [72]. For this reason, D-optimal designs are used for screening trials and I-optimal designs for the RSM experiments in the present work.

In Chapter 7, several statistical tools are used to facilitate the discussion of results. One of the less common, the perturbation plot, shall be reviewed shortly. The perturbation plot is a special form of graphic representation of the empirical equations (or response surface equations) determined in RSM experiments. Particularly for multi-factor models, they help to asses which parameters are most significant to the response and show the effect of changing each factor individually while holding all others constant at an arbitrarily chosen point of the experimental space. For its representation, the response surface equation in terms of dimensionless coded factors, where the range of each factor in natural units of measurements is transformed according to [min,max]→[-1,+1], is used. Figure 5.6 displays a qualitative perturbation plot for a simple linear model response as a function of 3 factors, A, B and C, where all lines emanate from the centre of the experimental space – the “intercept”.

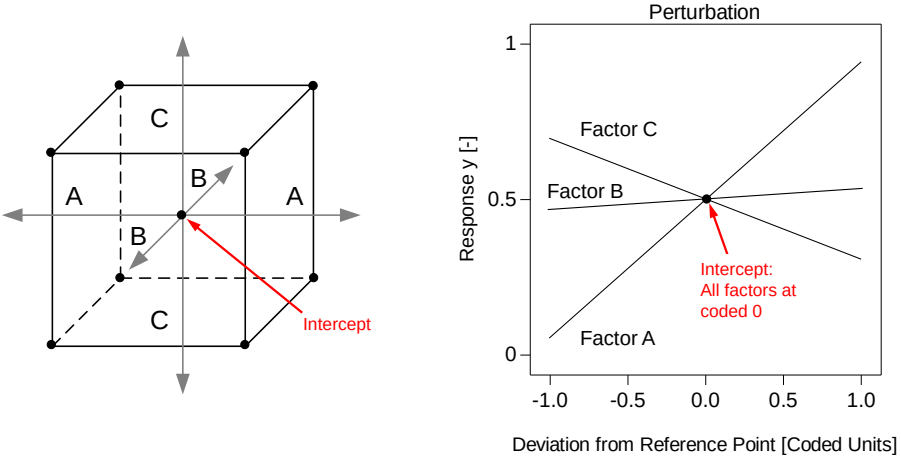

Figure 5.6: Perturbation plot for a model response dependent on 3 factors.

It can be seen that an increase of factors A and B translates into an increase of response

y, while factor C has the opposite effect. The comparison of gradients, given by the factor coefficients a, reveals that the response is most sensitive to changes in A and C, while the effect of B is less significant. When applied to an actual experiment, this may indicate that most attention in data evaluation, model building or process optimisation should be paid to factors A and C, and it may be reasonable to remove B from the model due to its small contribution.

5.3 CFD and Combustion Simulation Model

To analyse the complex interaction between hot surface and in-cylinder flow that eventually leads to mixture inflammation, a 3D CFD calculation model was set up in AVL Fire v2013. Figure 5.7 illustrates the corresponding simulation workflow.

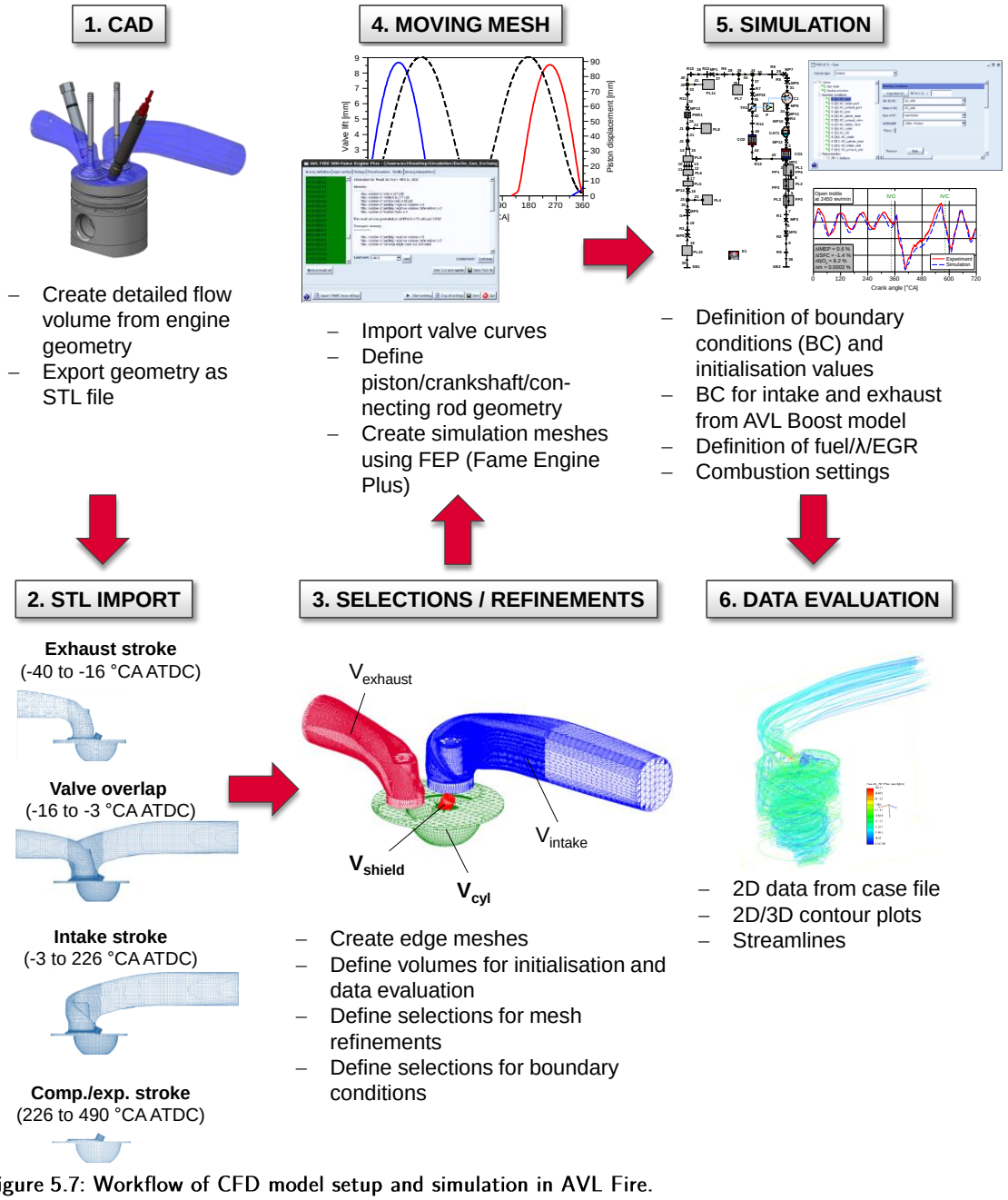

Figure 5.7: Workflow of CFD model setup and simulation in AVL Fire.

5.3.1 Simulation Setup

Whether a calculation model allows for accurate simulations of real engine conditions strongly depends on the quality of the applied boundary conditions. In this work, boundary conditions for the intake and exhaust ports were defined as a function of crank angle. Intake pressure and temperature as well as exhaust pressure were computed by an extensively validated 1D simulation model of the test bed engine in AVL Boost. This model allows reproducing gas dynamic effects of the gas exchange accurately. Details on model setup and validation can be found in [97].

Calculation intervals and employed calculation meshes are depicted in Figure 5.7. Valve and piston motion is accounted for by continuously adjusting the calculation meshes according to defined valve curves and engine geometry, such as piston displacement and connecting rod length. High mesh refinements are set for regions of high interest for the analysis of mixture inflammation (e.g. shield volume) or those responsible for shaping the in-cylinder flow (e.g. intake valve). The number of cells ranges between 500,000 and 1,400,000 depending on the current simulation interval, valve lift and piston position. For better evaluation of the results, cylinder geometry was divided in two sections: the shield volume V_{shield} and the remaining volume cylinder volume V_{cyl}. For the tip of the glow plug, a uniform temperature boundary condition was set and kept constant for the whole simulation cycle. Table 5.5 gives an overview of selected simulation parameters.

Table 5.5: Selected parameters of CFD simulation.

Number of cells	500k-1400k
Cell size (refinement = 0)	2 mm
Max. cell refinement	4
Turbulence model	k-ζ-f
Combustion model	ECFM-3z
Calculation time	ca. 108 h for 530 °CA

5.3.2 Ignition and combustion model

Both ignition and flame propagation were simulated using an enhancement of the CFM combustion model (Coherent Flame Model), the ECFM-3z (Extended Coherent Flame Model – 3 Zones). Common to all CFM combustion models is the assumption that the turbulent flame is composed of an ensemble of laminar flamelets. The models further suppose that the chemical reaction of fuel oxidation occurs in a very thin layer. In premixed combustion, as it is the case in this investigation as a result of the external air-fuel-mixing, this layer separates burned and unburned gases and propagates through the combustion chamber containing air, fuel and residual gas [37]. The ECFM-3z model was developed for both premixed and diffusion combustion and virtually divides a computational cell in 3 zones: unburnt and burnt mixture and flame. It therefore distinguishes between three main regimes: autoignition, premixed and non-premixed flame (diffusion combustion). The autoignition pre-reactions are calculated for the in-cylinder charge,

with an ignition delay that is governed by local temperature, pressure, equivalence ratio and residual gas fraction. For homogeneous mixtures, as it is the case in a naturally aspirated gas engines, local autoignition is followed by premixed combustion of the mixture in form of a propagating flame.

The calculation of ignition delay in AVL Fire is based on tabulated values for methane ignition delay data as a function of pressure, temperature and residual gas fraction derived from GRI-Mech 3.0, as those presented in Section 2.1.2. Alhough engine relevant temperature and pressure exceed the validated region of the GRI-Mech 3.0 reaction mechanism, the computed flame speeds are in good agreement to measurement data available in literature [10, 73, 117]. For the actual determination of the autoignition delay in the CFD simulation, a transport equation for a tracking, non-reacting intermediate species Y_P is solved. Its formation rate is calculated as follows [15, 111]:

$$\frac{dY_P}{dt} = Y_{FM} \cdot f\left(t_{delay}\right) \tag{5-3}$$

with Y_{FM} being the mixture fraction and $f\left(t_{delay}\right)$ the function for the delay time. Similar to the integral ignition delay method presented in Section 2.1.2, when species Y_P reaches a threshold value equal to local mixture fraction, autoignition is triggered, and an initial value of flame surface density is defined in the according region. Subsequently, tabulated GRI-Mech 3.0 data is used for calculating laminar flame speed, used to compute flame surface density, which, in turn, describes combustion speed. Combustion is calculated through a 2-step reaction, where fuel is first partly oxidised to CO and CO_2, followed by CO oxidation and can be tracked by the reaction progress variable c (0: unburnt, 1: burnt). Detailed information on basics and implementation of the ECFM-3z model can be found in [11, 15, 37, 111].

5.4 0D HSI Engine Process Simulation

As an aid for experimental data interpretation and a tool to optimise controller parameters and derive new controller strategies, a 0D engine process calculation model for HSI operation was developed in Matlab/Simulink. Figure 5.8 depicts the basic program structure, comprising a predictive in-cylinder pressure model with a resolution of 0.5 °CA and a thermo-electric hot surface model as its core elements. The programme only requires the input parameters shown in block DATA INPUT and uses submodels to calculate auxiliary variables, such as start and end of combustion, cycle-by-cycle variations or HSI adapter temperature. Alternatively, when the aim is to reproduce actual recorded operating points, the model can be fed with raw experimental data.

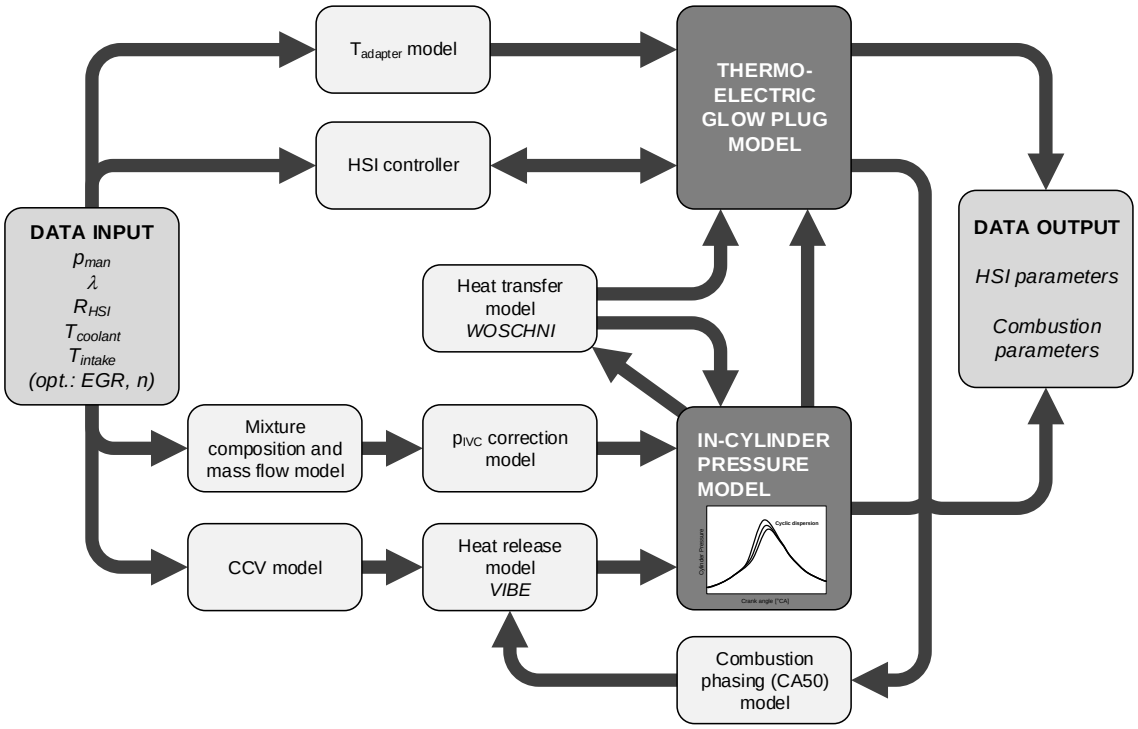

Figure 5.8: Basic structure of the 0D HSI Matlab/Simulink model.

5.4.1 In-Cylinder Pressure Model

The in-cylinder pressure model consists of two submodels, one for both intake and exhaust stroke (open valves) and one for the compression and expansion strokes (closed valves). Mass, composition and thermodynamic state of the in-cylinder charge at IVC is derived from input data (e.g. intake manifold pressure p_{man} and relative air-fuel ratio λ) and fine-tuned by an empirical correlation to account for gas-dynamic effects of the specific test bed configuration (see details in Section 7.3.3). Heat release is computed using a parametric Vibe function, whose form parameters were adjusted using experimental data at different intake manifold pressures, combustion phasings and relative air-fuel ratios (see Appendix A.3). Start of combustion (SOC) and combustion duration (CD) are calculated using empirical correlations determined in the RSM experiments presented in Section 7.4. A CCV model subjects the set values for SOC and CD to cyclic variations following a normal distribution with specified values for standard deviation (σ_{SOC} and σ_{CD}). The specific heat capacities of each species required to calculate mixture temperature as a function of crank angle are taken from JANAF polynomials [31]. Heat transfer to the piston and the cylinder walls is computed using a 1-zone model after Woschni (1990). Following simplifications are made: In-cylinder volume is only made up by one zone with mean properties, fuel only contains CH_4, blow-by is not considered, dissociation processes at high temperatures are neglected and complete combustion is assumed.

5.4.2 Thermo-electric Glow Plug Model

Since glow plug data like exact dimensions, composite composition, specific material

properties and manufacturing tolerances were not available, the glow plug was approximated by a simple nonlinear lumped-capacitance model with a total of 13 segments (see Figure 5.9). Temperature distribution and material properties in each segment or lump are assumed to be constant, while their temperature is governed by energy conservation, basic heat transfer relations and simple Joule heating. Three of these segments protrude into the shield volume (segments A-C) and form the glow plug tip. Segment A embodies the thin heating cap layer, where most heat is produced (P_{HC}) and whose temperature is T_{HS}. Through its outer surface, i.e. the hot surface, it interacts with the in-cylinder charge (convection) and the cylinder and adapter shield walls (radiation). With segment B, the glow plug core, and segment C, heat is exchanged by conduction, where the heat flow rate is governed by the area of adjacent surfaces, an elemental conduction resistance and the driving temperature difference. The remaining 10 cylindrical lumps determine the 1-dimensional convective heat transfer towards the HSI adapter, with $T_{adapter} = T_{adapter,front}$. By virtue of the gap between the protective sleeve and the feed-through bore of the HSI adapter, the sides of all segments are assumend to be adiabatic. The range in which T_{HS} is varied is limited to about 800 – 1250 °C. For this reason, changes in thermal properties, such as thermal conductivity, are expected to be minor and were therefore set as constant.

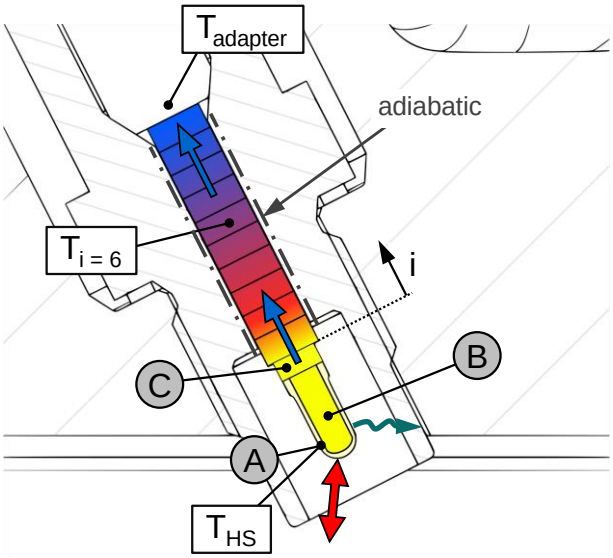

Lumped element model:

- Segment A (heating cap) that interacts with in-cylinder charge:
  - Convection
  - Radiation

  and with segments B and C:
  - Conduction
- 12 segments (including B and C) for convective heat transfer to engine block
- ODE for each element
- Uniform temperature and thermal properties in each element
- Joule heating in each conducting element proportional to its temperature.

Figure 5.9: Lumped element model for simulation of hot surface temperature.

Glow plug resistance R_{HSI}, consisting of R_{HC}, R_{leads} and R_0 is calculated from HS temperature and HSI adapter temperature after the correlation from Eq. (6-1), which will be explained in the following section, and is adjusted by a controller algorithm in identical form to that used in the experiments (see Section 4.3). To compute the heat generated in each segment, R_0 is distributed evenly among all 13 segments and R_{leads} among the 12 leads segments, directly proportional to their temperature, while R_{HC} is assigned to the heating cap, i.e. segment A. As will be explained later on in Section 6.3, it was not possible to measure HS temperature during engine operation and several assumptions regard-

ing the heat transfer relations had to be made:

- Convection: Thermal interaction between the in-cylinder charge and the hot surface is modelled through a non-dimensional 2-zone Woschni correlation, assuming that the glow plug tip is exposed to the hot burnt zone after the onset of combustion.
- Conduction: Constant heat conductivity is assumed in all segments.
- Radiation: The hot surface is assumed to be a grey body with an emissivity of $\varepsilon = 0.9$. Radiation is only exchanged with the shield volume assuming a view factor of 1 and a constant shield temperature.

Since the process of convective heat transfer is highly complex and depends on many factors such as the variable flow field, mixture composition and physical state of the mixture, the error of using a generic heat transfer model cannot be quantified without further experiments and precise measurement of HS temperature. The relations for conduction and radiation, on the other hand, are simpler to formulate and remain nearly constant over the engine cycle. Using a full-factorial design, where every unknown factor involved in heat transfer is set to several levels, a simple sensitivity analysis using Eq. (4-5) and setting $\dot{Q}_{conv} = 0$ was performed (see Appendix A.4). The aim was to determine the effect of each factor on the required heating power P_{HC} to satisfy the condition $dU/dt = 0$ and quantify the error when faulty assumptions are made. In terms of conduction, specific heat conductivity k proved to be the largest source or error in calculated P_{HC}. At an assumed value for k of 30 W/mK, an uncertainty of +/-5 W/mK would cause a significant error in P_{HC} of about +/- 7.3 W when T_{HS} is set to 1200 °C. Radiation proved to be most sensitive to HS temperature and the emissivity of the shield. Under the assumption that the highly reflective surface of the shield has an emissitivity of $\varepsilon = 0.3$ +/- 0.1, the error in P_{HC} at $T_{HS} = 1200$ °C amounts to approximately +/- 1.7 W. At the same temperature, an uncertainty in T_{HS} of +/- 50 °C causes an error in P_{HC} of about +/- 1.9 W.

In its current state, the model is able to show trends and basic dependencies and controller behaviour when subjected to CCV is in very good agreement to that in real engine operation. The sensitivity analysis yields the most important factors to be tuned in future model validation in order to eliminate differences between measured and simulated energy consumption under otherwise identical operating conditions.

6 Preliminary Investigations

This chapter gathers important findings from both experiment and simulation that were crucial during the development process of the HSI System and made conducting and discussing the main experiments presented in Chapter 7 possible in the first place.

The aim of the first part of this chapter, which interpolates some material from papers published before by the author [121, 123], is to analyse the conditions that lead to mixture ignition by a combined approach of numerical simulation and engine experiments with multiple single-fibre optical accesses to the combustion chamber. The focus of the second part is to determine if glow plugs are intercheangable or if the HSI induced combustion process is sensitive to glow plug manufacturing tolerances. This of vital importance when glow plug durability is unknown and large series of experiments, like those presented in Chapter 7, need to be conducted. Finally, the third part covers the thermoelectric properties of different glow plugs in an engine environment and presents a simple alternative approach to improve their temperature sensing functionality.

6.1 Process of Mixture Preparation and Ignition

In resistance sweeps at full load using an early stage of resistance control (low frequency and small PI gain) presented in [99], stable HSI operation was only possible in a quite narrow λ range, between 1.74 and 1.84. The experiments were run at full load using engine block A prior to being machined for fitting the optical adapter and before conditioning intake air and coolant temperature. At $\lambda = 1.74$, stable engine operation was only possible when setting very high HS temperatures, leading to overadvanced combustion phasing close to TDC. Above $\lambda = 1.84$, high cyclic variations paired with slow flame kernel development lead to recurring partial burn and misfire events (misfire limit). Figure

6.1 shows CA50 versus HSI resistance for tested λ. It can be seen that the dependency between HSI resistance and combustion phasing does not show a monotone correlation and HSI operation can be divided into two different sections. Starting from low resistances, an increase leads to advanced CA50 (henceforth referred to as "*section 1*"). Upon reaching a certain resistance, however, raising it further has either no significant effect on CA50 at all or even leads to slightly retarded combustion phasings (referred to as "*section 2*"). At first glance, this effect contradicts the integral ignition delay correlation in Eq. (2-8) that yields a reduction in ignition delay as the temperature is increased. Due to the existence of *section 2* and the inability to operate at lower R_{HSI} in *section 1*, it was not possible to control combustion phasing below $\lambda = 1.80$. Since understanding what causes the existence of both sections was key to improving HSI operation and enhancing its operating window, the numerical and experimental investigations in the following Sections 6.1.1 and 6.1.2 were carried out.

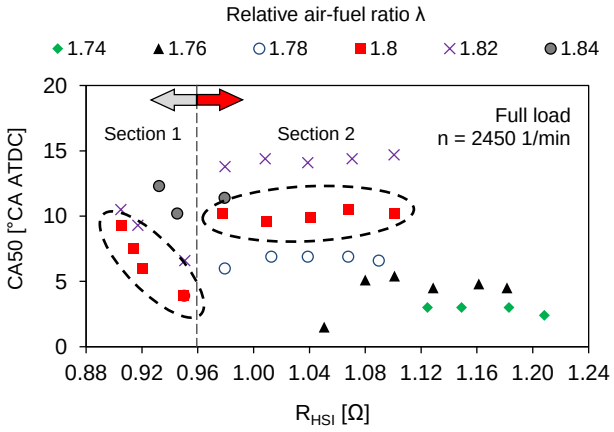

Figure 6.1: Combustion phasing CA50 versus HSI resistance for relative air-fuel ratios $\lambda = 1.74 - 1.84$ at full load prior to controller optimisation [123].

6.1.1 Gas Exchange and Combustion Simulation

The process of gas exchange was simulated at nominal engine speed with boundary conditions derived from the full load reference operating point and a relative air-fuel ratio of $\lambda = 1.8$. Figure 6.2 illustrates characteristic properties of the flow field inside combustion chamber and shield volume during the intake stroke. At gas exchange TDC (defined as 0 °CA), both cylinder and shield volumes are only filled with hot residual gas and charge motion is characterised by rather low flow speeds. As intake valve lift increases while the piston is moving downwards, fresh mixture is inducted and mixes with residual gas. Only 20 °CA after TDC, the shield already fails at fulfilling its primary function, that of avoiding premature contact between fresh mixture and the hot surface. Although flow velocities inside the shield remain at a rather low level overall, unburnt mixture is able to penetrate the shield volume and impinge on the tip of the hot surface at a very early stage of the cycle. This results from the characteristic vortex flow caused by the engine's swirl port combined with the relative angular offset of the HSI assembly to the cylinder axis.

At 90 °CA ATDC, charge already shows rather good through-mixing and differences in fresh mixture fraction between shield and cylinder volume are minimal.

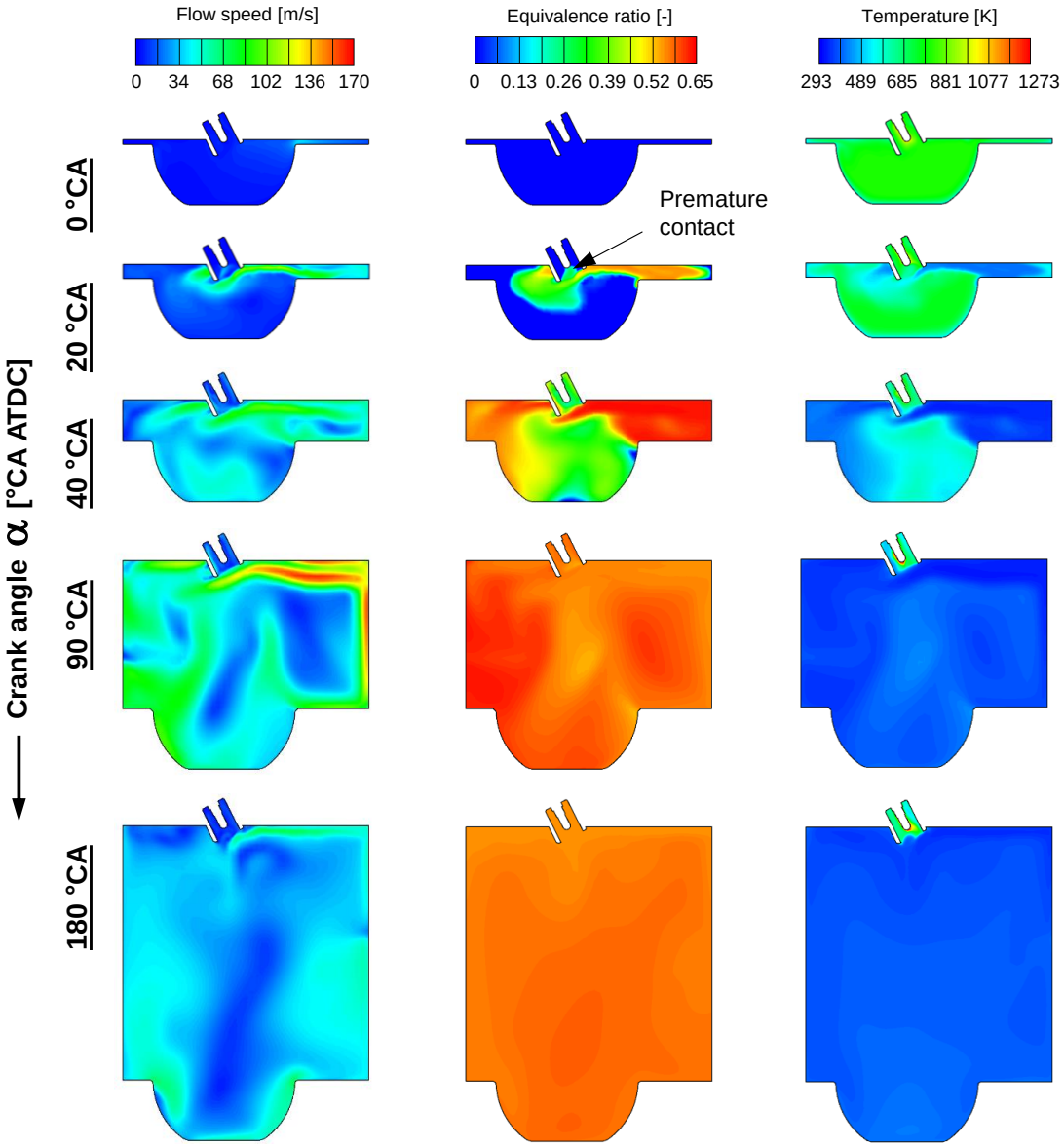

Figure 6.2: Colour plots showing simulated flow speed (left), equivalence ratio (middle) and mixture temperature (right) at selected times of the intake stroke ($\Phi = 0.65/\lambda = 1.80$, $n = 2450$ 1/min, $T_{HS} = 1073$ K).

Several cases with HS temperature ranging from 973 to 1473 K were simulated for unthrottled operation at $\lambda = 1.8$ in order to determine the effect of temperature on mixture ignition and combustion of the bulk cylinder charge. A simulated temperature of 973 K did, however, not suffice to enflame the mixture. Figure 6.3 depicts mean reaction progress variable c_{mean} in the cylinder volume (ranging from 0 – unburnt mixture – to 1 – burnt mixture), i.e. the cumulated gross heat release, and the corresponding in-cylinder pressure traces for $T_{HS} = 1073/1273/1473$ K. With increasing HS temperature, computed heat release in the main combustion chamber is retarded, thus exhibiting the same trend observed in experiments when operating in *section 2*. The difference is most noticeable

for both extreme values, for what reason both simulations will be reviewed in detail in the ensuing section.

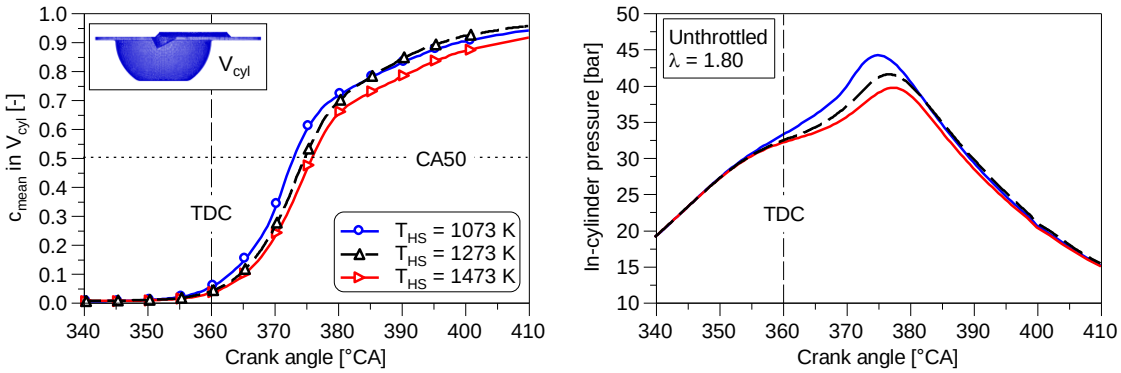

Figure 6.3: Mean progress variable c_{mean} in the cylinder volume V_{cyl} (left) and in-cylinder pressure trace (right) against crank angle for T_{HS} = 1073/1273/1473 K (unthrotlled, λ = 1.80).

Figure 6.4 (top) shows colour plots of the calculated local reaction progress variable c in the reaction zone inside the shield (V_{shield}) and the entire combustion chamber (V_{cyl}) for cases T_{HS} = 1073 K and T_{HS} = 1473 K. The lower diagram shows the corresponding values of c_{mean} in V_{shield} against crank angle. To support the discussion of results, Figure 6.5 lays out the time histories of total mixture and CH_4 mass in V_{shield}, the mean gas temperature in the shield and the mole fraction of the intermediate combustion product OH for both V_{cyl} and V_{shield} for the same simulation cases. Analysing the evolution of OH concentration is quite useful as it represents a suitable means for tracking both timing and duration of chemical reactions. Under real engine conditions, OH radicals are present during the entire combustion process [73] but also for post-flame reactions, which is also considered by the ECFM-3z combustion model [37].

As can be seen from the increase of c in the shield volume, pre-reactions already begin in early stages of the intake stroke for both temperatures (1). While c rises gradually for T_{HS} = 1473 K, leading to a distinct flame kernel at BDC (2), for T_{HS} = 1073 K it remains rather constant and at a low level over the entire cycle. For the 1073 K case, the process that eventually leads to combustion of the main charge is as follows: During the compression stroke, unburnt mixture is pressed into the shield volume, leading to a gradual increase of both total mixture and fuel mass. At about 300 °CA ATDC (3), favoured by the increasing gas pressure and temperature, a small flame kernel forms close to the glow plug tip. As a result, both c_{mean} and the mean calculated OH concentration in the shield begin to rise, while fuel mass is still increasing due to piston motion. At 330 °CA ATDC, CH_4 mass peaks, followed by a fast fuel depletion close to TDC. The developing flame produces high gas temperatures in the shield, able to initiate the main combustion at about 340 °CA ATDC (4). It is expected that this occurs principally through thermal diffusion, as no mass is ejected from the shield volume. As a result of this rather slow process, without entrainment effects that would increase the volume of activated mixture, it takes until TDC (5) to consume 5 % of the bulk fuel and develop a marked flame con-

tour, stretched by a pronounced in-cylinder swirl and squish flow.

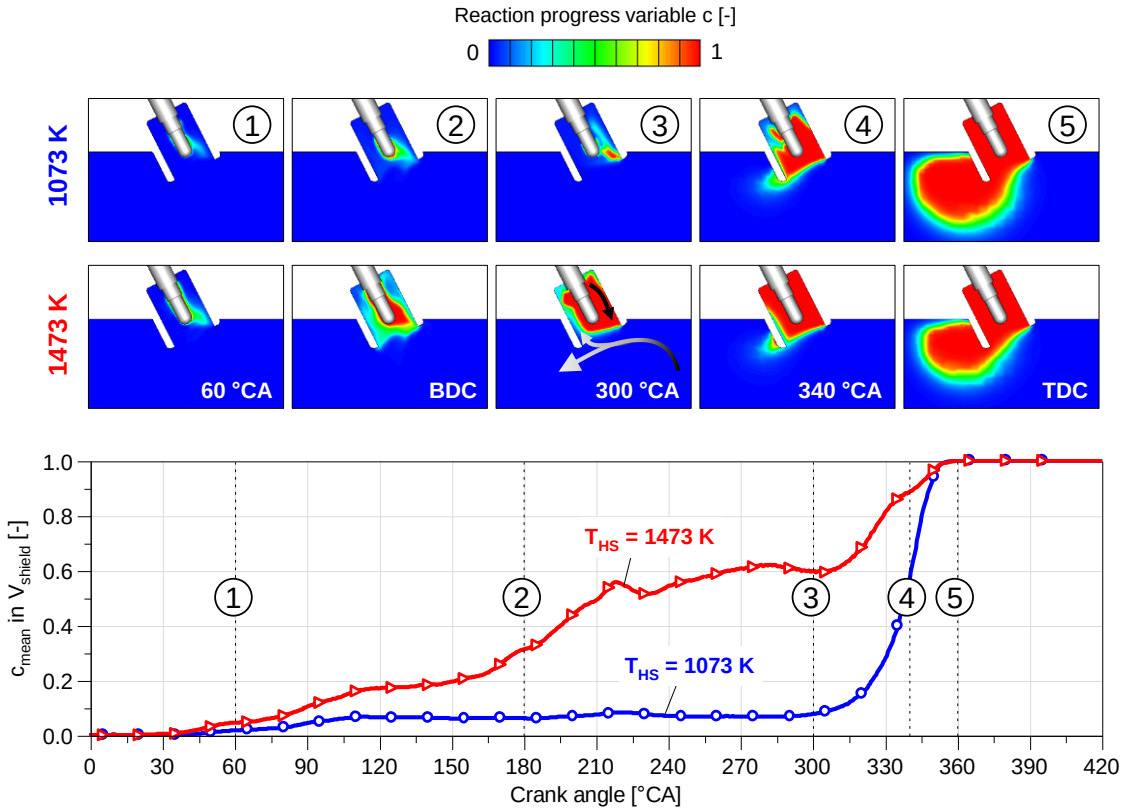

Figure 6.4: Selected colour plots showing local reaction progress variable c in the vicinity of the hot surface (top) and trace of mean reaction progress variable c_{mean} in the shield volume V_{shield} versus crank angle (bottom) for T_{HS} = 1073/1473 K at λ = 1.80, unthrottled.

The analysis of the same traces in Figure 6.5 shows substantial differences for T_{HS} = 1473 K. In response to the increased mixture reactivity that manifests in promoted reaction rates and shorter ignition delay, the flame kernel already forms close to BDC (2). The mass of CH_4 in V_{shield} at the end of the intake stroke is lower due to the higher gas temperatures, and therefore lower mixture density, caused by the enhanced heat flow rate from the glow plug to the surrounding gas. Despite fresh mixture being fed to the shield volume continuously during the compression stroke, CH_4 mass does not increase significantly (see Figure 6.5, left). This is a result of the virtually immediate depletion of the inflowing air-fuel mixture. Due to the small amount of fuel burnt, however, OH levels in the shield remain practically unnoticed until about 270 °CA ATDC. 3D data suggests that the high in-cylinder charge motion is what hinders the flame kernel from developing into a self-sustained flame front capable of initiating the main combustion. As a result of the characteristic flow pattern caused by intake port and the moving piston, unburnt mixture enters the shield on the left, thereby creating a tumble-shaped flow that pushes the hot combustion products towards the lower right side (see time step 3 in Figure 6.4). While this leads to direct interaction between the hot residual gas and the air-fuel mixture from V_{cyl}, the species in the reaction zone are entrained by the in-cylinder flow and re-enter the shield volume. This recirculation effect inhibits the onset of the main com-

bustion and only ceases once the piston approaches TDC and charge motions subsides. For case $T_{HS} = 1073$ K, on the other hand, the rapid heat release before TDC stops the mixture from recirculating, causing almost quiescent conditions at around 340 °CA ATDC ($\dot{m}_{shield} \approx 0$). This enables the flame to exit the shield and advances the start of main combustion compared to case $T_{HS} = 1473$ K, as indicated by the OH concentration traces in V_{cyl} in Figure 6.5 (bottom-right).

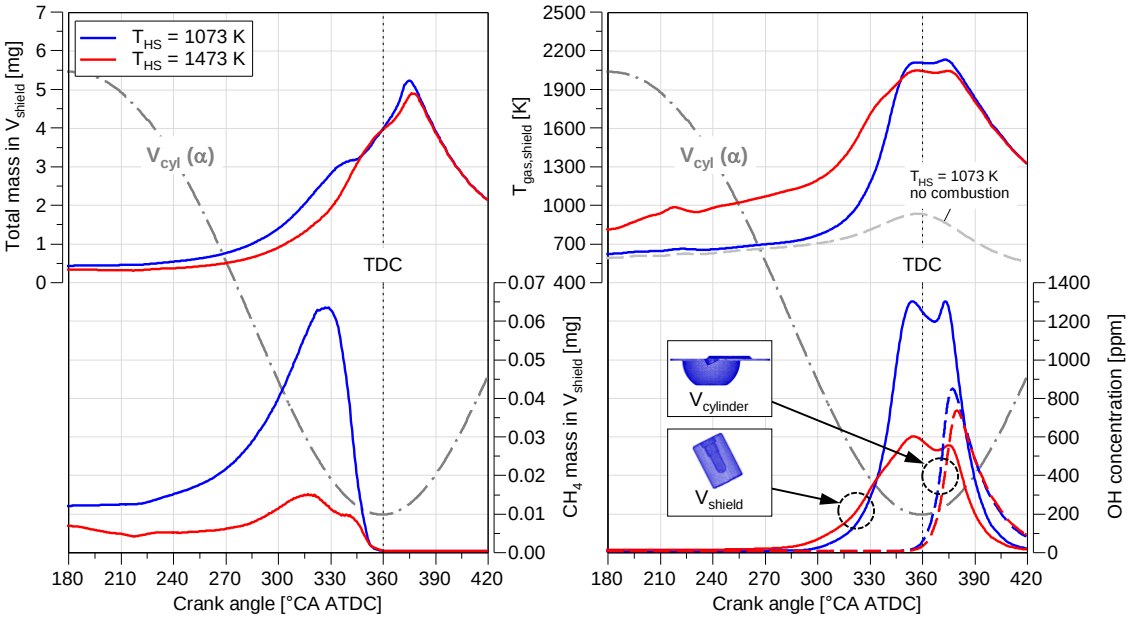

Figure 6.5: History of total mass and CH_4 mass inside the shield volume (left), history of mean gas temperature inside the shield volume and mean OH concentration in the shield and cylinder volume (right) for $T_{HS} = 1073/1473$ K at $\lambda = 1.80$, unthrottled.

The finding derived from this direct comparison gives a possible explanation of why combustion phasing is retarded when increasing HS temperature. Unlike in the experiments, however, where increasing T_{HS} in *section 1* would advance combustion phasing, all simulated cases showed the abnormal ignition behaviour, even so at low temperatures. This may be caused by the fact that the GRI-Mech. 3.0 reaction mechanism underpredicts ignition delay times at pressures above 10 bar. This leads to an increased reactivity of the mixture and could potentially shift the anomaly to lower HS temperatures.

Since the ignition anomaly appears to be caused by particular flow conditions inside the shield volume, it can be presumed that changes to the shield design (e.g. no inclination relative to the cylinder axis) and/or the geometry that shapes the in-cylinder flow field (e.g. squish area) would greatly alter the results obtained.

6.1.2 Optical Experimental Results

The simulation results presented suggest that premature mixture ignition is responsible for the abnormal combustion behaviour in *section 2*. For experimental validation of these findings, engine tests were run with engine block A, employing the multi-fibre optical

adapter shown in Figure 5.3. The primary function of the ensemble of optical probes was to give timing and location of mixture ignition as a function of HSI resistance so as to explain the combustion anomaly. This target was met satisfactorily but due to limited durability of the optical probes, experimental time was limited and only few operating points could be recorded. Figure 6.6 (left) plots operating points recorded using the multi-fibre adapter, with a resistance controller at an early development stage (LabVIEW control, 20 Hz and small controller gain). R_{HSI} sweeps were conducted for two relative air-fuel ratios $\lambda = 1.72$ and 1.76.

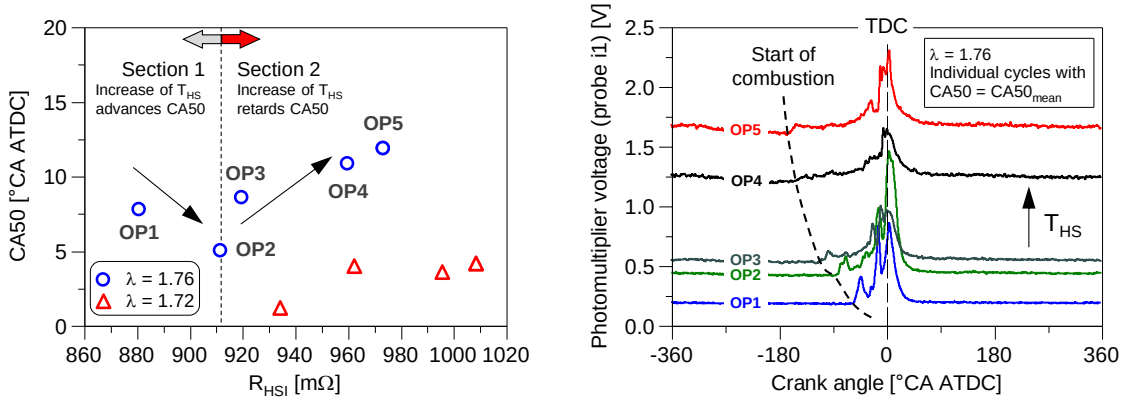

Figure 6.6: CA50 vs. HSI resistance for $\lambda = 1.72/1.76$ (left) and corresponding radiation history detected by optical probe i1 in the HSI shield over crank angle for $\lambda = 1.76$ (right).

At $\lambda = 1.72$, the engine could only be operated in *section 2*, while $\lambda = 1.76$ exhibited distinctive *sections 1* and *2*. For $\lambda = 1.76$, individual cycles showing same combustion phasing as the ensemble-average $CA50_{mean}$ were selected to plot the traces of photomultiplier (PM) voltage in Figure 6.6 (right). The PM voltage levels shown correspond to the amount of radiation detected over crank angle by the inner optical probe "i_1" mounted inside the shield. At first glance, it can be seen that considerable levels of radiation are recorded over the entire engine cycle for all operating points. The fact that radiation is detected throughout, even when no mixture is available for combustion, implies that a significant part of it is emitted as incandescence by the glowing hot surface itself. This can be affirmed when comparing the absolute radiation voltage levels for different R_{HSI}, since an increase in resistance, i.e. HS temperature, leads to higher absolute radiation levels. Start of combustion (SOC) in the shield volume, detected by a prompt increase of radiation between BDC and TDC during the compression stroke, advances as HSI resistance is raised. In *section 1* (OP 1 and 2), on the one hand, mixture inflames in the hot surface's vicinity close to TDC, leading to a comparatively fast combustion and high radiation levels. In *section 2* (OP 3 – 5), on the other hand, combustion starts as early as 170 °CA BTDC and shows comparatively low radiation levels during the compression stroke, thus indicating a low rate of heat release and also, that the flame kernel formed inside the shield is unable to develop into a propagating flame that initiates the main combustion.

With the aid of the external optical probes, distributed evenly around the shield, it was

possible to determine where the combustion process is initiated. Internal probe "i_2" as well as external probes "e_1" and "e_6" were not available for combustion evaluation as they failed shortly before starting the campaign. From the variation at $\lambda = 1.76$, Figure 6.7 depicts normalised PM voltage detected by all functioning optical accesses for OP 1 in *section 1* (left) and OP3 in *section 2* (right) for an individual cycle . Regardless of λ and the section of operation, probe "i_1" showed to always be first in detecting any combustion radiation. The time delay between the increase of radiation levels detected by the inner and outer probes proves that the flame kernel is formed inside the shield volume, allowing for other ignition sources than the glow plug to be ruled out. Another interesting finding is that among the outer probes, "e_3" and "e_4" detect radiation before "e_2" and "e_5", which indicates that the flame kernel is stretched by the macroscopic swirl still present when the piston approaches TDC (see Figure 6.7, right).

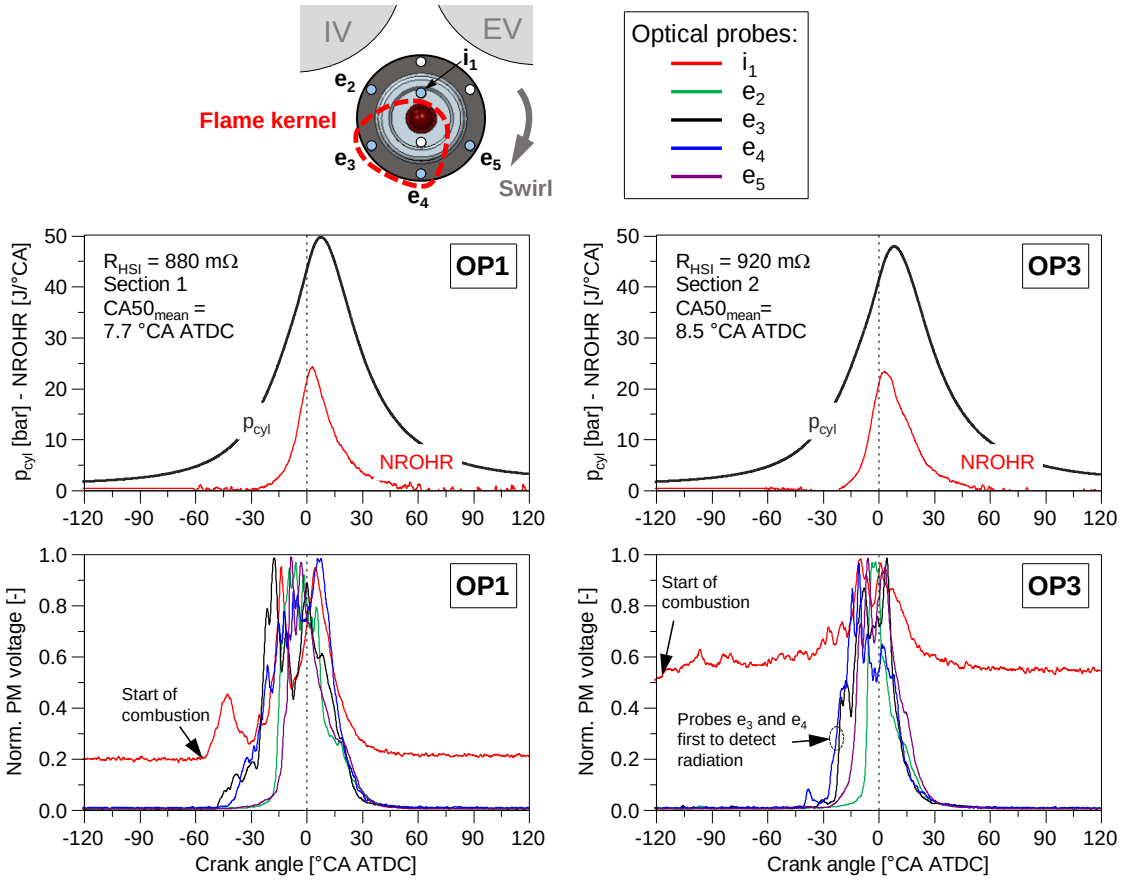

Figure 6.7: Pressure and net rate of heat release NROHR (top) and radiation detected by the optical probes (bottom, norm. photomultiplier voltage) against crank angle for individual cycles with CA50 = $CA50_{mean}$.

To determine if there is a direct correlation between the timing of mixture inflammation and combustion phasing, individual cycles with most advanced, mean and most retarded combustion phasing were selected for both operating points (OP1 and OP3). The traces of PM voltage from probe "i_1" in Figure 6.8 reveal that there is a substantial difference between *section 1* and *2*: While combustion phasing advances with the start of combustion in *section 1*, the direct opposite is true for *section 2*. According to the CFD results, retarded combustion phasing is caused by the lack of sufficient unburnt mixture able to

combust rapidly close to TDC, thus unable to initiate a fast main combustion. It seems very likely that the characteristic peak in radiation shortly after SOC in *section 1* stems from a prompt combustion of the shield mixture. Since in *section 2* only the trace of $CA50_{min}$ has a slight peak prior to the onset of the main combustion, the experimental results strongly support the possible explanation given by simulation. It can therefore be concluded that for specific engine operating conditions (λ, intake pressure…), temperature-timed rapid inflammation of the main cylinder charge is only possible below a specific HSI resistance (HS temperature), when ignition delay is sufficiently long to allow unburnt mixture to accumulate in the shield volume during the compression stroke. After formation of the flame kernel, a large mass of air-fuel mixture is burnt rapidly, enabling the flame to propagate and initiate main combustion before the piston reaches TDC. Too high HS temperatures, on the other hand, cause premature fuel oxidation in early stages of the compression stroke. The continuous, sluggish fuel depletion leads to very low fractions of unburnt fuel in the shield volume when approaching TDC, unable to produce enough radicals to initiate a fast main combustion.

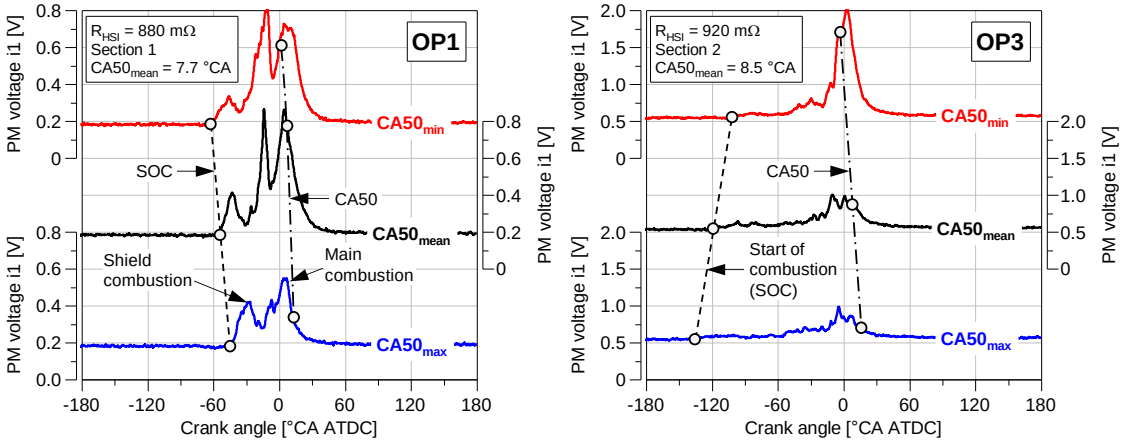

Figure 6.8: Photomultiplier (PM) voltage detected by probe i1 inside the shield volume for individual cycles of 100-cycle-ensemble showing most advanced, mean and most retarded combustion phasing at R_{HSI} = 880 mΩ (section 1), left, andR_{HSI} = 920 mΩ (section 2), right (full load, λ = 1.76).

The excessively high HS temperatures in *section 2* may result in glow plug failure, yet combustion stability is another reason why operating the engine in *section 2* should be avoided. After the development of the high-frequency resistance controller and conditioning the test bed, it was possible to determine the exact transition point from one section to the other as a function of the relative air-fuel ratio and manifold pressure (see details in Section 7.1.2.1) and record two operating points showing same combustion phasing in different sections. Using selected combustion data of 600 consecutive cycles, Figure 6.9 allows a direct comparison of combustion stability in both sections. In *section 1*, the spread in CA50 is moderate, as illustrated in the scatter plot of CA50 of cycle "i+1" plotted against that of its preceding cycle "i" for the entire ensemble. The circular scatter shape indicates that the variability in combustion phasing is not caused by deterministic effects or prior cycle interactions. The right histogram suggests that the frequency of

CA50 is normally distributed, with a standard deviation of σ_{CA50} = 3.3 °CA. In *section 2*, on the other hand, the spread in CA50 is much more significant with σ_{CA50} = 6.3 °CA, albeit still quite symmetrical and non-deterministic. Unlike in *section 1*, where frequency density is highest around the mean of the distribution, the probability density function becomes more rectangular in *section 2*, with no pronounced frequency maximum at the mean. The reduced combustion stability translates into a drop of mean IMEP by 2.4 %, an increase of indicated specific fuel consumption (ISFC) by 2.8 % as well as an increase of the emitted NO_x concentration by around 48 %. A detailed analysis of why CCV in combustion phasing are detrimental to IMEP, ISFC and NO_x are given in Chapter 7, Section 7.5.2.

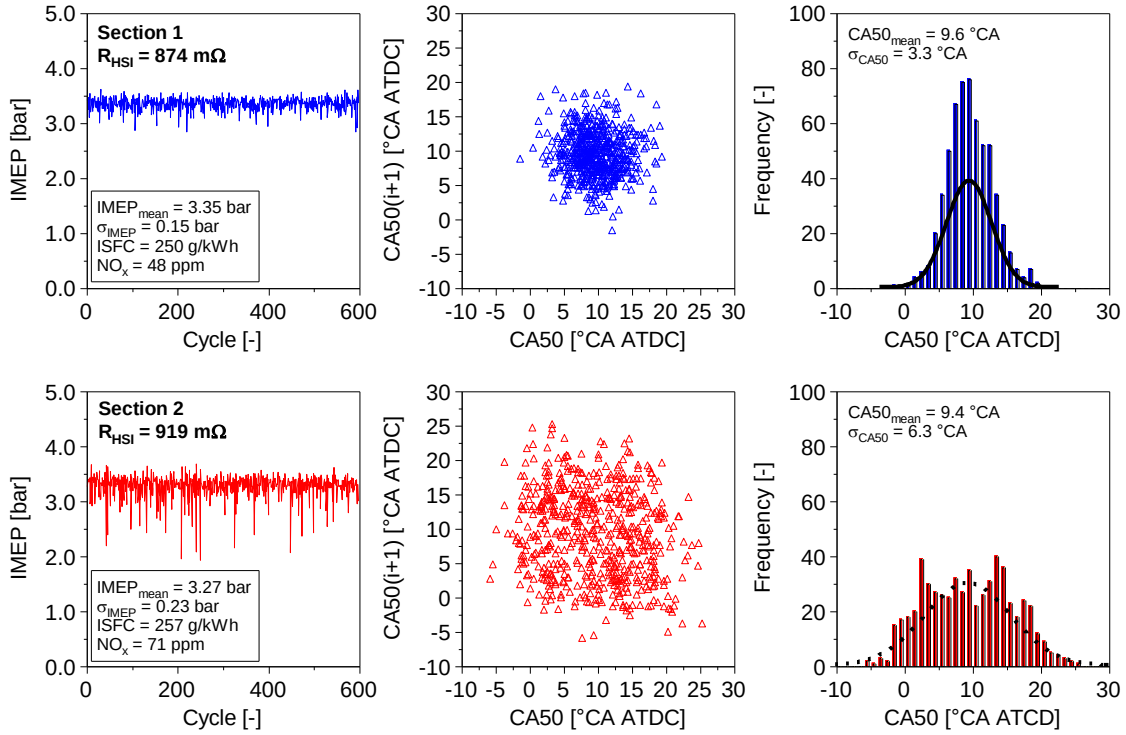

Figure 6.9: Comparison of HSI operation in Section 1 and Section 2 at same combustion phasing (p_{man}= 950 mbar, λ = 1.75, CA50$_{mean}$ ≈ 9.5 °CA ATDC $T_{coolant}$ = 60 °C, T_{intake} = 23 °C).

6.2 Influence of Glow Plug Manufacturing Tolerances

In light of the extensive experimental investigations to follow, it was necessary to examine the impact of glow plug manufacturing tolerances on the characteristics of combustion in advance. A total of 5 new specimens from the same manufacturing batch were tested in CA50 sweeps at CA50 = 0/5/10 °CA ATDC by adjusting HSI resistance at otherwise constant operating conditions. The experiments were conducted with the optimised high-speed resistance controller using a standard S10 HSI adapter, thus allowing for a significant enhancement of the HSI operating range compared to the previous section. The findings obtained were expected to clarify whether glow plugs are interchangeable if limited durability called for glow plug replacement during a measurement cam-

paign. Because ignition delay is a function of HS temperature, it is safe to assume that different glow plugs will require the same temperature for timed ignition, given that all other parameters (geometry, intake conditions, λ…) remain constant.

Figure 6.10 shows the experimental results for the glow plugs tested. Here, the absolute values and traces of combustion-related data are irrelevant and only aim to uncover differences and similarities among the tested glow plugs. The plots of IMEP, combustion duration (CA5-CA90), NO_x and ISFC prove that variability in combustion is minimal among the tested glow plugs, a finding that is further supported by non-appreciable differences in combustion stability regarding CA5/CA50 (not shown). This allows the important conclusion that, at least in terms of the combustion process, glow plugs are interchangeable. Analysing glow plug related variables R_{HSI} and P_{HSI}, on the other hand, reveals marked differences in the set resistance and auxiliary electric power required to sustain a constant temperature at the glow plug tip. Common to all specimens is that R_{HSI} needs to be increased almost linearly to advance combustion phasing. The very similar gradients of R_{HSI} against CA50 suggests that the overall R_{HSI}-T_{HS} correlation of all glow plugs tested must be fairly constant, albeit subject to individual offsets. When this reasoning is applied to Eq. (4-8), the gradient a must be nearly constant, and the offset must be caused by different individual cold resistances R_0. Experimental data, however, did not reveal any statistically significant correlation between R_0 and the resistance level required to operate at specific combustion phasing and implies that the resistance of the internal glow plug leads R_{leads} must play an important role in the glow plug's thermo-electric behaviour.

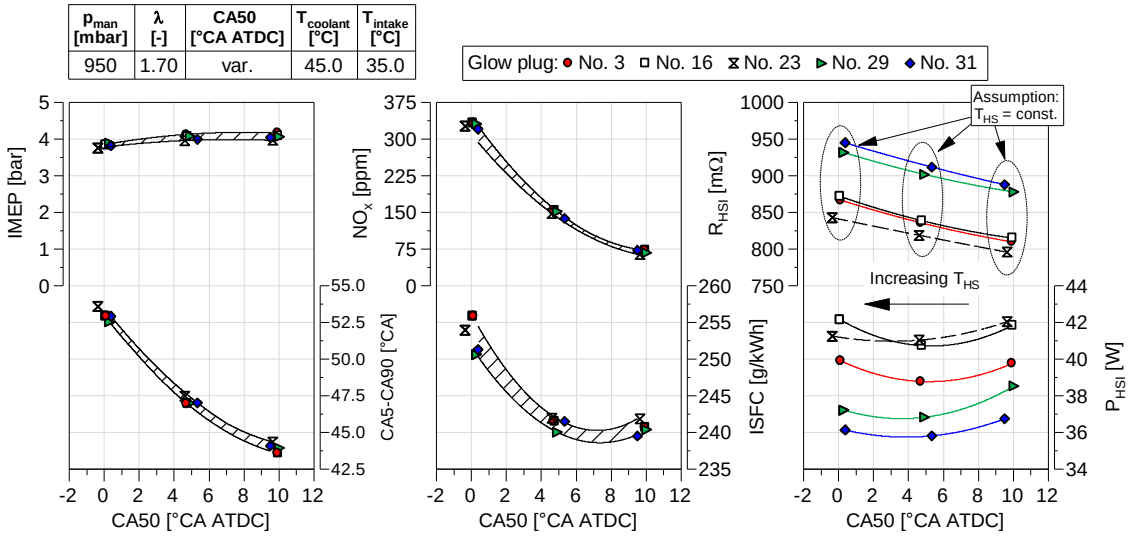

Figure 6.10: Selected data from CA50 sweep for glow plugs No. 3/16/23/29/31.

It is interesting to note that glow plugs No. 29 and 31, which show the highest values of R_{HSI}, require the lowest electric power to operate. Since the current flowing through the glow plug is also lowest, the heat generated in the heating cap must be lower compared to glow plugs No. 3, 16 and 23. When assuming that all parameters but the glow plug

specimen are constant, it applies that convective heat transfer between the glow plug and the mixture as well as radiation between the glow plug and the shield and cylinder walls remain constant ($\dot{Q}_{conv}$, $\dot{Q}_{rad}$ = const.). If P_{HSI} and, in turn, the heat generated in the heating cap P_{HC}, changes from one glow plug to another, the basic requirement to satisfy Eq. (4-6) is that the conductive heat losses $\dot{Q}_{cond}$ must change as well. Therefore, the only apparent explanation for this phenomenon is that an increasing leads resistance R_{leads} can help reduce P_{HSI} by dissipating more heat into the glow plug body, which causes its temperature to raise and $\dot{Q}_{cond}$ to diminish.

From the calculated values of HS temperature during engine operation using Eq. (4-8), it was found that T_{HS} is overpredicted by up to several hundred degrees celsius despite using individual values for R_0. Figure 6.11 plots calculated HS temperature against combustion phasing CA50 for all glow plugs tested, giving maximum temperatures at most advanced combustion phasing of 1380 – 1590 °C. These temperature levels can certainly not be sustained without overheating and damaging the heating cap layer. Because of the importance of determining HS temperature during engine operation, not only for data evaluation but also for the validation of the thermo-electric model presented in Section 5.4, the subsequent section addresses the questions of why the linear model from Eq. (4-8) gives wrong values and *if* and *how* the RT correlation can be improved.

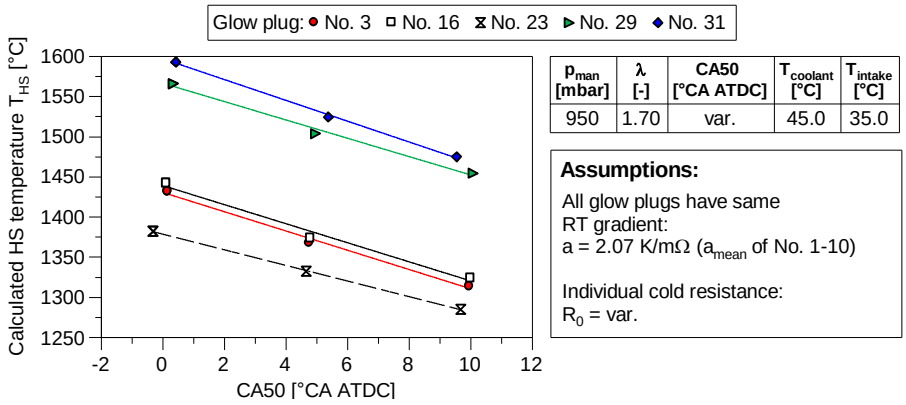

Figure 6.11: Calculated HS temperature T_{HS} against combustion phasing CA50 for different glow plugs.

6.3 Resistance-Temperature Correlation under Engine Conditions

Due to of the inapplicability of Eq. (4-7) to predict HS temperature reliably, the steady-state RT correlation of three randomly chosen new glow plugs was determined under ambient conditions by use of a pyrometer at the Institute for Sensors and Information Systems at Hochschule Karlsruhe. Figure 6.12 shows the test setup used (left) as well as the measured HS temperature against glow plug resistance for glow plugs No. 9, 10 and 19, including two reference measurements provided by the manufacturer (right). From the plotted data, the following important conclusions can be drawn:

– The correlation between temperature and resistance is fairly linear but is approximated best using a quadratic polynomial, particularly for the high temperature range.

Alternatively, a low temperature (200 – 800 °C) and high temperature (800 – 1250 °C) range can be defined, both with linear regression.

– Manufacturing tolerances cause substantial differences among the glow plugs tested, even if cold resistances are practically identical ($R_{0,9} = 217$ mΩ, $R_{0,10} = 218$ mΩ).
– Reference measurements from the manufacturer (Ref_9 and Ref_{10}) require lower glow plug resistance to reach reference temperature (1250 °C).

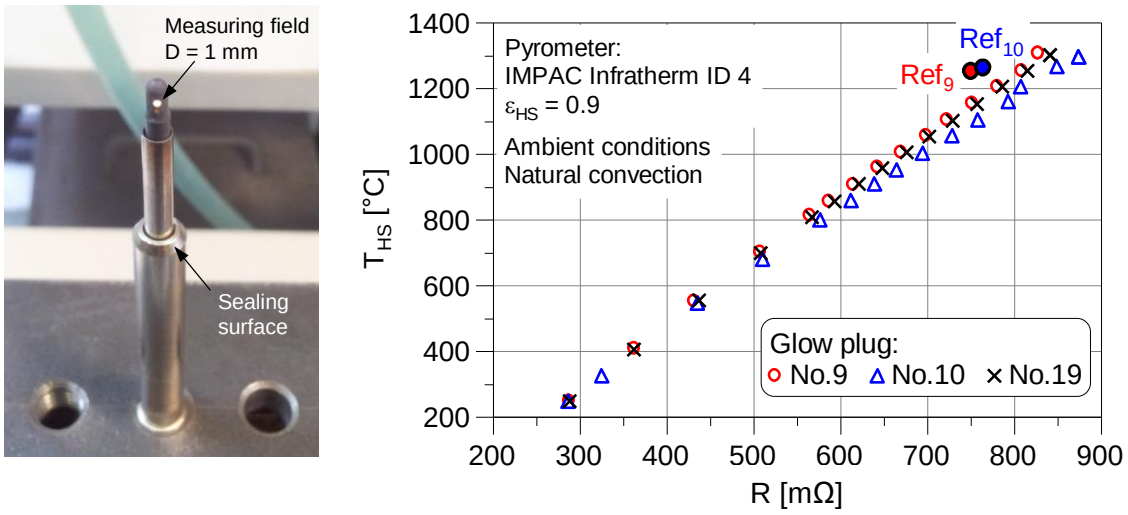

Figure 6.12: Experimental setup for determining the resistance-temperature correlation of glow plugs No. 9, 10 and 19 (left), measured glow plug (hot surface) temperature T_{HS} versus glow plug resistance R (right). Ref_9 and Ref_{10} represent reference measurements provided by the manufacturer for the respective glow plugs.

End-of-line test conditions of Ref_9 and Ref_{10} are unknown, yet it is expected that they conform to actual temperature conditions during Diesel engine cold start, where conductive heat transfer is mainly governed by engine coolant temperature. When mounted in the engine block, the heat flow path to dissipate most thermal losses of the glow plug is rather short and spans from its heated tip to the conical sealing surface. For the internal experimental setup, however, the path ended at the glow plug's thread (see Figure 6.12, left), hindering the conductive heat transfer thereby and leading to higher glow plug body temperatures overall. The test for glow plugs No. 10 and 19 (No. 9 had already been used in other trials) was repeated to analyse the temperature distribution along the glow plug axis using a thermal camera. To account for the low emissivity of the reflective glow plug body surface, a coating of black high temperature low-reflectance paint was applied and emissivity of the camera set to $\varepsilon = 0.95$. 4 measuring points were defined, one in the centre of the protective sleeve and 3 along the outer body. Figure 6.13 shows thermal images of both glow plugs at steady-state at $T_{HS} \approx 1200$ °C. The fairly high temperatures right below the sealing cone at measuring position 1 (sp1) suggest that a hotter glow plug body is very likely to be responsible for differences between own and manufacturer data. Furthermore, it is interesting to note that glow plug No. 10, which requires a higher resistance for same HS temperature, is hotter at each measuring point. This proves that more heat is dissipated along the leads due to their higher resistivity com-

pared to No. 19 and confirms the conjecture formulated in the previous section that the glow plug's thermo-electric behaviour is highly sensitive to manufacturing tolerances of the leads.

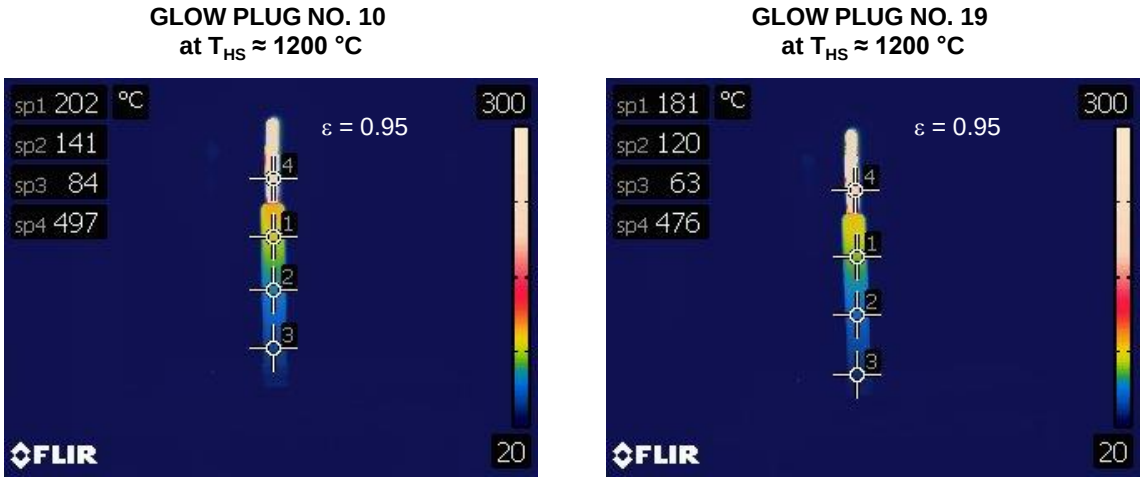

Figure 6.13: Temperature distribution along the glow plug body for glow plugs No. 10 and 19 at T_{HS} ≈ 1200 °C, recorded with thermal camera FLIR T440 (steady-state conditions, free convection, T_{amb} = 23.5 °C).

In order to scrutinise the effect of glow plug body temperature on the RT correlation, the optical HSI adapter presented in Section 5.1.3 (Figure 5.4) was employed in ad hoc experiments to record voltage step responses when the glow plug is cooled (mounted in cold engine block) or only subjected to natural convection (unmounted). Photomultiplier (PM) voltage recorded is proportional to the visible part of incandescence emitted by the glow plug, detected by a single optical fibre protruding into the shield volume, thus being a qualitative indicator for HS temperature. Figure 6.14 shows the step responses of R_{HSI}, PM voltage, P_{HSI} and $T_{adapter}$ when a voltage of 6 V is applied to the glow plug.

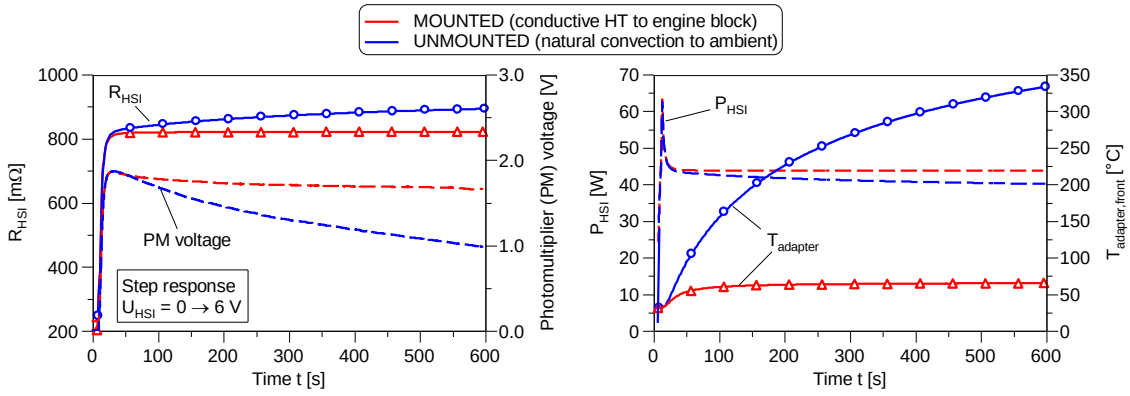

Figure 6.14: Voltage step responses 0-6 V for mounted and unmounted HSI adapter.

In the first few seconds, there are no noticeable differences between both configurations. As time proceeds, however, adapter temperature increases gradually for the unmounted adapter. The respective traces of R_{HSI} and PM voltage deliver a clear explanation of the impact of increasing adapter and glow plug body temperatures on the glow plug's RT correlation: Resistivity of inner and outer electric leads must show considerable PTC

dependence, leading to a rising resistance R_{leads} when the heat dissipated by conduction is not enough to keep glow plug body temperature constant. This causes an increase of total resistance R_{HSI} that, in turn, limits the electric current flowing through the heating cap. Since less heat is produced, hot surface temperature drops (see decrease of PM voltage). These findings allow concluding that increasing glow plug body temperatures reduce the achievable temperature at the glow plug tip when applying a specific voltage or controlling to a specific resistance and explains why Eq. (4-8) cannot be used for engine operation. For this reason, the following alternative method that includes a simplified linear temperature dependency of the inner electrical leads was used (see Appendix, Section A.4, for its derivation):

$$T_{HS} = \frac{1}{a_{HC}}\left[R_{HSI} - R_0 - a_{leads} \cdot \left(T_{adapter} - T_0\right)\right] + T_0 \tag{6-1}$$

Where a_{HC} is the temperature gradient of the heating cap ($R_{HC} \rightarrow f(T_{HS})$) and a_{leads} the temperature gradient of the electric leads ($R_{leads} \rightarrow f(T_{adapter})$). To determine a_{leads}, a glow plug was mounted inside the optical adapter and without applying any voltage, the adapter was exposed to an even stream of hot air. Once the readings of thermocouples $T_{adapter,front}$, $T_{adapter,back}$ and T_{shield} reached steady-state, glow plug resistance was measured using the *5 V/5 ms* method. By adjusting the temperature of the air flow stepwise it was possible to derive the correlation between $T_{adapter,front}$ and the measured leads resistance R_{leads} plotted in Figure 6.16 (left). This temperature was chosen as the measuring position is very close to the inner ceramic leads, in the front section of the glow plug, while $T_{adapter,back}$ is closer to the inner metallic lead (see Figure 6.15). Linear regression gives a value of a_{leads} = 0.669 mΩ/K, with a remarkable correlation coefficient of R^2 = 0.9999. To assess whether the resistance of the inner metallic is sensitive to temperature, one glow plug was disassembled and its resistance measured at different temperatures. Its cold resistance of 5.1 mΩ made up less than 3 % of total glow plug resistance and showed a neglectable dependence on temperature, with a gradient of 5 µΩ/K. As a consequence, only the ceramic leads experience a significant increase in resistivity with temperature and a_{leads} can be used to calculate T_{HS} during engine operation.

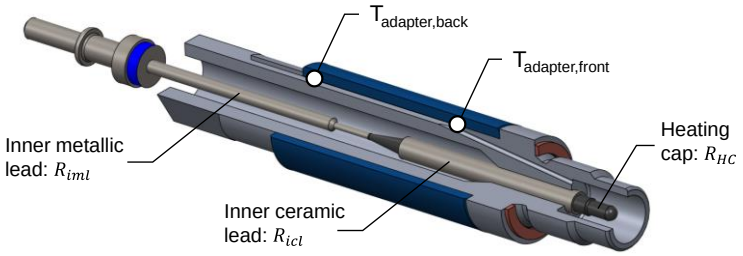

Figure 6.15: Cutaway view of the single-fibre optical HSI adapter showing the inner metallic and ceramic leads and the measuring positions of $T_{adapter,back}$ and $T_{adapter,front}$.

While still an approximation, Eq. (6-1) accounts for variable glow plug body temperatures and gives more realistic temperature values compared with Eq. (4-8). Figure 6.16 shows the adjusted RT dependency as a function of adapter temperature using the enhanced model used in all following experiments.

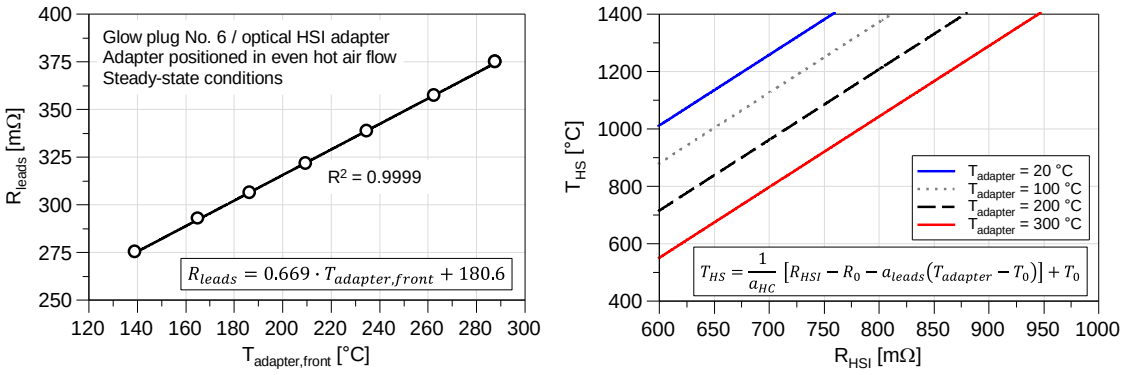

Figure 6.16: Measured leads resistance R_{leads} versus adapter temperature $T_{adapter,front}$ (left) and calculated hot surface temperature T_{HS} acc. to Eq. (6-1) versus HSI resistance R_{HSI} for different adapter temperatures (right).

Viable methods to measure high temperatures in an engine environment were considered with the objective of recording the actual HS temperature in engine operation and validate the dependencies shown in Figure 6.16. In principle, there are two common ways to do so: either contactless by detecting the electromagnetic radiation emitted by the object, especially in the short-wave part of the IR spectrum; or via direct contact using a sensing element, such as thermocouples. Measuring HS temperature optically, e.g. by means of a single-fibre pyrometer, holds the advantage of being prompt, not interfering with the in-cylinder flow in the vicinity of the glow plug and not altering its temperature. However, system complexity and costs are high, this being the reason why a simpler approach relying on relatively inexpensive high-temperature thermocouples was followed. For most accurate results when measuring HS temperature, the heat capacity of the thermocouple needs to be small and therefore of small diameter. This diminishes the cooling effect that the thermocouple exerts on the hot surface and avoids significant alteration of the thermo-electric properties of the glow plug. The small diameter is also a requirement for minimising both the sensors's impact on flow conditions inside the shield and the increase of the hot surface area involved in mixture ignition. A $d = 0.5$ mm thermocouple was chosen as the best compromise between low reading distortion and durability. It was glued along the glow plug tip using ceramic two-component adhesive and tested under ambient conditions after concluding the curing process. The smooth ceramic surface, however, did not allow for permanent adhesion of the thermocouple, despite testing several curing strategies and other high temperature glues. In consequence, HS temperature could not be measured during engine operation and it was necessary to resort to HSI resistance and adapter temperature to calculate an approximate value, with the incandescence emitted by the glow plug and recorded by the photomultiplier being an additional qualitative indicator.

6.4 Conclusion

The CFD simulations and optical experiments conducted and presented in this chapter proved very helpful in understanding how flow dynamics and reaction kinetics affect the ignition process. Owing to the combination of HSI assembly inclination in relation to the cylinder axis and the distinct swirl during mixture induction, fresh mixture enters the shield volume early in the intake stroke and impinges on the heated glow plug, this being the starting point for the production of chain-carriers that eventually cause the mixture to ignite. Since ignition delay is kinetically controlled, it is highly sensitive to HS temperature. Both simulation and experiment show that the start of combustion in the shield volume can be advanced by increasing HS temperatures, but also that this does not necessarily translate into advanced combustion phasing. It was found that the HS temperature level needs to be sufficiently low to allow for unburnt air-fuel mixture to accumulate in the shield volume, ignite close to TDC and cause a fast main combustion (operation in *section 1*). Excessive temperatures, on the other hand, deplete most of the inflowing fuel during the compression stroke, the heat release is not sufficient to produce a propagating flame and main combustion becomes more sluggish and retarded (operation in *section 2*). This allows the conclusion that only HS temperatures and, in turn, HSI resistances, below a certain value allow appropriate control of combustion phasing. Higher temperatures and premature ignition should be avoided due to several disadvantages in engine performance and stability, emission output and glow plug durability.

Experimental CA50 sweeps were carried out using 5 glow plug specimens from the same manufacturing batch in order to determine the influence of manufacturing tolerances on the combustion process and the thermo-electric properties of the glow plug. The results obtained give evidence that combustion parameters are not sensitive to the individual glow plug employed, as long as CA50 is the controlled parameter. Electric properties such as HSI resistance and power, however, proved to differ significantly among the specimens tested due to differences in their resistance-temperature correlation. The practical implication of these findings is that the actual control value of the HSI controller, R_{HSI}, should not be used as a factor in subsequent trials but replaced by combustion phasing CA50.

Despite the rather linear resistance-temperature relationship of conventional PTC heaters, such as the glow plug's heating cap, a simple linear RT correlation was found to overpredict HS temperature of the CA50 sweep data. Further experiments revealed that not only the resistivity of the heating cap but also that of the inner electric leads is temperature-dependent. As a direct consequence, increasing HSI adapter temperatures increase the total resistance of the glow plug and cause a reduction of HS temperature if the voltage applied is kept constant. The fact that measuring the temperature of the glow plug tip directly during engine operation was not possible encouraged the development of an enhanced HS temperature model. It accounts for varying glow plug body

temperatures by including a linear dependency between adapter temperature and the resistance of the inner leads, and was expected to give more realistic results in the experiments presented in the next chapter.

7 Experimental Results

Improvements in HSI controller design, the ability to control the operating conditions of the test bed and the substantial findings from the preliminary trials were the basis for conducting the experiments presented in this chapter. Optimising the HSI controller in terms of hardware and tuning parameters allowed for smooth engine start and robust temperature control during engine operation. In consideration of the ignition system's high sensitivity to varying thermal conditions, temperature conditioning and ensuring that all measurable dependent non controllable factors from Table 5.2 (e.g. intake manifold and oil temperature) reached steady-state conditions prior to recording an operating point was essential for acquiring reproducible data. With respect to the independent non-controllable factors, humidity, fuel composition and exhaust back pressure were monitored constantly but showed only marginal variance. Following the chart from Figure 7.1, the primary goals of the experimental work presented in this chapter are to:

1. Identify the limits of HSI operation in screening trials (Section 7.1).
2. Asses and analyse glow plug degradation that manifested during the series of measurements (Section 7.2).
3. Analyse the individual effect of adjustable engine operation parameters to the characteristic parameters of HSI operation in OFAT experiments (Section 0),
4. Comprehend which individually adjustable engine operation parameters are statistically significant over the entire HSI engine operation map in RSM experiments (Section 7.4).
5. Determine if HSI is a feasible alternative to state-of-the-art prechamber spark ignition (Section 7.5).
6. Derive possible improvements for future developments (Section 7.6).

The adjustable parameters or factors chosen to study HSI operation are given by all independent controllable factors of the test bed shown in Table 5.2, with exception of the EGR rate. Therefore, a total of 5 individually adjustable variables were investigated:

- Intake manifold pressure p_{man}
- CHP coolant inlet temperature $T_{coolant}$
- CHP intake air temperature T_{intake}
- Relative air-fuel ratio λ
- Combustion phasing CA50

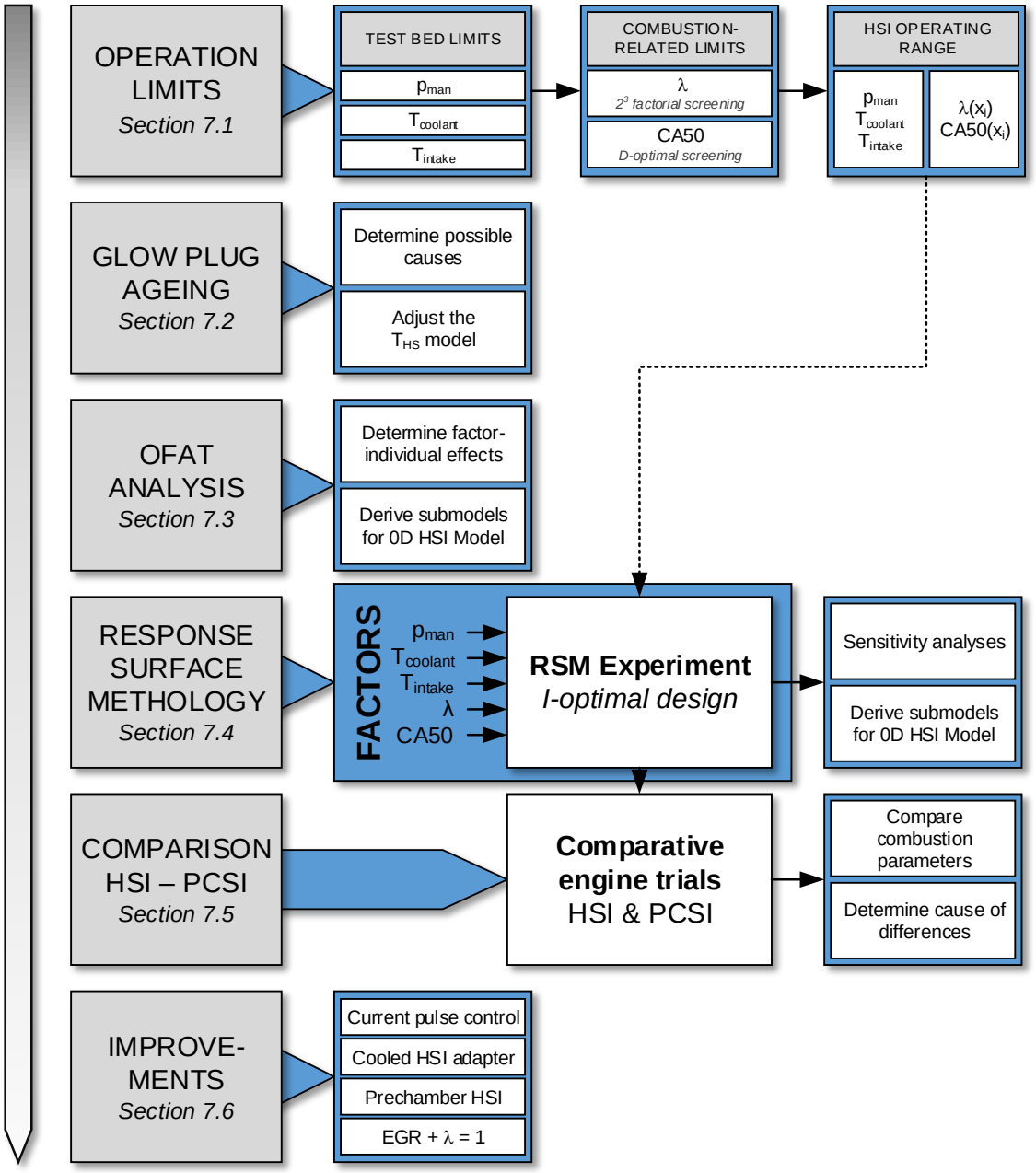

Figure 7.1: Workflow of investigations presented in Chapter 7.

7.1 Operation Limits

A prerequisite for conducting engine map experiments using the response surface methodology (RSM) based on computer-generated optimal designs is knowing the permissible range of all input factors. p_{man}, $T_{coolant}$ and T_{intake} can be set independently and their limits solely depend on the technical specifications of the test bed and the employed actuators. The limits were determined initially using the series ignition system and set to $p_{man} = 500 - 950$ mbar, $T_{coolant} = 25 - 65$ °C and $T_{intake} = 25 - 45$ °C. $p_{man} = 950$ mbar was chosen as upper limit for the following reason: At wide open throttle, the pressure drop from the CHP unit's intake (p_{man}) and the intake manifold is about 28 mbar. Since natural gas pressure is controlled relative to the ambient by a zero pressure regulator, when setting $p_{man} > 952$ mbar (forced induction) on days with minimum ambient pressure ($p_{amb} \approx 980$ mbar), the pressure difference at the Venturi of the gas mixer would not suffice to supply enough fuel for $\lambda = 1$ operation. This means that none of the subsequent operation points were recorded at wide open throttle (WOT).

The limits of the remaining factors, λ and CA50, are more complex as they are directly linked to the thermodynamic state of the in-cylinder charge and the processes of mixture ignition and combustion. The following two subsections describe the screening experiments run to determine the lower and upper limits as a function of p_{man}, $T_{coolant}$ and T_{intake}.

7.1.1 Relative Air-Fuel Ratio λ

In order to determine the range of λ in which stable HSI operation is possible, a randomised two-level full factorial screening with p_{man}, T_{intake} and $T_{coolant}$ as continuous factors was conducted. Each factor was set to its low (-1) and high (1) level, yielding a total of 8 parameter combinations and 16 runs (λ_{min} and λ_{max} for each combination). Figure 7.2 depicts the investigated 3 dimensional experimental space, where each vertex represents a tested factor combination. If possible, CA50 was set to 5 °CA ATDC by adjusting R_{HSI}. While this particular combustion phasing is neither optimal with regard to IMEP nor NO_x, it was chosen due to the relatively low cyclic combustion variations, particularly in terms of σ_{CA50}. For most lean operating points at the lean-burn limit (LBL), a transition to *section 2* with premature mixture inflammation was observed (see also Chapter 6.1), therefore impeding advanced combustion phasings. For these operating points, CA50 was set to the earliest possible crank angle, thus representing the transition from *section 1* to *section 2* ($R_{HSI,trans}$). The arbitrarily chosen LBL criteria was $COV_{IMEP} = 10$ %.

The experiments showed that stoichiometric HSI operation is possible for all tested combinations and λ_{min} is, therefore, not dependent on any other factor. Note that operation at $\lambda < 1$ was not considered. The controller proved very robust and capable of keeping

HS temperature constant, in spite of the increasing heat input from combustion when increasing the mixture strength. However, the screening revealed one limitation of the test bed: When both manifold pressure and coolant temperature are at their high level (1), exhaust gas, oil, casing and coolant outlet temperatures reach critically high values above those permitted without harming the engine and its components. In subsequent trials, coolant temperature was thus limited to 60 °C.

Factor	Low level (-1)	High level (1)
A: T_{intake}	25 °C	45 °C
B: p_{man}	500 mbar	950 mbar
C: $T_{coolant}$	25 °C	65 °C

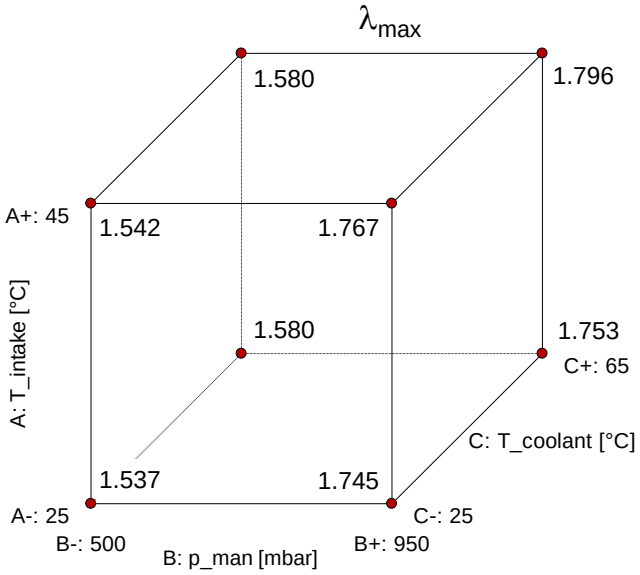

Figure 7.2: 3 dimensional design space showing λ_{max} for all recorded parameter combinations.

Each vortex of the cube in Figure 7.2 depicts the corresponding value of λ_{max}, i.e. the lean-burn limit (LBL). The analysis of variance (ANOVA) of the factorial model gives an F-value of 118.99, implying that the model is significant and there is only a 0.02 % chance that an F-value this large could occur due to noise. The p-values shown in Table 7.1 help assessing which model terms are most and least significant: while p_{man} appears to be very significant, $T_{coolant}$ is somewhat significant and T_{intake} not significant at all. The weak impact of intake temperature on HSI operation can be explained by the specific CHP unit design: The flow path between the CHP's admission, where T_{intake} is measured, and the engine's intake manifold is approximately 2000 mm long and acts as a heat exchanger for the inflowing air-fuel mixture. Due to the casing that surrounds the engine and all of its components, all ducts show faily similar temperature levels close to that of the air inside the casing itself (T_{casing} = 61 – 89 °C, depending on the operating point). The effect of T_{intake} becomes most noticeable when mass flow is high, i.e. at high intake manifold pressures, and casing temperature is low. On the contrary, a decreasing mass-flow lengthens the retention time of the mixture inside the ducts, allowing for an enhanced heat transfer to the mixture (see Section 7.4.1.1 for detailed explanation). As a result, the effect of inlet temperature on T_{man} is almost diminished and T_{man} mostly depends on casing temperature. Despite the evident effect at high intake manifold pressures, it was decided to treat T_{intake} as a trivial factor, which not only allow removing it from the model to determine λ_{max} but also as a parameter for subsequent CA50 screen-

ing experiment, thus helping to reduce the number of runs considerably.

Table 7.1. Analysis of Variance of λ_{max} screening.

Source	Sum of Squares	df	Mean Square	F-value	p-value	
Model	0.087	3	0.029	118.99	0.0002	significant
A-T_intake	4.500E-004	1	4.500E-004	1.85	0.2450	not significant
B-p_man	0.084	1	0.084	347.93	< 0.0001	significant
C-T_coolant	1.741E-003	1	1.741E-003	7.17	0.0554	slightly significant
Residual	9.710E-004	4	2.428E-004			
Cor Total	0.088	7				

Assuming that all dependencies are linear, the upper limit of the relative air-fuel ratio λ_{max} to be used for planning the RSM experiments can be calculated through linear regression from the ANOVA using Eq. (7-1). As illustrated in Figure 7.3, increasing manifold pressures and coolant temperatures have an enhancing effect on the lean-burn limit.

$$\lambda_{max} = 4.567 \cdot 10^{-4} \cdot p_{man} + 7.375 \cdot 10^{-4} \cdot T_{coolant} + 1.298 \tag{7-1}$$

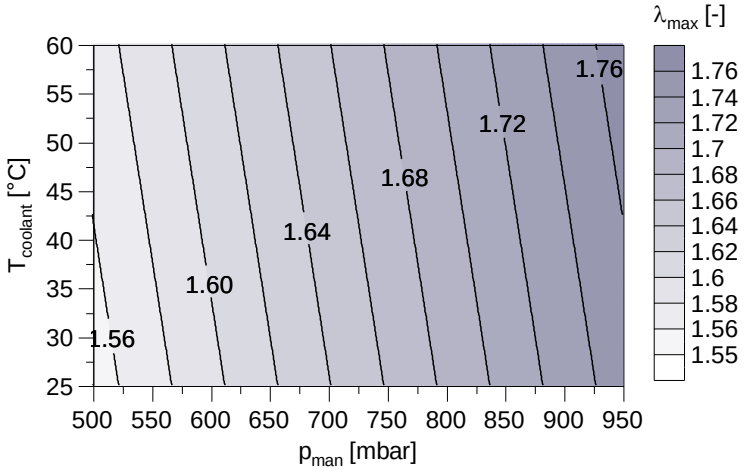

Figure 7.3: λ operation limits of HSI as a function of intake manifold pressure p_{man} and engine coolant temperature $T_{coolant}$.

7.1.2 Combustion Phasing CA50

After deriving the formula constraint for λ_{max}, a D-optimal RSM screening for defining the limits in terms of combustion phasing CA50 as a function of p_{man}, λ and $T_{coolant}$ was conducted. The experimental design comprised 10 model and 5 additional lack-of-fit points, capable of detecting interactions and quadratic correlations. As both limits, $CA50_{min}$ and $CA50_{max}$, needed to be found, a total of 30 runs were recorded. In the subsequent evaluation of the acquired experimental data it was found that neither of the models were statistically significant, indicating that the limits were too complex to be adequately described by quadratic functions. Nevertheless, the screening revealed that when operating at relative air-fuel ratios below λ_{max}, combustion phasings at and before TDC could always be set ($CA50_{min} \leq 0$ °CA ATDC). For operating points close to the lean-

burn limit, on the other hand, only more retarded values $CA50_{min}$ were possible. To either side, adjusting R_{HSI} would only retard combustion further, hence representing the transition point from regular *(section 1)* to premature mixture ignition *(section 2)* - $R_{HSI,trans}$. Highest values for $CA50_{max}$ of 15 – 20 °CA were achieved in the middle of the investigated λ range and at low to moderade pressures. HSI operation was particularly limited for high pressures and stoichiometric combustion, where stable engine operation beyond CA50 ≈ 8 °CA ATDC was not possible due to occasional misfires.

Despite providing important insights, the screening did not give all constraints required to formulate simple equations to describe the CA50 operating range mathematically. With the objective of determining $CA50_{min}$ and $CA50_{max}$ as a function of p_{man} and λ, two more series of experiments with a higher resolution of measuring points were conducted. The effect of $T_{coolant}$ on the combustion process was found to be marginal and was therefore removed as a factor and held constant at 45 °C. Likewise, T_{intake} was set to 35 °C.

7.1.2.1 Determination of $CA50_{min}$

The procedure for determining $CA50_{min}$ close to the lean-burn limit at constant p_{man} = 500/750/950 mbar was the following:

1. Find the relative air-fuel ratio that exhibits the transition from *section 1* to *section 2* at CA50 = 0 °CA ATDC. This is the case when neither an increase nor a decrease of R_{HSI} advances combustion further ($R_{HSI} = R_{HSI,trans}$).
2. *Record the operating point.*
3. Increase λ stepwise and increase R_{HSI} so that the condition $R_{HSI} = R_{HSI,trans}$ remains true.
4. *Record the operating point.*
5. Repeat steps 3-4 until the misfire limit is reached.

Each point obtained following this procedure represents the earliest combustion phasing at which the engine can operate without premature mixture ignition at a given relative air-fuel ratio and manifold pressure. Overadvanced combustion phasings before TDC were not investigated as most heat release would occur during the compression stroke opposed to piston motion, leading to increased pressure-volume work, poor IMEP and ISFC and a significant increase in NO_x. Figure 7.4 (left) depicts the results of the series of experiments. $CA50_{min}$ appears to be a linear function of λ for all intake pressure levels. Judging from the fairly constant gradient for the polynomial regressions, it is highly unlikely that $CA50_{min}$ would depend on p_{man} and λ on a higher order than 2. Therefore, all experimental data were used to calculate the ANOVA for a quadratic model shown in Table 7.2. When not significant terms form part of the model, as it is the case in Table 7.2, the model becomes over-fitted and tries to predict model response when factors AB and B^2 change, in spite of actually not having any influence. When removing them, the F-value and the R^2_{pred} of the reduced quadratic model increase and $CA50_{min}$ can be ex-

pressed as a function of the significant terms as a second order polynomial. Including the quadratic term for p_{man} increases prediction accuracy in the middle of the investigated intake pressure range. However, the employed DoE software Design Expert only allows the user to introduce multiple linear constraints (MLC). For this reason, the model was reduced to the first order polynomial shown in Eq. (7-2):

$$\mathrm{CA50}_{min} = -5.628 \cdot 10^{-2} \cdot p_{man} + 150.432 \cdot \lambda - 202.981 \tag{7-2}$$

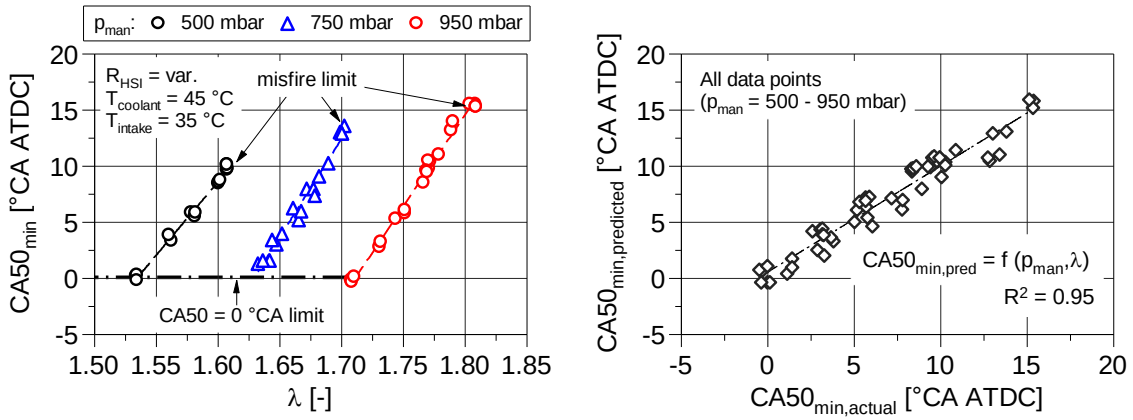

Figure 7.4: Lower combustion phasing limit $CA50_{min}$ as a function of λ and p_{man} (left) and predicted versus actual values of $CA50_{min}$ using the linear regression model from Eq. (7-2) (right).

The scatter plot in Figure 7.4 (right) lays out predicted against actual $CA50_{min}$ for all recorded data points using Eq. (7-2). The maximum absolute error is below 2 °CA and is deemed sufficiently accurate for describing the lower CA50 limit.

Table 7.2: Analysis of Variance (ANOVA) of quadratic $CA50_{min}$ model

Source	Sum of Squares	df	Mean Square	F-value	p-value	
Model	1036.79	5	207.36	617.73	< 0.0001	significant
A-p_man	446.12	1	446.12	1329.02	< 0.0001	significant
B-Lambda	618.43	1	618.43	1842.34	< 0.0001	significant
AB	3.257E-003	1	3.257E-003	9.703E-003	0.9219	not significant
A^2	2.47	1	2.47	7.37	0.0092	significant
B^2	0.17	1	0.17	0.50	0.4833	not significant
Residual	16.11	48	0.34			
Lack of Fit	15.98	47	0.34	2.63	0.4596	not significant
Pure Error	0.13	1	0.13			
Cor Total	1052.90	53				

7.1.2.2 Determination of $CA50_{max}$

A very similar strategy was followed to determine the limit of CA50 to the upper end, $CA50_{max}$: Start at λ = 1 and CA50 = 0 °CA ATDC and increase λ stepwise, setting the latest possible CA50 without misfires by reducing R_{HSI} for each recorded operating point.

As shown in Figure 7.5, $CA50_{max}$ shows a strong and non linear dependency of p_{man} and λ. Starting from stoichiometric combustion, leaning the mixture leads to a moderate but

gradual increase of $CA50_{max}$ at both low and medium intake manifold pressure (p_{man} = 500/750 mbar) and, therefore, to an enhancement of the operating range. The only significant differences lie in the not surprising enhanced lean-burn limit for medium pressure, and the increased values for $CA50_{max}$ at $\lambda \geq 1.4$. At high pressure (p_{man} = 950 mbar), on the other hand, an entirely different behaviour is observed: Up to $\lambda = 1.4$, $CA50_{max}$ is limited to around 8 °CA ATDC, to then increase gradually until the lean-burn limit is reached. Reducing R_{HSI} in an attempt to retard combustion further proved to cause occasional misfires. These misfiring cycles showed no detectable combustion radiation and there was no apparent determinism respective to the preceding cycle. To illuminate these different tendencies in function of intake manifold pressure, combustion data is subsequently analysed with regard to similarities and differences in the combustion process.

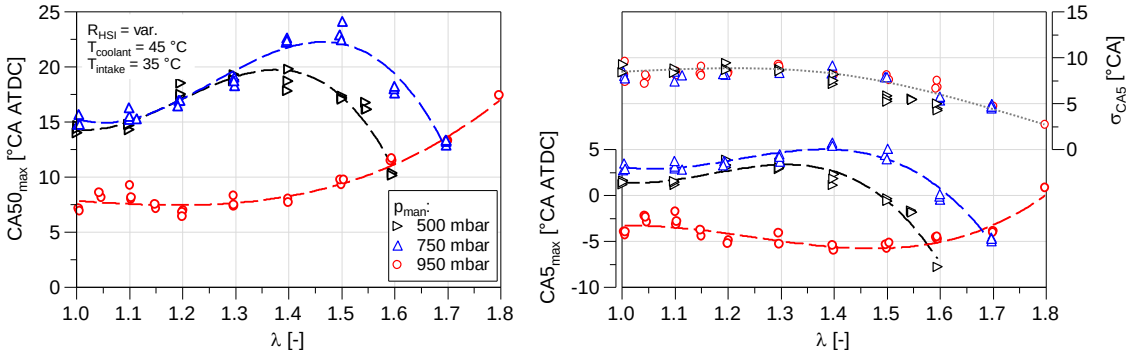

Figure 7.5: Upper combustion phasing limit $CA50_{max}$ as a function of λ and p_{man}.

In terms of similarities, the right plot in Figure 7.5 reveals that all operating points at the $CA50_{max}$ limit show very similar cyclic variations in CA5. In the range $\lambda = 1.0 - 1.4$, σ_{CA5} is fairly constant with values around 8 °CA. With further leaning, combustion stability is improved, enabling values of σ_{CA5} as low as 2.5 °CA for maximum mixture dilution. In terms of differences, throttling generally slows down the combustion process, primarily as a result of the increasing residual gas fraction and reduced combustion temperatures [12]. To compensate for the longer combustion duration and keep combustion phasing constant, the start of combustion needs to be advanced by increasing HS temperature. This is illustrated qualitatively in Figure 7.6, where the pre-reaction state I_{pr}, calculated using Eq. (2-8), and the according pressure traces are plotted against crank angle for p_{man} = 500/750/950 mbar. Temperature in the boundary layer was approximated by $T = (T_{cyl} + T_{HS})/2$, where T_{cyl} represents the temperature of the in-cylinder charge. According to Gorenflo [59], the main cause of CCV in premixed combustion are spatial inhomogenieties in mixture composition during the process of mixture inflammation. If this reasoning is applied to the computed ignition delays in Figure 7.6, given by the condition $I_{pr} = 1$, the following conclusions concerning the effect of load on combustion stability at constant combustion phasing can be made:

– As the ignition delay needs to be increased with load by reducing T_{HS}, the time during which pre-reactions are exposed to the stochastic nature of the flow inside the

shield volume is increased.

- As T_{HS} is lowered, its relative impact on ignition delay is reduced, making ignition delay more susceptible to cyclic variations in local mixture temperature (T_{cyl}) and composition.
- As the start of combustion moves closer to TDC, the gradient of I_{pr} becomes increasingly smaller due to the only minor changes in the thermodynamic state of the mixture in terms of pressure and temperature, and therefore the rate of pre-reactions. As a direct consequence, small gradient changes will result in a considerable shift of the start of combustion.

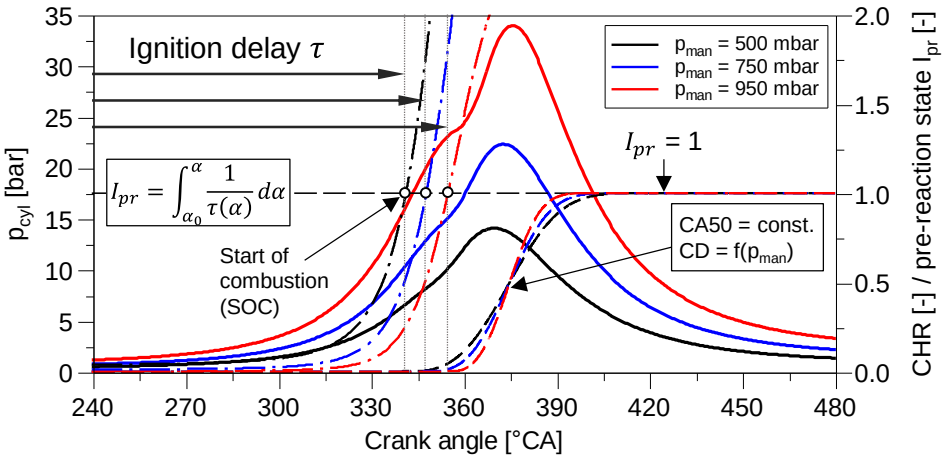

Figure 7.6: Simulated in-cylinder pressure p_{cyl}, pre-reaction state I_{pr} and cumulative heat release (CHR) traces for p_{man} = 500/750/950 mbar.

The three points mentioned do not only explain why the scatter range of mixture ignition timing increases with intake manifold pressure, but also why the scatter range is smallest for advanced combustion phasing and increases as combustion is retarded (compare Figure 3.7). Nevertheless, two open questions remain: 1. What causes misfires when operating beyong the limit of $CA50_{max}$ for low and medium load, and 2. Why $CA50_{max}$ is significantly lower in the range $\lambda = 1.0 - 1.5$ for $p_{man} = 950$ mbar despite showing more advanced values of CA5. A crucial aspect when addressing question 1, is that CA5, and therefore SOC, are very close to TDC when operating at the $CA50_{max}$ limit. The high values for σ_{CA5} imply that some cycles start burning long after TDC. As the piston moves downwards during the expansion stroke, the production rate of radicals required to induce ignition are lowered, leading to a more sluggish increase of I_{pr}, thereby causing longer ignition delays. If ignition delay times are too long they will either not give sufficient time for the entire mixture to combust prior to EVO (partial burns) or not ignite the mixture at all ($I_{pr} < 1$, misfires), this being the primary factor limiting late combustion phasing at low and medium load. In fact, the same rationale yields the answer to question 2: The need for retarding the start of combustion at high intake manifold pressure and fuel-rich mixtures by lowering T_{HS} and increasing the ignition delay enhances the risk of misfiring cycles. The ignition process becomes more sensitive to inhomogeneities in mixture composition and, in particular, to individual cycles where the mixture

shows poor ignition quality and may impede a timed mixture inflammation (e.g. higher fraction of residual gas in the shield volume). To allow stable engine operation without misfires it is therefore necessary to reduce the ignition delay and advance the start of combustion by increasing HS temperature, giving the reason why the $CA50_{max}$ limit at $\lambda = 1.0 - 1.5$ is lower at high intake manifold pressure.

7.1.2.3 Conclusions for RSM trials

The two previous sections revealed that $CA50_{min}$ can be easily expressed as a function of intake pressure and λ, see Eq. (7-2), while deriving a similar correlation for $CA50_{max}$ was not possible due to the complex interaction of chemical kinetics and cycle-by-cycle variations in mixture composition and temperature inside the shield volume. At the time of building the RSM design, it was therefore decided to adopt a constant limit of $CA50_{max} = 15$ °CA ATDC, a valid constraint for most input combinations. This approach has two main impacts:

- Areas where the engine can operate at more retarded combustion phasings will not be considered. Hence, the resulting polynomial correlations might not be suitable for describing HSI operation at CA50 > 15 °CA ATDC.
- For high intake manifold pressure, the DoE software may suggest runs with combustion phasings that cannot be set without misfires. CA50 will have to be advanced during the experiments and the factor change will be accounted for in post-processing, although manually changing parameters of an existing design entails the risk of reducing prediction quality.

7.2 Glow Plug Ageing

While conducting the engine trials presented in the following sections, it appeared that the HSI resistance required to start the engine kept increasing from one day to another. After post-processing the recorded data, the direct comparison of operating points with similar settings provided proof that, in fact, the set resistance for an adequately phased combustion had to be raised by up to 75 mΩ. According to the manufacturer, the operating temperature of the glow plug can decrease up to 40 K over its life time. Using the mean RT gradient from glow plugs No. 1 – 10, $a_{mean} = 2.07$ K/mΩ, and assuming that only the heating cap is affected by the ageing process, normal degradation would result in an absolute resistance change of about 19 mΩ. Based on this comparatively small expected change, combined with the short period over which glow plug degradation manifested in the experiments (ca. 40 h), normal thermal degradation can be ruled out as the principal cause for the resistance increase. In order to get to the bottom of this phenomenon, it is worth examining the different operating conditions of the glow plug when used as part of an HSI system to those in conventional Diesel applications:

- For HSI, the glow plug is powered constantly rather than only for limited time during

cold start. The permanently high surface temperature may induce diffusion processes in the heating layer (e.g. formation of silicon oxides on the glow plug tip) that change its resistivity.

- The glow plug is not mounted directly inside the engine block but inside the HSI adapter. As a result, cooling of the glow plug body is reduced, leading to higher temperatures along the glow plug body.
- The single-cylinder engine is subject to more vibration, particularly during engine start and stop. In combination with high temperature environments, this may produce higher structural stress on the inner components of the glow plug.

During the first experiments with voltage control, the glow plug had to be operated at extremely high temperatures to enable stable engine operation, which lead to several cases of overheating. On the one hand, glow plug body overheating manifested in partial or complete melting of the polyamide (PA) insulating bush which, however, did not necessarily provoke a glow plug failure. Glow plug pin overheating, on the other hand, would cause the heating cap layer to melt, form bubbles, and eventually lead to a total failure of the component ($R \to \infty$). After the development of the resistance controller and enhancing the HSI operation window, both types of overheating could be fully avoided. Nevertheless, it was found that the glow plug part formed by the push-on connector and the inner metallic lead exhibited an increasing play respective to the glow plug body after several hours of HSI operation. For a new glow plug, the inner positive metallic lead and the glow plug body form a tight crimped insulated connection. It seems reasonable to assume that a loosened crimping would go along with an increased contact resistance between the inner metallic and ceramic electric leads. In consequence, more electric energy would be dissipated, the glow plug's total resistance would increase, thus changing it thermo-electric behaviour. This intrinsic phenomenon of the HSI system in its current design stage sets limits to the comparability of electric properties during engine operation, such as resistance or electric power, when comparing operating points from different series of experiments or even within the same series lying hours apart. Despite otherwise identical operating conditions (ambient conditions, engine temperatures, fuel composition, air-fuel ratio, combustion phasing…), the required glow plug resistance and power to operate the engine is likely to change in the course of an experiment. For the subsequent discussion of results, Eq. (6-1) is therefore augmented by a resistance term that accounts for glow plug ageing, R_{ageing}, calibrated using operating points with identical or, if not available, similar factor settings. HS temperature is then calculated according to Eq. (7-3):

$$T_{HS} = \frac{1}{a_{HC}}\left[R_{HSI} - R_0 - R_{ageing} - a_{leads} \cdot \left(T_{adapter} - T_0\right)\right] + T_0 \tag{7-3}$$

7.3 Individual Factor Influence

In light of the aforementioned screening trials from Section 7.1, it became evident that some factors needed to be examined more in detail to understand what system responses are caused by the ignition system and which are inherent to the particular test bed configuration. For this purpose, a classic OFAT analysis of all factors was performed prior to conducting the RSM experiments. The series of measurements, where every factor was set to several levels while keeping all others constant, was run chronologically in the order CA50, λ, p_{man}, $T_{coolant}$, T_{intake} with the same glow plug (No. 5, preaged condition), using the optical adapter from Figure 5.4. Every factor setting was recorded in three consecutive times, with combustion data being recorded for 200 cycles and slow data averaged over 30 s.

Due to the recessed position of the sapphire, the optical access to the HSI shield became blocked with deposits over time, thus diminishing the transmission efficiency of the optical measurement chain and gradually reducing the level of detected radiation by the photomultiplier. The detected visible radiation stemming from the hot surface can therefore not be used as a reliable indicator for HS temperature when comparing experiments conducted with significant time offset in between. Nevertheless, Eq. (7-3) allows determining T_{HS} based on the recorded total resistance R_{HSI} and adapter temperature $T_{adapter} = T_{adapter,front}$. Glow plug degradation was accounted for by adjusting the resistance offset R_{ageing}. For the first variation (CA50 sweep), a value for R_{ageing} was assumed, based on the RT experiments from Section 6.3. In subsequent variations, similar operating points that were expected to show same T_{HS} were used to calibrate R_{ageing} so that Eq. (7-3) would yield the same value for T_{HS}. Following this procedure, Table 7.3 shows calculated R_{ageing} for each sweep conducted in chronological order, showing a clear glow plug degradation trend over time. For simplicity, a single correction offset was applied to the entire data set of each sweep.

Table 7.3: Correction offset R_{ageing} employed to calculate T_{HS} for the OFAT analysis of the main influencing factors (glow plug No. 5, preaged, total experimental time from day 1-4: 40 h).

		R_{ageing} [mΩ]
Day 1	CA50 sweep	92
Day 2	λ sweep	99
	p_{man} sweep	
Day 3	$T_{coolant}$ sweep	136
Day 4	T_{intake} sweep	168

7.3.1 Effect of Combustion Phasing

The effect of combustion phasing was determined at $p_{man} = 950$ mbar, $\lambda = 1.70$, $T_{coolant} = 60$ °C and $T_{intake} = 22.5$ °C by varying the set resistance of the HSI control-

ler. A total of 7 parameter settings were recorded with set values of CA50 in the range 0 – 15 °CA ATDC. The CA50 sweep was conducted in a time frame of 90 min and glow plug degradation effects did not appear to be significant. Figure 7.7 lays out selected measured and calculated parameters plotted against CA50:

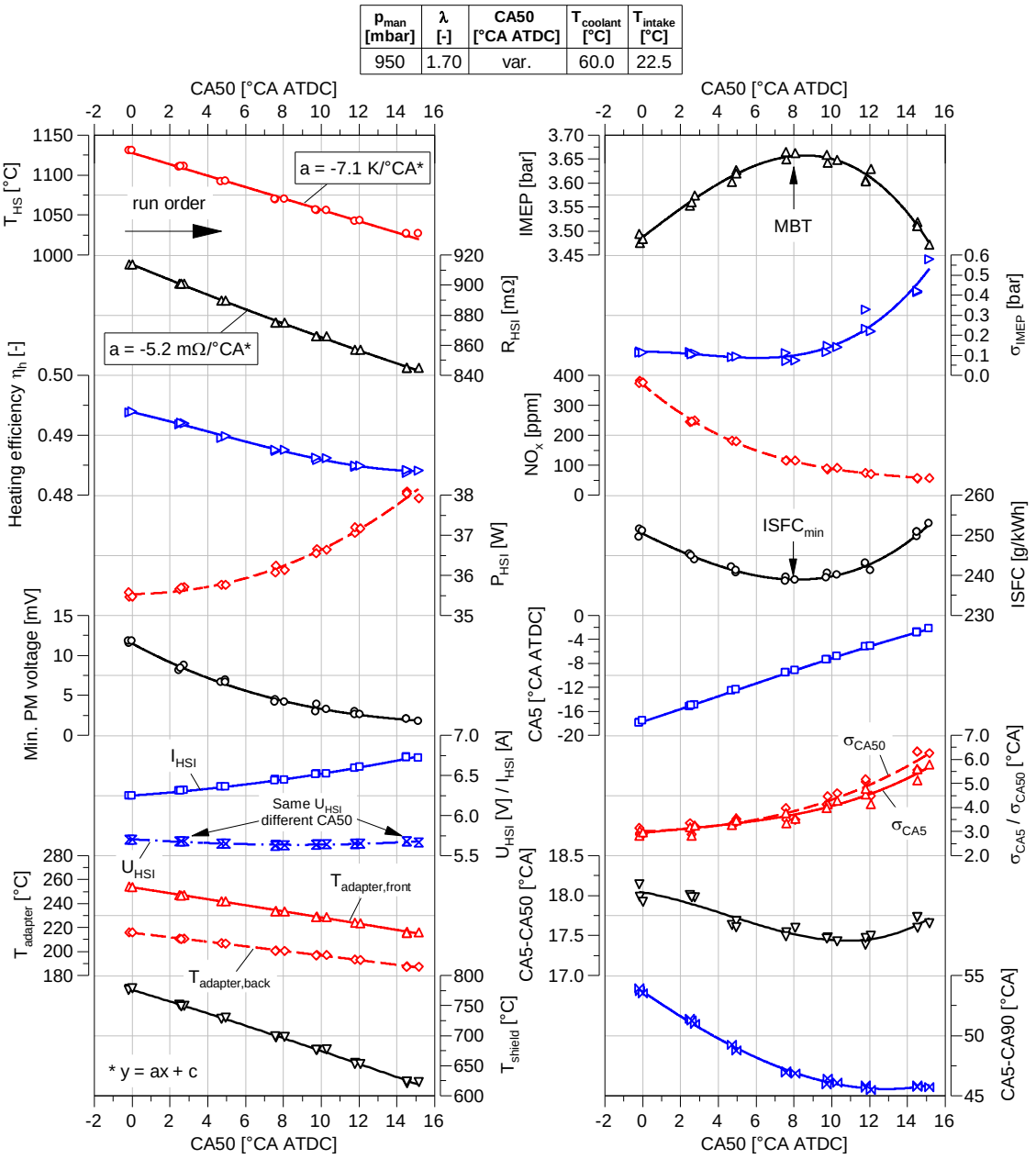

Figure 7.7: Selected experimental data against combustion phasing CA50 (glow plug No. 5).

As expected, hot surface temperature T_{HS} needs to be raised by increasing the set value for R_{HSI} in order to advance combustion phasing. As a direct consequence of increasing combustion temperatures, indicated by T_{shield} and the emitted NO_x, and the gains in convective heat input from combustion to glow plug and HSI adapter, $T_{adapter,front}$ increases by about 38 K from latest to earliest CA50 ($a \approx 2.5$ K/°CA). This causes an only moderate increase of the resistance of the inner electric leads of the glow plug ($\Delta R_{leads} \approx 27$ mΩ), leading to an almost linear relationship between R_{HSI} and T_{HS}. The

ensemble-average minimum photomultiplier voltage detected during the engine cycle shows a trend akin to the monotone and fairly linear correlation between CA50 and R_{HSI} and T_{HS}, but is of higher order, as expected from the proportionality $P_{rad} \sim T^4$. All three traces combined give proof that increasing HS temperature does, in fact, shorten ignition delay and advance the start of combustion (see also CA5 trace) and, in turn, combustion phasing. According to the gradient of the T_{HS}-CA50 correlation, T_{HS} needs to be increased by about 7 K to advance combustion phasing by 1 °CA, equivalent to an adjustment of about 5 mΩ in R_{HSI}.

Another essential dependency is given by the trace of the electric power P_{HSI}. Despite the increasing HS temperature required to advance combustion phasing, P_{HSI} shows a distinc downward trend. As mentioned previously, the electric power required to maintain HS temperature at a specific level solely depends on the heat losses from the glow plug pin by conduction and radiation and the convective heat exchange between the pin and the mixture. The enhanced heat gains from combustion allow for the thermal energy provided by Joule heating in the heating cap region (P_{HC}) to be reduced in spite of raising HS temperature levels. As the reduction of P_{HC} outweighs the increase in P_{leads} caused by the raised adapter temperatures, total electric power P_{HSI} can also be reduced. As a matter of fact, increasing losses in the leads are not necessarily detrimental to the power required to operate the HSI system: As the losses are dissipated in the glow plug in the form of heat, its temperature is increased, thus reducing the driving temperature difference for heat conduction between glow plug tip and HSI adapter. This may explain the slight increase in heating efficiency (see definition in Eq. (4-4)) at advanced CA50.

The plot of U_{HSI} reveals why controlling HSI resistance should be chosen over controlling HSI voltage, even when cyclic variability in the combustion process is low: In spite of a significant change of HS temperature over the whole CA50 range, the variation in U_{HSI} is marginal with less than 100 mV. In addition, HSI voltage exhibits a minimum around maximum IMEP, i.e. at maximum brake torque (MBT) combustion phasing, increasing slightly to either side. As a consequence, CA50 is not unambiguously defined by U_{HSI}, and the same set voltage may lead to combustion phasings either before or after MBT. This entails the risk that even small disturbances from cyclic combustion variations would shift combustion phasing from one stable operating point to the other. Maximum IMEP is found around 8 °CA ATDC, which agrees well with values reported in literature, e.g. [87]. Since the concave curve of ISFC also shows its minimum at same CA50, MBT combustion phasing should be set for maximum engine power and efficiency. Another fundamental finding of the CA50 sweep can be derived from the plots of standard deviation of CA50 and IMEP, two distinct statistical values employed to quantify CCV in combustion. Interestingly, σ_{CA50} increases steadily with retarding combustion phasing, while σ_{IMEP} is lowest at MBT and only increases significantly for more retarded combustion. As discussed before in Section 7.1.2.2, cyclic variations in combustion phasing augment as ignition delay increases and CA5 moves closer to TDC. In order to explain the

different trend for σ_{IMEP}, the entire ensemble (600 engine cycles) of three operating points at $CA50_{mean}$ = 0/8/15 °CA ATDC will be discussed next in detail.

The histograms of Figure 7.8 provide insights into how the recorded cycles are distributed in terms of cycle-individual CA50 and IMEP. While for CA50 = 0 °CA ATDC the histogram for CA50 is comparatively narrow and displays near normal distribution, it becomes broader as combustion phasing is retarded, as a result of the larger spread in CA50. Furthermore, at CA50 = 15 °CA ATDC it can be seen that the distribution stops being symmetrical and is skewed to the right (gamma distribution). From this it follows that a large number of cycles burn very late in the expansion stroke, thereby shifting the ensemble mean to 15 °CA while most cycles burn at about 12.5 °CA (frequency maximum). The histograms of IMEP shown below give a different picture: At MBT combustion phasing, the distribution is relatively narrow, leading to low calculated σ_{IMEP}. From this starting point, advancing combustion phasing leads to a moderate increase of cyclic variation, while retarding results in a major spread in IMEP.

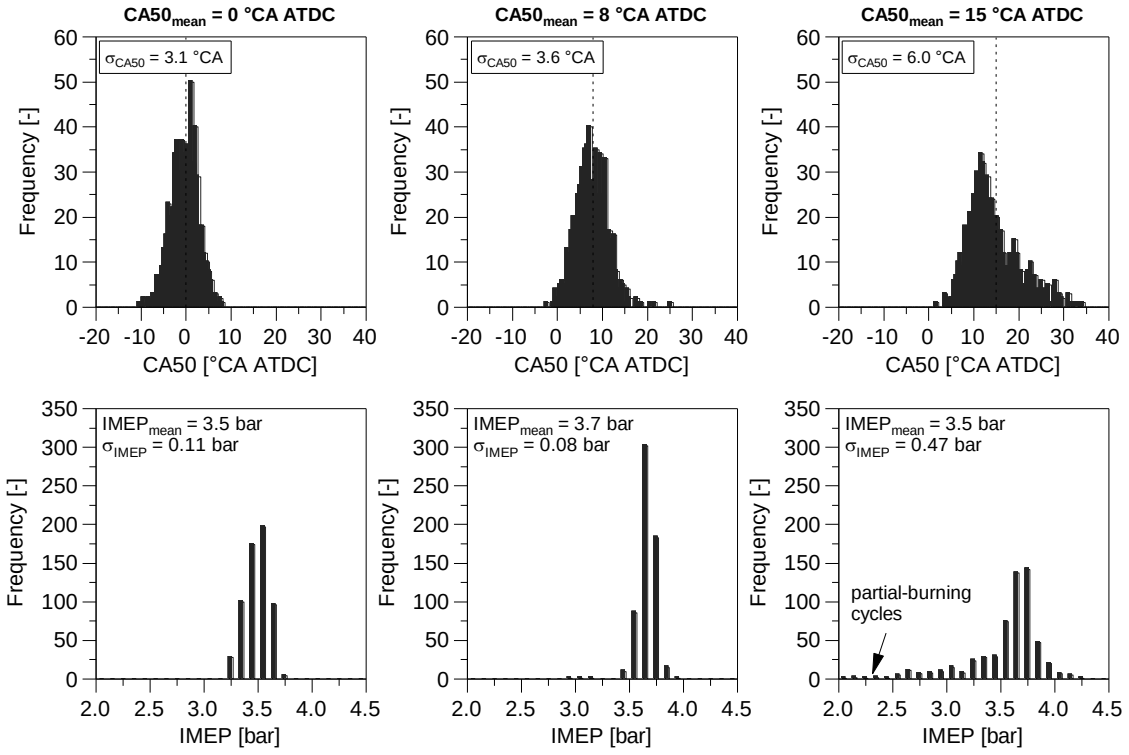

Figure 7.8: Histograms of CA50 (top) and IMEP (bottom) from 600 cycles for mean combustion phasing CA50 = 0/8/15 °CA ATDC (p_{man}= 950 mbar, λ = 1.70, $T_{coolant}$ = 60 °C, T_{intake}= 22.5 °C).

The scatter plot from Figure 7.9 (left), showing individual IMEP against CA50, gives an explanation why MBT combustion phasing exhibits lower variability in IMEP despite larger fluctuations in CA50. To avoid data overlapping, constant offsets were applied to the data sets of $CA50_{mean}$ = 0 and 8 °CA ATDC. While cycles with combustion phasing at about 8 °CA ATDC produce highest IMEP, the curvature of the IMEP response to CA50 around that maximum appears to be very small. As a consequence, IMEP is quite insensitive to cyclic variations in combustion phasing, and individual cycles that are ei-

ther advanced or retarded moderately respective to MBT all show a modest loss in IMEP. At CA50 = 0 °CA ATDC, on the other hand, overadvanced CA50 leads to most fuel to be depleted during the compression stroke, thus further decreasing IMEP, while late-burning cycles approach MBT and produce higher IMEP. The opposing signs lead to an increased variability in IMEP, despite operating at lower σ_{CA50} compared to MBT. The operating point at CA50 = 15 °CA ATDC exhibits a similar trend, yet to the other side. Nonetheless, the larger scatter range in combustion phasing, the steeper loss in IMEP as combustion is retarded and and numerous partial-burn cycles lead to almost fivefold levels of σ_{IMEP}.

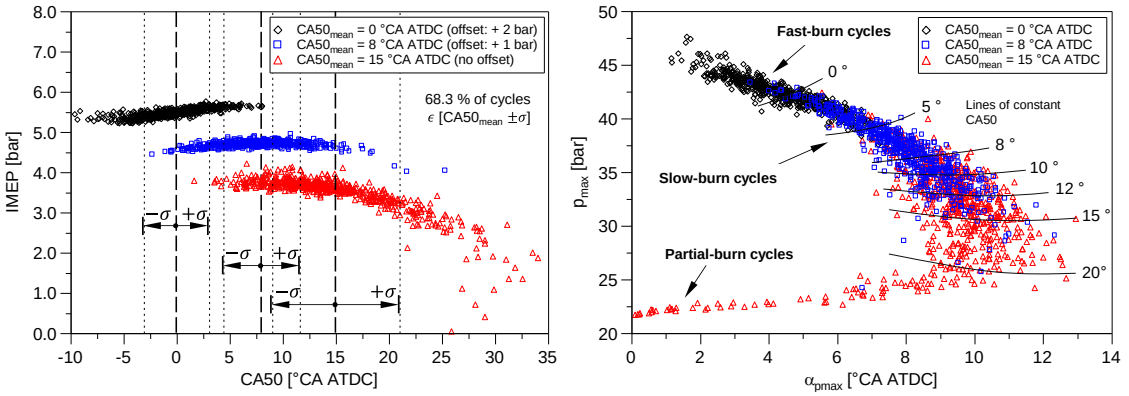

Figure 7.9: Cycle-individual IMEP versus combustion phasing CA50 (left) and cycle-individual peak-pressure p_{max} versus crank angle where it occurs α_{pmax} (right) for mean combustion phasing CA50$_{mean}$ = 0/8/15 °CA ATDC (p_{man}= 950 mbar, λ = 1.70, $T_{coolant}$ = 60 °C, T_{intake}= 22.5 °C).

The relationship between individual-cycle peak pressure p_{max} and the crank angle at which maximum pressure is recorded, α_{pmax}, illustrated in Figure 7.9 (right), shows another interesting dependency. Regardless of the operating point, the spread in α_{pmax} is increased with CA50. When following the lines of constant CA50, cycles to the left side have a slow-burning heat release profile, while those to the right are fast-burning ones. In fact, there is a direct negative correlation between the duration of the first part of combustion (CA5 – CA50) and the position of p_{max}. The increasing difference between fast- and slow-burning cycles as CA50 is shifted indicates that retarding the start of combustion increases cyclic variations in combustion duration.

From the 600-cycle ensemble with CA50$_{mean}$ = 15 °CA ATDC, individual fast-, slow- and a medium-burning cycles at same combustion phasing (15 °CA ATDC) were selected for the direct comparison in Figure 7.10. The plots of net rate of heat release prove what is evident: the reduced burn rate of the slow-burn cycle requires an earlier start of combustion and leads to longer overall combustion. The increase in combustion duration causes IMEP to fall off and, what is remarkable, results in higher levels of p_{max} due to the larger fraction of fuel burnt before TDC. Slow-burn cycles are therefore not only detrimental to engine power and efficiency but, as suggested by the higher peak pressure, also produce higher NO_x emissions. According to Figure 7.9 (right), however, this effect only occurs for late combustion phasing (CA50$_{mean}$ > 10 °CA ATDC).

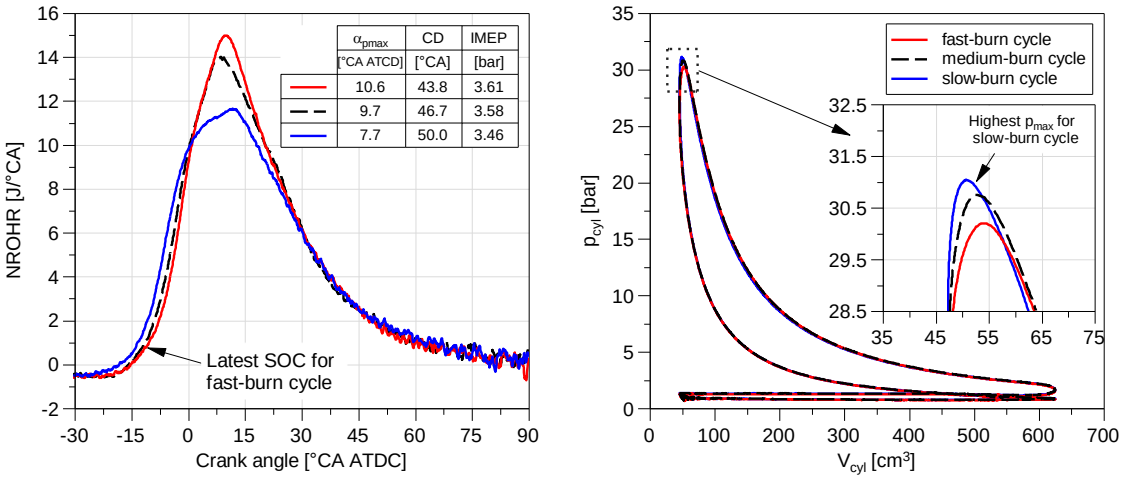

Figure 7.10: Net rate of heat release (NROHR, left) and pV diagram (right) and for individual fast-, medium- and slow-burn cycles all showing same CA50 = 15 °CA ATDC from 600-cycles ensemble with $CA50_{mean}$ = 15 °CA ATDC (p_{man}= 950 mbar, λ = 1.70, $T_{coolant}$ = 60 °C, T_{intake}= 22.5 °C).

7.3.2 Effect of Relative Air-Fuel Ratio

The influence of relative air-fuel ratio on ignition temperature and combustion parameters is reviewed at constant settings for p_{man} = 950 mbar, CA50 = 5 °CA ATDC, $T_{coolant}$ = 45 °C and T_{intake} = 23.0 °C. This particular combustion phasing, while not optimal in terms of IMEP and ISFC, was chosen due to the comparatively low cyclic combustion variability, even for stoichiometric mixtures. The plot of T_{HS} versus λ in Figure 7.11 indicates that the required HS temperature increases as the mixture is leaned out, a finding that agrees with the observations reported in literature [23, 118]. As suggested by the results determined via the analytical approach in Section 3.1.1, critical ignition temperature should decrease slightly as a function of λ, due to the increasing reaction rate. For constant combustion phasing, however, the timing of mixture ignition needs to be advanced by raising T_{HS} to account for the reduced laminar burning velocity.

In similar fashion to the effect of advancing combustion phasing, increasing mixture strength causes an almost linear increase of $T_{adapter}$. In the recorded range, $T_{adapter,front}$ increases by 88 K, causing an increase in R_{leads} of 62 mΩ and a drop in heating efficiency η_h from 51.1 to 42.2 %. Despite the higher losses of approximately 10 W, P_{HSI} can be brought down to 17 W at λ = 1.0, with only about P_{HC} = 7 W required to compensate for the overall heat losses of the glow plug tip to the surrounding due to convection, conduction and radiation. This substantial finding can be used to make predictions on the aptitude of controlled hot surface ignition at higher engine load (full load or supercharged) an/or increased compression ratios. Increasing heat gains from combustion warrant a decrease in the auxiliary power P_{HSI} required to sustain combustion. As the energy fed to the glow plug tip is reduced, the power reserve of the HSI controller, i.e. the maximum change in P_{HSI} from one controller event to another, is diminished. This is particularly problematic for cycles with overadvanced combustion phasing that cause a larger

temperature rise of the hot surface. To avoid premature mixture ignition in the subsequent cycle, P_{HSI} needs to be reduced rapidly to bring T_{HS} back to the set value. The restriction given by the fact that the glow plug can only be either powered or not, and not actively cooled, leads to settings where $P_{HSI} = 0$ may not suffice to counteract the temperature increase. The increased T_{HS} promotes the formation of chain carriers in the succeeding cycle, shortening the ignition delay and advancing combustion which, in turn, causes T_{HS} to rise even further. As a result, a runaway surface ignition with highly overadvanced heat release is induced, which, in a best-case scenario, leads to worsened engine efficiency and high emission output, and in a worst-case scenario, to knocking, overheating and engine failure.

p_{man} [mbar]	λ [-]	CA50 [°CA ATDC]	$T_{coolant}$ [°C]	T_{intake} [°C]
950	var.	5.0	45.0	23.0

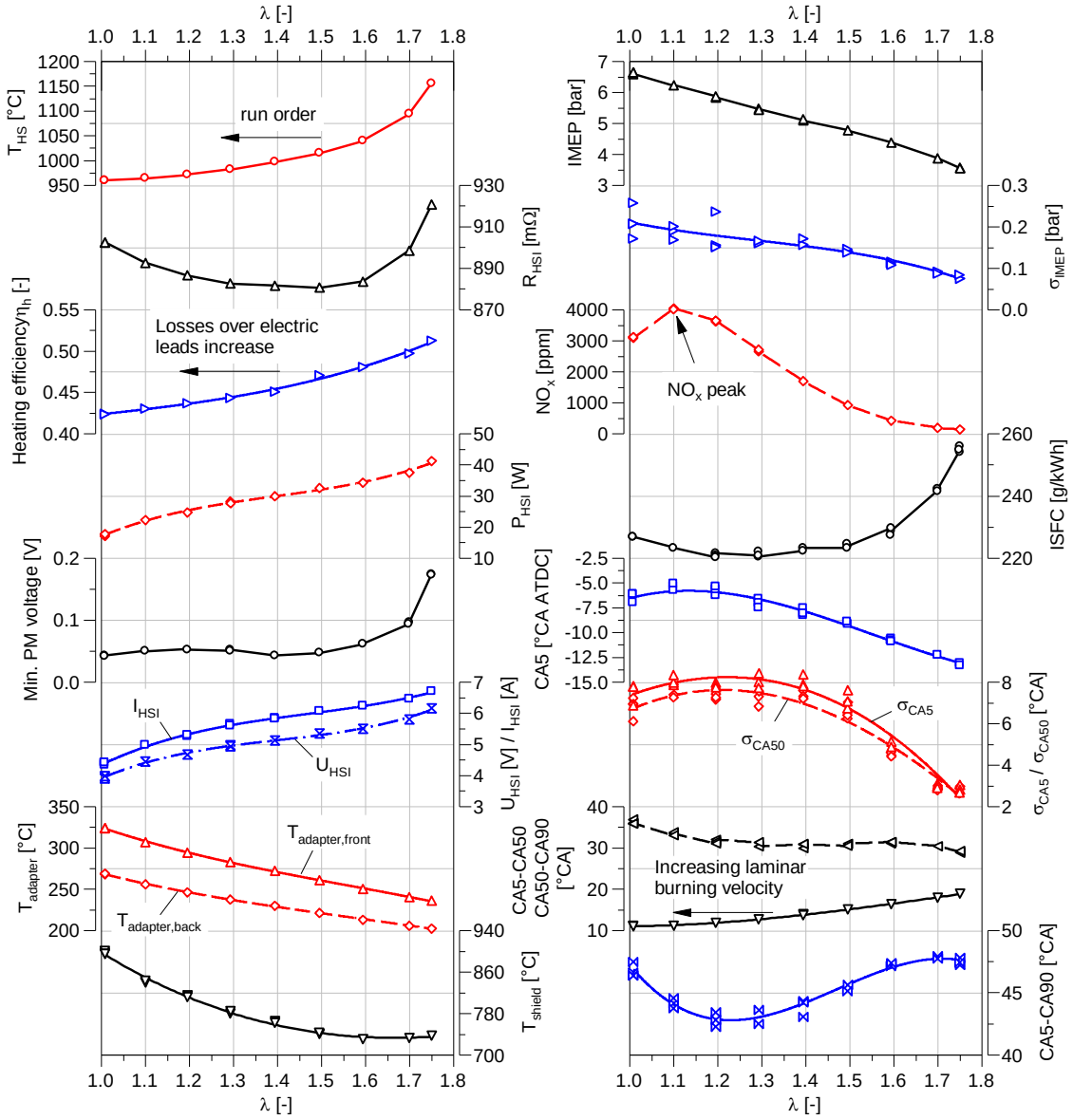

Figure 7.11: Selected experimental data against relative air-fuel ratio λ (glow plug No. 5).

It is true that P_{HSI} should be minimised for best overall efficiency. Nonetheless, even when assuming an ideal combustion without CCV, *passive* HSI, where heat gains and

losses balance out, should be avoided as the controller loses its ability to adjust combustion phasing. In consequence, controlled HSI operation becomes challenging, if not impossible, when the overall temperature level in the cylinder increases. However, this could be counteracted by several viable approaches, all aiming to increase P_{HSI} and avoid passive HSI:

- Active cooling of the HSI adapter to enhance conductive heat losses.
- Reduction of the protruding length of the glow plug into the shield to reduce the surface area for convective heat transfer.
- Lengthened shield volume with a recessed glow plug position to reduce shield gas temperature and, consequently, the reactivity of the mixture in order to increase the required T_{HS} for timed ignition.

Figure 7.12 shows the detected photomultiplier radiation (left) and net rate of heat release NROHR (right) for single cycles with combustion phasing at 5 °CA ATDC against crank angle for different λ. Owing to the falling laminar flame speed and the smaller absolute amount of heat released due to the reduced mass of inducted fuel, NROHR is reduced when leaning out the mixture. As less fuel is burnt in longer time, the concentration of radicals in the flame front decrease, leading to lower radiation levels detected by the photomultiplier. The instant when PM voltage surpasses the ground level caused by glow plug incandescence gives an indication of the start of combustion. Just like CA5 (see Figure 7.11), it needs to be advanced when leaning the mixture while retaining same combustion phasing. As shown in both Figure 7.11 and Figure 7.12, the first part of combustion (CA5-CA50) is significantly shorter than the second one (CA50-CA90). A surprising observation is that CA5-CA50 increases and CA50-CA90 decreases with λ, leading to a nearly constant combustion duration (CA5-CA90) regardless of mixture dilution (maximum difference: 5 °CA). Examining the CFD results from Section 6.1.1 allows the conclusion that this phenomenon is caused by the combination of three factors: high flame propagation speed, advanced combustion phasing and piston geometry.

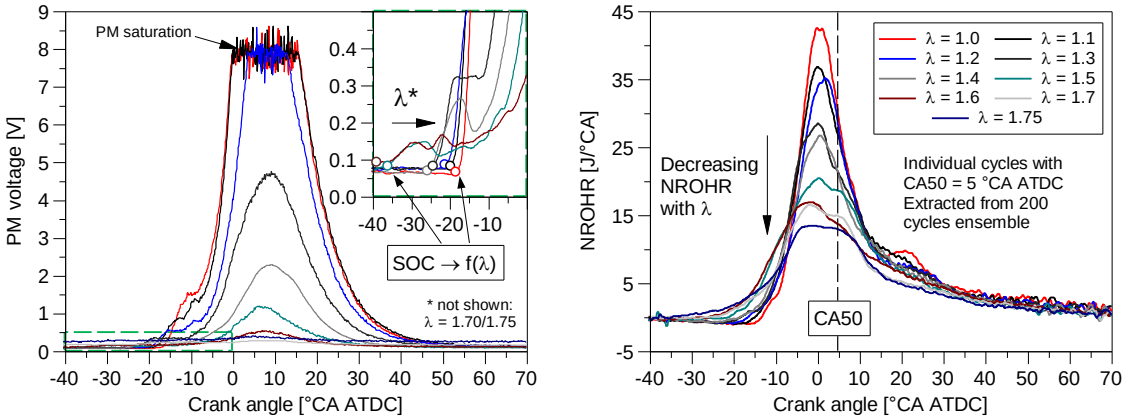

Figure 7.12: Photomultiplier voltage (left) and net rate of heat release (NROHR, right) versus crank angle for individual engine cycles at CA50 = 5 °CA ATDC for the range λ = 1.0 – 1.75 (p_{man}= 950 mbar, λ = 1.70, $CA50_{mean}$ = 5 °CA ATDC, $T_{coolant}$ = 45 °C, T_{intake}= 23 °C).

Figure 7.13 visualises the simulated flame front shortly after TDC during the second part of combustion for $T_{HS} = 1073$ °C, with the according cumulated heat release against crank angle shown in Figure 6.3. Setting early combustion phasings results in most heat being released when the piston is close to TDC, at thermodynamic conditions that favour quick fuel depletion. Initially, the turbulent flame is able to propagate freely in the compact heron combustion chamber, characterised by the deep piston bowl. As the flame travels faster than the piston moves downwards, the flame front eventually impinges on the piston. From this moment on, the flame front is divided in sub-flames and stops being sphere-like. According to Eq. (2-11), the mass flow through the reaction zone, and therefore the combustion rate, depends on flame front area and propagation speed. For an idealised spherical flame front, its area increases with its radius (e.g. the distance to the point of flame kernel formation) to the power of 2 as it propagates at a specific speed. Once the flame begins to travel through the crevice volume formed by the piston and the cylinder head (squish crevice), however, the increase in surface area is reduced. While this alone already leads to reduced rate of heat release, the small gap for flame propagation enhances the heat losses to the cylinder walls, thus further reducing flame speed and causing the sluggish second part of combustion.

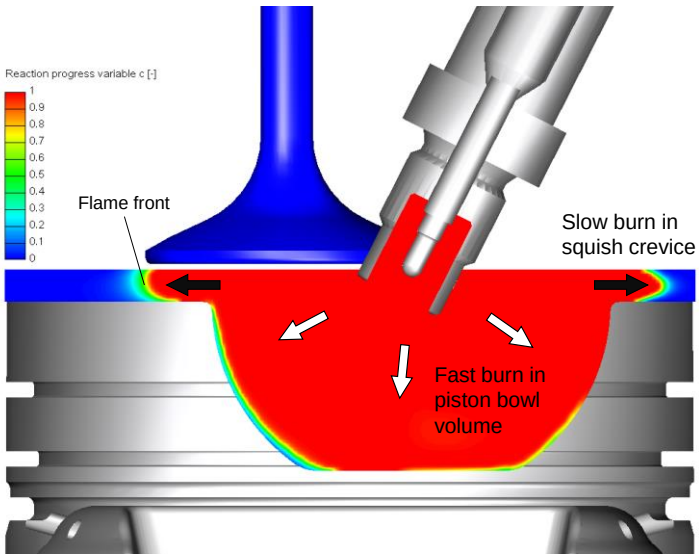

Figure 7.13: Flame front propagation through squish crevices in the second part of combustion ($\alpha = 15$ °CA ATDC).

In more general terms, Figure 7.11 (p. 130) shows that IMEP decreases linearly as the mixture is leaned due to the lessened amount of chemical fuel energy released and converted into engine work. In the range $\lambda = 1.0 - 1.5$, differences in ISFC are marginal, although the values indicate a minimum around $\lambda = 1.2 - 1.3$. Above $\lambda = 1.5$, fuel consumption exhibits a steep increase, as expected due to the slower combustion process. NO_x concentration in the exhaust shows a maximum at $\lambda = 1.1$, which agrees with data for SI engines commonly found in literature [69]. σ_{CA50} is at a constantly high level from $\lambda = 1.0$ to 1.4. Above 1.4, CCV in the timing of mixture inflammation decrease gradually with λ, caused, again, by the advancement of CA5, as stated in the previous section. To

illustrate the effect of leaning the mixture on combustion stability, Figure 7.14 depicts pressure trace ensembles and frequency plots of CA50 for λ = 1.0/1.4/1.75. It should be noted that mean combustion phasing was slightly advanced for λ = 1.0, leading to slightly lower values in σ_{CA50}. The large spread in pressure histories and CA50 for λ = 1.0 and 1.4 are proof of a highly irregular combustion. Despite the reduced hot surface temperature at λ = 1.0, some outlier cycles with very advanced combustion phasing (about 15 °CA BTDC) producing light engine knocking were recorded. Controller instability can be disregarded as causal agent for the high CCV as there is no significant alteration of hot surface temperature from cycle to cycle (indicated by minimal variability in both photomultiplier radiation and R_{HSI}). At λ = 1.75, on the other hand, combustion is fairly stable due to the requirement of advancing CA5, which is, in fact, where HSI operates best in terms of CCV.

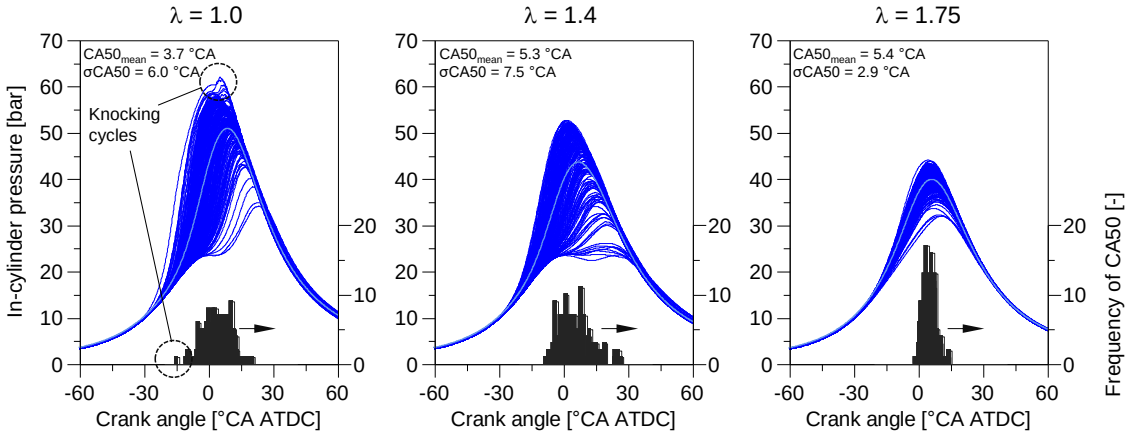

Figure 7.14: In-cylinder pressure versus crank angle and histogram of individual CA50 for 200-cycle ensemble at λ = 1.0/1.4/1.75 (p_{man}= 950 mbar, $T_{coolant}$ = 45 °C, T_{intake}= 23 °C).

7.3.3 Effect of Intake Manifold Pressure

Due to the lowered lean-burn limit in throttled operation, λ was reduced to 1.5 for carrying out the sweep of intake manifold pressure p_{man}. Other main factors were set to CA50 = 5 °CA ATDC, $T_{coolant}$ = 45 °C and T_{intake} = 23.0 °C. According to the plot of T_{HS} against p_{man} in Figure 7.15, throttling increases the temperature demand of the hot surface, a fact that is also indicated by the curves of R_{HSI} and min. PM voltage. The thermal explosion theory in Section 3.1.2 gives the principal reason for this relationship: When lowering the pressure in the combustion chamber, concentration of reactants in the boundary layer of the hot surface decreases, forming less reactive radicals to promote ignition. As a result, the heat produced by the chemical reaction is lowered and becomes imbalanced with respect to the heat losses by conduction through the mixture. To restore the balance required for a properly timed combustion, the reaction rate needs to be increased by raising HS temperature. Further influencing factors that arise from reduced intake manifold pressures are an increasing residual mass fraction [69] and reduced mixture temperatures due to the lower pressures levels during the compression stroke. The

reduced charge motion during the intake stroke may also decrease the turbulence level in the shield volume, thereby increasing the ignition delay.

The trends of T_{shield} and NO_x show that both mean gas temperature and peak combustion temperature increase with intake manifold pressure. The larger heat input to the HSI adapter causes higher glow plug body temperatures, which results in a drop in glow plug heating efficiency. Nevertheless, the enhanced convective heat flow to the hot surface enables the HSI controller to reduce P_{HSI} by about 10 W over the entire investigated range.

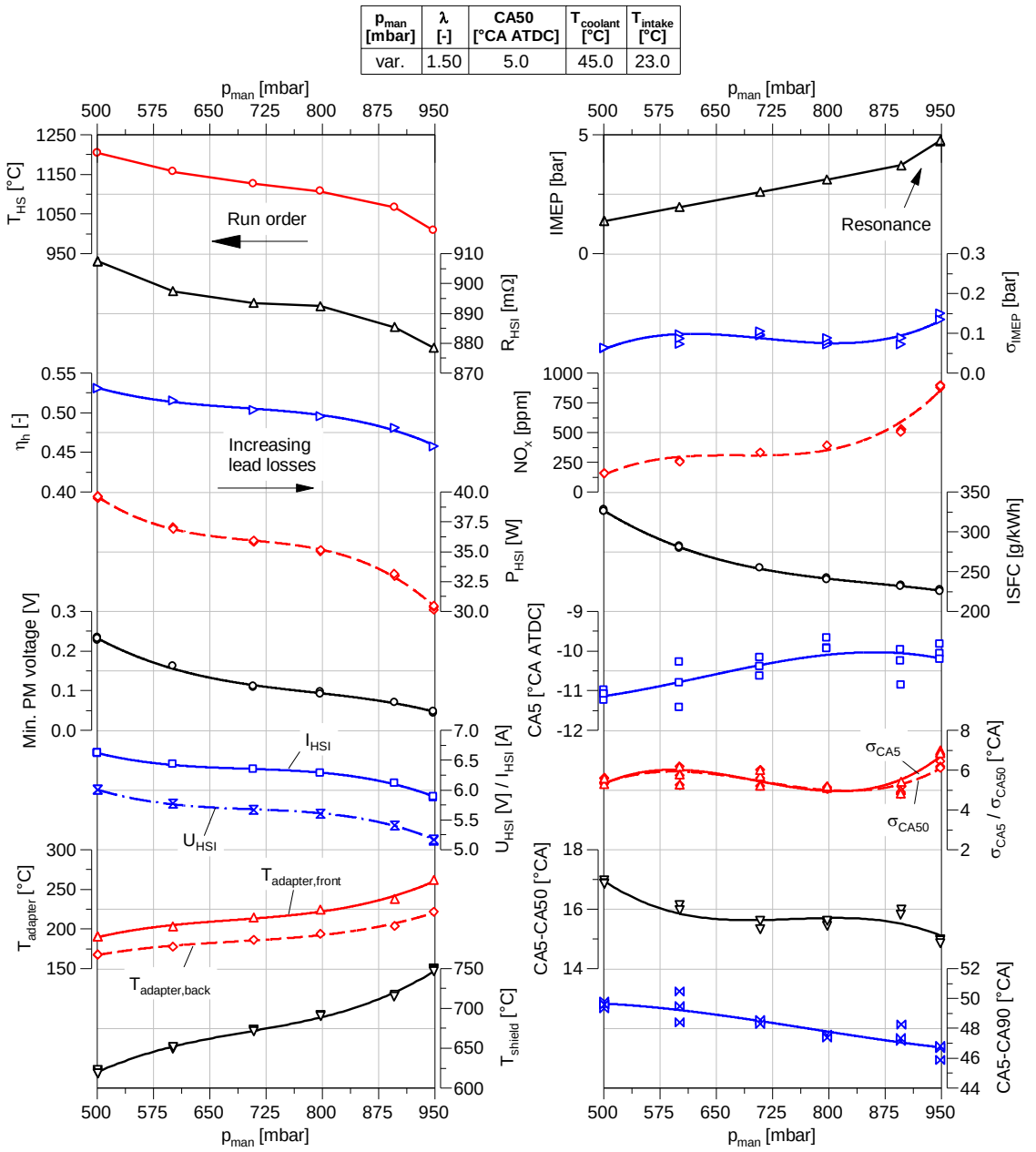

Figure 7.15: Selected experimental data against mean intake manifold pressure p_{man} (glow plug No. 5).

Evidently, throttled operation is detrimental to fuel consumption by virtue of increased pumping losses, increased relative wall heat losses and a slowed combustion. CCV in CA5

and CA50 are rather constant in the range $p_{man} = 500 - 900$ mbar. Only at 950 mbar a statistically significant increase can be observed. This corresponds to a particular rise of IMEP in an otherwise linear dependency of IMEP on intake manifold pressure. To examine this phenomenon in detail, Figure 7.16 (left) shows IMEP, fuel mass flow $\dot{m}_{fuel}$ and mixture density at the intake manifold ρ_{man} as a function of p_{man}. While mixture density can be rouled out as a causal agent due to its linear trend, the trace of fuel mass flow exhibits the same qualitative behaviour as IMEP, thereby giving evidence of what causes the sudden change in IMEP slope from 900 to 950 mbar. Figure 7.16 (right) depicts the ensemble-mean gas exchange loops for all six recorded levels of p_{man}. The crutial finding from this plot is that from 1 to 5, pressure at inlet valve closing (IVC) increases in a quite linear manner, with readings slightly below the respective intake manifold pressure. For operating point 6, on the other hand, p_{IVC} lies well above p_{man}, leading to a significant increase in inducted cylinder mass. Since this finding cannot be explained by the mean reading of the pressure sensor, it must be caused by gas dynamic effects. On account of lacking a low-pressure indication system on the test bed, the effect of intake manifold pressure on gas-dynamics was analysed with the aid of the 1D simulation model in AVL Boost. Data from the pressure sweep shown in Figure 7.17 were obtained by adjusting the opening grade of a throttle valve positioned about 400 mm before the cylinder's inlet, in identical position to the experiments. All cases were simulated assuming a constant normalised heat release profile derived from the series SI operating point of the engine (CA50 = 18.5 °CA ATDC). The effect of throttling on the heat release process was therefore not considered.

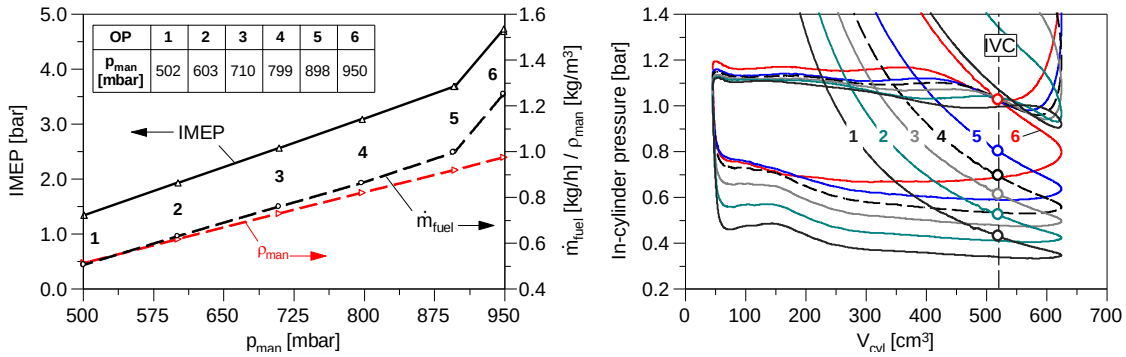

Figure 7.16: Experimental data of operating points 1-6 on IMEP, fuel mass flow $\dot{m}_{fuel}$, intake manifold density ρ_{man} against intake manifold pressure p_{man} (left), and gas exchange loop for the ensemble mean of each operating point (right).

The simulation results showed the exact same trend in IMEP as the experimental data. For operating points $1 - 4$ ($p_{man} = 416 - 858$ mbar), there is a significant back flow of residual gas into the intake manifold shortly after the intake valve opens (IVO). During the intake stroke, mass flow peaks at around 40 °CA ATDC and then decreases gradually until IVC. In contrast, for operating points $4 - 7$ ($p_{man} = 858 - 951$ mbar), mass flow increases after a brief inflection point, an effect that is most marked for 7, i.e. at maximum load. This can be explained by the following effect: Regardless of the operating

point, instantaneous pressure in the intake manifold drops with the start of mixture induction (positive mass flow at about 10 °CA ATDC). With increasing throttle valve opening, however, the decrease is attenuated, and even counteracted for OP 7, by an oncoming high-pressure wave. As a result, the driving pressure difference between the intake port and the cylinder as the piston is moving down is increased, leading to a larger mass flow during mixture induction. When forming the integral of the mass flow trace it becomes clear that in-cylinder increases disproportionately from 4 – 7, causing increasing pressure levels at IVC. When also taking into consideration that the engine's flow path was optimised for maximum cylinder filling, it becomes clear that resonance effects in the ducts have a charging effect on the engine, thus increasing the volumetric efficiency when the mixture flow is not or only slightly throttled. This gives a plausible explanation for the sudden increase of IMEP in the experimental range p_{man} = 900 – 950 mbar.

OP	1	2	3	4	5	6	7
$p_{man,mean}$ [mbar]	416	686	792	858	908	934	951

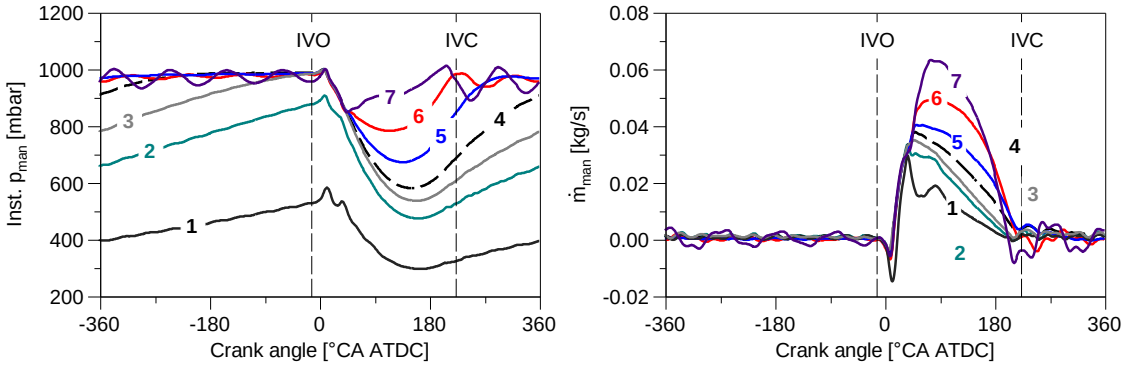

Figure 7.17: Simulated traces of p_{man} (left) and mixture mass flow $\dot{m}_{man}$ for different throttle positions (λ = 1.54, CA50 = 18.5 °CA ATDC, T_{intake} = 25 °C, constant normalised heat release profile, gas exchange TDC at 0 °CA).

7.3.4 Effects of Intake and Coolant Temperature

The factorial screenings to determine λ_{max} and the range of CA50 indicate that the effect of intake and coolant temperatures on the combustion process is much smaller than that of the other factors (CA50, λ and p_{man}). Nevertheless, it seems conducive to analyse the effect of adjusting each temperature individually at maximum intake manifold pressure, given that the CHP engine is usually operated at full load under changing ambient and coolant temperatures. For the subsequent variations, following settings were used: p_{man}= 950 mbar, λ = 1.70, CA50 = 5 °CA ATDC. T_{intake} was adjusted in the range 20 – 45 °C, $T_{coolant}$ in the range 25 – 65 °C.

Main results of both temperature sweeps that were ran on two consecutive days are depicted with a common x-axis in Figure 7.18. The magnitudes on the right show that, indeed, neither parameter is particularly significant to the combustion process. Minor trends, e.g. in IMEP and ISFC, can be attributed to the slight rise of intake manifold

temperature as T_{intake} and $T_{coolant}$ increase, causing a decrease of mixture density and, in turn, of mixture mass flow. As can be seen in Figure 7.19 (left), both temperatures exert a similar linear effect on T_{man}, with a slightly larger gradient for T_{intake}. The much lower effect of $T_{coolant}$ on $T_{throttle}$, indicates that most heat from the hot casing to the mixture is transferred over the approximately 400 mm long tube between the measuring positions of $T_{throttle}$ and T_{man}. Over the whole range of T_{intake}, both mixture density and IMEP decrease linearly by around 2.3 %. For $T_{coolant}$, mixture density drops by approximately 3 %, while IMEP experiences a slightly lower decrease of 2.5 % due to the diminished wall heat losses at maximum coolant temperature, which presumably allow for the slight improvement in ISFC (about 1.2 %).

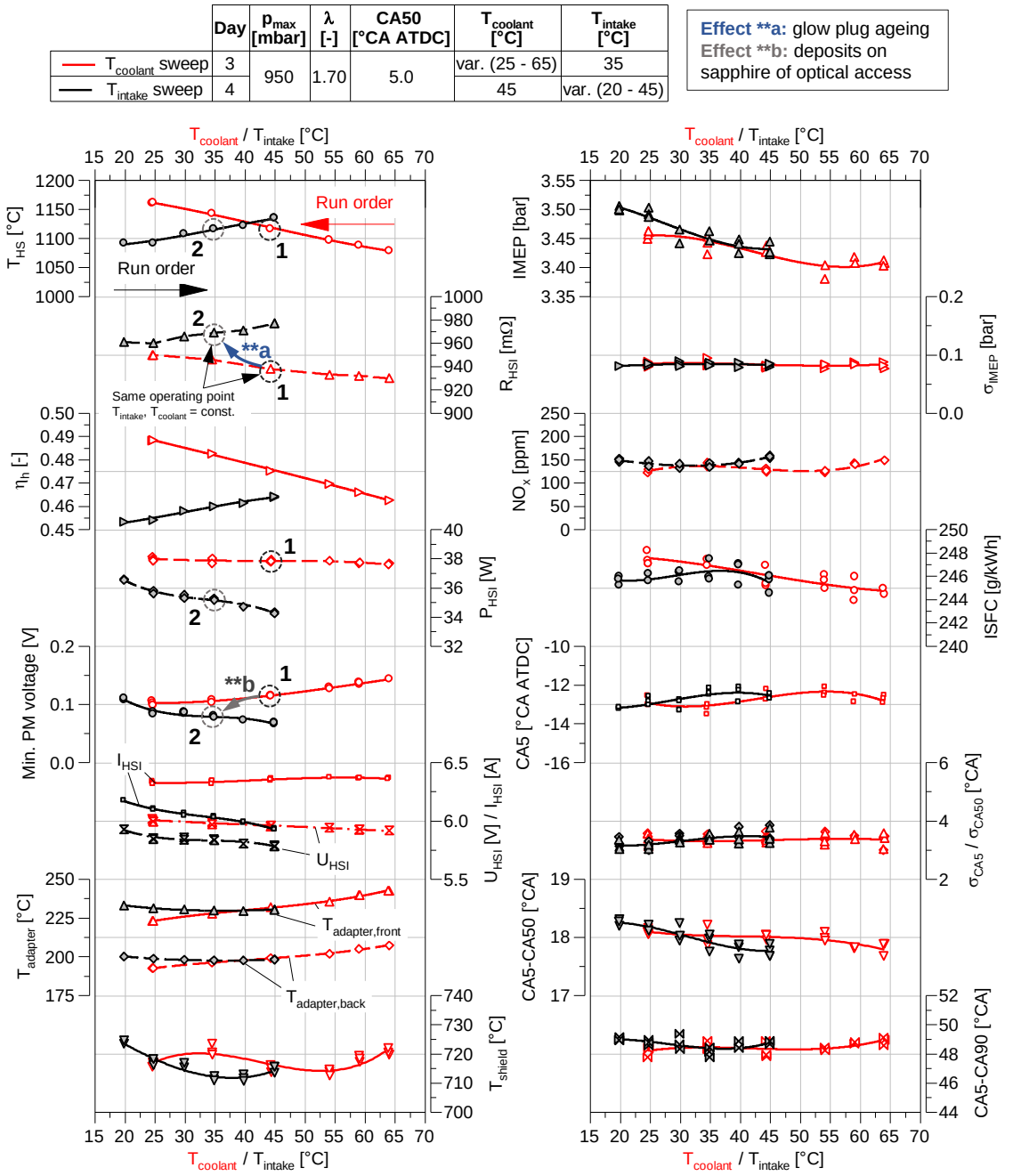

Figure 7.18: Selected experimental data against coolant temperature $T_{coolant}$ and intake tempetrature T_{intake} (glow plug No. 5).

Figure 7.19 (right) reveals the strong linear response of casing and oil temperature to $T_{coolant}$, while the effect of T_{intake} is noticeable but negligible:

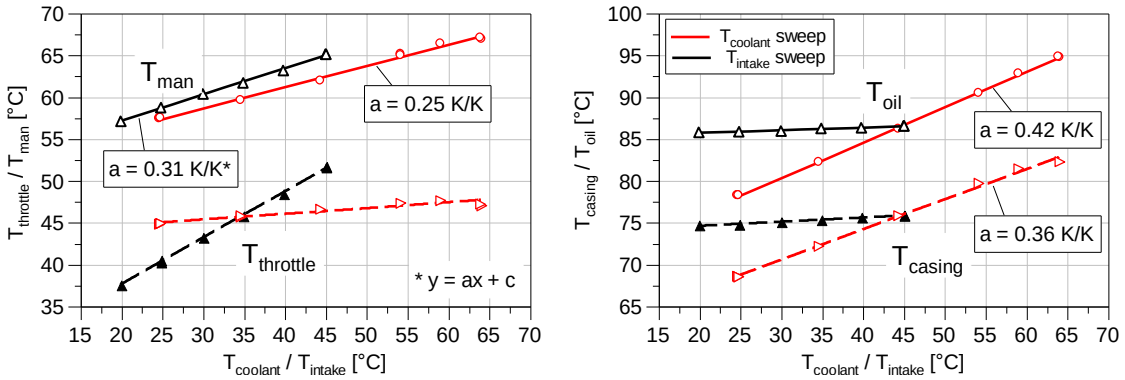

Figure 7.19: Mixture temperatures at the throttle and the intake manifold (left) and casing and oil temperatures (right) as a function of coolant temperature $T_{coolant}$ and intake temperature T_{intake}.

In light of fairly constant combustion parameters, one would expect only marginal differences in the thermo-electrical parameters of the HSI system. Nonetheless, calculated T_{HS} shows a significant spread over both T_{intake} and $T_{coolant}$, with opposing trends for both factors. The circled operating points 1 and 2 from Figure 7.18 represent engine operation on two consecutive days with identical factor settings. All temperatures and combustion parameters are in good agreement, indicating that T_{HS} had to be constant. Under this assumption, data was used to determine R_{ageing}, which increased by 32 mΩ from one day to another (see effect **a). Such considerable glow plug deterioration rate implies that ageing may have been significant while conducting the trials. As constant ageing conditions are assumed for the entire sweep, T_{HS} calculated from Eq. (7-3) would be biased and give wrong values to either side of the calibrated operating point. This conjecture is supported by the direct correlation between the run order, i.e., the operation time of the glow plug, and the gradual increase of both T_{HS} and R_{HSI}. Unfortunately, the trends of PM voltage do not contribute to shedding light on this phenomenon as the amount of detected radiation decreased gradually over time due to deposits agglomerated on the sapphire surface (effect **b). When supposing that T_{HS} remained constant over both sweeps, an individual value for R_{ageing} can be determined for each operating point. From start till end, this gives an increase of resistance of $\Delta R_{ageing} = 55$ mΩ.

As stated in Section 6.2, an increasing leads resistance can help reduce the energy demand of the HSI system by lowering the convective heat losses between the glow plug tip and the adapter. This appears to be the case when comparing operating points 1 and 2, showing that the required electric power P_{HSI} did in fact decrease by approximately 2.5 W as a result of glow plug ageing from day 3 to day 4. Since all other parameters governing conduction remain constant, a lowered temperature gradient ΔT between glow plug tip and body must cause a reduction in $\dot{Q}_{cond}$, and ultimately in P_{HSI}. This seems reasonable when assuming that the heat dissipated by R_{ageing} rises glow plug temperature, which is however not supported by the fact that adapter temperatures are not di-

rectly affected by the deterioration process and practically remain constant. While the main focus of future research should be to fully avoid glow plug degradation, e.g. by means discussed in Section 7.6.2, its effect on the thermo-electric properties of the HSI system is in need of further investigation.

7.3.5 Conclusion

To conclude this section concerning the individual effects of all adjustable factors, Figure 7.20 gives an overview of the qualitative responses of the most significant operation parameters to individual factor changes. In summary, the experiments give strong indication that intake manifold pressure, relative air-fuel ratio and combustion phasing have a strong impact on combustion, while intake and coolant temperature only play a subordinate role. Two essential dependencies that are inherent to the test bed were determined: The charging effect for high engine load due to gas dynamic effects in the intake system, and the flame front-piston interaction at advanced combustion phasings. Part of the large experimental data pool was subsequently used to derive empirical models for tuning the 0D engine process calculation model, as described in detail in the Appendix (Section A.3).

FACTOR	Description	$T_{adapter}$	T_{shield}	$T_{throttle}$	T_{man}	T_{casing}	T_{oil}	IMEP	PMEP	CCV	ISFC	HC	CO	NO_x
CA50	Combustion phasing	-	-	-	-	-	-	+/-	-	++	+/-	+	+	- -
λ	Relative air-fuel ratio	- -	- -	-	- -	- -	- -	- -	-	- -	+/-	++	+/-	- -
p_{man}	Intake manifold pressure	++	++	+	0	++	++	++	- -	+/-	- -	- -	+/-	++
$T_{coolant}$	Coolant temperature	+	0	+	+	++	++	-	-	0	-	-	0	0
T_{intake}	Intake temperature	≈ 0	0	++	+	≈ 0	≈ 0	-	-	0	0	-	≈ 0	≈ 0

Legend: 0 No change; +/- Min/max across the range; + Minor increase; ++ Major increase; - Minor decrease; - - Major decrease

Figure 7.20: Qualitative effects of factors from OFAT analysis. Convention of factor change is positive.

7.4 HSI Operation Map

The results of the OFAT experiments presented in the previous section imply that not all dependencies can be represented accurately by linear or quadratic polynomials. For this reason, the order of the formulated RSM design was set to cubic and an I-optimal design was chosen for highest prediction accuracies over the entire experimental range. Low and high levels of all factors were set according to the values shown in Figure 7.21. λ and CA50 were constrained according to the limits determined in the screening experiments. Previous trials revealed that the time between setting an operating point and reaching steady-state conditions could amount up to 120 min. Limiting experimental time by minimising the number of runs was therefore an essential aspect of experiment design. Choosing a full cubic 5-factor-RSM design with 5 lack-of-fit, 5 replicate and 1 centre points would require a total of 67 runs. Assuming that high order interactions among the factors (such as $x_1 \cdot x_2 \cdot x_3$ or ${x_1}^2 \cdot x_2$) are of minor importance to model responses, the

number of runs was reduced significantly to 37 by only including cubic main effects ($x_p{}^3$). The ensuing selection of factor model points is done such that the integral of the standard error of mean (SEM) is minimised over the entire design space. In other words, the area below the *Fraction of Design Space* (FDS) graph is minimised. FDS plots are a graphical tool to examine a design's prediction variance properties. They display the fraction of the design space where the scaled prediction variance (SPV) is lower or equal to a specific value for all observed values. FDS graphs enable the experimenter to study the SPV distribution of a design and to compare its quality to other designs [104]. Using the FDS plot approach it was found that 5 supplementary model points would provide significantly better model predictability. Figure 7.21 compares the FDS graphs for the standard RSM design to the enhanced model with 42 runs, showing that the extended RSM allows for a significant reduction of SEM across the whole design space. For the sake of model accuracy, it was decided to record 42 operating points and accept the increased experimental effort. To minimise the risk of systematic errors, all runs were recorded in a randomised order, as shown in the design matrix provided in Appendix A.5, Table A.4.

Factor	Low level (-1)*	Intercept (0)*	High level (1)*
A – p_{man} [mbar]	500	725	950
B – $T_{coolant}$ [°C]	25	42.5	60
C - λ [-]	1.0	1.39	1.77
D – CA50 [°CA ATDC]	0	7.5	15
E – T_{intake} [°C]	25	35	45

* Coded factors

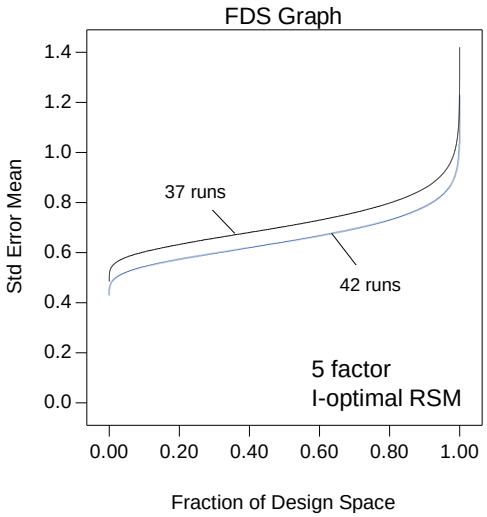

Figure 7.21: FDS graph for reduced I-optimal cubic RSM design with and without additional model points.

The first 12 runs of the RSM design were conducted using glow plug No. 5, previously used in the screening trials. After setting all factors for Run 13 and waiting for steady-state conditions, an abrupt retarding of CA50 was observed for constant R_{HSI}. In order to set CA50 back to its target value, the set value of the controller R_{set} had to be increased but the controller became increasingly unstable at the same time. It was found that the flow of electric current was cut intermittently, indicating that the connectors joining the metallic and ceramic leads inside the glow plug became loose. The sporadic reading $I_{HSI} = 0$ evidently led to faulty values of calculated R_{HSI} and cycles where the controller tried to counteract this apparent disturbance. As a result, controller output U_{HSI} began to fluctuate and impeded setting stable combustion phasing. Since the combustion process does not show any sensitivity to glow plug tolerances as long as CA50 is controlled (see Section 6.2), it was decided to replace glow plug No. 5 and continue the series of

experiments with a new glow plug (No. 6).

7.4.1 Experimental RSM results

The purpose of this section is to present the most relevant findings on HSI induced premixed combustion based on statistical analysis of the recorded experimental data. The derived fitted regression models (response surfaces) provide mathematical relationships between the changed factors A-E, and the responses of interest (e.g. temperatures, ISFC, NO_x or σ_{CA5}), valid for the entire experimental range. This allows determining sensitivities and interactions among the factors, find optimum operating conditions, but also to derive empirical models used to tune the 0D model.

7.4.1.1 Temperatures

Table 7.4 shows the response surface equations in coded notation of selected temperatures, where each cell of a column represents the factor coefficient a_i according to Table 5.4. The coded representation is useful for identifying the relative impact or sensitivity of the factor or interaction, as the coefficients represent the change in the response as the factor level is changed by one coded unit. To highlight the most important factors, each coefficient cell in the table is coloured according to scale, where dark grey corresponds to the largest and white to the lowest impact factor. The actual response y can be derived in the following manner, with coded factor inputs (-1, 1) and c being the intercept:

$$y = a_1 p_{man} + a_2 T_{coolant} + a_3 \lambda + a_4 \mathrm{CA50} + a_5 T_{intake} + a_1 a_2 p_{man} T_{coolant} + \dots + c \tag{7-4}$$

Using the simple example of mixture temperature at the throttle, predictions about its response to changes in factors A, B, C and E can be made according to Eq. (7-5):

$$T_{throttle} = -2.8 \cdot p_{man} + 1.7 \cdot T_{coolant} - 1.1 \cdot \lambda + 3.4 \cdot T_{intake} - 0.8 \cdot p_{man} T_{coolant} + 1.6 \cdot p_{man} T_{intake} + 1.3 \cdot {p_{man}}^2 + 47.8 \tag{7-5}$$

The predicted coefficient of determination R^2_{pred} is a measure of how well the model predicts responses for new observations. A value of R^2_{pred} much lower than R^2 gives strong indication that a model is overfitted and too many terms are part of the model. The values given in Table 7.4 (expressed as Pred. R^2) show that predicted responses are in very good agreement with experimental data ($R^2_{pred} > 0.95$). Regarding the weight of factors on the response, similar patters can be seen for T_{man}, $T_{coolant,out}$, T_{casing} and T_{oil} as well as for $T_{adapter}$, T_{exh} and T_{shield}. In the first group, all temperatures increase substantially with $T_{coolant}$ and fall with λ. With exception of T_{man}, p_{man} also causes a moderate rise in temperature. In the second group, temperatures fall with λ but increase significantly with p_{man}. CA50 is also significant to $T_{adapter}$ and T_{shield} as advancing combustion pro-

duces higher combustion temperatures. At the same time, however, more heat is converted into engine work, leading to a decrease of T_{exh}, an thus, to an opposed coefficient sign.

Since both T_{man} and $T_{adapter}$ are parameters that need to be defined in the 0D model, their responses will be discussed in detail hereinafter.

Table 7.4. Equations for response surfaces of temperatures in °C as a function of factors A-E in coded notation (-1, 1).

	Response [°C]	T_throttle	T_man	T_coolant_out	T_casing	T_oil	T_adapter	T_exh	T_shield
	Intercept	47.8	62.8	70.6	73.3	84.8	215.2	525.1	660.1
MAIN EFFECTS	A – p_man	-2.8	0.6	3.7	3.7	3.1	24.8	24.4	48.7
	B – T_coolant	1.7	4.5	7.5	6.0	7.2	8.2	6.2	2.2
	C – Lambda	-1.1	-2.5	-3.5	-4.6	-5.3	-29.6	-109.9	-53.7
	D – CA50				-0.1	-0.6	-17.1	13.7	-67.1
	E – T_intake	3.4	1.8	-0.2	0.2			1.6	-1.6
INTERACTIONS	AB	-0.8	-1.6	-1.7	-0.8	-0.7	-1.9		
	AC				-1.1	-1.2	-8.3	-8.4	-16.9
	AD					-0.4	-5.8		-13.2
	AE	1.6	1.0						
	BC		0.6	1.2	0.7	0.5	2.2	4.5	
	BD								-2.8
	BE							-4.3	
	CD						3.3		6.1
	CE								
	DE				-0.3				
HIGHER ORDER EFFECTS	A2	1.3	1.1		1.1	0.9	8.0		7.2
	B2								
	C2						1.4	-21.4	40.1
	D2							5.5	
	E2			-0.5					
	A3		-1.2		1.7	2.1	10.6		8.1
	B3								
	C3						-5.9	-26.6	
	D3								
	E3								
	Pred. R^2	0.954	0.966	0.978	0.986	0.990	0.995	0.991	0.997

Empirical T_{man} model

For calculating the mass flows of inducted air and fuel at a given engine speed, the 0D model requires mixture density calculated from intake manifold pressure p_{man} (user input) and temperature T_{man} (dependent variable). Figure 7.22 (left) depicts the perturbation plot of the response of T_{man} at the intercept (all factors = 0). Factor D, CA50, proved not to be statistically significant and is therefore not part of the model. As can be seen, Factor A (p_{man}), is the only variable showing higher order effects, while the perturbation response of the other factors is linear. A is also involved in the two most significant factor interactions AB and AE. If interactions show positive coefficients, as it is the case for AE, the response is always positive given that both factors have the same sign, while being negative if the sign is opposed. Evidently, the contrary applies to interactions

with negative coefficients, like AB. Both interactions are of particular interest since previously it was not possible to derive clear trends for λ_{max} in the screening trials.

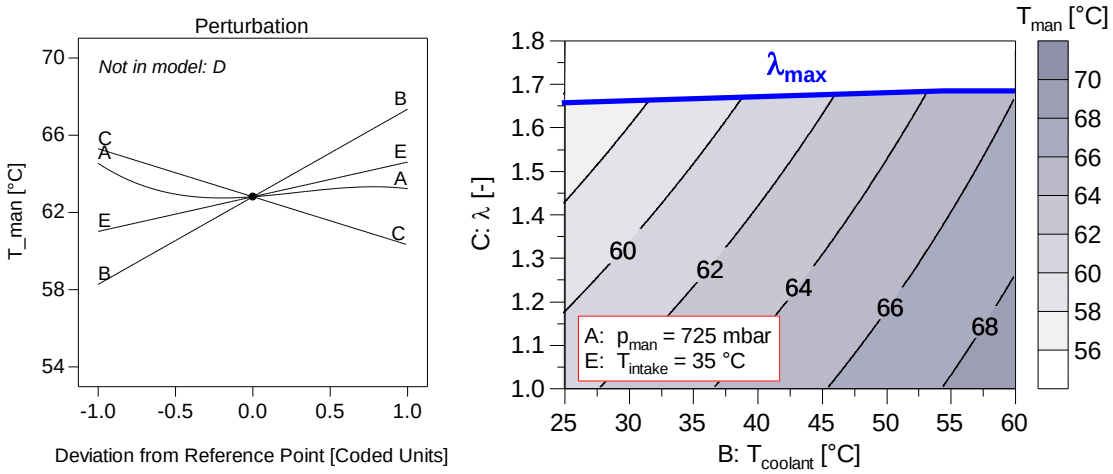

Figure 7.22: Perturbation plot of T_{man} (left) and the respective contour plot (right) when setting the less significant factors A (p_{man}) and E (T_{intake}) to coded 0 (intercept).

The interaction plots in Figure 7.23 allow examining the effect of throttling on intake manifold temperature when intake and coolant temperature are set to their respective min and max values (-1, 1). If p_{man} is set constant, both T_{intake} and $T_{coolant}$ cause a linear rise of intake manifold temperature. Due to the interactions, however, dethrottling exerts a decreasing effect on T_{man} as coolant temperature is raised, and an increasing effect as intake temperature is raised. The AB interaction is governed by two competing parameters: the retention time of the mixture in the intake system and the heat release from combustion. The low mass flow at low pressures results in high retention times of the high pressure mixture before the throttle valve, making mixture temperature highly susceptible to casing temperature. As the mass flow is increased by gradually opening the throttle, retention time is reduced, which initially lowers the heat input from the casing. At the same time, however, the larger heat release from combustion increases T_{casing}. For low coolant temperatures, the enhanced convective heat transfer from casing to mixture is able to overcompensate the heat losses arising from the diminished retention time, leading to rising temperatures before the inlet valve. At the intercept of factor B ($T_{coolant} = 42.5$ °C) both effects are rather balanced over the entire range of p_{man} ($\Delta T_{max} \approx 1$ °C), while a further increase of $T_{coolant}$ has the opposing effect. The AE interaction is also directly linked to the two parameters mentioned but in this case, the enthalpy flow of the mixture is varied prior to entering the CHP unit. It applies again that T_{man} is mostly a function of T_{casing} at low pressures. As pressure is increased, T_{intake} gains weigth in proportion to the aspirated mass flow. As indicated by the positive interaction coefficient, increasing intake temperatures attenuate the losses from the reduced retention time.

Figure 7.22 (right) shows the contour plot of T_{man} as a function of the two most significant factors, B ($T_{coolant}$) and C (λ), while setting the remaining model variables to coded

0, i.e. to the middle of their respective range. Both factors have a large impact on intake temperature. However, this is not a direct effect but linked to casing temperature. In summary, it can be inferred that the dependent variables casing temperature and inducted mass flow are most significant to intake manifold temperature.

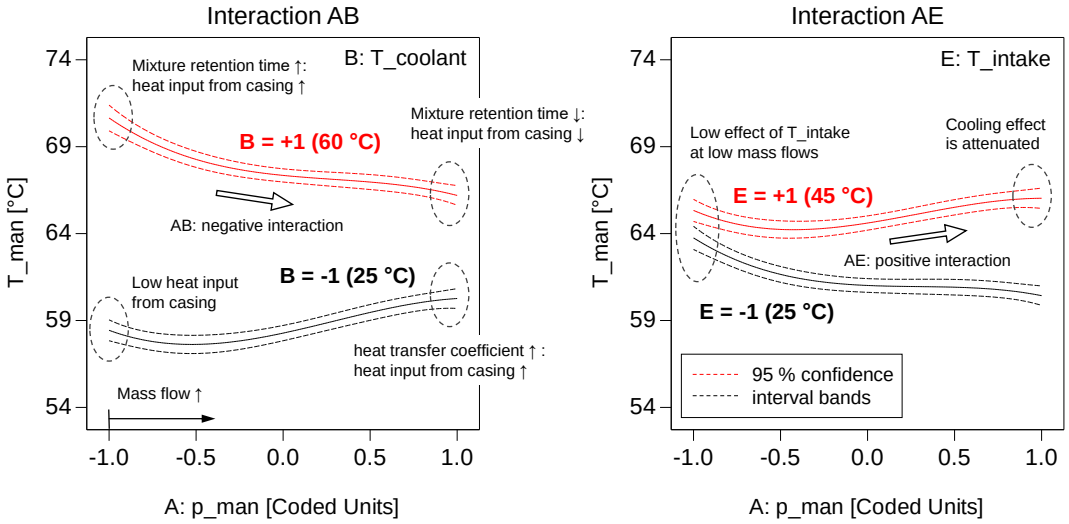

Figure 7.23: Interaction plots for AB (p_{man}-$T_{coolant}$ interaction, left) and AE (p_{man}-T_{intake} interaction, right) with other model factors set to coded 0 (intercept).

Empirical $T_{adapter}$ model

As previously stated, the thermo-electric behaviour of the glow plug depends strongly on the temperature of the HSI adapter. Seeing as the combustion-adapter interaction is not simulated in the 0D model, being able to predict adapter temperature accurately for calculating the electric losses along the glow plug is therefore decisive for obtaining useful results. The perturbation plot in Figure 7.24 illustrates that all factors that affect combustion and/or engine block temperature produce a marked response in adapter temperature.

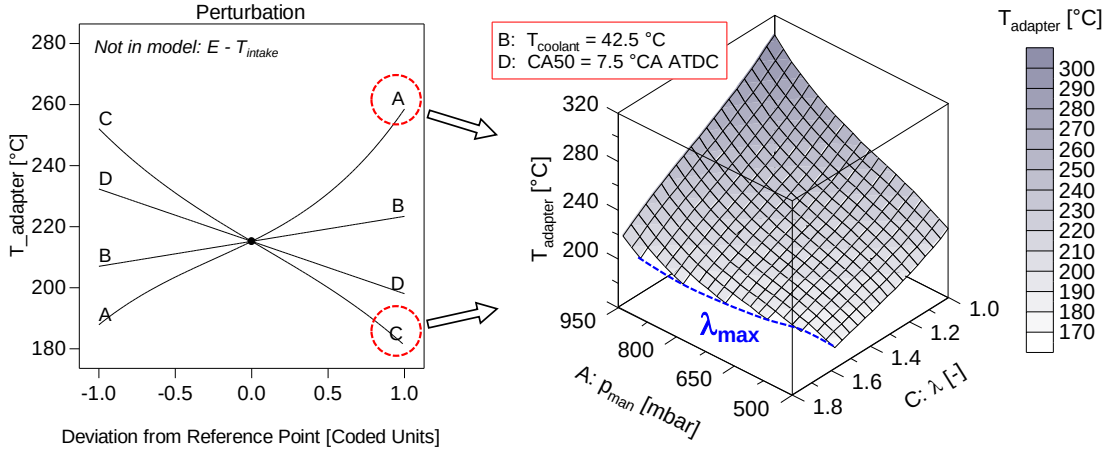

Figure 7.24: Perturbation plot of $T_{adapter}$ (left) and the respective response surface (right) for factors A (p_{man}) and C (λ) with remaining, less significant factors set to coded 0 (intercept).

In agreement with the OFAT trials, intake temperature is not significant and of all remaining model factors, coolant temperature exerts the lowest impact on the response. The response surface in Figure 7.24, right, shows that $T_{adapter}$ increases quite evenly (in terms of coded factors) when dethrottling and enriching the mixture. Both measures produce higher combustion temperatures that a) enhance the heat gains that the HSI adapter experiences due to convection from the in-cylinder charge and b) reduce adapter cooling due to increased engine block temperatures. Higher order effects are less significant, although in the case of p_{man}, they allow representing the charging effect at higher intake pressures.

7.4.1.2 Combustion parameters

Table 7.5 gives the response surface equations for selected combustion parameters. The regression analysis reveals that IMEP is primarily a function of p_{man} and λ with higher order effects to account for gas dynamics and the worsened combustion efficiency when approaching the lean burn limit, respectively. The equivalent response surfaces of IMEP and σ_{IMEP} are shown in Figure 7.25 as a function of both variables (plots a and b). It is noteworthy that the shape of the IMEP response is very similar to that of $T_{adapter}$ in Figure 7.24, suggesting that both parameters are positively correlated. With a correlation coefficient of $R^2 = 0.76$, $T_{adapter}$ can be predicted relatively well when knowing IMEP, giving a sensitivity of about 24 K/bar (not shown).

Table 7.5: Equations for response surfaces of combustion parameters as a function of factors A-E in coded notation (-1, 1).

	Response	IMEP [bar]	σIMEP [bar]	PMEP [bar]	σPMEP [bar]	CA5 [°CA ATDC]	σCA5 [°CA]	σCA50 [°CA]	CD [°CA]	σCD [°CA]
	Intercept	2.86	0.07	-0.52	0.05	-6.29	6.43	6.58	43.78	4.96
MAIN EFFECTS	A – p_man	1.21	0.05	0.12	0.02	0.18	0.42		-1.07	
	B – T_coolant	-0.02	-0.01		0.00		-0.04	-0.05	0.33	-0.02
	C – Lambda	-0.91	0.02	-0.02	-0.04	-4.67	-1.81	-1.70	6.27	-1.43
	D – CA50	0.02	0.05	-0.01	0.00	7.42	0.90	1.68	-5.32	-0.62
	E – T_intake	-0.03	-0.01	0.00						
INTERACTIONS	AB									
	AC	-0.34		0.01	-0.02				-0.60	
	AD		0.03	-0.01		0.15				
	AE	-0.05								
	BC		-0.02		0.00					0.32
	BD				0.00		-0.47	-0.52		
	BE	0.06								
	CD			0.01					1.41	
	CE									
	DE									
HIGHER ORDER EFFECTS	A2	0.27		-0.04	0.01	-0.50				
	B2	0.09								
	C2	-0.23	0.04		-0.01	-0.93	-1.54	-1.87	2.16	-1.32
	D2	-0.13	0.09			-0.38		0.72	2.16	
	E2									
	A3	0.43								
	B3									
	C3	-0.26				1.06			-4.67	
	D3									
	E3									
	Pred. R^2	0.993	0.804	0.997	0.954	0.998	0.746	0.739	0.965	0.776

σ_{IMEP} responds most sensitive to changes in A (p_{man}) and D (CA50), showing lowest variability around MBT combustion phasing and low intake pressure. Evidently, CA5 proved to be dominated by CA50, but also by λ, due to the reduced laminar flame speed when leaning the mixture. At the same time, the variation in CA5 can be reduced drastically by increasing λ and advancing combustion phasing (see plots c and d). As explained in Section 7.1.2.2, the improvement in combustion stability is a direct result of the need of advancing the start of combustion. The shortened ignition delay times reduce the sensitivity to CCV of the process of mixture inflammation and lead to a narrowed scatter range in CA5. Late combustion phasings and increased mixture strength, on the other hand, require late starts of combustion, thus showing highest variability in the phasing of heat release from cycle to cycle.

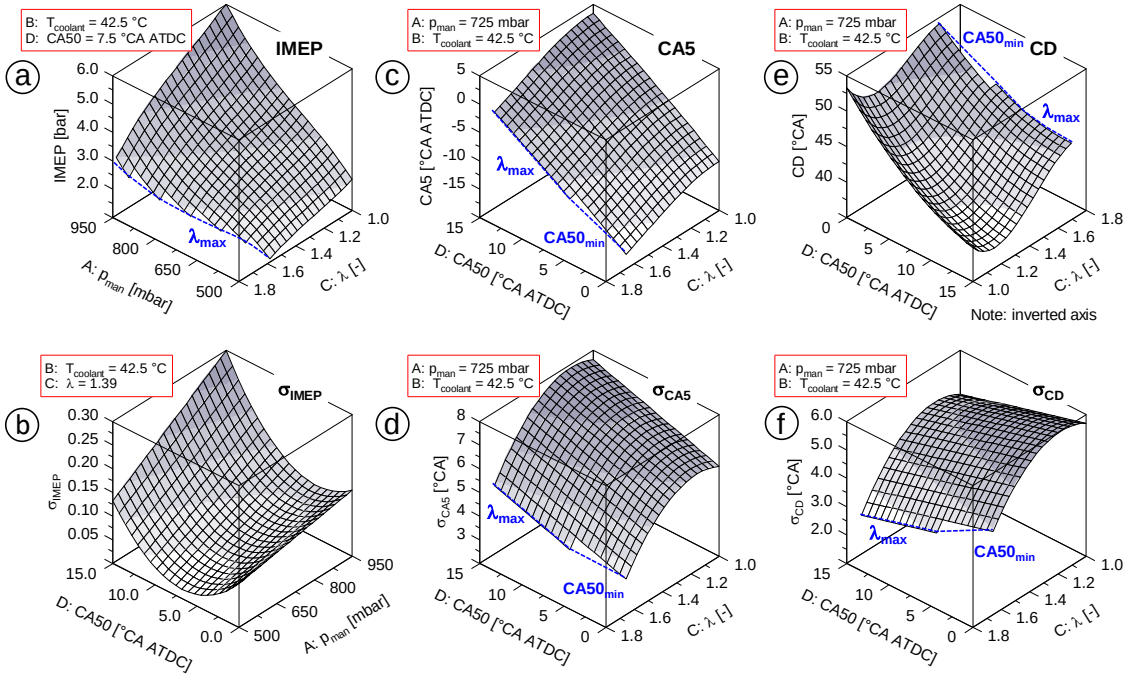

Figure 7.25: Response surfaces of IMEP, CA5 and CD and their respective standard deviations as a function of most significant factors (Other factors set to coded 0, mesh resolution = 0.1 in coded notation). λ_{max} represents the lean-burn limit, $CA50_{min}$ the transition from section 1 to section 2.

Cyclic variability in the start of combustion directly translates into variability in combustion phasing. Figure 7.26 plots predicted σ_{CA50} as a function of λ and CA50 and underlines how closely combustion stability is linked to both factors in HSI operation. The lowest value of σ_{CA50} that can be set is about 3 °CA, at CA50 = 0 °CA ATDC and λ = 1.70, thus representing the lowest variability in combustion phasing that can be achieved with the tested HSI design.

On account of the flame front-piston interaction, the response surface of combustion duration in Figure 7.25 (plot e) appears to be fairly complex, showing several higher order effects. For the entire λ range, combustion duration is reduced with CA50 when holding λ constant. It applies throughout that λ = 1.15 – 1.2 exhibits highest ROHR, decreasing

moderately towards stoichiometric mixtures and considerably towards leaner mixtures. This explains the minimum in CD when tracing the curves of constant CA50 in the response surface. This minimum is caused by two opposing trends: On the one hand, leaning the mixture leads to reduced flame speed and a lengthened duration of the first part of combustion CA5-CA50. On the other hand, the lowered ROHR reduces the flame-piston interaction, shortening the duration of the second part of combustion CA50-CA90. Therefore, the CD minimum represents the transition point above which, in terms of λ, the increase in CA5-CA50 outweighs the decrease in CA50-CA90. The standard deviation of combustion duration σ_{CD} (see plot f) is also primarily governed by factors C and D. Cyclic variations increase when approaching $\lambda = 1$, an effect that is attenuated linearly when retarding CA50.

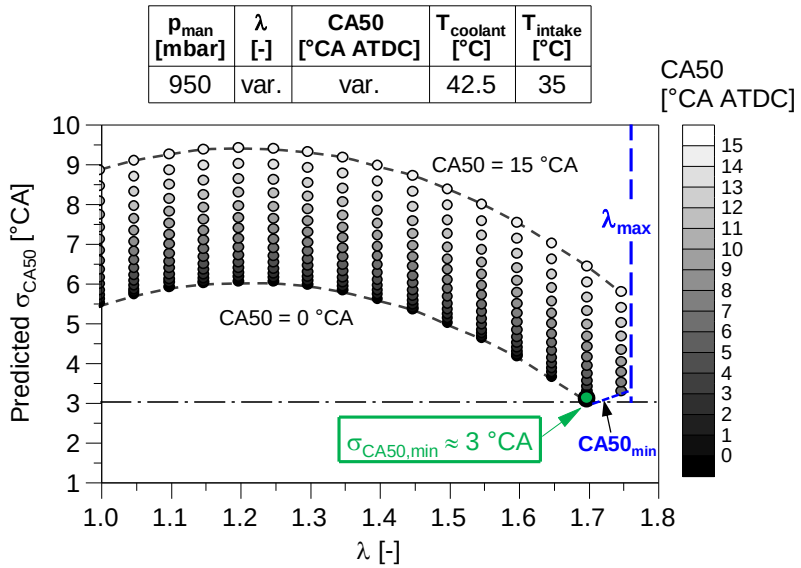

Figure 7.26: Predicted σ_{CA50} as a function of relative air-fuel ratio λ and combustion phasing CA50.

One implemented functionality in the 0D model is that both phasing and duration of heat release can be subjected to cycle-by-cycle variations. Amongst others, this allows assessing how CCV affect the thermal and electric state of the glow plug and derive strategies to increase controller robustness against external disturbances. To this end, the response equation of σ_{CA5} is used to add a cycle-individual offset to the set value of α_{SOC} (crank angle for the start of combustion) given by the Vibe function. In the same manner, the equation for σ_{CD} allows adjusting α_{EOC} in order to add cyclic variation to combustion duration.

7.4.1.3 Fuel Consumption and Emissions

Arguably the biggest combustion-related challenge of naturally aspirated lean-burn engines is to operate at high fuel economy while producing low NO_x emissions. Results of statistic data analysis for ISFC, NO_x as well as for HC and CO emissions are given in Table 7.6. The trials did not reveal any significant relationship between intake and coolant temperature (factors B and E) and both ISFC and NO_x. This agrees well with the

findings from the OFAT analysis, where both factors only exerted a minor influence, not sufficient to matter statistically when a wide spread in the response is recorded.

Table 7.6: Equations for response surfaces of indicated specific fuel consumption (ISFC) and emissions as a function of factors A-E in coded notation (-1, 1).

	Response	ISFC [g/kWh]	ln(NOx) [ppm]	sqrt(HC) [ppm]	ln(CO) [ppm]
	Intercept	241.56	6.57	51.01	6.89
MAIN EFFECTS	A – p_man	-36.39	0.36	-5.90	-0.23
	B – T_coolant			-2.64	-0.03
	C – Lambda	23.04	-2.64	37.42	0.18
	D – CA50	-3.11	-0.65	-0.60	-0.03
	E – T_intake			4.84	-0.03
INTERACTIONS	AB				-0.09
	AC	-18.99	0.28	-3.32	0.10
	AD	4.48		2.01	
	AE				-0.14
	BC			-2.21	
	BD				
	BE			1.66	
	CD		-0.39	2.16	
	CE				
	DE			2.09	0.10
HIGHER ORDER EFFECTS	A2	22.20	-0.08	-2.57	
	B2				-0.14
	C2	33.72	-1.11	24.22	0.55
	D2	8.86			0.11
	E2			-0.64	-0.15
	A3		0.27		
	B3				
	C3	14.05	0.36		-0.23
	D3				
	E3			-6.38	
	Pred. R^2	0.956	0.988	0.983	0.720

The perturbation plot in Figure 7.27 (top) shows the individual effect of relevant factors A, C and D on ISFC (note that emission responses are natural logarithm or square root transformations). While the role of factors A (p_{man}) and C (λ) is predominant, factor D (CA50) is also significant but has a relatively small quadratic effect on the response. It causes a minimum in ISFC slightly to the right of the intercept (CA50 = 7.5 °CA ATDC), in the range of MBT combustion phasing. Increasing pumping losses, residual gas fractions and wall heat losses are responsible for the gradual increase in ISFC when throttling. The response to λ is slightly more complex due to the impact of interaction AC in combination with quadratic and cubic effects. As can be seen in the response surface, at maximum intake pressure fuel consumption is lowest around $\lambda = 1.3 - 1.4$. When reducing p_{man}, the minimum shifts gradually towards stoichiometric, predominantly as a result of the slowed combustion. For $p_{man} \leq 700$ mbar it applies that $ISFC_{min}$ is at $\lambda = 1.0$.

For the NO_x response (see Figure 7.27, bottom), combustion phasing proves to be similarly important to intake manifold pressure, with a quadratic term to account for the non-linear increase of NO_x when advancing CA50. NO_x production is enhanced quite linearly with p_{man} until about 900 mbar. For higher pressures, however, gas dynamic effects

that improve cylinder filling provoke a sudden rise in combustion temperature and higher NO_x emissions. This effect is represented well by the cubic term of factor A. The perturbation trace of λ shows a well-known shape with a peak at slightly lean-of-stoichiometric mixtures. To the lean side of the NO_x formation maximum, increasing λ is a very effective means to reduce NO_x. Nonetheless, the trace shows an inflexion point close to the intercept (λ = 1.39), making further mixture dilution less effective due to the decreasing slope of the function.

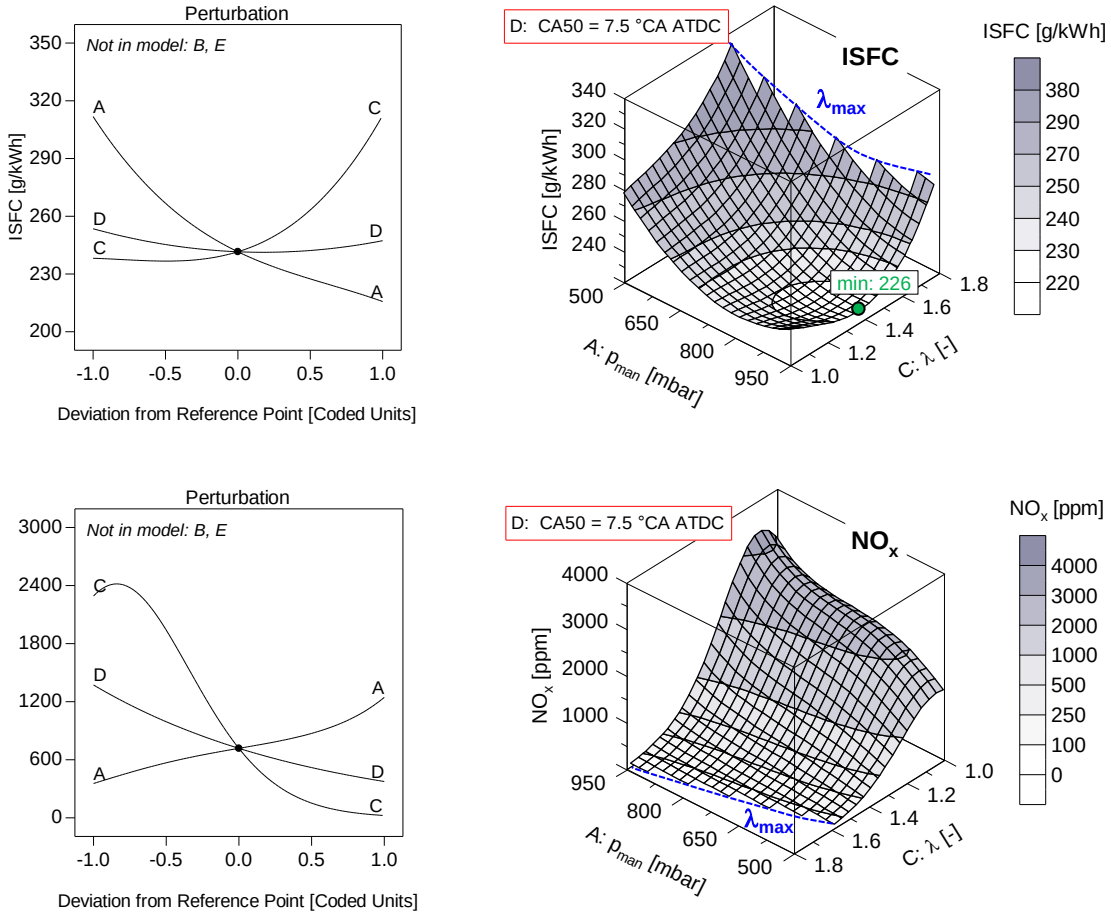

Figure 7.27: Perturbation plots of ISFC (top) and NO_x (bottom) and the respective response surfaces for factors A (p_{man}) and C (λ) with factor D (CA50) set to coded 0 (intercept).

HC and CO emissions show dependencies to all factors, yet they too are most sensitive to intake manifold pressure and λ. As can be seen in Figure 7.28 (left), HC is notably dependent on λ, exhibiting very high values at the lean-burn limit. This correlates well with the low-NO_x regime where combustion temperatures are low, promoting flame quenching effects (larger quenching distance) as well as partial burns. The CO output, on the other hand, is less sensitive to changing operating conditions. The contour plot in Figure 7.28 (right) shows a CO minimum in the middle of the investigated λ range, with a moderate increase when throttling.

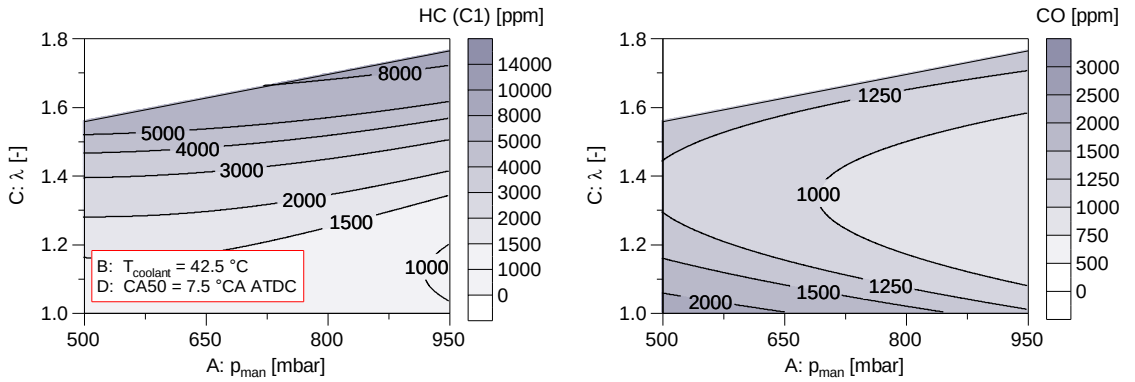

Figure 7.28: Contour plots of HC (right) and CO (left) response equations as a function of factors A (p_{man}) and C (λ) when setting less significant to coded 0 (intercept).

7.4.1.4 HSI Operating parameters

Even after replacing the faulty glow plug after Run 12, the new glow plug showed clear signs of degradation along the RSM experiment. Still, it was possible to derive useful correlations when analysing parameters U_{HSI}, I_{HSI} and P_{HSI} for Runs 13 – 42 statistically. Table 7.7 shows their prediction equations as well as the ones for R_{HSI} and calculated T_{HS}. U_{HSI}, I_{HSI} and P_{HSI} all depend on the same main effects and interactions, leading to the following uniform trends: The value of their response decreases with p_{man} and $T_{coolant}$, and increases with λ. To the contrary, the response to CA50 is strongly influenced by interactions, leading to different trends over the experimental space. To analyse these relationships in depth, Figure 7.29 lays out constant pressure responses for all variables as a function of CA50, derived from the response surface equation with λ and $T_{coolant}$ set to coded 0 (λ = 1.39, $T_{coolant}$ = 42.5 °C). First, however, it is important to revisit the two essential dependencies determined in the CA50 sweep from Section 7.3.1: a) that P_{HSI} decreases when advancing CA50 although HS temperature is raised, and b) that U_{HSI} remained practically constant, in spite of the adjusted combustion phasing. As can be seen from the curves of U_{HSI} and P_{HSI}, this only applies for specific factor combinations. Initially, starting at maximum intake manifold pressure, U_{HSI} needs to be reduced when advancing CA50. With decreasing pressure, the positive slope of the constant pressure line is gradually reduced. Once the gradient is 0, indicated by the dashed horizontal line between 700 and 750 mbar, U_{HSI} remains constant, regardless of combustion phasing. As p_{man} is reduced further, the slope becomes negative and U_{HSI} needs to be increased to advance the combustion. The same effect can be observed for P_{HSI}, where the horizontal line (between 600 and 650 mbar) can be used to bisect the operating range into two regimes. In regime A, on the one hand, the increased convective heat input from combustion when advancing CA50 outweighs the increased losses by conduction and radiation resulting from the higher hot surface temperature. As a result, electric power can be reduced. In regime B, on the other hand, higher temperatures are necessary for timed ignition while the amount of heat released decreases. Both factors combined cause increasing thermal losses when advancing CA50, which exceed the heat gains from combus-

tion and require an increase of P_{HSI}. The traces of I_{HSI} indicate a similar behaviour, yet only at the lower end of the p_{man} range. Since the terms $\dot{Q}_{conv}$ and $\dot{Q}_{loss} = \dot{Q}_{cond} + \dot{Q}_{rad}$ are responsible for this behaviour, all factors involved in the respective heat transfer relations, such as flow conditions in the vicinity of the glow pug tip or material and emissivity of the HSI adapter, can considerably alter the dependencies presented herein. In fact, when leaning the mixture, the traces in Figure 7.29 rotate clockwise, shifting the transition line to higher intake manifold pressures.

Table 7.7: Equations for response surfaces of HSI parameters as a function of factors A-E in coded notation (-1, 1). Runs 1 – 12 with glow plug No. 5 were excluded from the analysis.

	Response	U_HSI [V]	I_HSI [A]	P_HSI [W]	R_HSI [mΩ]	T_HS [°C]	T_HS (grad. ageing) [°C]
	Intercept	5.58	6.14	34.60	903.1	1048.7	1084.3
MAIN EFFECTS	A – p_man	-0.35	-0.35	-3.87	-6.3	-67.7	-72.1
	B – T_coolant	-0.05	-0.07	-0.69	1.2	-8.4	-16.7
	C – Lambda	0.65	0.67	7.48	9.5	67.0	90.4
	D – CA50	0.00	0.17	0.83	-25.8	-32.2	-49.5
	E – T_intake				-2.3		
INTERACTIONS	AB				8.9	23.8	
	AC	0.14	0.21	1.48			
	AD	0.17	0.18	1.86			
	AE				-8.4		
	BC						
	BD						
	BE						
	CD	-0.14	-0.13	-1.31			
	CE						
	DE						
HIGHER ORDER EFFECTS	A2						
	B2						
	C2				14.9		69.5
	D2						
	E2						
	A3						
	B3						
	C3						
	D3						
	E3						
	Pred. R^2	0.915	0.916	0.926	0,662	0.779	0.923

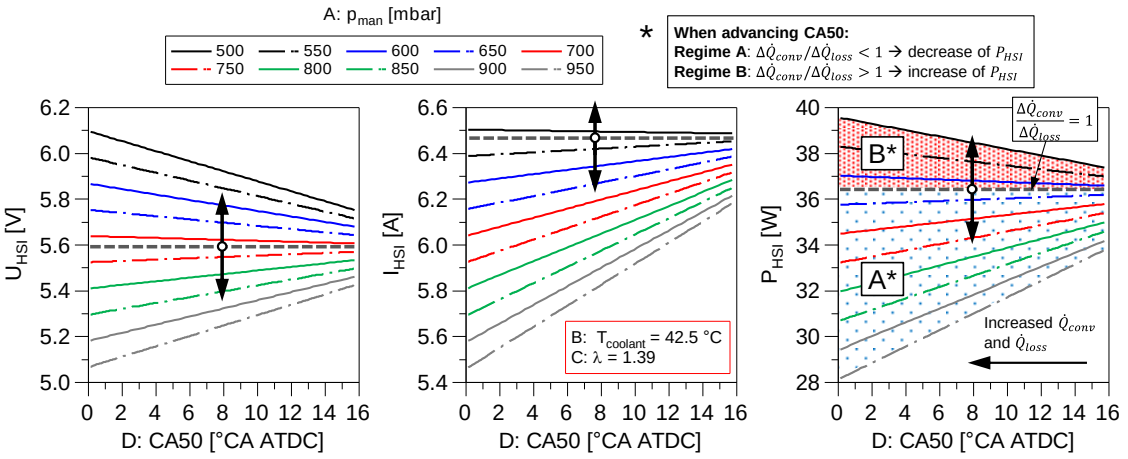

Figure 7.29: Response curves of U_{HSI}, I_{HSI} and P_{HSI} against CA50 for different intake manifold pressures p_{man} (factors B and C set to coded 0).

Figure 7.30 (left) depicts predicted against actual R_{HSI}. The value of $R^2 = 0.808$ suggests a rather strong linear correlation but the calculated $R^2_{pred} = 0.662$ is much lower. Large differences in both numbers are indicators for a biased prediction and indicate that glow plug ageing was significant. For this reason, in an attempt to increase the accuracy of the calculated value of HS temperature, a linear time-dependent correction factor was applied to R_{ageing}. Figure 7.30 (right) compares the respective model response of T_{HS} to the response when a constant ageing condition is assumed for all runs. For both cases, R_{ageing} was calibrated using an additional run at the end of the RSM experiment. It can be seen that the assumption of a gradual increase of R_{ageing} (1.6 mΩ/OP) allows for a significant improvement of model quality. This is reflected in a slope of the regression close to unity, a reduced offset, a higher R^2 and, most importantly, a greatly improved R^2_{pred}. This gives strong indication that glow plug degradation occurs while the engine is operating, yet it is still unclear if caused thermally (e.g. by molecular diffusion), mechanically (e.g. by engine vibration) or a combination of both.

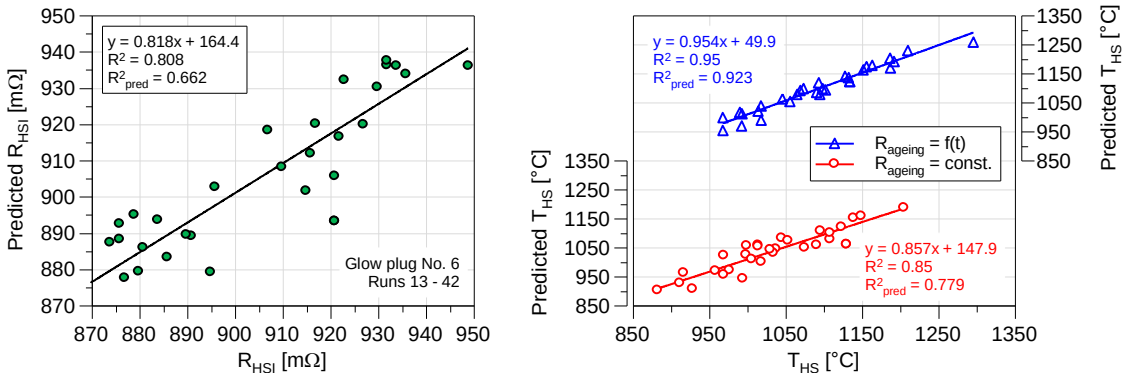

Figure 7.30: Predicted R_{HSI} from response surface equation against actual R_{HSI} (left) and predicted T_{HS} against actual calculated T_{HS} (right).

7.4.1.5 Combustion Process Optimisation

The response surfaces for ISFC, NO_x and IMEP are very helpful for determining optimal engine operation settings when trade-offs or particular restrictions apply. This shall be illustrated briefly with the aid of two specific examples using the calculated ISFC-NO_x trade-off from Figure 7.31. In both plots, each grey marker represents the prediction from the response surface equation of a specific factor combination at variable intake manifold pressure, λ and combustion phasing. Coolant and intake temperatures were kept constant. When supposing that IMEP > 6.0 bar is a requirement and an according filter is applied to the candidate data set shown in the left plot, it becomes clear that maximum p_{man} and a stoichiometric mixture mixture are required to set this engine load. At the same time, the minimum NO_x output achievable is at a very high level of approx. 2900 ppm. If, on the contrary, the aim were to meet an arbitrary NO_x limit of 100 ppm at maximum possible load, as shown in the right plot, the mixture would need to be leaned significantly to λ = 1.7, causing a drop in IMEP to 3.5 bar at the point of mini-

mum fuel consumption. In future experiments, this optimisation procedure can be used to find optimal factor settings for meeting the CR EU No. 813/2013 NO_x limit, while maximising IMEP and minimising ISFC in unthrottled operation.

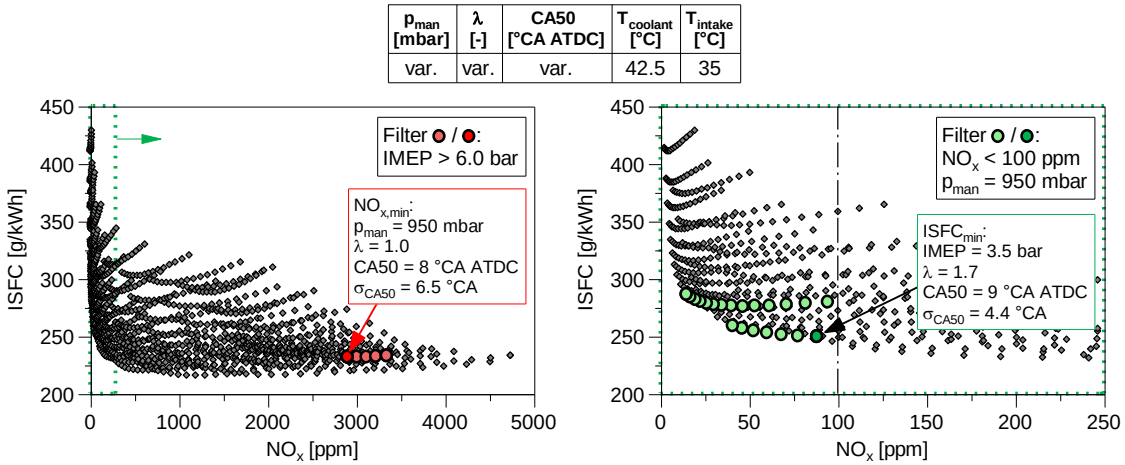

Figure 7.31: Predicted ISFC-NO_x trade-off with exemplary filters.

7.4.2 Replicate Points

Five additional replicate points (RP), randomly chosen and spread over the entire experimental space, were added to the RSM design as a test for repeatability (see RSM run sheet in Table A.4 from the Appendix). Table 7.8 shows the overview of the pairwise comparison of runs:

Table 7.8: Overview of replicate operating points from RSM experiment. Runs with white filling were recorded using glow plug No. 5, runs with grey filling with glow plug No. 6.

		R_{HSI} [mΩ]		P_{HSI} [W]		$T_{adapter}$ [°C]		ISFC [g/kWh]		NO_x [ppm]		σCA50	
		OP1	OP2	OP1	OP2	OP1	OP2	OP1	OP2	OP1	OP2	OP1	OP2
RP 1	OP1: Run 4	962	877	33.5	34.1	221.5	229.9	231.3	226.2	329	429	10.6	9.2
	OP2: Run 35												
RP 2	OP1: Run 5	995	874	33.9	36.5	214.4	219.1	234.8	236.0	197	193	6.5	7.0
	OP2: Run 21												
RP 3	OP1: Run 6	1017	1101	26.8	27.0	248.7	247.5	231.8	231.5	2544	2499	6.0	6.3
	OP2: Run 12												
RP 4	OP1: Run 17	879	884	35.2	34.2	208.0	206.7	271.4	271.1	948	938	7.0	7.2
	OP2: Run 29												
RP 5	OP1: Run 9	1027	921	30.0	32.5	212.9	215.4	253.3	254.1	1464	1449	6.5	6.1
	OP2: Run 41												

Due to glow plug failure, only two replicate points were recorded using the same glow plug in each run. With exception of RP 1, where the same combustion phasing could not be set due to high CCV ($\Delta CA50 = 2.3$ °CA), differences in factor settings (A-E) were negligible. The content of the table allows for the following conclusions:

– *Glow plug ageing:* Glow plug ageing is significant as R_{HSI} increases from one run to another (see RP 3 and 4) but no uniform trend of the effect of ageing on the electric power demand P_{HSI} can be found. Similarly, ageing does not seem to have a significant effect on HSI adapter temperature.

- *Glow plug specimen:* Glow plug No. 5 has a moderately lower power demand and shows somewhat lower HSI adapter temperatures. These differences are the result of different ageing conditions and manufacturing tolerances that result in individual resistance-temperature correlations.
- *Combustion parameters:* With exception of RP1, values of ISFC, NO_x and CCV in combustion phasing are in exceptional agreement, giving proof that operating points are highly reproducible, regardless of the glow plug specimen used and its ageing condition.

7.4.3 Conclusion

The systematic Design of Experiments approach using the Response Surface Methology presented gives a comprehensive understanding of how dependent engine parameters (responses) react to changes in operating conditions (factors) and allows for these relationships to be expressed through multiple regression equations, valid for the entire investigated HSI operating range. The correlations found for $T_{adapter}$, T_{man}, combustion duration and CCV can be implemented as empirical submodels in the 0D HSI engine process simulation model, thereby limiting the number of required numerical model inputs. From the correlations for ISFC, NO_x and IMEP, optimal operating points can be derived. A practical example are predictions about the achievable IMEP and ISFC when a specific NO_x limit needs to be met. Furthermore, the statistical analysis of the RSM data revealed a systematic error in the calculated response of HS temperature. The prediction quality of the response surface equation could be improved considerably by assuming a time-dependent ageing condition of the glow plug, defined by an increasing resistance R_{ageing}. This gives strong indication that the degradation process is gradual and directly linked to engine operation time rather than single events like engine start and stop. Finally, a finding that was already presented in Section 6.2 and confirmed by the replicate points recorded is that the combustion process is not sensitive to glow plug ageing or the glow plug specimen, i.e. thermo-electric properties of the HSI system, as long as HSI resistance is set such that combustion phasing remains constant.

7.5 Comparison to Prechamber Spark Ignition

The HSI system presented in this work was developed as an alternative to the state-of-the-art prechamber spark ignition (PCSI) technology employed in the production cogeneration engine. Besides the prospect of enhanced durability and reduced systems costs, HSI was expected to yield combustion-related advantages such as an accelerated process of mixture inflammation, the enhancement of the lean-burn limit and an improvement of the trade-off between engine efficiency/ISFC and NO_x emissions. For a direct comparison between both ignition systems, several runs from the RSM design were selected. Prior to this, however, the operating limits of PCSI in terms of λ and CA50 was determined in

full factorial screening trials (following the same procedure as shown for HSI in Figure 7.1). The lean-burn limits for both HSI and PCSI are displayed in Figure 7.32 as a function of intake manifold pressure, giving proof that significantly leaner mixtures ($\Delta\lambda = 0.1 - 0.15$) can be ignited safely with HSI. For spark ignition, further leaning is limited by misfires caused by quenching effects during the formation of the flame kernel. The convoluted CA50 limitation that manifests in HSI operation (see Section 7.1.2) was not given for PCSI. On the contrary, below the LBL it was possible to set combustion phasings over the entire CA50 range considered (0 – 30 °CA ATDC), regardless of intake pressure.

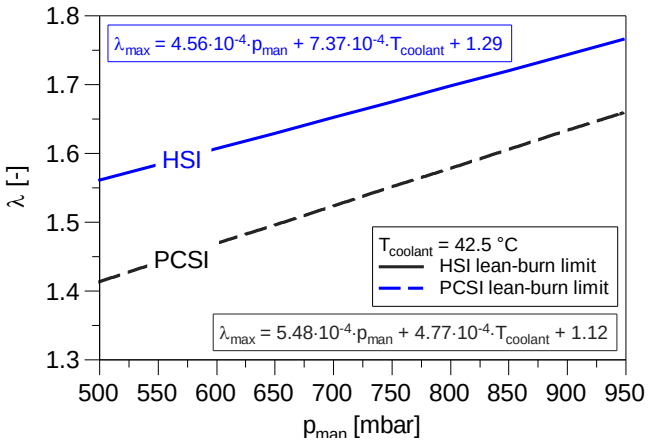

Figure 7.32: Lean-burn limit (LBL) of Hot Surface Ignition (HSI) and Prechamber Spark Ignition (PCSI) as a function of intake manifold pressure p_{man} at constant coolant temperature $T_{coolant}$ = 42.5 °C.

After deriving the limitations for PCSI operation, the five runs shown in Table 7.9 were selected under the premise of being dispersed over the entire experimental space and having a relative air-fuel ratio below the LBL of PCSI. Unfortunately, the lower LBL for PCSI impedes a direct comparison in the regime where HSI performs best in terms of CCV, i.e. at very high mixture dilution ($\lambda > 1.7$) and maximum intake manifold pressure. As can be seen from the recorded factor readings provided in the table, it was possible to reproduce the settings from HSI operation with very low error.

Table 7.9: Selected RSM operating points for direct comparison between HSI and PCSI operation

	p_{man} [mbar]		$T_{coolant}$ [°C]		λ [-]		CA50 [°CA ATDC]		T_{intake} [°C]	
	HSI	*PCSI*	*HSI*	*PCSI*	*HSI*	*PCSI*	*HSI*	*PCSI*	*HSI*	*PCSI*
Run 4	949.1	949.2	32.1	32.7	1.484	1.482	15.49	15.36	32.7	32.7
Run 24	776.7	775.9	24.8	24.7	1.489	1.490	3.75	3.86	27.7	27.6
Run 30	950.4	950.6	59.4	59.5	1.076	1.078	3.63	3.66	44.5	44.6
Run 31	500.5	501.0	50.4	50.3	1.171	1.171	-0.03	-0.01	45.1	45.3
Run 34	501.6	499.7	59.3	59.4	1.309	1.310	15.09	15.17	42.4	42.8

The experimental results of ISFC and NO_x for both ignition systems are presented in the trade-off plot in Figure 7.33. It shows that PCSI performs better in all runs, allowing for better fuel economy while producing lower levels of NO_x. Thus, the HSI system is unable

to improve the trade-off in the range where both ignition systems function. To determine what causes the significant disadvantages in HSI operation and derive strategies to further improve the ignition system, the combustion process as a whole is subjected to a detailed examination in what follows.

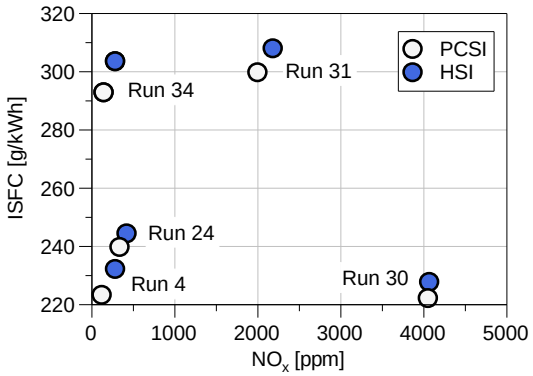

Figure 7.33: Comparative ISFC-NO_x trade-off for selected RSM operating points for Hot Surface Ignition (HSI) and Prechamber Spark Ignition (PCSI).

IMEP, CA5, their respective standard deviations and the duration of characteristic parts of combustion are presented in Figure 7.34 for both HSI and PCSI. A first major advantage of spark ignition is the substantially lower values of σ_{IMEP} and σ_{CA5} that give evidence of a lower variability in combustion for all operating points recorded. Unlike for HSI, where the timing of mixture inflammation depends on the ignition delay of the mixture, for spark ignition it depends on spark timing and burning delay. Due to the low variability in flow conditions inside the prechamber, burning delay proved fairly reproducible from cycle to cycle, yielding a low standard deviation of CA5, with values spanning between 0.3 and 0.9 °CA. As opposed to this, HSI shows much higher values, between 4.9 and 8.9 °CA. As a result, the phasing of heat release fluctuates from cycle to cycle, causing a larger spread in IMEP. With the exception of Run 30, this produces a loss in IMEP of 2.1 – 3 %. The advantage of 2.8 % in Run 30 is ultimately caused by a combination of reduced flame-piston interaction and a large fraction of cycles burning close to MBT. The second combustion-related advantage of PCSI is revealed when analysing the trends in σ_{CA5} and combustion duration. Unlike initially expected, the duration CA5-CA10 shows that HSI does not increase the reaction rate at the beginning of combustion. On the contrary, this phase takes about 13 to 56 % longer. The first part of combustion CA5-CA50 exhibits an identical trend, suggesting that the flame torches ejected from the prechamber are a more effective means to promote rapid flame growth and shorten combustion than the increased reactive mixture of the hot surface. The fact that the second part of combustion is also prolonged, albeit not to the same extent as the first part, gives strong indication that the torches also increase the surface area of the flame front by self-generated turbulence in the main combustion chamber and a larger number of initial flame kernels. Since every phase of HSI combustion is slower, evidently, the result is a longer combustion duration CA5-CA90. For the factor combinations considered, the increase amounts to 6.3 – 22.9 %.

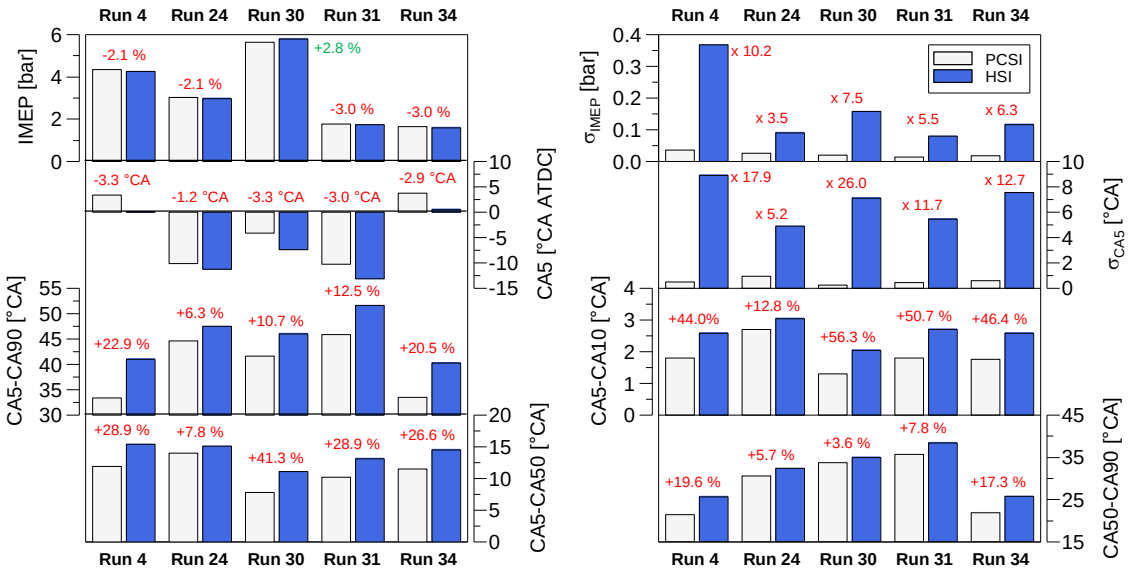

Figure 7.34: Comparison of selected combustion data for HSI and PCSI.

To address the question of whether the increased combustion duration is merely a result of the increased cyclic variability or also caused by the way the mixture is inflamed, Run 4, an operating point that shows particularly high CCV when operating with HSI, was chosen for a cycle-individual combustion analysis of the entire 1000-cycle ensemble. Figure 7.35 compares selected combustion data as a function of CA5:

Run	p_{man} [mbar]	$T_{coolant}$ [°C]	λ [-]	CA50 [°CA ATDC]	T_{intake} [°C]
4	950	32.9	1.484	15.0	32.7

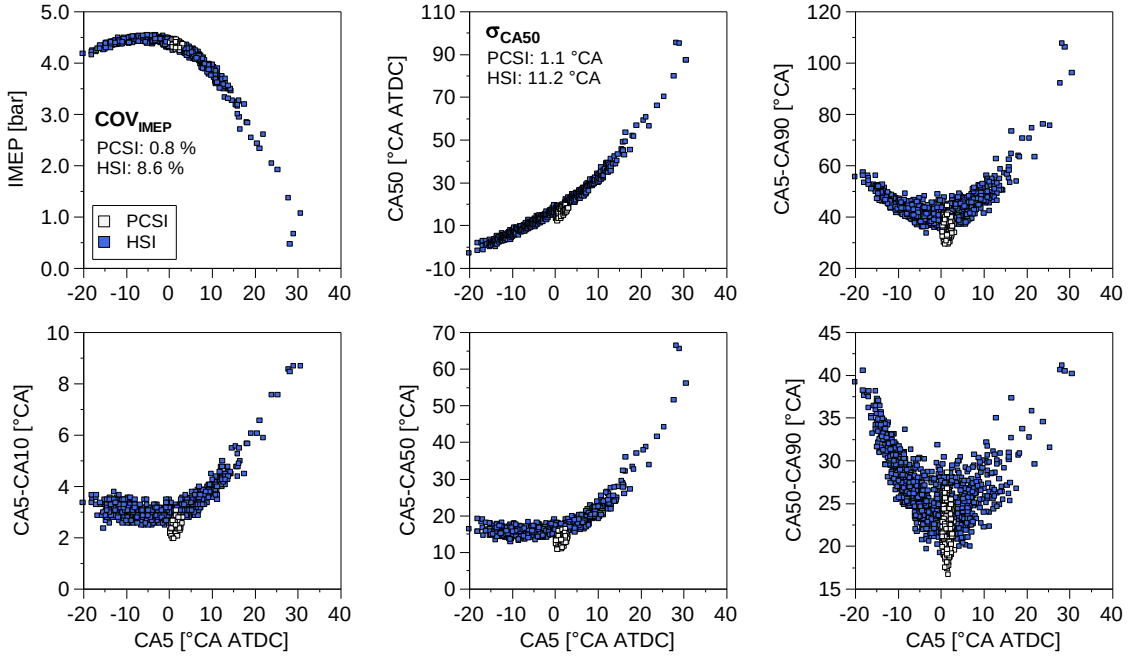

Figure 7.35: Comparison of cycle-individual IMEP, combustion phasing CA50 and combustion duration against CA5 for Hot Surface Ignition (HSI) and Prechamber Spark ignition (PCSI) for Run 4.

Due to the long ignition delay and late combustion phasing, it can be seen that HSI operation is highly unstable, with cycles spanning from overadvanced combustion to partial

burns. The scatter plot of duration CA5-CA10 against CA5 shows a slight downwards trend until TDC and then increases markedly, indicating a reduced rate of flame kernel growth. The same trend can be observed in the plot for CA5-CA50, causing the relationship between CA5 and CA50 to cease being linear when moving further along the x-axis. This is a result of several factors reducing the flame propagation speed: Firstly, mixture temperature falls during the expansion stroke, causing a decrease in laminar flame speed; Secondly, if SOC is retarded, the turbulence level of the cylinder charge is lower during flame propagation, as calculated using the CFD model; Finally, the flame travel distance increases as the piston moves downwards. The plot of CA50-CA90 shows a distinct parabolic shape with a minimum shortly after TDC. As outlined in Section 7.3.2, this dependency is characteristic of the flame-piston interaction. It is interesting to note that the spread in the duration of the second part of combustion peaks at this minimum, suggesting that piston interaction adds some variability to the combustion process, regardless of the ignition system used.

7.5.1 Effect of Combustion Duration

For an isolated examination of combustion duration and variability in the combustion process without the influence of CCV in combustion phasing, all cycles with same CA50 (15 °CA +/- 0.5 °CA) were selected for both HSI and PCSI operation. Figure 7.37 depicts cycle-individual combustion duration divided in three phases: CA5-CA10, CA10-CA50 and CA50-CA90. PCSI provides a much larger data pool for analysis than HSI (367 to 39 cycles) due to the much lower fluctuation in CA50. The key findings when comparing both ignition systems is that, in fact, HSI induced combustion is slower in every phase (CA5-CA10: +0.5 °CA, CA10-CA50: +1.8 °CA, CA50-CA90: +2.5 °CA) showing higher cyclic fluctuations as indicated by the standard deviation SDEV. For both ignition systems, the variance in combustion duration is highest for the phase CA50-CA90. During this part of combustion the large flame front becomes increasingly distorted by the turbulent flow field in the combustion chamber. Since cycle-by-cycle variations in local turbulence intensity and scale are intrinsic of the turbulent flow, shape and surface of the flame front are subject to fluctuations, leading to an enhanced variability in heat release rates.

To determine how a slower combustion affects in-cylinder pressure, the cycles with longest and shortest combustion duration at same combustion phasing were selected. As can be seen from their pressure histories over crank angle shown in Figure 7.37, a slowing combustion causes a larger heat release before TDC. This results in higher peak pressures, which, in turn, portends higher combustion temperatures. Since the peak pressure is moderately higher than for PCSI, it is expected that HSI operation produces higher levels of NO_x when operating at same combustion phasing. Nevertheless, it is more likely that CCV in combustion phasing play the predominant role in NO_x formation. Because CCV are directly linked to the engine operation factors and both the mass flow meter

and the exhaust gas analyser only give integral readings, the isolated effect of cyclic variability on fuel consumption and NO_x cannot be examined in HSI operation. Therefore, an alternative method using the prechamber spark plug was developed, where variability in the start of combustion is simulated by a cycle-by-cycle adjustment of spark timing.

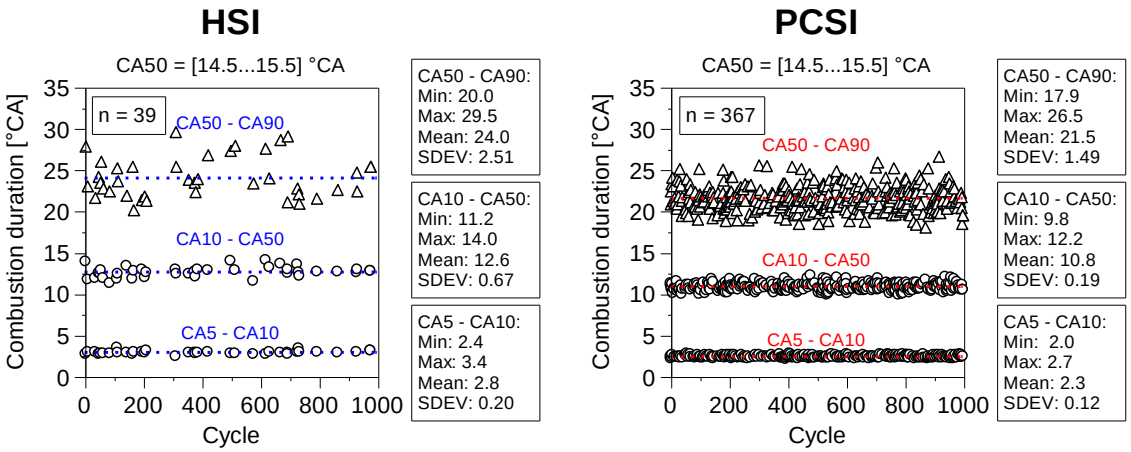

Figure 7.36: Combustion duration for HSI (left) and PCSI (right) operation for cycles with same combustion phasing CA50 = 15 °CA ATDC (Run 4, p_{man} ≈ 950 mbar, λ ≈ 1.48).

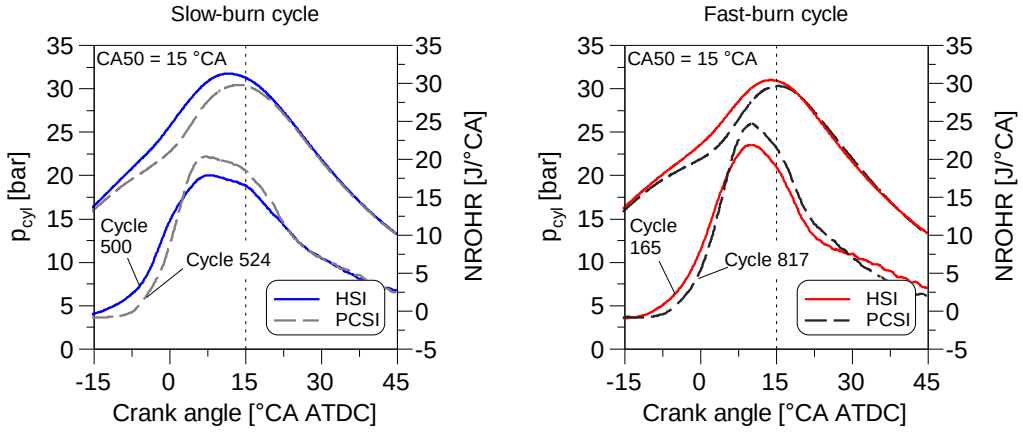

Figure 7.37: Comparison of fastest- and slowest-burning cycles with combustion phasing CA50 = 15 °CA ATDC (Run 4, p_{man} ≈ 950 mbar, λ ≈ 1.48).

7.5.2 Effect of Cyclic Variations in Start of Combustion

To simulate the high combustion variability of HSI operation with prechamber spark ignition, the following approach was adopted: As illustrated in Figure 7.38, a vector with normally distributed numbers $N(0,1)$ was created using the Marsaglia polar method. This vector is multiplied by the additional parametric variable σ_{ST} introduced in the LabVIEW GUI to give a distribution in the form $N(0,\sigma_{ST}^2)$. The result is then added to the set value of spark timing, also defined by the user, yielding a vector with cycle-individual spark timings with μ = ST and $\sigma = \sigma_{ST}$ that is sent to the ECU. To avoid misfires caused by outliers with extremely retarded or advanced spark timings, particularly for high values of σ_{ST}, the distribution was limited to +/- 2 σ. CA50 sweeps in the normal HSI operating range (0 – 15 °CA ATDC) were run for different values of σ_{ST}. Remaining

factors were set to p_{man} = 950 mbar, λ = 1.5, $T_{coolant}$ = 45 °C and T_{intake} = 25 °C.

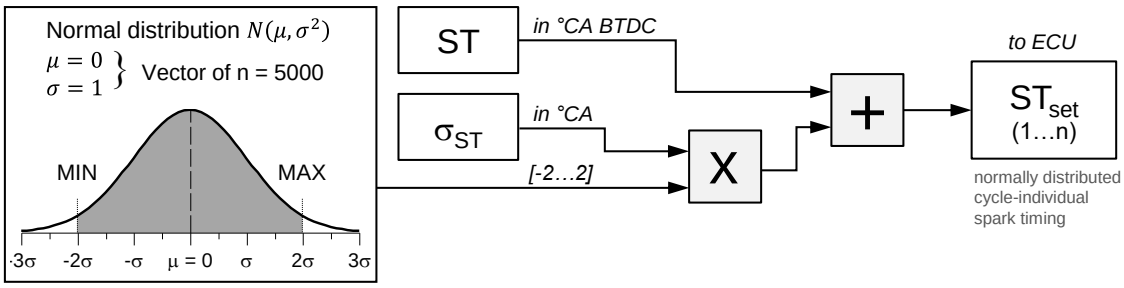

Figure 7.38: Process for creating normally distributed variations in spark timing.

Figure 7.39 shows the influence of increasing cyclic variability in spark timing on CA5 and CA50. Spark timing was set to MBT at $\sigma_{ST} = 0$. As expected, an increase of σ_{ST} translates into and increase of both σ_{CA5} and σ_{CA50}, although the relationship is not linear. While the effect of spark timing on combustion variability is low for small values of σ_{ST}, it is enhanced gradually, resulting in comparable standard deviations at σ_{ST} = 10 °CA.

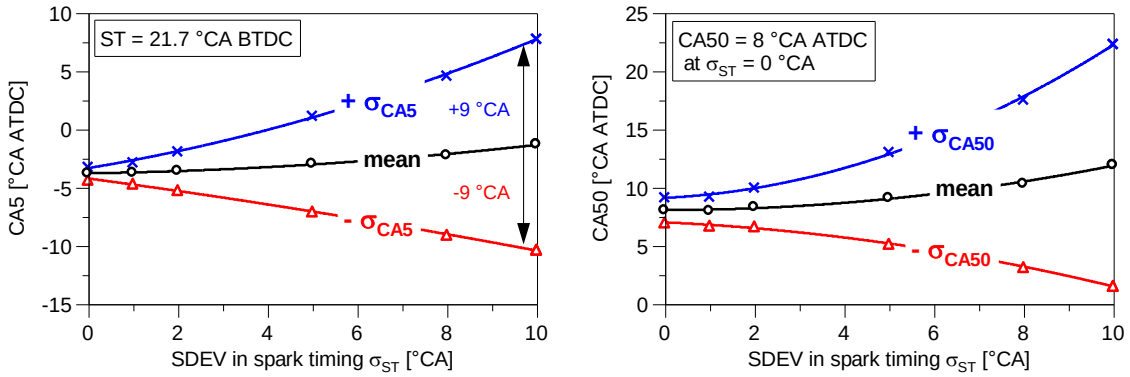

Figure 7.39: Spread in CA5 and CA50 as the standard deviation in spark timing σ_{ST} is increased (p_{man} = 950 mbar, λ = 1.5, $T_{coolant}$ = 45 °C and T_{intake} = 25 °C).

To understand what causes the retarding values of CA5 and CA50 in spite of a constant mean spark timing, relative frequencies of IMEP, CA50 and p_{max} of the 1000 cycle-ensemble of three operating points at σ_{ST} = 0/5/8 °CA are compared directly in Figure 7.40. The dependency between CA5 and CA50 can be approximated well with linear regression for early to moderate starts of combustion. As combustion phasing is retarded, however, main combustion (CA5 – CA50) is lengthened, leading to a fairly quadratic functional dependency. Since variation in spark timing is equally distributed to both sides of the mean, cycles with advanced spark timing will give rise to a linear advancement of CA50, while later spark timings will cause a quadratic retarding of CA50. Therefore, late-burning cycles will have bigger leverage on mean CA50, causing it to be retarded relative to the operating point with same spark timing at σ_{ST} = 0 °CA. With increasing variability in spark timing, IMEP drops as an increasing fraction of cycles show significantly lower cycle-individual IMEP. The absolute value of the loss is lowest when mean combustion phasing is set to MBT and increases moderately for advanced and markedly for

retarded combustion phasings. The increasing spread in p_{max} correlates strongly with CA50, producing few cycles with significantly higher, and many with lower peak pressures, causing the mean to decrease with increasing CCV. Owing to the variability in the heat release profile, combustion parameters such as combustion efficiency, combustion temperature, wall heat losses and engine work also become subject to cycle-by-cycle variations.

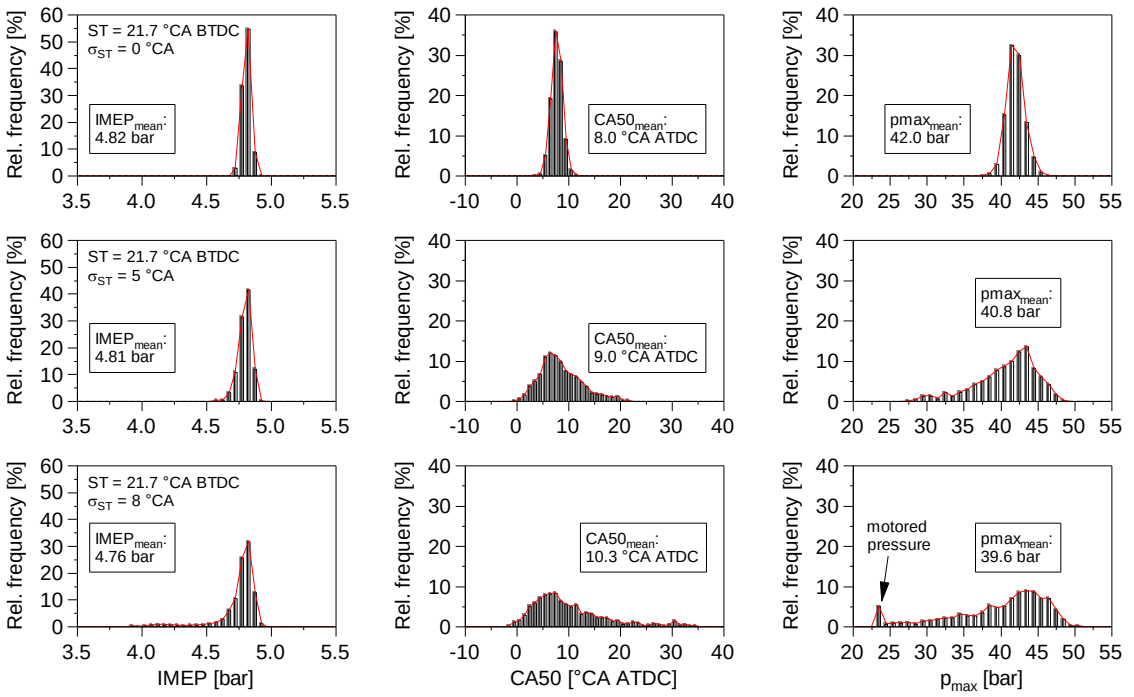

Figure 7.40: Relative frequencies of IMEP, CA50 and p_{max} for 1000-cycle ensemble for σ_{ST} = 0/5/8 °CA (p_{man} = 950 mbar, λ = 1.5, $T_{coolant}$ = 45 °C and T_{intake} = 25 °C).

Figure 7.41 depicts how increasingly unstable starts of combustion exert leverage on the NO_x output and fuel economy:

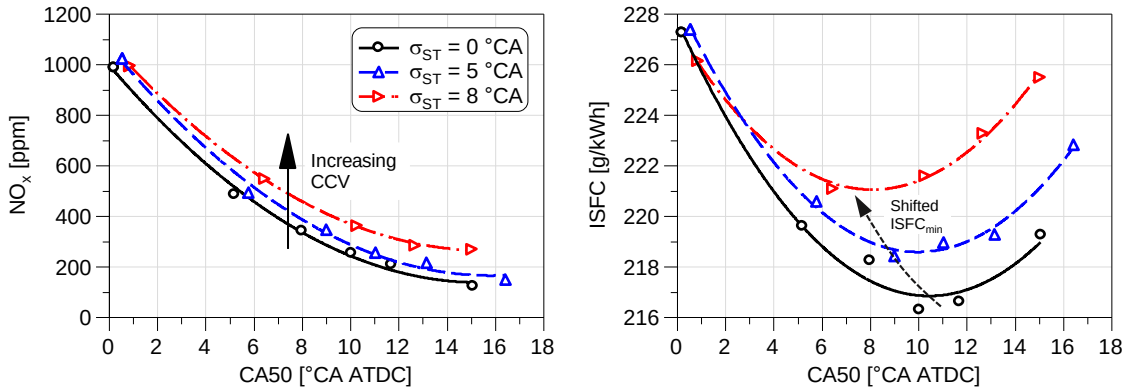

Figure 7.41: NO_x emissions and ISFC as a function of combustion phasing CA50 and standard deviation in spark timing σ_{ST} (p_{man} = 950 mbar, λ = 1.5, $T_{coolant}$ = 45 °C and T_{intake} = 25 °C).

An increasing standard deviation in spark timing leads to a considerable rise in NO_x. The effect is most pronounced for late CA50 (increase of about 100 ppm at σ_{ST} = 8 °CA) and decreases when approaching TDC. This behaviour arises from the non-linear relationship

between combustion phasing and NO_x. The kinetics that control NO_x formation depend exponentially on combustion temperature, thus explaining the exponential increase as CA50 is advanced. When the combustion process is subject to large fluctuations, early-burning cycles will produce proportionally higher NO_x than equally retarded cycles. As a result, they exert a larger influence on mean NO_x and cause an increase respective to operation with lower CCV. In a similar manner, CCV prove to be detrimental to ISFC. While no direct effect can be observed at CA50 = 0 °CA ATDC, retarding CA50 leads to an increasing fuel penalty (up to 3.1 % at CA50 = 15 °CA ATDC and σ_{ST} = 8 °CA). Another interesting finding is that with CCV, the minimum in ISFC shifts slightly towards TDC, owing to the increasing number of late, poor-burning cycles that produce low engine work.

In summary, the series of experiments presented shows how cyclic variations in the start of combustion tend to increase NO_x and ISFC while causing a drop in IMEP. In order to verify if simulated CCV in spark timing allow reproducing HSI operation qualitatively, both ignition systems are compared directly for engine operation with similar factor settings (see Figure 7.42). The slightly leaner mixture and lower intake manifold pressure for PCSI cause mildly lower IMEP (-1.3 %).

Ignition system	p_{man} [mbar]	$T_{coolant}$ [°C]	λ [-]	CA50 [°CA ATDC]	T_{intake} [°C]	σ_{CA50} [°CA]	COV_{IMEP} [%]	IMEP [bar]	ISFC [g/kWh]	NO_x [ppm]	CA5-CA90 [°CA]
HSI	950.4	45.1	1.498	5.6	23.0	6.5	2.9	4.73	223.1	868	45.4
PCSI	949.8	45.0	1.501	7.5	25.0	7.3	3.0	4.66	223.4	513	41.3

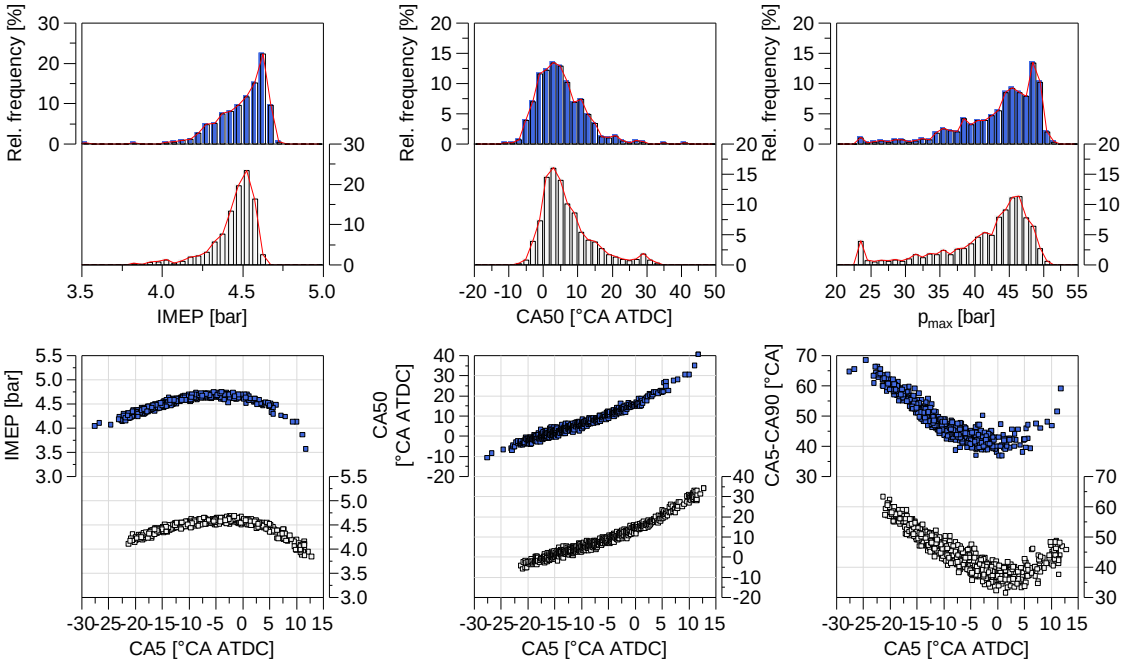

Figure 7.42: Comparison of selected 1000-cycle ensemble data for HSI and PCSI with similar variability in combustion phasing.

All dependencies and trends agree exceptionally for both ignition systems. The only noticeable difference in the combustion process is the slightly lengthened combustion for HSI (+4.1 °CA). While ISFC is on the same level, NO_x emissions are significantly higher

for HSI, a fact that cannot be explained solely by the slightly more advanced CA50 (-1.9 °CA) and higher IMEP but must be caused by the larger fractions of cycles with higher peak pressures and combustion temperatures. Cyclic variations in combustion phasing are very similar for both ignition systems and do not show a distinct sensitivity to combustion phasing.

7.6 Conclusion and Possible Improvements

The experiments conducted prove that HSI enables the engine to operate without misfires over a large experimental space. As a result of the increased reactive mixture volume, HSI is capable of enhancing the lean-burn limit compared to prechamber spark ignition and ignite premixed air-NG mixtures with significantly lower ignition quality reliably. At the same time, however, the experiments reveal that cycle-by-cycle variations in the timing of mixture inflammation are the underlying problem of HSI in its current design version. It was found that all factors that increase or require an increase of ignition delay haven an enhancing effect on CCV. When combustion is timed such that the start of combustion is close to TDC, pre-reactions taking place in the vicinity of the hot surface become more susceptible to local and cycle-individual mixture composition and temperature. This explains why CCV are highest for fuel-rich mixtures and retarded combustion phasings (low HS temperature and long ignition delay) and very lean mixtures ($\lambda > 1.7$) and advanced combustion phasings (high HS temperature and short ignition delay). In the region where both ignition systems can operate, PCSI shows significantly better combustion stability, performance and lower emission output. Nevertheless, HSI has the ability to ignite leaner mixtures, an interesting attribute when the loss in mean effective pressure can be compensated by forced induction (turbocharged engines) or for igniting low-grade gases with poor ignition quality like biogas or landfill gas. The expected advantage regarding an increased durability was not given due to experienced glow plug ageing. Based on these findings, the following subsections present possible improvements to the current system design.

7.6.1 HSI Control

Due to the random nature of the in-cylinder turbulence, a certain degree of combustion variability is unavoidable. Nevertheless, a steep increase of HS temperature towards the end of the compression stroke could help reducing the cyclic variations in inflammation timing to a level comparable to spark ignition. Boulouchos [23] proposed and tested an alternative approach to constant temperature control based on a timed short high-current pulse shortly before TDC. At an engine speed of 1500 1/min, he determined that about 1.5 J were necessary to raise the temperature of the platinum wire used by 100 K. To avoid large temperature losses during the pulse, its duration was minimised (about 0.1 ms), leading to an instantaneous electric power demand of 15 kW, provided by a

170 VDC power source. The system worked satisfactorily but the platinum coil employed suffered from rapid degradation, leading to short life-time. In this section, current pulse control is reviewed using the 0D HSI engine process calculation model presented in Section 5.4. The current pulse is generated by applying a constant DC voltage to the glow plug. Commonly, standard high-power switched-mode power supplies (SMPS) have rated voltages of 12, 24 and 48 V and are relatively inexpensive. For this reason, these voltage levels were tested and compared to conventional resistance control. Figure 7.43 shows controller behaviour for a simulated operating point at p_{man} = 950 mbar and λ = 1.50. The duration of the pulse was adjusted for each voltage until reaching steady-state temperature conditions (same T_{HS} at start and end of the cycle).

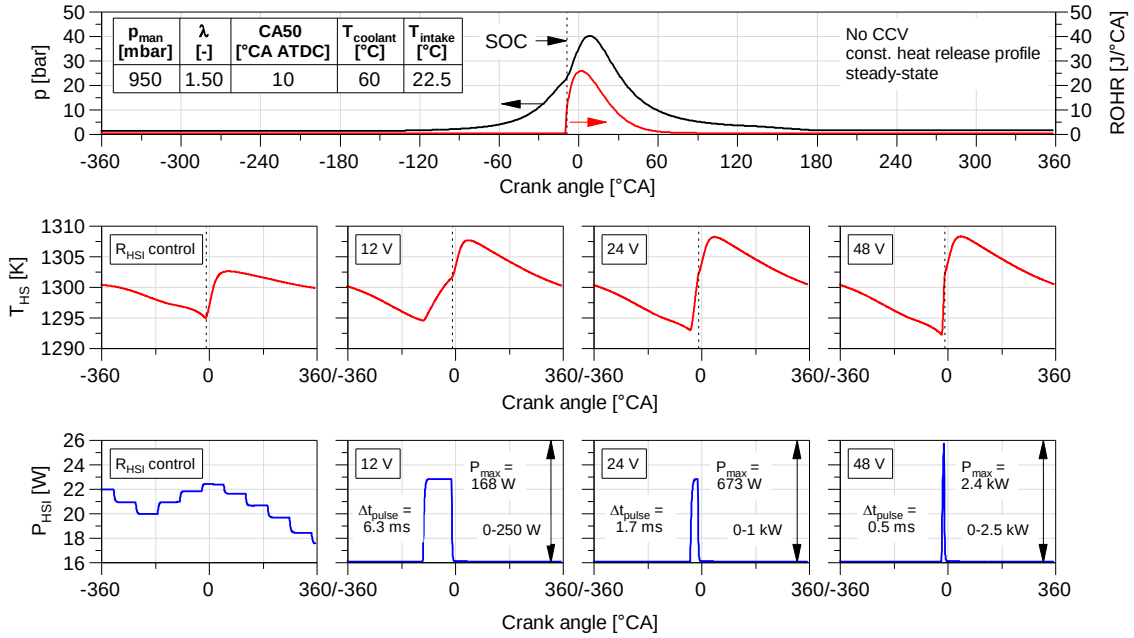

Figure 7.43: Comparison of individual cycles with resistance control and current pulse control with varying voltage and pulse duration.

When controlling R_{HSI}, the calculated electric power is about P_{HSI} = 20.7 W, equivalent to 1.06 J of thermal energy provided each engine cycle. The simulation results on current pulse control show that the energy required to keep T_{HS} constant remains practically constant as well, regardless of the voltage tested. The energy provided is too small to cause significant differences in radiation, convection or conduction. Just like the energy per pulse, the maximum step in temperature is prescribed by the engine operation parameters that influence convection and radiation (manifold pressure, λ, combustion phasing…), and those influencing conduction (adapter conductivity and temperature). It further depends on the the thickness of the heating cap layer, and the heat capacity of the glow plug, thus being subject to manufacturing tolerances. It generally applies that the possible temperature step increases with increasing energy demand (cold combustion and high HS temperature) as the heat losses across the engine cycle are highest. All tested voltages showed similar temperature increases, all below 10 K. The only major difference is the gradient of that increase, being about 0.1, 0.4 and 1.6 K/°CA for 12, 24 and 48 V,

respectively. Whether an increased temperature gradient allows for a reduction in the scatter range of the start of combustion, as suggested in [23], needs to be determined in future experiments. To retain the ability to control R_{HSI}, resistance could be measured either during the current pulse or at any other instant during the engine cycle to feed a controller that adjusts the duration of the current pulse on a cycle-to-cycle basis. Furthermore, the sensing functionality of the resistance signal could be used to determine the start of combustion (resistance and temperature increase after the onset of combustion), to implement an adaptive controller, robust to glow plug ageing and moderate changes in ambient and fuel conditions.

7.6.2 Glow Plug Durability

When assuming that the degradation the glow plug experiences over time is caused by overheating of the glow plug body and does not affect the resistance of the heating cap, active cooling the HSI adapter may be a viable solution to the problem. In principle, CHP unit coolant would be available for this purpose at different temperature levels. To determine how cooling the adapter temperature would affect the energy demand of the HSI system, an adapter temperature of 80 °C was simulated using the 0D model and compared to the same operating point at $T_{adapter}$ = 238 °C (calculated from the response surface equation), using the same factor settings as in Section 7.6.1. Selected HSI-related results are shown in the bar diagram of Figure 7.44. For constant HS temperature, a reduction of adapter temperature leads to lower computed values of R_{leads} and, in turn, to a lower total resistance R_{HSI} (ΔR_{HSI} ≈ -100 mΩ). The larger temperature gradient increases the losses through conduction by nearly 50 %, which, however, only needs to be compensated by an increase of P_{HSI} by about 12 % as a result of the lower electric losses and the increased heating efficiency η_h. These qualitative results, while preliminary, indicate that the increase in HSI power consumption when reducing adapater temperature is maneagable. For this reason, the development of a cooled adapter, either by water or air, is strongly recommended as long as there is no glow plug available that retains its thermo-electric properties over time.

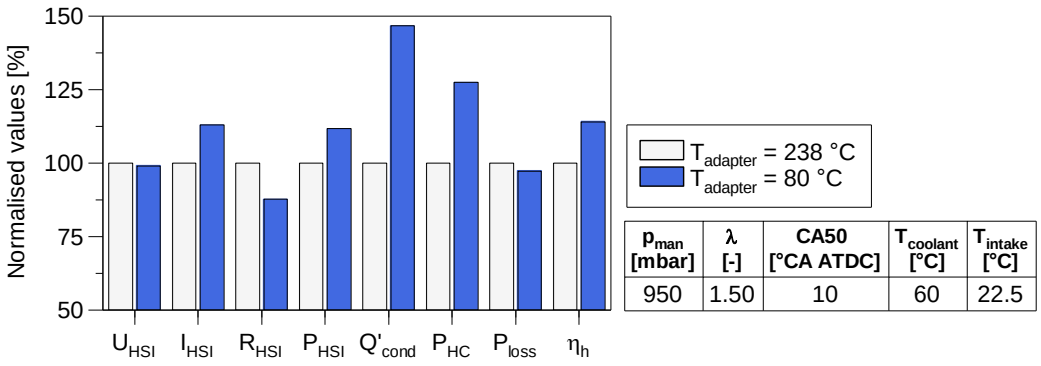

p_{man} [mbar]	λ [-]	CA50 [°CA ATDC]	$T_{coolant}$ [°C]	T_{intake} [°C]
950	1.50	10	60	22.5

Figure 7.44: Comparison of selected steady-state values for $T_{adapter}$ = 80/238 °C.

7.6.3 HSI Adapter Design

Since the HSI adapter design was frozen prior to controller optimisation, the prechamber concept should be revisited. The main advantages expected from a prechamber adapter are the reduced variability in the flow field that surrounds the hot surface, and the formation of flame jets that promote a faster main combustion. Furthermore, the glow plug is exposed to hot residual gas over most part of the engine cycle, causing reduced convective heat losses. The challenge of designing a prechamber adapter is defined by two opposing requirements: on one side, premature contact between the inflowing mixture and the glow plug needs to be avoided, on the other side, once the reactive mixture impinges on the hot surface (contact angle in °CA), ignition delay needs to be minimised to reduce CCV in the flame development phase. For short ignition delays, HS temperature needs to be increased or, as done by other researchers [23, 34, 96], the surface needs to be coated with a catalytic material to reduce the activation energy of the mixture. If T_{HS} is sufficiently high, mixture inflammation would ensue almost immediately and the most advanced combustion phasing that can be set would solely depend on the contact angle. Reducing T_{HS} would most likely allow for combustion phasing to be retarded but cause increasing cyclic variability in combustion. As a result, it is expected that each particular prechamber design would have a *sweet spot* in terms of combustion phasing where combustion stability is highest. In full-load series application, however, the engine might manage without a major CA50 adjustment range, although engine start may be challenging due to the requirement of having to adjust inflammation timing according to engine speed.

7.6.4 Alternative Approach of Mixture Dilution

Exhaust gas recirculation (EGR) represents another viable approach of mixture dilution. The higher heat capacity of exhaust gas, particularly due to the large fractions of H_2O and CO_2, can be utilised to bring combustion temperatures down to even lower levels compared to conventional lean-burn operation. Furthermore, the reduced laminar burning velocity is expected to require shorter ignition delays by increasing HS temperature, thus being beneficial to combustion stability. More importantly, however, the combination of $\lambda = 1$ and EGR would enable the use of standard three-way aftertreatment to achieve lowest NO_x levels without losses in engine power. To determine how increasing fractions of EGR affect the parameters of HSI operation, an EGR sweep with volumetric rates spanning from 0 to 25 % using the experimental setup shown in Figure A.1 from the Appendix was run. EGR is extracted after the exhaust gas heat exchanger at about 150 °C but then cools down significantly until it is fed to the air-fuel mixture after the throttle in the intake manifold (depending on EGR mass flow, to 85 – 128 °C). The procedure for recording the sweep was the following: Starting from an arbitrary reference point of $\lambda = \lambda_{ref} = 1.50$, the EGR valve was opened gradually, while closing the air-fuel mixture throttle valve to account for the dethrottling effect of EGR and avoid an in-

crease of p_{man}. Fuel mass flow and combustion phasing were kept constant. The calculated EGR rate is based on the assumption that the volume flow through the cylinder, calculated from pressure and temperature at the intake port and the mass flows of air and fuel, remains constant and air is directly replaced by exhaust gas. Figure 7.45 (left) shows that at constant CA50, the demand of HSI resistance and HS temperature increases considerably with increasing fractions of EGR, an observation that can be attributed to the diminished reactivity of the mixture. The combination of lengthened ignition delays and decreasing laminar burning velocities [54] warrants an increase of HS temperature in order to advance inflammation timing and attain the same combustion phasing. In fact, the excessive temperatures required to ignite the mixture at EGR rate > 0.25 would have resulted in glow plug overheating and failure, thus being the reason why the engine was not operated at $\lambda = 1$ (EGR rate ≈ 0.3).

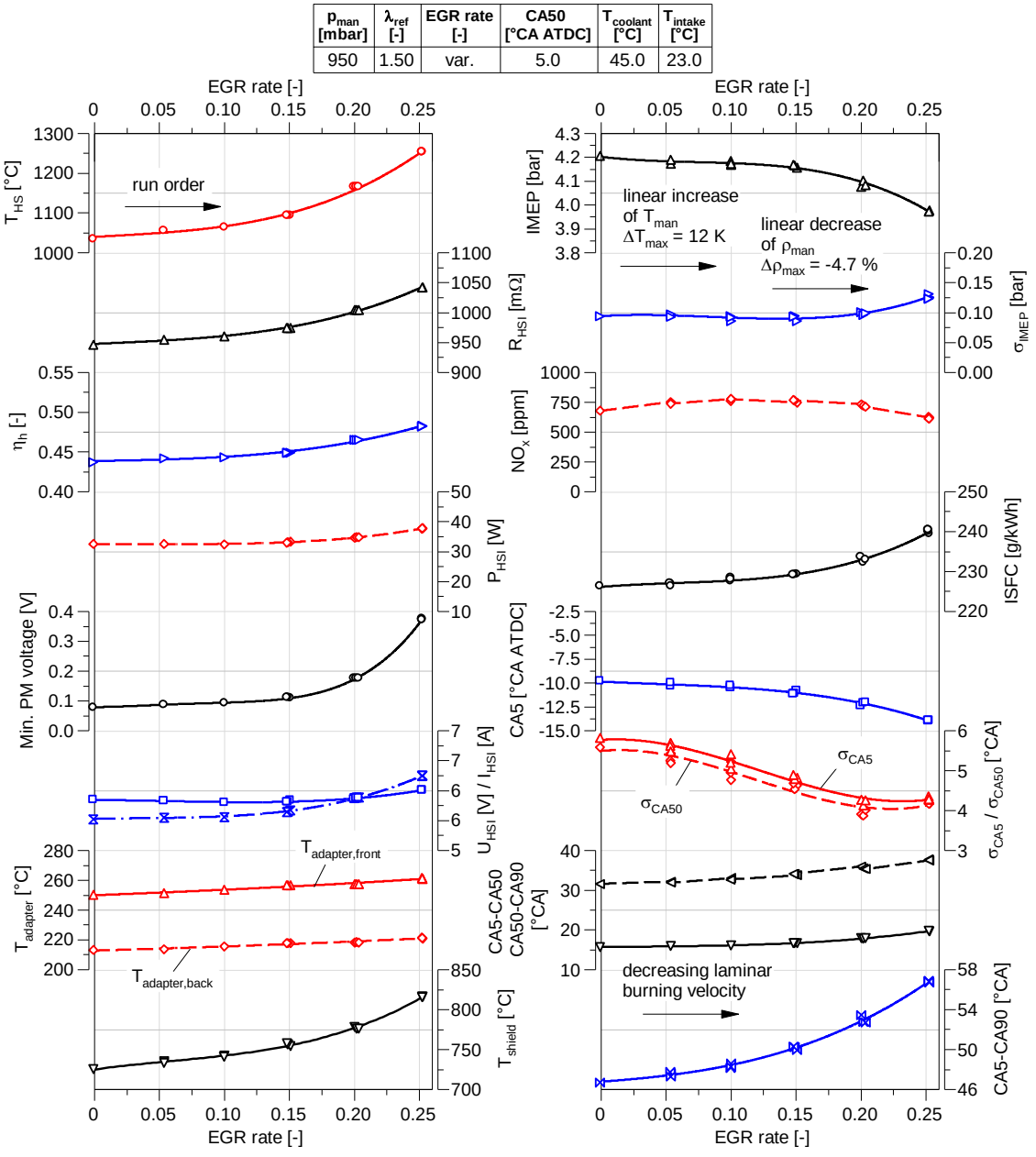

Figure 7.45: Selected experimental data against EGR rate (glow plug No. 6).

While high temperatures are adverse to glow plug durability and HSI power consumption, combustion phasing stability benefits from the necessity of advancing CA5. In this regard, the effect of EGR is similar to additional leaning by excess-air, as advancing the mean start of combustion respective to TDC reduces its variability, allowing for lower values in σ_{CA5} and σ_{CA50}. IMEP remains nearly constant up to an EGR rate of 0.15, but then falls rapidly with increasing EGR rates. This can be partially ascribed to the lower degree of constant volume combustion that arises from the slower combustion, the reduced ratio of specific heat capacities γ of the mixture due to increasing fractions of CO_2 and H_2O, but also to losses in cylinder filling. The fact that the recirculated exhaust gas is hotter than the aspirated air-fuel mixture leads to a proportional increase of temperature at the intake when the EGR rate is increased. Between 0 and 25 % EGR, T_{man} is raised by 12 K, causing a drop in density in the intake manifold of nearly 5 %. Following the same rationale, the reduction in inducted mass flow is also expected to be the primary cause for drawbacks in fuel consumption of up to 5.8 %. Contrary to what was initially stated, the relationship between the EGR rate and the NO_x concentration in the exhaust does not show a clear trend. In fact, dilution by excess-air and by 25 % EGR both produce very similar NO_x levels. These readings of raw volumetric data in ppm, however, do not consider that the exhaust gas mass flow emitted by the unit is diminished with increasing EGR rate. For being directly comparable, emissions need to be expressed either in reference to generated power, e.g. indicated specific NO_x ($ISNO_x$), as mass concentration (e.g. as mg/m_N^3 at 5 % O_2) or as volumetric concentration with a common reference oxygen content (e.g. in ppm at 5 % O_2). Figure 7.46 (left) gives the direct comparison between 4 different ways of quantifying the NO_x output against the EGR rate. When compared to the raw value of the analyser, increasing EGR fractions certainly have a mitigating effect on the absolute amount of NO_x emitted, ranging between 38 and 43 % from 0 to 25 % EGR, depending on the calculation method employed. Plotting ISFC against $ISNO_x$ in Figure 7.46 (right) finally gives the trade-off for HSI operation at constant mixture dilution when gradually replacing excess-air by exhaust gas. For the tested settings it applies that EGR enables a significant NO_x reduction, though improvements in the emission output are always at the expense of penalties in fuel consumption, as indicated by the dashed pareto limit.

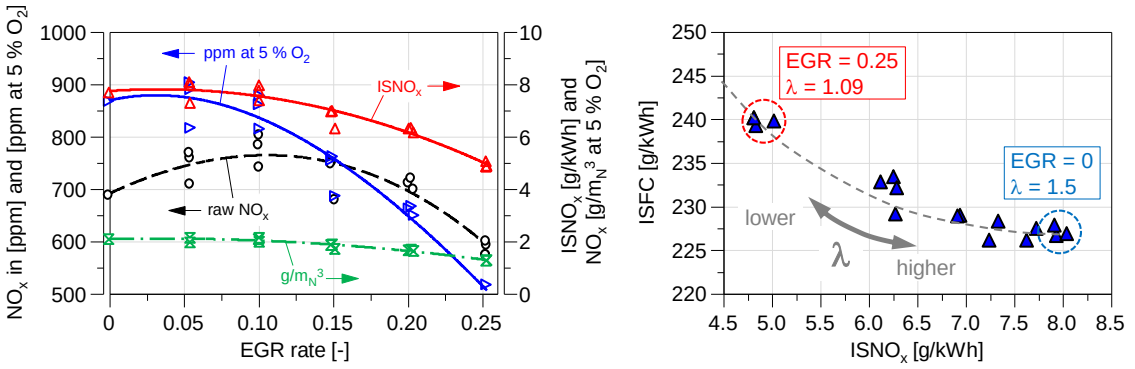

Figure 7.46: Comparison of raw NO_x and indicated specific NO_x as a function of EGR rate (left) and ISFC-$ISNO_x$ trade-off (right).

In light of a full-load series CHP application, based on the results presented, the only condition that may justify the increased system complexity given by an external EGR system is the ability to operate the engine with stoichiometric mixtures and three-way aftertreatment. In this context, the focus of combustion process development shifts more towards improving fuel consumption, while limiting combustion temperatures may only be a secondary requirement derived from component durability considerations, less from NO_x. There are several measures to increase the efficacy of EGR in terms of ISFC. The dethrottling effect of EGR, for instance, can be used to reduce the pumping losses and increase the in-cylinder mass at IVC. Furthermore, cooling the recirculated exhaust gas lowers mixture temperature at the intake manifold and can therefore help reduce losses in cylinder filling. If the exhaust gas is cooled way below its condensation temperature, the combustion process may further benefit from an increased γ (increased thermal efficiency) and a shorter combustion overall due to the partial removal of H_2O. However, if engine power is prescribed by the generator unit, the arguably largest challenge of the transition from lean-burn to $\lambda = 1$ operation is providing enough mass flow of diluents at full-load operation. To this end, the natural scavenging pressure gradient between the exhaust and the intake manifold needs to be optimised, preferably using the validated 1D model, in due consideration of the gas exchange process.

8 Conclusions and Future Work

Motivated by future tightening of NO_x emission limits and high maintenance cost an alternative Hot Surface Ignition (HSI) system for small-scale naturally aspirated cogeneration engines running on lean premixed air-natural-gas mixtures was developed. The present thesis describes the systematic approach adopted to study the process of HSI induced combustion, including the identification of the ignition system's operating limits and limitations, the determination of sensitivities of the ignition and combustion process on engine operating parameters using Design of Experiments (DoE) methods, and the direct comparison to state-of-the-art prechamber spark ignition (PCSI). The main experiments conducted required extensive preparatory work, such as the conversion of a series CHP unit into a fully instrumented and controllable single-cylinder test bed, the development of a conditioning unit for reproducible intake conditions, and the design of a robust, high-speed resistance/temperature controller that enables autonomous engine start and shows optimal disturbance behaviour during engine operation. For an in-depth analysis of the conditions that lead to mixture ignition and the processes of mixture inflammation and combustion, a combined approach of numerical simulation and engine experiments with multiple single-fibre optical accesses to the combustion chamber was pursued. To this end, optical adapters to record the chemiluminiscence emitted during the combustion process were designed and a detailed 3D CFD model with simple chemical reaction kinetics to simulate the process of mixture ignition and subsequent combustion was set up. A 0D HSI engine process simulation model was developed in Matlab/Simulink to broaden the understanding of the thermo-electric behaviour of the glow plug, governed by heat transfer relations between the hot surface, the in-cylinder mixture and the engine block. Most importantly, the model represents a helpful tool for future case studies and deriving new controller strategies without the need of conducting large number of engine experiments.

8.1 Conclusions

The hot surface ignition process of premixed air-fuel mixtures studied is highly complex, depending on all parameters that shape the flow field in the proximity of the hot surface and those that affect reaction kinetics controlling ignition delay. From theoretical considerations and both numerical and experimental investigations carried out in the scope of this work, it is possible to formulate the following conclusions concerning the processes of ignition and combustion using the developed ignition system:

- Ignition delay is kinetically controlled and thus a function of hot surface (HS) temperature, the thermodynamic state of the mixture and its composition. Increasing temperatures reduce ignition delay time and advance the start of combustion which, in turn, advances combustion phasing. Since the glow plug's surface heating element is a resistor with positive temperature coefficient, its operating resistance can be used as an indicator for HS temperature and was therefore chosen as the control variable to be adjusted during engine operation. Parallels between HSI and SI operation can be drawn, as both resistance and spark timing allow for an adjustment of combustion phasing.
- The developed resistance controller is very robust to cyclic combustion variations and keeps HS temperature constant regardless of the engine operation parameters. Despite practically constant HS temperatures, fluctuating timings of the start of combustion are the main challenge inherent to the current HSI design. CFD results revealed that fresh mixture impinges on the hot surface at early stages of the intake stroke, this being the beginning for pre-reactions that eventually cause the mixture to ignite. For operating points that require late starts of combustion close to TDC, e.g. at high mixture strength or retarded combustion phasings, ignition delay needs to be lengthened by lowering HS temperature. This enhances the relative impact of local mixture temperature, composition and flow on the pre-reaction state and causes ignition delay time to become more susceptible to stochastic cycle-by-cycle variations. Conversely, it can be asserted that operating points that demand an early onset of combustion and high HS temperatures, such as very lean mixtures at advanced combustion phasing, show lowest cyclic variability.
- It was found that the onset of combustion can be detected as a sudden increase in HSI resistance. Provided that signal noise is low, the resistance trace could be used to implement an adaptive controller for combustion phasing, without the need of actual temperature measurement during engine operation.
- The influence of 5 engine operation parameters on the combustion process was investigated, namely intake manifold pressure, CHP coolant temperature, CHP intake air temperature, relative air-fuel ratio λ and combustion phasing. The first three factors could be set independently, with their limits being prescribed by the installation, whereas the limits of the latter two were subject to multifactor constraints. In screen-

ing experiments it was found that the lean-burn limit is positively correlated with intake manifold pressure and coolant temperature, with pressure being the primary influencing factor. Stoichiometric operation was possible for all factor settings tested. The limits for combustion phasing were found to be more convoluted but can essentially be broken down into most advanced and most retarded combustion phasing possible for given engine operation parameters. For most factor settings, combustion phasings $CA50_{min} \leq 0$ °CA ATDC could be set. Only close to the lean-burn limit, the limit is retarded respective to TDC. Optical experiments, aided by 3D combustion simulation, revealed that this is caused by premature mixture ignition at the beginning of the compression stroke. It was found that the basic requirement for a timed and shiftable fast main combustion is that HS temperature needs to be low enough to allow for sufficient unburnt air-fuel mixture to accumulate in the shield of the HSI adapter and burn rapidly when approaching TDC (operation in *section 1*). At excessive temperatures, on the other hand, the reactivity of the mixture is increased and most fuel in the shield is depleted early in the cycle, with a flame kernel unable to develop into a propagating flame. This results in a sluggish inflammation of the bulk mixture close to TDC, causing a retarded main combustion (operation in *section 2*). The upper limit of combustion phasing, $CA50_{max}$, was found to be determined by increasing CCV in combustion phasing arising from increasing ignition delay when lowering HS temperature. For occasional cycles where local mixture in the shield shows worsened ignition quality (e.g. higher residual gas fraction, reduced fuel concentration or lower mixture temperature), the critical pre-reaction state required to induce combustion cannot be reached at the right time, thereby causing partial-burning or even misfiring cycles.

- Through the 5 factor I-optimal DoE approach it was possible to gain comprehensive understanding of how dependent engine and HSI parameters (responses) react to changes in engine operating conditions (factors) and express these relationships through multiple regression equations, valid for the entire investigated HSI operating range. The statistical analysis allows concluding that intake manifold pressure, relative air-fuel ratio and combustion phasing have a strong impact on the combustion process and the thermo-electric properties of the HSI system, while coolant and intake temperature only play a subordinate role. From the response surface equations for parameters like IMEP, ISFC, NO_x, optimal operating conditions can be derived. A practical example are predictions about the achievable IMEP and ISFC when a specific NO_x limit needs to be met. Other correlations, like for combustion duration, CCV in combustion phasing σ_{CA5} or intake manifold temperature can be used as empirical submodels in the 0D HSI engine process simulation model.

Additional questions that were addressed in this work were whether glow plugs are interchangeable in terms of the HSI induced combustion process and if they show any signs of degradation when constantly powered under engine operating conditions. From the ex-

periments conducted, the following conclusions can be drawn:

- Comparative experiments using several glow plug specimens from the same manufacturing batch give evidence that combustion parameters are not sensitive to the individual glow plug employed, as long as CA50 is the controlled parameter. Electric properties such as HSI resistance and power, on the other hand, proved to differ significantly among the specimens tested due to differences in their resistance-temperature correlation. As a practical consequence, the resistance required to set the same HS temperature changes and when different glow plugs are used.
- The resistance-temperature correlation of individual glow plugs appeared to change over time. This process of glow plug ageing is reflected in an increase of required set resistance for same HS temperature and, as suggested by statistical data analysis, is a function of engine operation time. The conjecture is formulated that the degradation process is caused by a gradual loosening of the crimping connection of the inner electric glow plug leads as it eventually results in glow plug failure.

A major finding from comparative experiments to PCSI is that HSI allows for a significant enhancement of the lean-burn limit by $\lambda = 0.1 - 0.15$, owing to the larger activated mixture volume. It is therefore possible to ignite mixtures with lower ignition quality safely without misfires. Several operating points across the HSI operating range were selected for a direct comparison to PCSI. The experiments disclosed two main differences between both ignition systems: much higher CCV in combustion phasing and longer combustion durations in HSI operation. Based on a specially developed strategy to simulate increasing degrees of CCV in SI operation, the following fundamental conclusions can be drawn:

- At similar CCV, the combustion processes are very similar, the main difference being the shortened combustion for PCSI. This gives proof that torch jets ejected from the prechamber are a more effective means to accelerate the combustion process than the increased reactive mixture volume, activated by the glow plug tip.
- High CCV in the start of combustion/combustion phasing are detrimental to NO_x, ISFC and IMEP, representing the main reason why HSI operation shows significant disadvantages in this regard.

8.2 Future Work

It has been shown that the developed HSI system allows for an enhancement of the lean-burn limit and enables the engine to operate without misfires over a wide range of engine operation parameters. Future work should address its current challenges of high CCV in combustion phasing, comparatively long combustion duration and limited glow plug durability:

- *CCV*: Possible means to reduce the scatter range in the start of combustion are to

avoid premature interaction between the hot surface and mixture, e.g. by means of a prechamber adapter, or to replace constant temperature control by a timed current pulse during the compression stroke. Both approaches aim at reducing the absolute ignition delay time, making the inflammation process less susceptible to CCV in mixture composition, temperature and flow conditions.

- *Combustion duration*: Prechamber HSI holds out the prospect of accelerating the main combustion without changes in engine design. It is therefore suggested to revisit its potential with regard to its ability to facilitate reproducible and adjustable starts of combustion and the formation of strong, turbulent torch jets to induce a wide and fast main combustion.
- *Glow plug durability*: For an in-depth analysis of the glow plug ageing process, it is essential to measure HS temperature during engine operation using a non-intrusive method, such as single-fibre pyrometer measurements. Not only would this allow determining the actual critical ignition temperature but also optimising and validating the thermo-electric HSI model. With a tuned model, it would be possible to quantify changes in energy balance and monitor the degradation process. Since the cause of limited durability is believed to be of thermal nature, the development of a cooled adapter is further encouraged.

Finally, given the ability to measure HS temperature during engine operation, it is suggested to enhance the 0D HSI model by a phenomenological submodel to compute ignition delay. An approach based on reaction kinetics, such as the Livengood and Wu integral, would reduce the amount of test bed-dependent empirical correlations and increase the model's applicability to other engine configurations.

References

[1] Adomeit, G., “Thermische Zündung strömender Gasgemische an heißen Oberflächen unter stationären Bedingungen", Forsch. Ing.-Wes. 32(2):33–68, 1966.

[2] Æsøy, V., “Hot Surface Assisted Compression Ignition in a Direct Injection Natural Gas Engine", Ph.D. Thesis, University of Trondheim, 1996.

[3] Æsøy, V. and Valland, H., “Hot Surface Assisted Compression Ignition of Natural Gas in a Direct Injection Diesel Engine", SAE Technical Paper 960767, 1996, doi:10.4271/960767.

[4] Æsøy, V. and Valland, H., “The Influence of Natural Gas Composition on Ignition in a Direct Injection Gas Engine Using Hot Surface Assisted Compression Ignition", SAE Technical Paper 961934, 1996, doi:10.4271/961934.

[5] Albahri, T.A., “Flammability characteristics of pure hydrocarbons", Chemical Engineering Science 58(16):3629–3641, 2003, doi:10.1016/S0009-2509(03)00251-3.

[6] Anderson, M.J. and Whitcomb, P.J., “RSM simplified: Optimizing processes using response surface methods for design of experiments", CRC Press, Boca Raton, ISBN 1-56327-297-0, 2005.

[7] ASTM International, “ASTM E659-15, Standard Test Method for Autoignition Temperature of Chemicals", 2015.

[8] ASUE - Arbeitsgemeinschaft für sparsamen und umweltfreundlichen Energieverbrauch e.V., “BHKW-Kenndaten 2014/2015", 2015.

[9] Attard, W.P., Kohn, J. and Parsons, P., “Ignition Energy Development for a Spark Initiated Combustion System Capable of High Load, High Efficiency and Near Zero NOx Emissions", SAE Int. J. Engines Vol. 3(2), 2010, doi:10.4271/2010-32-0088.

[10] Auer, M., “Erstellung phänomenologischer Modelle zur Vorausberechnung des Brennverlaufes von Magerkonzept-Gasmotoren", Ph.D. Thesis, Universität München, 2010.

[11] AVL List GmbH, “Combustion Module: AVL Fire v2013", 2013.

[12] Ayala, F.A., Gerty, M.D. and Heywood, J.B., “Effects of Combustion Phasing, Relative Air-fuel Ratio, Compression Ratio, and Load on SI Engine Efficiency", SAE Technical Paper 2006-01-0229, 2006, doi:10.4271/2006-01-0229.

[13] Ballal, D.R. and Lefebvre, A.H., “The influence of flow parameters on minimum ignition energy and quenching distance", Symposium (International) on Combustion 15(1):1473–1481, 1975, doi:10.1016/S0082-0784(75)80405-X.

[14] Ballal, D.R. and Lefebvre, A.H., “Ignition and flame quenching in flowing gasous mixtures", Proc. R. Soc. Lond. A(357):163–181, 1977, doi:10.1098/rspa.1977.0161.

[15] Ban, M., “Numerical Modelling of Autoignition Chemistry Kinetics in Computational Fluid Dynamics", Ph.D. Thesis, University of Zagreb, 2011.

[16] Bargende, M., Spicher, U., Köhler, U. and Schwarz, F., “Entwicklung eines allgemeingültigen Restgasmodells für Verbrennungsmotoren. Vorhaben Nr. 674 (AIF-Nr. 12247)", FVV-Informationstagung Motoren, 2002.

[17] Bartknecht, W., “Explosionsschutz: Grundlagen und Anwendung", Springer, Berlin, ISBN 3-540-55464-5, 1993.

[18] Bartunek, B., Gosse, P., Hilger, U. and Schrey, E., “Entwicklung eines schadstoffarmen Nutzfahrzeugmotors mit Hochdruck-Direkteinblasung von Erdgas für den Einsatz in Stadbussen", Final report of DBU research project 14100, 2004.

[19] Bartunek, B. and Hilger, U., “Direct Induction Natural Gas (DING): A Diesel-Derived Combustion System for Low Emissions and High Fuel Economy", SAE Technical Paper 2000-01-2827, 2000, doi:10.4271/2000-01-2827.

[20] Becker, M., Rixecker, G., Brichzin, V., Günther, M. et al., “Corona Ignition as an Enabler for Lean Combustion Concepts Leading to Significantly Reduced Fuel Consumption of Turbocharged Gasoline Engines", 22nd Aachen Colloquium Automobile and Engine Technology, 2013.

[21] Böckhoff, N., Mondrzyk, D. and Terbeck, S., “Kontinuierliche Weiterentwicklung des 51/60G zum 51/60G TS der MAN Diesel & Turbo SE: Continuous Development of the 51/60G to the 51/60G TS of the MAN Diesel and Turbo SE", Proceedings of the 10th Dessau Gas Engine Conference:61–71, 2017.

[22] Bohne, S., Rixecker, G., Brichzin, V. and Becker, M., “Hochfrequenz-Zündsystem mittels Korona-Entladung", MTZ Motortechnische Zeitschrift 75(1):50–54, 2014.

[23] Boulouchos, K., “Entflammung und Energieumsetzung im fremdgezündeten Motor durch temperaturgesteuerte Oberflächen", Ph.D. Thesis, ETH Zürich, 1984.

[24] Brettschnieder, J., “Berechnung des Luftverhältnisses Lambda von Luft-Kraftstoff-Gemischen und des Einflusses von Messfehlern auf Lambda", Bosch Techn. Berichte 6(4), 1979.

[25] Bunce, M., Blaxill, H., Kulatilaka, W. and Jiang, N., “The Effects of Turbulent Jet Characteristics on Engine Performance Using a Pre-Chamber Combustor", SAE Technical Paper 2014-01-1195, doi:10.4271/2014-01-1195.

[26] Bundesministerium für Umwelt, Naturschutz, Bau und Reaktorsicherheit, “Entwurf

zur Anpassung der Ersten Allgemeinen Verwaltungsvorschrift zum Bundes–Immissionsschutzgesetz", www.bmub.bund.de/N53642/, August 17, 2017.

[27] Bundesministerium für Wirtschaft und Energie, “Fünfter Monitoring-Bericht zur Energiewende", 2016.

[28] Bundesumweltministerium für Umwelt Naturschutz und Reaktorsicherheit, “Technische Anleitung zur Reinhaltung der Luft - TA Luft", 2002.

[29] Byun, J.J., “Laminar Burning Velocities and Laminar Flame Speeds of Multi-Component Fuel Blends at Elevated Temperatures and Pressures", Ph.D. Thesis, University of Texas at Austin, 2011.

[30] Caron, M., Goethals, M., Smedt, G. de, Berghmans, J. et al., “Pressure dependence of the auto-ignition temperature of methane/air mixtures", Journal of Hazardous Materials 65(3):233–244, 1999, doi:10.1016/S0304-3894(99)00004-7.

[31] Chase, M.W., Davies, C.A., Downey, J.R., Frurip, D.J. et al., “NIST JANAF Thermochemical Tables", http://kinetics.nist.gov/janaf/, August 28, 2017.

[32] Cherry, M.A., “Catalytic-Compression Timed Ignition,” US000005109817A, 1992.

[33] Cherry, M.A. and Elmore, C.L., “Timing Chamber Ignition Method and Apparatus,” US000004977873A, 1990.

[34] Cherry, M.A., Morrisset, R.J. and Beck, N.J., “Extending Lean Limit with Mass-Timed Compression Ignition Using a Catalytic Plasma Torch", SAE Technical Paper 921556, 1992, doi:10.4271/921556.

[35] Cho, H.M. and He, B.-Q., “Spark ignition natural gas engines - A review", Energy Conversion and Management 48(2):608–618, 2007, doi:10.1016/j.enconman.2006.05.023.

[36] Cimarello, A., Grimaldi, C.N., Mariani, F. and Battistoni, M., “Analysis of RF Corona Ignition in Lean Operating Conditions Using an Optical Access Engine", SAE Technical Paper 2017-01-0673, 2017, doi:10.4271/2017-01-0673.

[37] Colin, O. and Benkenida, A., “The 3-Zones Extended Coherent Flame Model (ECFM3Z) for Computing Premixed/Diffusion Combustion", Oil & Gas Science and Technology Vol. 59(6):593–609, 2004, doi:10.2516/ogst:2004043.

[38] Colin R. Ferguson, A. T. Kirkpatrick, “Internal Combustion Engines: Applied Thermosciences", 3rd ed., Wiley, Chichester, ISBN 978-1118533314, 2015.

[39] Cordon, D. and Beyerlein, S., “Homogeneous Charge Catalytic Ignition of Ethanol-Water/Air Mixtures in a Reciprocating Engine: Compression Ratio and Catalyst Aging Effects on Aqueous Ethanol", Final Report KLK752A, 2009.

[40] Cordon, D., Beyerlein, S., Cherry, M.A. and Steciak, J., “Homogeneous Charge Catalytic Ignition of Ethanol-Water/Air Mixtures in a Reciprocating Engine", Proceedings of the ASME International Mechanical Engineering Congress and Exposition IMECE2008-68899, 2008, doi:10.1115/IMECE2008-68899.

[41] Cordon, D., Clarke, E., Beyerlein, S., Steciak, J. et al., “Catalytic Igniter to Support Combustion of Ethanol-Water/Air Mixtures in Internal Combustion Engines: 2002-01-2863", SAE Technical Paper, 2002, doi:10.4271/2002-01-2863.

[42] Cordon, D., Walker, M., Beyerlein, S. and Steciak, J., “Catalytically Assisted Combustion of JP-8 in a 1 kW Low-Compression Genset", SAE Technical Paper 2006-32-0024, 2006, doi:10.4271/2006-32-0024.

[43] Cox, D.R. and Reid, N., “The Theory of the Design of Experiments", Chapman & Hall/CRC, Boca Raton, ISBN 1-58488-195-X, 2000.

[44] Daimler, G., “Gasmotor,” DE000000028022A, 1893.

[45] Damköhler, G., “Der Einfluss der Turbulenz auf die Flammengeschwindigkeit in Gasgemischen", Zeitschrift f. Elektrochem. u. angew. Chemie(46):601–626, 1940.

[46] European Committee for Standardization, “EN 14522: Determination of the auto ignition temperature of gases and vapours", 2005.

[47] European Union, “Commission Regulation (EU) No 813/2013 of 2 August 2013 implementing Directive 2009/125/EC of the European Parliament and of the Council with regard to ecodesign requirements for space heaters and combination heaters", Official Journal of the European Union, 2013.

[48] Ewald, J. and Peters, N., “On unsteady premixed turbulent burning velocity prediction in internal combustion engines", Proceedings of the Combustion Institute 31(2):3051–3058, 2007, doi:10.1016/j.proci.2006.07.119.

[49] Farrell, J.T., Johnston, R.J. and Androulakis, I. P., “Molecular Structure Effects On Laminar Burning Velocities At Elevated Temperature And Pressure", SAE Technical Paper 2004-01-2936, 2004, doi:10.4271/2004-01-2936.

[50] Fenn, J.B., “Lean Flammability Limit and Minimum Spark Ignition Energy", Industrial and Engineering Chemistry Vol. 43(12), 1951.

[51] Frank-Kamenetskii, D.A., “Diffusion and Heat Exchange in Chemical Kinetics", Princeton University Press, Princeton, 2016.

[52] Frank-Kamenetzki, D.A., “Stoff- und Wärmeübertragung in der chemischen Kinetik", Diffuzija i teploperedaca v chimiceskoj kinetike, Springer, Berlin, 1959.

[53] Furuhama, S. and Kobayashi, Y., “Development of a Hot-Surface-Ignition Hydrogen Injection Two-Stroke Engine", International Journal of Hydrogen Energy Vol. 9(3):205–213, 1984.

[54] Galmiche, B., Halter, F., Foucher, F. and Dagaut, P., “Effects of Dilution on Laminar Burning Velocity of Premixed Methane/Air Flames", Energy Fuels 25(3):948–954, 2011, doi:10.1021/ef101482d.

[55] Gaydon, A.G., “The Spectroscopy of Flames", Chapman and Hall, London, ISBN 978-94-009-5722-0, 1974.

[56] Geringer, B., Klawatsch, D., Graf, J. and Lenz, H.P., “Laserzündung: Ein neuer Weg für den Ottomotor", MTZ Motortechnische Zeitschrift 65(3):214–219, 2004.

[57] Getzlaff, J., Dingel, O., Kahrstedt, J., Kuhnert, D. et al., “Mageres CNG-Brennverfahren für minimale CO2-Emissionen: A lean-burn CNG-concept for minimum CO2-emissions", in: Dingel, O. (ed.), *Gasfahrzeuge: Die passende Antwort auf die CO2-Herausforderung der Zukunft?*, expert, Renningen, ISBN 3-8169-2439-5:58–73, 2004.

[58] Goodwin, D.G., Moffat, H.K., and Speth, R.L., “Cantera: An object- oriented software toolkit for chemical kinetics, thermodynamics, and transport processes: Version 2.2.1", http://www.cantera.org.

[59] Gorenflo, E., “Einfluß der Luftverhältnisstreuung auf die zyklischen Schwankungen beim Ottomotor", Ph.D. Thesis, Universität Karlsruhe, 1997.

[60] Graf, J., Lauer, T. and Geringer, B., “Zündsysteme für Hochaufgeladene Downsizingmotoren", MTZ Motortechnische Zeitschrift 74(11):898–903, 2013.

[61] Groote, S. de, “Turbulent jet ignition pushes engine combustion efficiency", http://www.f1technical.net/news/20316, August 17, 2017.

[62] Hampe, C., Kubach, H., Spicher, U., Rixecker, G. et al., “Investigations of Ignition Processes Using High Frequency Ignition", SAE Technical Paper 2013-01-1633, 2013, doi:10.4271/2013-01-1633.

[63] Hanenkamp, A., Terbeck, S. and Köbler, S., “32/40 PGI – Neuer Otto-Gasmotor ohne Zündkerze", MTZ Motortechnische Zeitschrift 67(12):932–941, 2006.

[64] Healy, D., Curran, H.J., Simmie, J.M., Kalitan, D.M. et al., “Methane/ethane/propane mixture oxidation at high pressures and at high, intermediate and low temperatures", Combustion and Flame 155(3):441–448, 2008, doi:10.1016/j.combustflame.2008.07.003.

[65] Healy, D., Curran, H.J., Simmie, J.M., Kalitan, D.M. et al., “Methane/ethane/propane mixture oxidation at high pressures and at high, intermediate and low temperatures: Supplemental Material", Combustion and Flame 155(3), 2008, doi:10.1016/j.combustflame.2008.07.003.

[66] Heghes, C.I., “C1-C4 Hydrocarbon Oxidation Mechanism", Ph.D. Thesis, Rupertus Carola University of Heidelberg, 2006.

[67] Heinz, C.E., “Untersuchung eines Vorkammerzündkonzepts für Großgasmotoren in einer Hochdruckzelle mit repetierender Verbrennung", Ph.D. Thesis, Technische Universität München, 2011.

[68] Heyne, S., Meier, M., Imbert, B. and Favrat, D., “Experimental investigation of prechamber autoignition in a natural gas engine for cogeneration", Fuel 88(3):547–552, 2009, doi:10.1016/j.fuel.2008.09.032.

[69] Heywood, J., “Internal Combustion Engine Fundamentals", McGraw-Hill, ISBN 0-07-028637-X, 1988.

[70] Hill, P.G. and McTaggart-Cowan, G.P., “Nitrogen Oxide Production in a Diesel Engine Fueled by Natural Gas", SAE Technical Paper 2005-01-1727, 2005, doi:10.4271/2005-01-1727.

[71] Hu, E., Li, X., Meng, X., Chen, Y. et al., “Laminar flame speeds and ignition delay times of methane–air mixtures at elevated temperatures and pressures", Fuel 158:1–10, 2015, doi:10.1016/j.fuel.2015.05.010.

[72] Jones, B. and Goos, P., “I-optimal versus D-optimal split-plot response surface designs", Journal of Quality Technology(44.2):85–101, 2012.

[73] Joos, F., “Technische Verbrennung: Verbrennungstechnik, Verbrennungsmodellie-

rung, Emissionen", Springer, Berlin, ISBN 10 3-540-34333-4, 2006.

[74] Kammerstätter, S., "Verbrennungsablauf und Schadstoffbildung in Erdgas-Großmotoren mit Vorkammerzündung", Ph.D. Thesis, Technische Universität München, 2012.

[75] Kettner, M., "Zündsysteme für magere Gemische", Study for the Forschungsvereinigung Verbrennungskraftmaschinen (FVV) e.V., 2004.

[76] Kettner, M., "Experimentelle und numerische Untersuchungen zur Optimierung der Entflammung von mageren Gemischen bei Ottomotoren mit Direkteinspritzung", Ph.D. Thesis, Universität Karlsruhe, 2006.

[77] Koch, T., "Numerischer Beitrag zur Charakterisierung und Vorausberechnung der Gemischbildung und Verbrennung in einem direkteingespritzen, strahlgeführten Ottomotor", Ph.D. Thesis, ETH Zürich, 2002.

[78] Kong, D., Eckhoff, R.K. and Alfert, F., "Auto-ignition of CH4/air, C3H8/air, CH4/C3H8/air and CH4/CO2/air using a 1 l ignition bomb", Journal of Hazardous Materials 40(1):69–84, 1995, doi:10.1016/0304-3894(94)00082-R.

[79] Laurendeau, N.M., "Thermal Ignition of Methane-Air Mixtures by Hot Surfaces: A Critical Examination", Combustion and Flame(46):29–49, 1982.

[80] Lavoie, G.A., Heywood, J.B. and Keck, J.C., "Experimental and Theoretical Study of Nitric Oxide Formation in Internal Combustion Engines", Combustion Science and Technology(1):313–326, 1970.

[81] Law, C.K., "Combustion Physics", Cambridge University Press, Cambridge, ISBN 978-0521154215, 2010.

[82] Law, C.K., Makino, A. and Lu, T.F., "On the off-stoichiometric peaking of adiabatic flame temperature", Journal of Combution and Flame 145:808–819, 2006, doi:10.1016/j.combustflame.2006.01.009.

[83] Lefebvre, A.H., "Gas turbine combustion", Hemisphere Pub. Corp., Washington, ISBN 0-07-037029-X, 1983.

[84] Lefebvre, A.H. and Ballal, D.R., "Gas turbine combustion: Alternative fuels and emissions", 3rd ed., CRC Press, Boca Raton, ISBN 978-1-4200-8604-1, 2010.

[85] List, H. (ed.), "Thermodynamik der Verbrennungskraftmaschine: Der Fahrzeugantrieb", 3rd ed., Springer, Wien, ISBN 978-3211-99276-0, 2009.

[86] Livengood, J.C. and Wu, P.C., "Correlation of autoignition phenomena in internal combustion engines and rapid compression machines", Proceedings of Fifth International Symposium on Combustion:347–356, 1955.

[87] Ma, F., Wang, Y., Wang, J. and Ding, S., "Effects of Combustion Phasing, Combustion Duration, and Their Cyclic Variations on Spark-Ignition (SI) Engine Efficiency", Energy Fuels 22(22):3022–3028, 2008, doi:10.1021/ef8003027.

[88] Maly, R.R., "Die Zukunft der Funkenzündung", MTZ Motortechnische Zeitschrift 59(7/8), 1998.

[89] Merker, G.P., Schwarz, C., and Teichmann, R. (eds.), "Grundlagen Verbrennungsmotoren", 5th ed., Vieweg + Teubner, Wiesbaden, ISBN 978-3-8348-1393-0, 2011.

[90] Merker, G.P. and Teichmann, R. (eds.), “Grundlagen Verbrennungsmotoren", 7th ed., Springer Vieweg, Wiesbaden, ISBN 978-3-658-03194-7, 2014.

[91] Morton, A., Munoz-Torrez, G., Beyerlein, S., Steciak, J. et al., “Aqueous Ethanol Fueled Catalytic Ignition Engine", SAE Technical Paper 1999-01-3267, 1999, doi:10.4271/1999-01-3267.

[92] Müller, M., “General Air Fuel Ratio and EGR Definitions and their Calculation from Emissions", SAE Technical Paper 2010-01-1285, 2010, doi:10.4271/2010-01-1285.

[93] Müller, R., “Einfluss der Zündernergie auf die Zündgrenzen von Gas/Luft-Gemischen unter Variation von Druck und Temperatur", Ph.D. Thesis, Universität Erlangen-Nürnberg, 1977.

[94] Mullins, B.P., “Spontaneous Ignition of Liquid Fuels", Butterworths Scientific Publications, London, 1955.

[95] Myers, R.H. and Montgomery, D.C., “Response surface methodology: Process and product optimization using designed experiments", 2nd ed., Wiley, New York, ISBN 0-471-41255-4, 2002.

[96] Nagalingam, B., Sridhar, B., Panchapakesan, N.R., Gopalakrishnan, K.V. et al., “Surface Ignition Initiated Combustion of Alcohol in Diesel Engines - A New Approach", SAE Technical Paper 800262, 1980, doi:10.4271/800262.

[97] Neher, D., “Miller Cycle and Exhaust Gas Recirculation for a Naturally Aspirated Lean Burn Gas Engine", Ph.D. Thesis, University of Valladolid & Hochschule Karlsruhe, 2017.

[98] Neher, D., Scholl, F., Scherf, H., Kettner, M. et al., “Entflammung von mageren homogenen Gemischen an heißen Oberflächen (engl. Inflammation of Lean Homogeneous Mixtures on Hot Surfaces)", 7th Dessau Gas Engine Conference, 2011.

[99] Neher, D., Scholl, F., Teschendorff, V., Kettner, M. et al., “Controlled Hot Surface Ignition in Stationary Petrol and Natural Gas Operation", SAE Technical Paper 2012-32-0006, 2012, doi:10.4271/2012-32-0006.

[100] Olberding, J., Cordon, D., Beyerlein, S., Steciak, J. et al., “Dynamometer Testing of an Ethanol-Water Fueled Transit Van", SAE Technical Paper 2005-01-3706, 2005, doi:10.4271/2005-01-3706.

[101] Olsen, D.B., Kohls, M. and Arney, G., “Impact of Oxidation Catalysts on Exhaust NO_2/NO_x Ratio from Lean-Burn Natural Gas Engines", Journal of the Air & Waste Management Association 60(7):867–874, 2010, doi:10.3155/1047-3289.60.7.867.

[102] Omaye, S.T., “Metabolic modulation of carbon monoxide toxicity", Toxicology Volume 180(2):139–150, 2002, doi:10.1016/S0300-483X(02)00387-6.

[103] Ozdor, N., Dulger, M. and Sher, E., “Cyclic Variability in Spark Ignition Engines - A Literature Survey", SAE Technical Paper 940987, 1994, doi:10.4271/940987.

[104] Ozol-Godfrey, A., “Understanding Scaled Prediction Variance Using Graphical Methods for Model Robustness, Measurement Error and Generalized Linear Models for Response Surface Designs", Ph.D. Thesis, Virginia Polytechnic Institute and

State University, 2004.

[105] Peters, H., “Der Einfluss von Zündungen an heißen Oberflächen auf den Verbrennungsablauf in Ottomotoren bei hohen Verdichtungsverhältnissen", Ph.D. Thesis, RWTH Aachen, 1964.

[106] Petersen, E.L., Hall, J.M., Smith, S.D., Vries, J. de et al., “Ignition of Lean Methane-Based Fuel Blends at Gas Turbine Pressures", Journal of Engineering for Gas Turbines and Power Vol. 129(4):937–944, 2007, doi:10.1115/1.2720543.

[107] Petersen, E.L., Röhrig, M., Davidson, D.F. and Hanson, R.K., “High Pressure Methane Oxidation Behind Reflected Shock Waves", Twenty-Sixth Symposium (International) on Combustion/The Combustion Institute:799–806, 1996.

[108] Pineda, D.I., Wolk, B., Chen, J.-Y. and Dibble, R.W., “Application of Corona Discharge Ignition in a Boosted Direct-Injection Single Cylinder Gasoline Engine: Effects on Combustion Phasing, Fuel Consumption, and Emissions", SAE Int. J. Engines 9(3), 2016, doi:10.4271/2016-01-9045.

[109] Pischinger, S., Geiger, J., Neff, W., Böwing, R. et al., “Einfluss von Zuendung und Strömung auf die Magerverbrennung", MTZ Motortechnische Zeitschrift 63(5):388–399, 2002.

[110] Prager, M., “Analytische Modellierung des Betriebsverhaltens eines Gasmotors mit neuem Gaszündstrahlverfahren für hohe Leistungsdichte", Ph.D. Thesis, Technische Universität München, 2010.

[111] Priesching, P., Ramusch, G., Ruetz, J. and Tatschl, R., “3D-CFD Modeling of Conventional and Alternative Diesel Combustion and Pollutant Formation – A Validation Study", SAE Technical Paper 2007-01-1907, 2007, doi:10.4271/2007-01-1907.

[112] Rager, J., “Funkenerosion an Zündkerzenelektroden", Ph.D. Thesis, Universität des Saarlandes, 2006.

[113] Rainer, M., “Verfahren und Vorrichtung zum Ermitteln der Temperatur von Glühstiftkerzen in einem Brennkraftmotor,” DE 102008007393 A1.

[114] Rallis, C.J. and Garforth, A.M., “The Determination of Laminar Burning Velocity", Prog. Energy Combust. Sci., Vol. 6:303–329, 1980.

[115] Ramesh, A., Nagalingam, B. and Gopalakrishnan, K.V., “Investigations on the Design and Performance of Two Types of Hot Surface Ignition Engines", SAE Technical Paper 921632, 1992.

[116] Ratzke, A., “Modellierung der Flammenausbreitung und des Flammenlöschens im Gasmotor", Ph.D. Thesis, Leibniz Universität Hannover, 2013.

[117] Ratzke, A., Schöffler, T., Kuppa, K. and Dinkelacker, F., “Validation of turbulent flame speed models for methane–air-mixtures at high pressure gas engine conditions", Combustion and Flame 162(7):2778–2787, 2015, doi:10.1016/j.combustflame.2015.04.011.

[118] Rohde, S., “Vergleich der Energieumsetzung bei Betrieb eines Ottomotors mit Glüh- und mit Funkenzündung", Ph.D. Thesis, Technische Universität Braunschweig, 1976.

[119] Schmidt, E. and Wenner, K., “Wärmeabgabe über den Umfang eines angeblasenen geheizten Zylinders", Forschung auf dem Gebiet des Ingenieurwesens Vol. 12(2), 1941.

[120] Scholl, F., Gerisch, P., Neher, D., Kettner, M. et al., “Development of a NOx Storage-Reduction Catalyst Based Min-NOx Strategy for Small-Scale NG-Fueled Gas Engines", SAE Int. J. Fuels Lubr. 9(3), 2016, doi:10.4271/2016-32-0072.

[121] Scholl, F., Neher, D., Burkard, D., Kettner, M. et al., “Experiments on Ignition and Combustion Induced by Controlled Hot Surface Ignition in Stationary Engines Running with Natural Gas", in: Günther, M. and Tröger, R. (eds.), *Ignition Systems for Gasoline Engines: 2nd International Conference on Ignition Systems for Gasoline Engines*:159–198, 2014.

[122] Scholl, F., Neher, D., Kettner, M., Hügel, P. et al., “Development and Analysis of a Controlled Hot Surface Ignition System for Lean Burn Gas Engines: ICES2012-81059", Proceedings of the ASME 2012 Internal Combustion Engine Division Spring Technical Conference, 2012, doi:10.1115/ICES2012-81059.

[123] Scholl, F., Neher, D., Kettner, M., Melgar Bachiller, A. et al., “Effects of Intake Pressure and Air-Fuel Ratio on Controlled Hot Surface Ignition operating with Natural Gas", SAE Technical Paper 2015-32-0721, 2015.

[124] Semenov, N.N., “Chemical Kinetics and Chain Reactions", Oxford University Press, London, 1935.

[125] Shah, A., “Improving the Efficiency of Gas Engines Using Pre-Chamber Ignition", Ph.D. Thesis, Lund University, 2015.

[126] Silvis, W.M., “The Algorithmic Structure of the Air/Fuel Ratio Calculation", Horiba Technical Reports, 1997.

[127] Simons, W., “Gleichungen zur Bestimmung der Luftzahl bei Ottomotoren (engl.: Equations to Determine the Air/Fuel Ratio in S.I. Engines)", MTZ Motortechnische Zeitschrift 46(7/8), 1985.

[128] Smith, G.P., Golden, D.M., Frenklach, M., and Moriarty, N.W., “GRI-Mech 3.0", http://www.me.berkeley.edu/gri_mech/.

[129] Spadaccini, L.J. and Colket, M.B., “Ignition Delay Characteristics of Methane Fuels", Prog. Energy Combust. Sci.(Vol. 20):431–460, 1994.

[130] Stat Ease, “Design Expert 10.01.1: User manual", 2017.

[131] Steciak, J., Beyerlein, S. and Budwig, R., “Progress in Catalytic Ignition Fabrication and Modeling: Fabrication Part 1", Final Report KLK762, 2012.

[132] Steciak, J., Beyerlein, S. and Budwig, R., “Progress in Catalytic Ignition Fabrication and Modeling: Modeling Part 2", Final Report KLK762, 2012.

[133] Stephan, K. and Laesecke, A., “The Thermal Conductivity of Fluid Air", J. Phys. Chem. Ref. Data Vol. 14(1):227–234, 1985.

[134] Stuart, H.A., “Improvements in Engines Operated by the Explosion of Mixtures of Combustible Vapour or Gas and Air,” 1890.

[135] Tauer, J., Kofler, H. and Wintner, E., “Laser-initiated ignition", Laser & Photon.

Rev. 4(1):99–122, 2010, doi:10.1002/lpor.200810070.

[136] Toedter, O., Heinz, A., Disch, C., Koch, T. et al., “Comparing Visualization of Inflammation at Transient Load Steps Comparing Ignition Systems", in: Günther, M. and Sens, M. (eds.), *Ignition Systems for Gasoline Engines*, Springer International Publishing, Cham, ISBN 978-3-319-45503-7:190–203, 2017.

[137] Trapp, C., Böwing, R., Birgel, A., Kopecek et al., “GE’s J920 Gasmotor – 10,3 MW Leistung bei bis zu 50 % elektrischem Wirkungsgrad: GE’s J920 gas engine – 10.3 MW power at up to 50 % electrical efficiency", Proceedings of the 10th Dessau Gas Engine Conference:75–89, 2017.

[138] Umweltbundesamt, “Treibhausgas-Emissionen in Deutschland", http://www.umweltbundesamt.de/daten/klimawandel/treibhausgas-emissionen-in-deutschland#textpart-1, May 16, 2017.

[139] Ungut, A. and James, H., “Autoignition of Gaseous Fuel-Air Mixtures Near a Hot Surface", SYMPOSIUM SERIES No. 148, 2001.

[140] United Nations Framework Convention on Climate Change, “Global Warming Potentials", http://unfccc.int/ghg_data/items/3825.php, June 28, 2017.

[141] United Nations Framework Convention on Climate Change, “Paris Agreement", 2015.

[142] van Basshuysen, R. (ed.), “Ottomotor mit Direkteinspritzung und Direkteinblasung", 4th ed., Springer Vieweg, Wiesbaden, ISBN 978-3-658-12214-0, 2016.

[143] van Basshuysen, R. and Schäfer, F. (eds.), “Handbuch Verbrennungsmotoren", 7th ed., Springer Vieweg, Wiesbaden, ISBN 978-3-658-04677-4, 2015.

[144] Vanpee, M., “On the Cool Flames of Methane", Combustion Science and Technology(93):363–374, 1993, doi:10.1080/00102209308935298.

[145] Warnatz, J., Maas, U., and Dibble, R.W., “Combustion: Physical and chemical fundamentals, modeling and simulation, experiments, pollutant formation", 4th ed., Springer, Berlin, ISBN 3-540-25992-9, 2006.

[146] Wember, T., “Technische Statistik und statistische Versuchsplanung", 1999.

[147] Weng, V., Gindele, J., Töpfer, G. and Spicher, U., “Investigation of the Bowl-Prechamber-Ignition (BPI) Concept in a Direct Injection Gasoline Engine at Part Load", SAE Technical Paper 1999-01-3658, 1999.

[148] Westbrook, C.K. and Dryer, F.L., “Chemical Kinetic Modeling of Hydrocarbon Combustion", Prog Energy Combust Sci Vol. 10:1–57, 1984.

[149] Willi, M.L. and Richards, B.G., “Design and Development of a Direct Injected, Glow Plug Ignition-Assisted, Natural Gas Engine", Journal of Engineering for Gas Turbines and Power Vol. 117:799–803, 1995.

[150] Witt, M. and Griebel, P., “Numerische Untersuchung von laminaren Methan/Luft-Vormischflammen: TM-50-00-07", Paul Scherrer Institute, 2000.

[151] World Health Organisation, “Health Aspects of Air Pollution with Particulate Matter, Ozone and Nitrogen Oxide", Report on a WHO Working Group, 2003.

[152] Worret, R., “Zylinderdruckbasierte Detektion und Simulation der Klopfgrenze mit

einem verbesserten thermodynamischen Ansatz", Ph.D. Thesis, Universität Karlsruhe, 2002.

[153] Wunsch, D., Heyne, S., Vos, J.B. and Favrat, D., "Numerical Flow Simulation of a Natural Gas Engine Equipped with an Unscavanged Auto-Ignition Prechamber", Proceedings of the European Combustion Meeting 2007, 2007.

[154] Zacharias, F., "Gasmotoren", Vogel, Würzburg, ISBN 3-8023-1796-3, 2001.

Appendix

A.1 Test Bed Setup

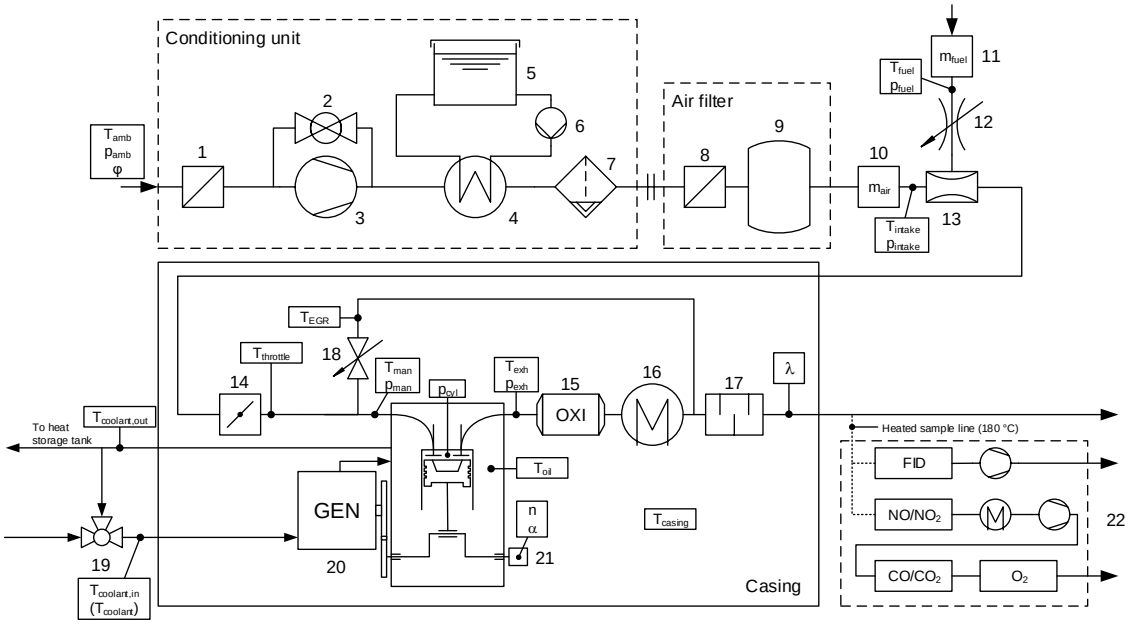

1: Throttle
2: Compressor
3: Bypass valve
4: Heat exchanger
5: Water storrage
6: Water pump
7: Condensation trap
8: Filter
9: Plenum
10: Hot-film air-mass meter
11: Thermal mass flow meter
12: Gas valve
13: Venturi gas-mixer
14: Mixture throttle
15: Oxidation catalyst (dummy used)
16: Exhaust gas heat exchanger
17: Muffler
18: EGR valve
19: 3-way coolant mixing valve
20: Generator
21: Encoder
22: Exhaust gas analyser

Figure A.1: Test bed configuration.

A.2 On the Accuracy of the Wideband λ Sensor Signal

There are several established methods for calculating the relative air-fuel ratio. Their main difference is the complexity of the required equipment and the accuracy of the result. The simplest way to determine λ in lean-burn operation is by using a wideband λ sensor, also referred to as wide range air-fuel ratio (WRAF) sensor, positioned in the preferably hot exhaust stream. The pump current of the sensor's measuring cell correlates with the concentration of wet O_2 in the exhaust gas and allows calculating λ when fuel composition is known. Due to the measuring principle, its readings are subject to error when emissions increase, especially those of unburnt hydrocarbons. Misfires and partial burns when approaching the lean burn or misfire limit are therefore detrimental to the λ signal. A slightly more complex method is employing the mass flows of both intake air and fuel to calculate λ from the actual AFR and the stoichiometric AFR of the fuel. However, small mass flows, strong pulsations and backflow phenomena make accurate measurements of the intake air mass flow of small single cylinder engines highly challenging. Arguably the most accurate method is calculating λ from exhaust gas analysis provided by an exhaust gas measurement system from equations describing the stoichiometry of combustion (e.g. [24, 126, 127]). Unlike the λ sensor, it takes into account the species produced by imperfect combustion, namely HC, NO_x, CO and H_2. Furthermore, both external EGR and internal residual gas can be accounted for, thus yielding the actual relative air-fuel ratio inside the combustion chamber. If residual gas is not considered, the calculated relative air-fuel ratio is that at the intake port, like that determined by the mass flows of air and fuel [92]. An overview of the characteristics of each method is shown in Table A.1:

Table A.1: Overview of conventional methods of determining the relative air-fuel ratio λ.

Method	λ type	Consideration of EGR/residual gas dependency	Consideration of incomplete combustion dependency
WRAF sensor	$\lambda_{throttle}$	no	no
Air and fuel massflow	$\lambda_{throttle}$	no	no
Exhaust gas analysis (EGA)	$\lambda_{throttle}$ / $\lambda_{combustion}$	possible	yes

Residual gas fraction in the cylinder is primarily a function of intake and exhaust pressure, engine speed, compression ratio and valve timing. Effects of combustion phasing, however, are negligible [69]. While all other parameters remain constant or their change is marginal, a reduction of intake pressure leads to a decrease of the exhaust pressure, causing a worsened scavenging of the cylinder, thus increasing the fraction of residual gas. To determine the quantitative effect of p_{man} on residual gas fraction, 1D simulations with a validated model of the test bed engine were carried out in AVL Boost. In Figure A.2 it can be seen that residual gas fraction increases from about 5 % at 950 mbar to nearly 10 % at 500 mbar intake pressure. Since this increase is not considered in the λ calculation algorithm of the ETAS ES635.1 λ meter, the relative air-fuel ratio is actually higher at lower intake pressures, leading to an error of nearly 0.1 in calculated λ.

λ [-]	CA50 [°CA ATDC]	$T_{coolant}$ [°C]	T_{intake} [°C]
1.50	5.0	45.0	23.0

Raw sensor readings:
1: ETAS ES635 Lambda meter + Bosch LSU4.9

Calculated from exhaust gas concentration assuming:
2: 0 % RG fraction
3: 5 % RG fraction
4: variable RG fraction → $f(p_{man})$

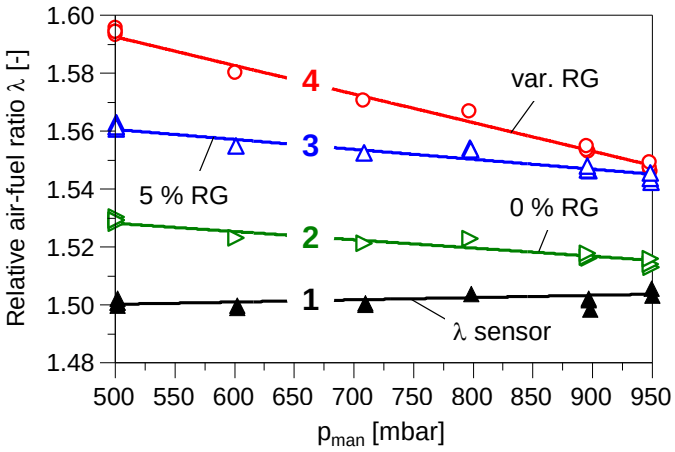

Figure A.2: Comparison of different methods to determine the relative air-fuel ratio λ.

A.3 Empirical Submodels for 0D HSI Engine Process Simulation

Mass flow model

Since the 0D model calculates the mass flows of air and fuel from the displacement volume and given intake manifold pressure and engine speed, an empirical mass flow correction factor c_m was employed to account for the gas dynamic effects presented:

$$c_m = 0.002323 \cdot p_{man} - 1.44 \qquad \text{for } p_{man} \geq 900 \text{ mbar}$$
$$c_m = 0.000201 \cdot p_{man} + 0.47 \qquad \text{for } p_{man} < 900 \text{ mbar} \tag{A-1}$$

It should be noted that this correction only allows for accurate predictions of the air and fuel mass flows at rated engine speed (2450 1/min) and without external EGR, as both parameters exert great influence on the gas exchange.

Residual Gas Model

Engine process calculation is highly sensitive to errors in the thermodynamic state of the in-cylinder charge at the beginning of compression. In-cylinder mass at IVC is calculated from the mass flows of air and fuel and the fraction of residual gas (RG). There are several models for calculating RG fraction, ranging from simple approaches using mean values of intake manifold and exhaust gas pressure to temporally resolved models for post-processing that require low-pressure indication [16]. The approach taken here to express RG fraction x_{RG} as a function of p_{man} was to evaluate the throttle position variation simulated using the 1D simulation model of the engine. The results revealed a faily linear dependency, with an increase of RG fraction from about 5.5 % at p_{man} = 950 mbar to about 9.5 % at p_{man} = 500 mbar. The following correlation was subsequently used in the 0D model:

$$x_{RG} = -0.00889 \cdot p_{man} + 13.99 \tag{A-2}$$

Inlet Valve Closing Pressure Correction Model

Knowing the mass flows and the residual gas fraction, the in-cylinder mass is defined and only one more parameter needs to be determined to fully describe the charge state at the start of compression, according to the ideal gas law:

$$\boldsymbol{p_{IVC}} \cdot V_{IVC} = m_{cyl} \cdot R_s \cdot \boldsymbol{T_{IVC}} \tag{A-3}$$

V_{IVC} is given by engine geometry, m_{cyl} and R_s by mixture composition and intake manifold pressure. p_{IVC} and T_{IVC} cannot be set independently but one is always proportional to the other, given that the other parameters remain unchanged. As p_{IVC} is readily measurable from the in-cylinder pressure trace while T_{IVC} needs to be calculated, an empirical model for p_{IVC} was derived. To this end, fired and motored pressure curves for varying intake manifold pressure were recorded. Valve closing vibration in the in-cylinder pressure signal was used to determine the exact position of α_{IVO}, and the required reading for p_{IVC}. The results for motored operation (only air) were always about 10 mbar higher than for fired operation due to a slight dethrottling effect (minor increase of p_{man}) when cutting off the gas supply. For this reason results from fired operation were taken for the following p_{IVC} correlation:

$$\begin{aligned} p_{IVC} &= 4.3462 \cdot p_{man} - 3103.8 && \text{for } p_{man} \geq 900 \text{ mbar} \\ p_{IVC} &= 0.9296 \cdot p_{man} - 45.4 && \text{for } p_{man} < 900 \text{ mbar} \end{aligned} \tag{A-4}$$

Heat Release Model

The OFAT experiments from Section 0 were used to find parameters a and m for the parametric Vibe function to simulate heat release in the 0D predictive model, according to the following equation:

$$MFB(\alpha) = 1 - e^{-a \cdot \left(\frac{\alpha - \alpha_{SOC}}{CD}\right)^{m+1}} \tag{A-5}$$

with the combustion duration

$$CD = \alpha_{EOC} - \alpha_{SOC} \tag{A-6}$$

where α_{SOC} is the crank angle for the start and α_{EOC} for the end of combustion. For spark ignition, parameter α_{SOC} can be determined easily by setting it equal to spark timing. For HSI, however, this parameter is unknown. It was initially expected that the timing of mixture inflammation could be determined from the photomultiplier signal but this was impeded by the low overall transmission efficiency combined with deposits on the optical access. Instead, following approach was used:

– Derive CA5 and CA90 from calculated heat release profile from experimental data.

- Set $a = 2.3$ (90 % of mass fraction burnt (MFB) at the end of α_{EOC}, alternatively it applies that $a = 6.908$ for 99.9 % MFB or $a = 2.995$ for 95 % MFB).
- Set α_{EOC} = CA90.
- Set α_{SOC} = CA5 – x.
- Adjust x and m for best fit for all experimental data.

The form factor m defines the evolution of MFB over crank angle. For $2 < m < 3$, the trace of ROHR is quite symmetrical. $m \to 0$ leads to a faster first part of combustion and a more sluggish second part. Conversely, setting $m > 3$ results in a slower first and a rapid second part of combustion. As illustrated in Figure A.3, one set of parameters works fairly well when the ensemble-mean pressure trace is used to calculate the normalised cumulated heat release. However, due to the flame front-piston interaction that occurs for fast-burning cycles with overadvanced combustion phasing, it is impossible to approximate them using a single Vibe function. Nonetheless, the fitted values for m and x proved to allow for a satisfactory approximation of the heat release for most operating points of the CA50 and p_{man} sweeps and were therefore used for the model.

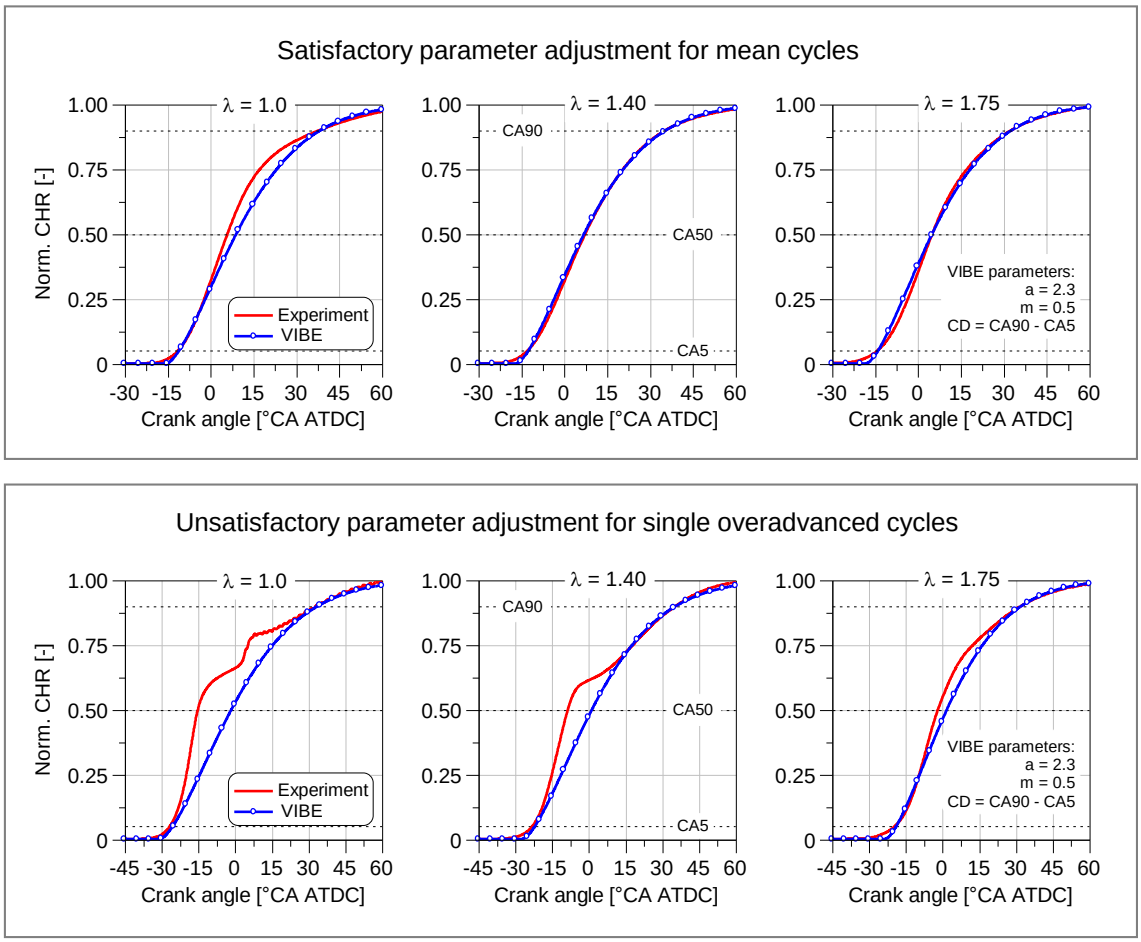

Figure A.3: Normalised cumulated heat release of experiment and adjusted Vibe function at $\lambda = 1.0/1.4/1.75$ for mean cycle (top) and single overadvanced cycles where single Vibe function fails in representing heat release satisfactorily ($CA50_{mean} \approx 5$ °CA ATDC, $p_{man} = 950$ mbar, $T_{coolant} = 45$ °C, $T_{intake} = 23$ °C). Experimental heat release is derived from the ensemble-mean pressure trace.

A.4 Thermo-electric glow plug model

Derivation of Eq. (6-1)

The resistance of the heating cap is calculated to:

$$R_{HC} = a_{HC} \cdot (T_{HS} - T_0) \tag{A-7}$$

with the linear RT correlation for the hot surface:

$$a_{HC} = \frac{R_{HC,ref}}{T_{HS,ref} - T_0} \tag{A-8}$$

The resistance of the electrical leads is calculated to:

$$R_{leads} = a_{leads} \cdot \left(T_{adapter} - T_0\right) \tag{A-9}$$

with the linear RT correlation for the electrical leads:

$$a_{leads} = \frac{R_{leads,ref}}{T_{leads,ref} - T_0} \tag{A-10}$$

Eq. (A-11) yields the total resistance of the glow plug:

$$R_{HSI} = R_0 + R_{HC} + R_{leads} \tag{A-11}$$

Since adapter temperature $T_{adapter}$ is measured, hot surface temperature T_{HS} can be calculated after inserting Eq. (A-7) and (A-9) into Eq. (A-11):

$$T_{HS} = \frac{1}{a_{HC}}\left[R_{HSI} - R_0 - a_{leads} \cdot \left(T_{adapter} - T_0\right)\right] + T_0 \tag{A-12}$$

Sensitivity Analysis for Conduction and Radiation

The equations to describe the transfer through conduction and radiation are rather simple and depend on a manageable number of parameters. Radiation between the hot surface and the shield walls can be expressed as:

$$\dot{Q}_{rad} = \frac{\sigma \cdot \left({T_{shield}}^4 - {T_{HS}}^4\right)}{\frac{1 - \varepsilon_{HS}}{A_{HS} \cdot \varepsilon_{HS}} + \frac{1}{A_{HS} \cdot F_{1\to2}} + \frac{1 - \varepsilon_{shield}}{A_{shield} \cdot \varepsilon_{shield}}} \tag{A-13}$$

with σ being the Stefan–Boltzmann constant. The heat losses through conduction to the adapter can be calculated from Eq. (A-14), when assuming an infinite wall with constant properties and thickness s_{HS}, at steady-state conditions:

$$\dot{Q}_{cond} = \frac{k}{s_{HS}} \cdot A_{cond} \cdot \left(T_{adapter} - T_{HS}\right) \tag{A-14}$$

HS is a grey body with an assumed emission coefficient of 0.9. Since bulk of the convex hot surface is enclosed in the concave shield, it is assumed that the view factor of thermal radiation $F_{1\to2} = 1$ and interaction with the piston is neglected.

To evaluate the possible error arising from made assumptions in unknown parameters, a full factorial DoE case study was performed using Eq. (4-5) and setting $\dot{Q}_{conv} = 0$, where each factor was set to several levels, as shown in Table A.2:

Table A.2: Parameter range for sensitivity analysis of factors determining heat losses of the hot surface by conduction Q'$_{cond}$ and radiation Q'$_{rad}$

Factor	Description	Low level (-1)	High level (1)
A - k	Specific heat conductivity of glow plug	10 W/mK	80 W/mK
B - $F_{1\to2}$	View factor between surface 1 and 2	0.6	1
C - ε_{shield}	Emissivity of shield	0.2	1
D - $T_{adapter}$	Adapter temperature	423 K	573 K
E - T_{HS}	Hot surface temperature	1273 K	1523 K
F - T_{shield}	Shield temperature	673 K	873 K

Figure A.4 depicts the perturbation plots for both types of heat transfer. In terms of conduction, the specific heat conductivity k has the largest impact on heat losses.

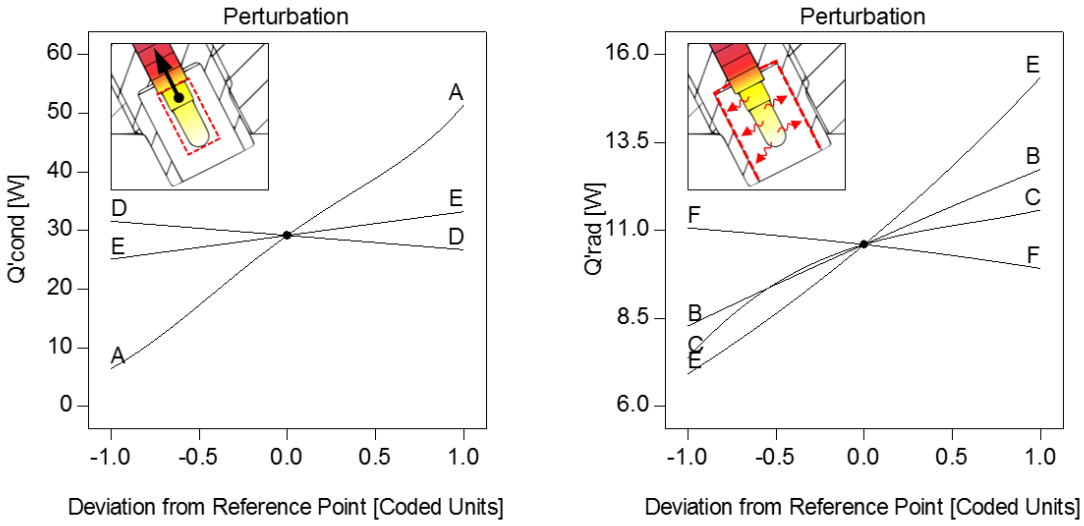

Figure A.4: Perturbation plot for heat transfer through conduction $\dot{Q}_{cond}$ (left) and radiation $\dot{Q}_{rad}$ (right).

As can be extracted from Table A.3, for an assumed value of $k = 30$ W/mK, an uncertainty of +/-5 W/mK would cause a significant error in $\dot{Q}_{cond}$ and, in turn, P_{HC}, of about +/- 7.3 W when operating at $T_{HS} = 1200$ °C. Radiation is most sensitive to HS temperature and the emissivity of the shield. Under the assumption that the highly reflective surface of the shield has an emissitivity of $\varepsilon = 0.3$ +/- 0.1, the error in P_{HC} at $T_{HS} = 1200$ °C amounts to approximately +/- 1.7 W. At the same temperature, an un-

certainty in T_{HS} of +/-50 °C causes an error in P_{HC} of about +/- 1.9 W. It can therefore be concluded that the heat transfer coefficient represents the largest source of error in the energy balance of the hot surface. Special attention should be paid to this parameter when validating the thermo-electric glow plug model with experimental data.

Table A.3: Computed error in $\dot{Q}_{cond}$ and $\dot{Q}_{rad}$ for assumed uncertainty.

Factor	Set value	Approx. uncertainty	Error in Q'cond	Error in Q'rad
A - k	30 W/mK	+/- 5 W/mK	+/- 3.63 W	
B - $F_{1\to2}$	1.0	0.1		- 0.81 W
C - ε_{shield}	0.3	0.1		+/- 0.84 W
D - $T_{adapter}$	280 °C	+/- 25 °C	+/- 0.52 W	
E - T_{HS}	1200 °C	+/- 25 °C	+/- 0.53 W	+/- 0.93 W
F - T_{shield}	450 °C	+/- 25 °C		+/- 0.11 W

A.5 RSM Run Sheet

Table A.4: Run sheet for RSM experiments from Section 7.4.

Run	Glow plug No.	Build Type	A: p_man	B: T_coolant	C: Lambda	D: CA50	E: T_intake
[-]	[-]	[-]	[mbar]	[°C]	[-]	[°CA ATDC]	[°C]
1	5	Model	950.0	60.0	1.685	11.0	29.6
2	5	Lack of Fit	752.0	55.6	1.000	0.0	36.0
3	5	Lack of Fit	709.3	41.7	1.000	5.9	25.0
4	5	Replicate	950.0	32.9	1.484	15.0	32.7
5	5	Model	862.3	52.1	1.530	11.5	45.0
6	5	Replicate	830.8	36.4	1.224	4.4	39.5
7	5	Model	626.0	25.0	1.205	0.0	29.7
8	5	Model	612.5	51.6	1.000	11.1	40.0
9	5	Model	635.0	36.6	1.221	7.4	38.0
10	5	Model	500.0	25.0	1.000	2.8	41.2
11	5	Model	847.6	30.4	1.708	12.1	25.0
12	5	Model	830.8	36.4	1.224	4.4	39.5
13	6	Model	862.3	35.5	1.000	0.0	30.9
14	6	Model	950.0	26.9	1.635	0.0	42.7
15	6	Model	950.0	25.0	1.000	9.0	25.0
16	6	Model	895.3	25.0	1.143	12.1	44.5
17	6	Model	567.5	48.3	1.232	10.1	31.0
18	6	Model	545.0	60.0	1.000	3.3	27.5
19	6	Model	950.0	50.9	1.770	15.0	41.7
20	6	Model	500.0	36.0	1.539	0.4	25.0
21	6	Replicate	862.3	52.1	1.530	11.5	45.0
22	6	Model	601.3	53.7	1.604	15.0	25.0
23	6	Model	885.3	53.2	1.706	3.9	30.5
24	6	Model	781.3	25.0	1.488	3.8	28.0
25	6	Model	598.5	35.0	1.597	4.5	45.0
26	6	Model	709.3	60.0	1.549	0.0	40.0
27	6	Lack of Fit	583.3	60.0	1.584	4.1	25.0
28	6	Model	500.0	31.0	1.077	14.6	26.7
29	6	Replicate	567.5	48.3	1.232	10.1	31.0
30	6	Model	950.0	60.0	1.077	3.6	44.5
31	6	Model	500.0	51.1	1.170	0.0	45.0
32	6	Model	500.0	25.0	1.545	12.6	38.4
33	6	Model	891.5	52.1	1.000	15.0	33.1

34	6	Model	500.0	60.0	1.310	15.0	42.3
35	6	Model	950.0	32.9	1.484	15.0	32.7
36	6	Model	614.8	31.1	1.000	15.0	45.0
37	6	Model	826.3	60.0	1.155	13.5	25.0
38	6	Lack of Fit	765.5	25.0	1.000	15.0	33.0
39	6	Centre	762.0	45.1	1.452	8.1	35.0
40	6	Model	950.0	52.0	1.329	1.1	25.0
41	6	Replicate	635.0	36.6	1.221	7.4	38.0
42	6	Lack of Fit	718.3	60.0	1.669	15.0	36.3